

NUMERICAL MODELLING OF THE SNOW FLOW CHARACTERISTICS
SURROUNDING SANAE IV RESEARCH STATION, ANTARCTICA

Dissertation approved for the degree

Doctor of Philosophy in Engineering Science
(Mechanical Engineering)

by

JOHANNES HENRICUS MEIRING BEYERS



in the Faculty of Engineering

Department of Mechanical Engineering

University of Stellenbosch

Stellenbosch, South Africa

December 2004

Promotor:

A/Prof. T.M. Harms

Declaration

I, the undersigned, hereby declare that the work contained in this dissertation is my own original work and that I have not previously in its entirety or in part submitted it at any university for a degree.

Signature :

Date :



ABSTRACT

This work is concerned with the numerical simulation of the aeolian snow transportation process (drifting or wind blown snow) and especially the snow deposition and erosion phenomenon (snow drift). The research work is interested in modelling the atmospheric boundary layer wind flow and its associated snow drifting processes around three-dimensional obstacles by means of computational fluid dynamics (CFD).

A modelling method is required to predict and evaluate the snow drifting phenomenon surrounding the SANAE IV research station in Antarctica. This station is of an elevated design to ensure that wind blown snow may travel around the structure relatively undisturbed and without deposition near the structure. This design is partly successful but localised drifts are formed especially leeward of the interconnecting structures that join the main building sections together.

The theoretical and numerical description to describe the turbulent transport of the two-phase mixture of air and snow particles is investigated. This theory is subsequently employed to describe the snow deposition and erosion process and two models are developed to determine the deposition flux onto the snow surface. These models presented and discussed are a threshold based approach and a conservative based approach. The first model is dependent on a threshold shear velocity to determine the onset of either erosion or deposition. The second model determines the deposition or erosion flux based on the conservation of the snow mass transport in the near surface control volume. A numerical scheme that evaluates the snow deposition flux at the surface and forces a temporal surface adaptation during the simulation is established and implemented in a commercial CFD software code by means of user subroutines.

Various test cases for which observed snow drift data are available are numerically modelled to validate the snow drift schemes presented in this work. These tests include the wind driven snow accumulation around a three-dimensional cube, around two adjacent three-dimensional cubes and near a typical porous snow fence. The results indicate that both methods can predict realistic snow drifts for a variety of wind flow conditions but also show that the conservative approach is superior to the threshold based approach in describing the snow drift process

around obstacles. This model allows drifts to form not only in areas of low flow velocities but also under high shear conditions. The theoretical investigation and the development and validation of the conservatively based snow drift scheme shows that drift formation depends strongly on the near surface flow divergence and secondary flow structures. To resolve the snow drift formation under a variety of flow conditions a three-dimensional field solution is required to determine velocity and snow concentration gradients and include the effects of near surface convective and turbulent entrainment.

The model is applied to numerically simulate and predict snow drifting around the SANAE IV base for a moderate as well as a high wind speed event. The predicted snow drift around the base agrees favourably with the observed drifts at the station. Further numerical simulations are carried out to evaluate the effects a few design modifications may have on the snow deposition. These results suggest that a simple baffle plate installation near the bottom of the interconnecting link structures may minimise the snow accumulation leeward of that area.

This study shows that to achieve realistic numerical snow drift predictions around, on or near obstacles, a conservative based snow drift scheme should be considered using some form of temporal terrain adaptation strategy. Only then does one include a sufficient level of important flow effects such as deposition along near surface boundaries of strong flow divergence which plays as an important role as vertical settling and entrainment in determining deposition rates.

OPSOMMING

Hierdie studie behels die numeriese simulatie van windgedrewe sneeubeweging asook die daarmee gepaardgaande sneeu neerslag en erosie eienskappe. Die navorsing het verder belang in die berekening van die atmosferiese grenslaag vloei en die simulatie van sneeu neerslag naby drie-dimensionele strukture deur gebruik te maak van berekeningsvloei-meganika (BVM).

'n Berekeningsmetodiek is nodig om die eienskappe van die sneeu neerslag rondom die SANAE IV navorsingsstasie in Antarktika te voorspel en te evalueer. Die bogrondse struktuur is spesifiek so ontwerp om te verseker dat wind gedrewe sneeu hoofsaaklik onversteurd verby die struktuur kan beweeg sonder neerslag teenaan die struktuur. Die ontwerp is grotendeels suksesvol alhoewel sneeu neerslag wel lokaal plaasvind, wind af vanaf die aansluitingsstrukture tussen die hoof geboue.

Die teoretiese en numeriese beskrywing van die twee-fase lug- en sneeumengsel beweging word ondersoek en gebruik om die sneeu neerslag en erosie eienskappe te beskryf. Twee modelle wat hierdie verskynsel beskryf word beskryf en bespreek naamlik 'n drumpel gebaseerde benadering en 'n konserwatief gebaseerde benadering. Die eerste model is afhanklik van 'n drumpel skuifsnelheid om die aanvang van of erosie of neerslag te bereken. Die tweede model bereken die neerslag eerder gebaseer op die behoud van die sneeu massa vloei in die kontrole volume naby aan die oppervlak. 'n Numeriese metode is ontwikkel en geïmplementeer in 'n kommersiële BVM sagteware pakket deur van gebruikerssubroetine gebruik te maak. Die ontwikkelde kode evalueer die sneeu neerslag vloei by die oppervlak en forsee 'n tydafhanklike oppervlak aanpassing gedurende die simulatie.

Die sneeu neerslag metode wat beskryf word in hierdie studie word ge-evalueer teen verskeie toetsgevalle waarvoor daar waargenome sneeu neerslag resultate beskikbaar is. Hierdie toetsluit in die wind gedrewe sneeu neerslag rondom 'n drie-dimensionele kubus, rondom twee naby geleë kubusse en naby 'n tipiese poruese sneeu heining. Die resultate dui aan dat beide die metodes realistiese sneeu neerslag voorspel vir verskeie wind toestande. Die studie wys ook dat die konserwatief gebaseerde benadering vir die beskrywing van die sneeu neerslag proses meer akkuraat is as die drumpel gebaseerde benadering aangesien die neerslag

voorspel kan word nie net alleenlik in gebiede met lae vloeisnelhede nie, maar ook in gebiede waar hoë skuifnelhede teenwoordig is. Die teoretiese ondersoek, ontwikkeling en toepassing van die konserwatief gebaseerde model dui daarop dat die neerslag afhanklik is van die divergensie van die vloeiveld asook van die sekondêre vloei patrone naby die oppervlak. Ten einde die sneeu neerslag vir verskeie toestande op te los is dit nodig om snelheids- en sneeukonsentrasie gradiënte te kan bereken in 'n drie-dimensionele vloei veld om sodoende die invloed van naby-oppervlak konveksie en turbulente verspreiding in ag te neem.

Die metode word toegepas deur die sneeu neerslag rondom die SANAE IV navorsingsstasie te voorspel vir 'n gematigde asook 'n hoë wind snelheid toestand. Die sneeu neerslag voorspelling stem gunstig ooreen met die waargenome neerslag by die struktuur. Verdere numeriese simulaties is uitgevoer om die invloed van ontwerpverandering op die neerslag te evalueer. Uit hierdie resultate blyk dit dat 'n eenvoudige plaat struktuur onder die aansluitingsstrukture die sneeu neerslag wind af mag verminder.

Hierdie navorsingsstudie dui daarop dat 'n tydafhanklike terrein aanpassing strategie saam met die konserwatiewe neerslag model noodsaaklik is ten einde realistiese resultate te behaal vir die sneeu opbou rondom of naby strukture. Sodoende word genoegsame vlakke van belangrike vloei verskynsels, soos die invloed van vloei divergensie, in ag geneem wat net so 'n belangrik rol in neerslag speel soos vertikale afsetting.

ACKNOWLEDGEMENTS

I wish to thank the following persons and institutions for their valuable contributions towards this research.

Dr. Thomas Harms as supervisor and mentor, for his encouragement, guidance and continued support during the course of this work. His interest and willingness to engage in stimulating discussions in this field is gratefully appreciated.

Dr. Per Arne Sundsbø for the invitation and research funding to stay at the Narvik Institute of Technology, Norway, and for the warm Norwegian welcome I received. The numerous discussions on numerical snow drift analysis and exciting field work experiences in the north of Norway was invaluable.

The Department of Environmental Affairs and Tourism, for the research funding and the logistical assistance to enable the Antarctic field work and their initiative to include engineering science into the South African National Antarctic Program. Without their financial support the attendance at international conferences would also have been impossible.

A few people kindly made valuable time and information available to assist this study namely Dr. Adam Goliger (CSIR), Dr. Salem Alhajraf (KISR), Dr. Thomas Thiis (ByggNorsk), Mr. Phillippe Delpech (CSTB), Mr. Bill Waechter (RWDI), Dr. David Blake (BAS), Mr. Axel Ruelke (AWI).

The Antarctic field experiments would not have been possible without the skilful and professional support of Mr. Mike Cotton (MCS) who took great care to supply the wind anemometers, Mr. Mike Struthers (CSIR) for the loan of logging equipment and the Centre for Mechanical Services (SMD) who was responsible for the fabrication of the experimental equipment and snow drift models.

And a very special thanks for their support to all the friends, to my parents, brother and sister and to my wonderful wife.

CONTENTS

DECLARATION	ii
ABSTRACT	iii
OPSOMMING	v
ACKNOWLEDGEMENT	vii
CONTENTS	viii
LIST OF FIGURES	xii
LIST OF TABLES	xvii
NOMENCLATURE	xviii
1. INTRODUCTION	1
1.1. SNOW DRIFTING IN ANTARCTICA	1
1.1.1. Habitation in the Antarctic environment	1
1.1.2. SANAE IV (South Africa)	6
1.1.3. Halley 5 (United Kingdom)	10
1.1.4. Amundsen-Scott (United States of America)	11
1.1.5. Concordia (France / Italy)	13
1.1.6. Summer base Kohnen (Germany)	14
1.2. SNOW DRIFT ANALYSIS	15
1.2.1. Observation, experimental modelling and numerical simulation	15
1.3. RESEARCH OBJECTIVE AND CONTRIBUTION	19
2. NUMERICAL SIMULATION OF WIND-BORNE SNOW AND SNOW DRIFTING	25
2.1. INTRODUCTION	25
2.2. MULTIPHASE FLOW IN THE ATMOSPHERIC SURFACE LAYER	26
2.2.1. The multiphase continuum	26
2.3. MULTIPHASE MODEL	29
2.3.1. Continuity equation for phase k	29

2.3.2. Momentum conservation of phase k	30
2.4. MIXTURE MODEL (DIFFUSION MODEL)	30
2.4.1. Mixture model properties	30
2.4.2. Mixture continuity	32
2.4.3. Mixture momentum conservation	33
2.4.4. Relative velocity (one dimensional derivation)	33
2.4.5. Particle size distribution	38
2.4.6. Mixture diffusion equation	42
2.5. TURBULENCE MODELLING	43
2.5.1. Reynolds averaged Navier Stokes equations (RANS)	43
2.5.2. Turbulence kinetic energy equation	44
2.5.3. Rate of turbulent energy dissipation equation	45
2.5.4. Wall functions	46
2.6. SNOW DRIFTING MODELLING	48
2.6.1. Saltation and suspension of snow	48
2.6.2. Erosion / Deposition scheme	57
2.7. NUMERICAL MODEL OF WIND-BORNE SNOW DRIFT	68
2.7.1. The modelling technique	68
2.7.2. Surface adaptation	77
2.7.3. Boundary conditions	78
2.7.4. Implementation of the snow drift model in FLOW3D	81
3. SIMULATION OF SNOW DRIFT AROUND A THREE-DIMENSIONAL CUBE	83
3.1. EXPERIMENTAL WORK AT SANAE IV, ANTARCTICA	83
3.2. THE NUMERICAL MODEL	85
3.2.1. The turbulent flow field	88
3.3. SNOW DRIFT SIMULATION MODEL I	95
3.4. SNOW DRIFT SIMULATION MODEL II	99

4. SIMULATION OF SNOW DRIFT AROUND A POROUS SNOW FENCE	107
4.1. EARLIER EXPERIMENTAL AND NUMERICAL WORK	107
4.2. TWO-DIMENSIONAL MODEL OF SNOW DRIFT AROUND A 50% POROUS FENCE	112
4.3. RESULTS AND DISCUSSION	114
4.4. THREE-DIMENSIONAL MODEL OF SNOW DRIFT AROUND A 50% POROUS FENCE	121
5. FURTHER SNOW DRIFT VALIDATION	129
5.1 INTRODUCTION	129
5.2 SIMULATION OF SNOW DRIFT AROUND TWO ADJACENT CUBICAL BUILDINGS	129
5.2.1. Experimental results	129
5.2.2. Simulation parameters	130
5.2.3 Results and discussion	132
6. MODELLING SNOW DRIFT AROUND SANAE IV	139
6.1. INTRODUCTION TO THE PROBLEM	139
6.2. OUTDOORS SNOW DRIFT EXPERIMENTAL MODEL	141
6.3. THREE-DIMENSIONAL NUMERICAL SIMULATION	144
6.3.1. The numerical model	144
6.3.2. Simulation results and discussion	146
6.4. SANAE IV DESIGN MODIFICATIONS NUMERICAL SIMULATION	162
6.4.1. Proposed design modifications	162
6.4.2. Results, discussion and recommendation	165
7. CONCLUSIONS	173
7.1. NUMERICAL SNOW DRIFT MODELLING	173
7.2. SANAE IV SIMULATIONS AND RESULTS	176
7.2. RECOMMENDATIONS FOR FUTURE WORK	178

APPENDIX A: VOLUME AVERAGE THEOREMS	183
APPENDIX B: VOLUME-TIME AVERAGING OF THE CONTINUITY EQUATION	187
APPENDIX C: VOLUME-TIME AVERAGING OF THE MOMENTUM EQUATION	189
APPENDIX D: THE DISPERSED PHASE MASS CONSERVATION EQUATION (DIFFUSION EQUATION)	193
APPENDIX E: ANALYTICAL SOLUTION OF THE TURBULENT VELOCITY PROFILE	195
APPENDIX F: ANALYTICAL SOLUTION OF THE SNOW CONCENTRATION PROFILE	199
APPENDIX G: EXPERIMENTAL MODELLING	203
APPENDIX H: VISIBILITY IN BLOWING SNOW	225
APPENDIX I: MODIFIED k-ϵ TURBULENCE MODEL	229
REFERENCES	233

LIST OF FIGURES

1.1	Large natural wind scour around the foot of Northern Butress, Vesleskarvet, 71°41'S, 2°49'W, Antarctica	3
1.2	SANAE IV research station situated on the nunatak, Vesleskarvet in Dronning Maud Land, Antarctica	7
1.3	Dronning Maud Land, Antarctica showing the location of SANAE IV (South Africa), Neumayer (Germany), Troll (Norway) and Maitri (Russia). Map courtesy of Mr. Axel Ruelke, Department of Geodesy, TU-Dresden, Germany	8
1.4	Halley 5 (75°S, 27°W) on the Brunt Ice Shelf, Antarctica (Picture from www.antarctica.ac.uk)	10
1.5	The layout and view of the new South Pole station under construction at the south pole with the old geodesic dome pictured located to the left of the new station (Picture from http://www.spole.gov)	12
1.6	The new South Pole station, Amundsen-Scott station under construction at the south pole (Picture M. Connor, NSF from http://photolibrary.usap.gov)	13
1.7	The jackable Concordia station (France / Italy) located at Dome C, East Antarctica	14
1.8	Snow drift numerical analysis specifications	16
2.1	Particle fall speed as a function of particle diameter	37
2.2	Particle drag coefficient vs. particle diameter	37
2.3	Height distribution of the mean particle diameter, reference height 0.5m	41
2.4	Height distribution of the particle mean fall velocity	41
2.5	Control volume with the near surface snow mass conservation	61
2.6	FAVOR description of the fractional area and volume	74
2.7	Surface adaptation and area and volume fraction modification	76
3.1	Extrapolated 10 m wind speeds, average wind speed and wind direction for the period 23/01/2002 – 26/01/2002	84
3.2	Observed snow build-up behind the 2 m cube, near SANAE IV, on 26/01/2002. Observer is looking west with Vesleskarvet and SANAE IV in the background	85
3.3	Computational domain for the three-dimensional cube simulation	86

3.4	Computational mesh for the fine grid for the cube snow drift simulation	87
3.5	Pressure coefficient calculation on the cube surfaces	90
3.6	Velocity distribution results in the x/z plane at y/h=0.0	90
3.7(a)	Vector field plot for x/y plane at z/h=0.055	91
3.7(b)	Vector field plot for x/z plane at y/h = 0.0	91
3.7(c)	Vector field plot for y/z plane at x/h=2.595	92
3.8(a)	Contour plot of the near surface friction velocity in the x/y plane at z/h=0.01	94
3.8(b)	Contour plot of the near surface snow fraction in the x/y plane at z/h=0.055	95
3.9	Three-dimensional snow drift prediction at the end of the simulation (Model I)	96
3.10	Snow drift height contours results from Model I simulation at the (a) beginning, (b) halfway through and (c) at the end of the simulation	98
3.11	Three-dimensional snow drift prediction at the end of the simulation for Model II	100
3.12	Snow drift height contour results from Model II simulation at the (a) beginning, (b) halfway through and (c) at the end of the simulation	101
3.13	Detailed view of windward accumulation at the end of the simulation (Model II)	102
4.1	Characteristic snow drift dimension around a Wyoming type snow fence, Tabler (1980a, 1991b) - not drawn to scale	109
4.2	Two-dimensional computational domain for a snow drift simulation around a 50% porous fence	112
4.3	Computational domain for the snow fence simulation - not to scale	113
4.4	Snow drift development over time for $u_* = 0.30 \text{ m}\cdot\text{s}^{-1}$, (a) $t=40 \text{ s}$, (b) $t=80 \text{ s}$, (c) $t=120 \text{ s}$, (d) $t=160 \text{ s}$, (e) $t=200 \text{ s}$	116
4.5	Snow drift development over time for $u_* = 0.35 \text{ m}\cdot\text{s}^{-1}$, (a) $t=40 \text{ s}$, (b) $t=80 \text{ s}$, (c) $t=120 \text{ s}$, (d) $t=160 \text{ s}$, (e) $t=200 \text{ s}$	117
4.6	Snow drift development over time for $u_* = 0.50 \text{ m}\cdot\text{s}^{-1}$, (a) $t=40 \text{ s}$, (b) $t=80 \text{ s}$, (c) $t=120 \text{ s}$, (d) $t=160 \text{ s}$, (e) $t=200 \text{ s}$	118
4.7	Velocity vectors in the vicinity of the two-dimensional snow fence before snow drifting starts (a) and at the end of the simulation (b) for an upstream shear velocity of $0.35 \text{ m}\cdot\text{s}^{-1}$	119
4.8	Snow drift profile development from simulated results for $u_* = 0.30 \text{ m}\cdot\text{s}^{-1}$, $u_* = 0.35 \text{ m}\cdot\text{s}^{-1}$ and $u_* = 0.50 \text{ m}\cdot\text{s}^{-1}$ compared to the empirical profile of Tabler	120

	(1980a) and Iversen (1981)	
4.9	Computational domain for the three-dimensional simulation of snow drift around a 50% porous fence - fence details for illustrative purposes only	121
4.10	Computational mesh details in the xz-plane (a) and the yz-plane (b) for the three-dimensional simulation around a 50% porous fence - position of the porous baffle for illustration only	122
4.11	Height contours of the snow drift development at the (a) start of the drift, (b) at an intermediate stage during the simulation and (c) at the end of the simulation	124
4.12	Two views of the three-dimensional profile of the snow drift surrounding a 50% porous fence with inlet wind friction velocity $u_* = 0.35 \text{ m}\cdot\text{s}^{-1}$	125
4.13	Snow drift profile in the x-z plane at $y=0.0\text{m}$ predicted by the three-dimensional simulation for $u_* = 0.35 \text{ m}\cdot\text{s}^{-1}$ compared to two-dimensional results and measurements from Tabler (1980a) and Iversen (1981)	126
5.1	Contour map of snow drift development around two cubicle structures. Contour data courtesy of Thiis (2003)	130
5.2	Computational domain for the three-dimensional simulation of the snow drift around two adjacent cubical buildings	131
5.3	Computational mesh for simulation of the two adjacent cubes	131
5.4	Streamline plot around the two adjacent cubes	134
5.5	Shear velocity contour plot for two adjacent cubes after $t=20 \text{ s}$	134
5.6	Near surface snow fraction contour plot around two adjacent cubes after $t=20 \text{ s}$ simulation	135
5.7	Snow deposition / erosion flux from surface for two adjacent cubes at $t=20 \text{ s}$	135
5.8	Snow drift height contour for two cubes at $t=30 \text{ s}$, $t=45 \text{ s}$ and $t=60 \text{ s}$	136
5.9	Three-dimensional snow drift development around two adjacent cubes at the end of the simulation	137
6.1	Panoramic view of SANAE IV viewed from the edge of the southern buttress of Vesleskarvet towards the north-east	140
6.2	SANAE IV layout on Vesleskarvet, Antarctica showing regions of localised snow drift	140
6.3	Computational domain for the three-dimensional flow simulation around	145

	SANAE IV	
6.4	Mesh details for SANAE IV simulation	146
6.5	u-velocity contour plot, Test 1, at t=20 s at main building section	148
6.6	u-velocity contour plot, Test 1, at t=20 s at interconnecting link section	148
6.7	Shear velocity contour plot for test 1 after t=20 s	149
6.8	Shear velocity contour plot for test 2 after t=20 s	149
6.9	v-velocity contour at the first near surface control volume, test 1, t=20 s	150
6.10	v-velocity contour at the first near surface control volume, test 2, t=20 s	150
6.11	Schematic of the swirling flow leeward of the link section between the main buildings at SANAE IV	151
6.12	Streamline plot around the leeward corner of the main building B	151
6.13	Vector plot (test 1) in the yz-plane at (a) x=12 m, (b) x=17 m and (c) x=25 m	152
6.14	Near surface snow fraction contour plot, Test 1, after t=20 s simulation	154
6.15	Near surface snow fraction contour plot, Test 2, after t=20 s simulation	154
6.16	Snow deposition / erosion flux from surface for test 1 at t=20 s	155
6.17	Snow deposition / erosion flux from surface for test 2 at t=20 s	155
6.18	Snow drift height contour for SANAE IV drift simulation Test 1 at t=60 s, t=120 s and t=200 s	157
6.19	Snow drift height contour for SANAE IV drift simulation Test 2 at t=60 s, t=120 s and t=200 s	158
6.20	Three-dimensional snow drift development at the end of the simulation Test 1	159
6.21	Three-dimensional snow drift development at the end of the simulation Test 2	159
6.22	Snow drift behind the interconnecting links on 3 January 2004 after a blizzard	160
6.23	Snow drift behind the interconnecting links on 12 January 2004 after a second blizzard	161
6.24	SANAE IV Modification 1 – 1 meter vertical baffle plate installation at the interconnecting link (a) Front view, (b) Side view	163
6.25	SANAE IV Modification 3 –Vertical and horizontal baffle plate installation at the interconnecting link (top) Front view, (bottom) Side view	164
6.26	Snow drift height contour for SANAE IV drift simulation Modification 1 at t=60 s, t=120 s and t=200 s	167
6.27	Snow drift height contour for SANAE IV drift simulation Modification 2 at t=60 s, t=120 s and t=200 s	168

6.28	Snow drift height contour for SANAE IV drift simulation Modification 3 at t=60 s, t=120 s and t=200 s	169
6.29	Three-dimensional snow drift development at the end of the simulation for Modification 1	170
6.30	Three-dimensional snow drift development at the end of the simulation for Modification 2	170
6.31	Three-dimensional snow drift development at the end of the simulation for Modification 3	171
G.1	Snow particles evaluated near Aboa during FINNARP-2000. Courtesy of Eija Karkas, Division of Geophysics, University of Helsinki, Finland. (left) Precipitating snow flakes, and (right) top surface layer	205
G.2	Extrapolated 10 m wind speeds measured at SANAE IV during January 2002	205
G.3	Weather mast for wind velocity profiles at first measurement site (left) and the author next to the SANAE IV 1:25 scale model (right)	206
G.4	Roughness height as a function of shear velocity at SANAE IV for the snow covered area and on top of Vesleskarvet (rock cover)	209
G.5	Shear velocity as a function of 10 m wind speed for SANAE IV at the snow covered area and on top of Vesleskarvet (rock cover)	213
G.6	(a) Snow build-up behind 1:25 scale model on 13 January 2002 at 10:45, L=1.2 m, H=0.15 m, W=0.3 m, T=1 h, u=10m·s ⁻¹ (b) Actual snow buildup behind SANAE IV interconnecting links	218
G.7	Snow build-up behind SANAE IV during 15-17 January 2002, L=40 m, H=3.0 m, W=15.0 m, T=66 h, u=15 m·s ⁻¹ . Contour map from GMT Version 3.4 done by Mr. Axel Ruelke, Institut fuer Planetare Geodaesie, TU Dresden, Germany	219
H.1	Visibility during blowing snow conditions at z=1.8 m above snow surface as a function of 10 m wind speed	226

LIST OF TABLES

2.1	Total snow transport ($\text{g}\cdot\text{m}^{-1}\cdot\text{s}^{-1}$) from 1 meter horizontal velocity data.	52
3.1	Simulation parameters for the three-dimensional cube simulation for Model I.	86
3.2	Cube separation zone characteristic dimension comparison.	93
3.3	Snow accumulation heights comparison between predicted and measured values.	97
3.4	Simulation parameters for the three-dimensional cube simulation for Model II.	99
3.5	Snow accumulation heights comparison between predicted (Model I and Model II) and observed values at SANAE IV field test.	104
4.1	Simulation parameters for the two-dimensional snow fence simulation using Model II	114
4.2	Simulated snow drift around a 50% porous fence: characteristic dimensions.	120
5.1	Parameters for the simulation around two adjacent cubes.	132
5.2	Snow accumulation heights comparison between predicted and observed values for two adjacent cubes.	137
6.1	Simulation parameters for the three-dimensional SANAE IV simulation using Model II	145
G.1	Proportionality constant c_1 for use in equation (G.19).	208
G.2	Modelling parameter values	221

NOMENCLATURE

A	Proportionality coefficient
A_i	Control volume interfacial open area fraction
A_k	Phase interfacial area (m^2)
B	Constant
C_D	Drag coefficient
C	Snow concentration ($kg \cdot m^{-3}$), Fall velocity coefficient (s^{-1}), Constant
C_μ	Turbulence model constant
$C_{\epsilon 1}, C_{\epsilon 2}$	Turbulence model constants
C_p	Pressure coefficient
c	Mass concentration fraction, Constant
c_1	Saltation constant
D_f	Inverse particle drag coefficient
D_p	Outdoors scale model particle diameter (m)
d	Particle diameter (m)
d_0	Particle diameter at the aerodynamic roughness height (m)
E_r	Erosion proportionality
e	Saltation efficiency
f	Snow volume fraction
F	Outdoors scale model reference length (m)
Fr	Froude number
g	Gravitational acceleration ($m \cdot s^{-2}$)
H	Reference height (m)
h_s	Saltation height (m)
h_f	Saltation focus height (m)
\bar{J}	Interfacial flux vector ($kg \cdot m^{-1} \cdot s^{-2}$)
K	Proportionality coefficient, eddy diffusivity
K_s	Suspended snow multiplier
L	Outdoors model reference length (m)
L_η	Particle stratification Obukhov length
l_s	Outdoors model saltation length (m)

k	Effective roughness height (m), Turbulence kinetic energy
k_r	Fence pressure loss coefficient
\dot{m}	Mass flow rate ($\text{kg}\cdot\text{s}^{-1}$)
n	Normal distance to wall, total number of phases
n_k	Outward normal directed vector and phase interface
P	Rate of snow precipitation ($\text{kg}\cdot\text{m}^{-2}\cdot\text{s}^{-1}$)
P_k	Turbulence production source term
p	Pressure (Pa)
Re	Reynolds number
Q	Total snow mass flux ($\text{kg}\cdot\text{m}^{-1}\cdot\text{s}^{-1}$)
Q_{acc}	Total erosive or deposition flux ($\text{kg}\cdot\text{m}^{-1}\cdot\text{s}^{-1}$)
q	Snow mass flux ($\text{kg}\cdot\text{m}^{-2}\cdot\text{s}^{-1}$)
R_c	Flow curvature
r	Particle radius (m)
\bar{r}	Mean particle radius (m)
S	Strain rate scale
Sc	Turbulent Schmidt number
s	Saltation roughness parameter
T	Total simulation time (s)
T_{acc}	Drift initiation time (s)
t	Time (s)
u	Velocity component in x-direction ($\text{m}\cdot\text{s}^{-1}$)
u_f	Outdoors scale model particle fall velocity ($\text{m}\cdot\text{s}^{-1}$)
u_s	Rate of change of the phase interface position ($\text{m}\cdot\text{s}^{-1}$)
$u(z)$	Horizontal wind velocity ($\text{m}\cdot\text{s}^{-1}$)
u_{10}	10 meter wind speed ($\text{m}\cdot\text{s}^{-1}$)
U	Drift velocity ($\text{m}\cdot\text{s}^{-1}$)
U_s	Streamwise velocity ($\text{m}\cdot\text{s}^{-1}$)
V	Impinging velocity ($\text{m}\cdot\text{s}^{-1}$), Control volume open volume fraction
V_{iz}	Eye level visibility (m)
v	Velocity component in y-direction ($\text{m}\cdot\text{s}^{-1}$)
W_p	Saltating snow weight over unit area of snow cover ($\text{N}\cdot\text{m}^{-2}$)



w	Velocity component in z-direction ($\text{m}\cdot\text{s}^{-1}$)
w_f	Fall velocity ($\text{m}\cdot\text{s}^{-1}$)
x	Local Cartesian direction vector component
y	Local Cartesian direction vector component
z	Height above surface (m), Local Cartesian direction vector component
z_0	Effective aerodynamic roughness parameter (m)

Greek symbols

α	Particle impinging angle (rad), Discreet phase volume fraction, Gamma function shape parameter
α_1	Turbulent entrainment coefficient
α_{22}	Drift relaxation factor
α_{ero}	Snow erosion multiplier
β	Suspended snow function coefficient, Gamma function parameter
Γ	Interfacial momentum transfer, diffusion constant
Δ	Delta operator
δ_{ij}	Kronecker Delta operator
ε	Turbulent dissipation rate, area porosity
η	Snow phase concentration ($\text{kg}\cdot\text{m}^{-3}$)
κ	Von Karman constant
μ	Dynamic viscosity ($\text{kg}\cdot\text{m}^{-1}\cdot\text{s}^{-1}$)
ν	Kinematic viscosity ($\text{m}^2\cdot\text{s}^{-1}$)
ξ	Eddy diffusivity ratio
ρ	Density ($\text{kg}\cdot\text{m}^{-3}$)
σ	Turbulent Schmidt number
σ^t, σ^e	Turbulent model constants
τ	Shear stress ($\text{N}\cdot\text{m}^{-2}$), Particle relaxation time (Stokes number)
ϕ	Discreet phase volume fraction, constant
φ	General transported scalar, maximum packing ratio, mass source term
Ω	Vorticity scale

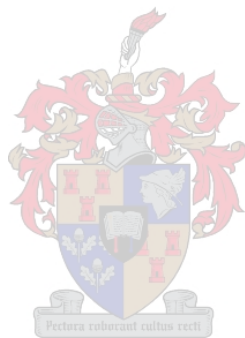
Superscripts

$+$	Dimensionless
-----	---------------

'	Fluctuating component
*	Modified eddy viscosity constant
i	Intrinsic average
η	Dispersed snow phase

Subscripts

a	Air phase
Dk	Diffusion velocity
depshear	Shear deposition component
e	Effective
eroimp	Impingement erosion component
eroshear	Shear erosion component
i,j	Cartesian coordinate index
f	Fluid phase
K	Impingement erosion coefficient
k	Dispersed phase index
m	Mixture property, interfacial momentum transfer component, scale model
P	Control volume central node
p	Dispersed phase, prototype
r	Reference height, relative velocity
s	Snow phase
salt	Saltation
saltero	Saltation erosion component
susp	Suspension
t	Turbulent condition, Threshold condition
w	Node adjacent to wall
x	Horizontal x-direction
y	Horizontal y-direction
z	Vertical direction
*	Shear (velocity)
10	Ten meter reference height
τ	Viscous stress component



1. INTRODUCTION

1.1. SNOW DRIFTING IN ANTARCTICA

1.1.1. Habitation in the Antarctic environment

Snow drifting is a fluid dynamic phenomenon that encompasses the transportation of wind borne snow particles in the atmospheric boundary layer and its characteristic erosion and deposition patterns on the snow surface. This term is often used when describing the accumulation or snow build-up pattern surrounding natural or man-made obstacles. Snow drifting is a natural occurring phenomenon where ever snow is present and may be influenced by many factors including meteorological conditions, the condition of an existing snow pack and the natural topography or presence of man made obstacles. Alternatively, the term *drifting snow* or *blowing snow* is used to describe only the aeolian process of wind driven snow transport, without the associated deposition or scour features. Often drifting snow is used to describe this aeolian transport process during low to moderate wind speeds, with very little and fine particles travelling in the lower layers above the surface and with little decrease in visibility. Blowing snow describes the same process but during strong wind conditions or blizzards and is associated with severe impairment to visibility up to levels high above the surface.

With the exception of coastal regions, Antarctica experiences limited snow precipitation due to its dry atmosphere. However, large amounts of snow are continuously transported and redistributed across the continent by means of powerful winds including inversion and katabatic winds. For one, a katabatic wind travels from the centre of the continent and increases in speed as it moves towards the shelf. Such winds, among others, relocate snow over an extremely large terrain and form small to large scale sastrugi or wind sculptured snow dunes. Large scale snow drifting with scouring and deposition may occur where such winds meet natural obstacles such as a nunatak (rocky outcrop and essentially the tips of large mountains protruding from the thick continental ice cap). Figure 1.1 shows the natural wind erosion of the ice cap on the northern side of Vesleskarvet, the rocky nunatak on which the new South Africa research station, SANAE IV, is built. Other natural snow sculptures of smaller scale are found near the vicinity of mountains or nunataks where large blocks of ice may have broken from higher lying glacier edges, falling and rolling down a slope to

eventually come to rest near the bottom of the wind scoured edges of the mountain. Here the high velocity of winds accompanied by wind blown snow and ice particles in the near surface layer may scour the ice blocks into natural sculptured ice formations. The shapes are sculptured by the high concentrations, as well as larger, abrasive snow and ice particles that are entrained in the near surface layers and the lower concentrations and particles sizes in the upper layers.

This thesis deals with the modelling of snow drifting surrounding man-made obstacles and specifically the drifts found surrounding SANAE IV, the South African research station in Antarctica. As a point of interest, member states of the Antarctic Treaty are required to “demonstrate its interest in Antarctica by conducting substantial scientific research activity there, such as the establishment of a scientific station or the dispatch of a scientific expedition”, (Antarctica Treaty Article VIII, Clause 2) in Kim et al. (1991). Thus any serious scientific activity on the Antarctic continent is accompanied by the construction of permanent and temporary structures for habitation and scientific purposes. Snow accumulation is observed in varying degrees around these man-made structures although mostly on smaller scales compared to natural snow drifts. However, the extreme cold climate and the absence of a sufficiently warm summer, ensures that these and any other naturally formed drifts, remain permanent fixtures on the continent unless they are removed by human intervention or are modified by additional snow drifting or by wind scouring. Both our polar caps do not generally possess the advantage of such a sufficiently warm summer to thaw, melt and eliminate formed drifts and any habitation or scientific activity here therefore poses some interesting challenges regarding the design for snow drifting. Man-made snow drifts create an environmental impact and it can also limit the useful life of structures as they may become completely buried, become inaccessible or structurally unsafe due to the weight of snow above and next to it. It was estimated that 1.5 billion US dollars worth of buildings were constructed in Antarctica by 1986 all of which suffer, some more severely than others, from the effects of snow drifting, Kim et al. (1991).



Figure 1.1. Large natural wind scour around the foot of Northern Butress, Vesleskarvet, 71° 41' S, 2° 49' W, Antarctica

An advantage of studying snow drifts in Antarctica is that one has the benefit of working with mostly isolated large scale structures in an isolated environment. This limits the possible dependent variables influencing the location, size and shape of a snow drift under consideration. Since the amount of precipitating snow may be negligible in such analysis for an Antarctic environment, it could be argued that it has limited applicability in, for example, the northern hemisphere where large amounts of precipitation occurs. It is, however, believed that successful analysis and simulation of these largely wind driven snow phenomena could become a very useful tool in the evaluation of designs for such extreme climate habitation.

Investigations into the effects of snow drifting on the activities of humans in Antarctica and other cold climates are not new as clearly illustrated by Sundsbø (1997) reporting on the work of Johnson (1852) to evaluate snow drifting around snow fences. Apart from habitation concerns, drifting snow severely handicaps air and ground transportation networks on the polar caps as well as the more temperate regions. Runways of compacted snow may develop finger drifts that can prove extremely hazardous to aircraft operation, Gerdel (1960). The

snow drift control in the temperate regions has focused largely on the winter maintenance of transportation networks as reported in early works by Finney (1939), Rikhter (1945) and Bekker (1951) in Gerdel (1960). Some mechanisms of snow control studied were natural and constructed snow fences as well as the design of roadside ditches to catch or deflect drifting snow. Finney (1939) evaluated snow drifting around highways using wind tunnels with artificial snow. Rikhter (1945) made snowdrift observations on the leeward and windward sides of typical obstacles all relevant to the design of highways for snow drift management. They indicate that an elevated roadway with suitable side slopes, of the order of 1:4, may automatically remove drifts.

An early example of Antarctic snow drift observations are the work of Roots and Swithinbank (1955) who studied the layout of Maudheim research station, Antarctica, during the Norwegian-British-Swedish research expedition of 1949-1952 and made some recommendations regarding the construction and operation of polar stations to minimise or manage snow drift formation. They suggested that stations may need a mechanism for periodic raising of the structure due to the gradual accumulation of snow without melting benefits. This early suggestion proved very effective in designs a few decades later with the construction of jackable platforms mentioned below. Other early recommendations in the same vein were, as per Gerdel (1960), elevating obstacles to allow snow bearing wind to travel underneath the structure, aligning the long axis of obstacles normal to the wind, keeping upper surfaces of obstacles as smooth as possible and spacing adjacent structures sufficiently to avoid coalescence of drifts. Gerdel (1960) already indicated that information and research is required in areas that influence and determine snow drifting such as the minimum clearance between buildings, dimensions of obstacles, pitch and orientation of building roofs, maximum roadway widths and design of roadway ditches and snow fence design and spacing.

During 1957-1958 an internationally coordinated research program was undertaken to carry out a series of geophysical observations around the globe. This was called the International Geophysical Year (IGY) and resulted in a number of new research stations being erected in Antarctica. The subsequent obliteration of several of these IGY research stations in Antarctica as a result of snow drifting lead to a renewed interest in studies for the design of buried and elevated stations, Radok (1977). The latter spawned wind tunnel test work and the subsequent

investigation into similarity laws for snow drifting. As mentioned by Radok (1977), the earlier wind tunnel studies mainly focused on providing answers to regions of likely snow accumulation while one of the research foci at that time was to establish whether upwind drifts could be allowed to continue to grow to their equilibrium profile. Kim et al. (1991) and Kwok et al. (1992) carried out snow drift wind tunnel experiments on elevated structures for Antarctic application and gave a detailed account of the historical development of snow drifting similitude theory, some of which will be described later in this thesis.

Research into the design for snow drifting was done by Melbourne and Styles (1967) who undertook wind tunnel tests to evaluate the efficiency of a proposed elevated design for a station near Wilkes station, Antarctica. Its purpose was to establish a layout and design that would maintain a maximum ground level wind velocity and minimise ground level separation. They also mention the fact that the Antarctic summer is too cold to ensure melting of snow accumulations around structures. Their analysis fixed a lower limit to the near ground velocity and mentioned that excessive drifts are likely to occur in regions where wind tunnel tests indicate a local drop in horizontal velocity below 60% of the upstream velocity or where ground separation is observed. They also found that by rounding the windward corner of the obstacle they could greatly increase the general downstream velocity although near ground velocities were somewhat lower than for square corners. An elevated building height of between 2.6 m and 3.3 m was suggested to minimise the occurrence of snow drifts. Casey Station, one of the first elevated stations in Antarctica, was subsequently built to replace Wilkes Station. This was commissioned in 1969 and consisted of modular blocks placed three meters above the surface on scaffolding. This station was placed with its long axis perpendicular to the predominant wind direction. The windward edge of the building was rounded and the leeward edge was flat. The design proved very effective and was only replaced after 20 years of service in 1989. During the early eighties another elevated station was erected by Germany on the Filchner-Ronne Ice Shelf in Antarctica. The design of this station included a novel jacking platform which could be raised every one or two years to allow for periodic snow drifting. This station worked effectively until 1999 when a portion of the shelf on which it was built caved in and took the station along with it. The station was salvaged and reappeared refurbished in 2000 as the Kohnen Summer base for ice drilling operations in Dronning Maud Land, as mentioned below.

Derivations of this type of jacking design was also employed later in various other Antarctic stations including Halley 5 (Britain), Concordia (France / Italy), Kohnen (Germany) and the New South Pole Station (United States). A few specific examples given below illustrate the continuous effects snow drifts have on modern scientific activities in Antarctica. These are mentioned to illustrate some aspects of snow accumulation around the latest and more modern designs of scientific facilities in Antarctica. These scientific facilities are SANAE IV (South Africa), Concordia (France/Italy), Halley V (Britain), Kohnen (Germany) and the New South Pole Station (United States of America). The information on some of the stations is taken from extracts from Brooks (2000).

1.1.2. SANAE IV (South Africa)

South Africa has been involved with science in Antarctica since the summer of 1959/1960 when the first South African Antarctic Expedition (SANAE), led by Hannes la Grange, took over a Norwegian base on the shelf ice in Dronning Maud land, Harris (1996). Since then, this base was replaced by new over wintering stations namely SANAE I, SANAE II and SANAE III, all situated on the shelf ice with the latter being replaced in 1997 by SANAE IV. The new SANAE IV station is situated on the continent at 71°40' S, 2°49' W on a rocky outcrop or nunatak called Vesleskarvet as shown in figure 1.2.

The scientific interest of South Africa in the Antarctica continent lies in the Norwegian sector 6°W to 3°E as indicated in figure 1.3. Originally mainly three scientific disciplines were part of the South African activities in Antarctica namely geology, biology and upper-air physics with the addition of a meteorological station permanently manned and operated throughout the year. Engineering science was first introduced into the South African National Antarctic Program (SANAP) in 2001, funded then by the Department of Environmental Affairs and Tourism (DEA&T), with the first engineering students conducting research at SANAE IV during the Antarctic summer of 2001/2002. Towards the end of 2003 the research funding administration for the SANAP programme was taken over from the DEA&T by the National Research Foundation of the Department of Science and Technology.



Figure 1.2. SANAE IV research station situated on the nunatak, Vesleskarvet in Dronning Maud Land, Antarctica

SANAE IV is an above ground facility situated on the continent itself as opposed to the earlier stations which were all based on the ice shelf and were all eventually completely submerged within the shelf. The last of these shelf stations, SANAE III, was abandoned in 1994 when the massive strain on the structure from the ice covering it, made it unsafe for further habitation. At that stage SANAE III was covered under more than 40 m of ice. The new SANAE IV station was designed to house a multinational contingent of scientists and support personnel and consists of an elevated structure raised approximately four meters above ground. The outcrop on which it is situated, Vesleskarvet, is a gently sloping nunatak when approached from the east with sharp cliffs surrounding its northern, southern and western edges. The nunatak is further split into the Northern Buttress and Southern Buttress. SANAE IV is located near the edge of the western cliff on Southern Buttress.

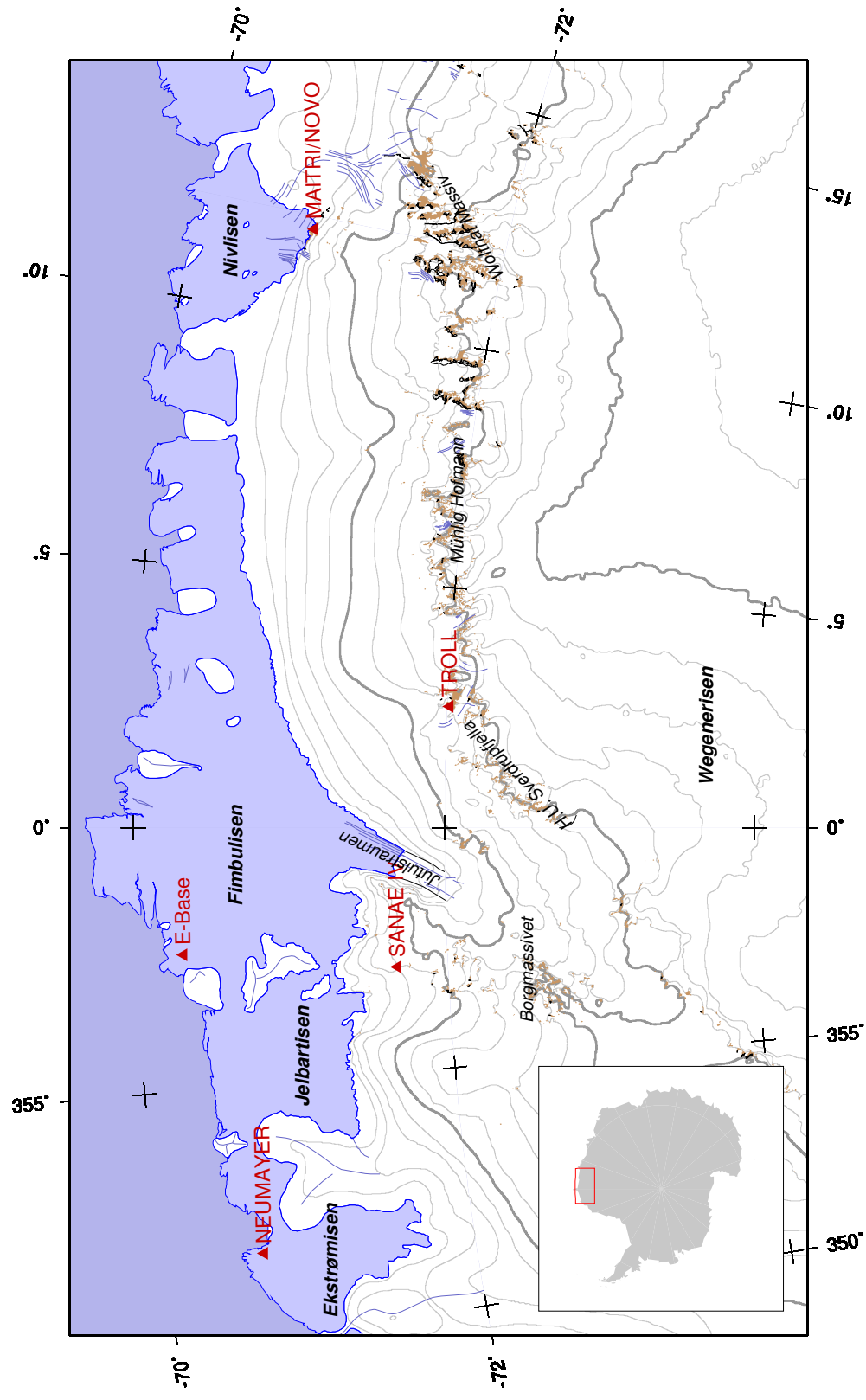


Figure 1.3. Dronning Maud Land, Antarctica showing the location of SANAE IV (South Africa), Neumayer (Germany), Troll (Norway) and Maitri (Russia). Map courtesy of Mr. Axel Ruelke, Department of Geodesy, TU-Dresden, Germany.

The station is an elongated structure with its longitudinal axis pointing nearly 10° east of north. This ensures that the station is aligned mostly perpendicular to the prevailing eastern winds. As shown in figure 1.2, the new station consists of three main buildings, block A, B and C, each approximately 44.0 meters long, 12.0-14.0 meters wide and 7.0 meters high. The main buildings sections are joined by interconnecting sections with access stairways, usually referred to as the “links”, between blocks A and B and between blocks B and C. These interconnecting sections are each approximately 10.0 m long, 8.0 m wide and 4.0 m high and their bottom outside panels are joined flush with the main buildings bottom panels. The whole structure is supported approximately 4.0 meters above ground on an array of support columns which in turn are securely anchored onto the rock bed of the nunatak. A helipad is situated on the northern edge of building C that also provides access to the base through the helihanger located in building C.

The aerodynamic shape of the main buildings and the interconnecting links is believed to have been selected in order to reduce the total form drag of the building and thereby reducing the strain on the support columns during wind storms. The curved peripheral edges of the base may reduce the separation of impinging flows as well as leeward wind flows leading to the reduced form drag of the building. The location of the structure on the edge of the cliff intends to allow wind driven snow to be channelled at high velocity over and underneath the structure and reach the edge of the cliff before decelerating sufficiently for possible accumulation. Wind tunnel testing was carried out on a 1:100 scale model of SANAE IV at the Council for Scientific and Industrial Research (CSIR) in South Africa to determine wind loading on the base and possible snow accumulation regions around it, Goliger (1991). A snow accumulation threshold criterion of 60% of upwind velocity was used to determine whether snow will deposit, similar to those employed by Melbourne and Styles (1960). This has been moderately successful with limited overall snow accumulation on the leeward side of the station. However, in the leeward vicinity of the interconnecting links, and on the outer edges of building A and the helipad, significant snow buildup does occur. These specific snow drifts are the focus of the numerical analysis presented in this thesis.

1.1.3. Halley 5 (United Kingdom)

The British Antarctic Survey (BAS) has since 1956 maintained research activities at Halley situated 75°S , 27°W on the Brunt Ice Shelf as mentioned in Moore (1995). The first four stations were all ice shelf based surface mounted structures designed to be submerged in the ice shelf. Halley I was constructed in 1955/1956 for the International Geophysical Year and operated until 1967/1968 when it was abandoned due to safety concerns. At this stage Halley 1 was 14 m underneath the snow. Halley 2 was constructed in 1967/1968 based on identical design as Halley 1 and was in operation for 7 years. Halley 3 was erected in 1972 and consisted of corrugated steel plates connected to form a pipe profile which housed prefabricated buildings inside. This station was abandoned 12 years later in 1984. Halley 4 was based on the same principle but constructed of wood. The design proved unsuccessful. The fifth station, Halley 5, replaced the earlier stations - each of which was eventually completely buried in snow on the shelf. This elevated station was designed by Christian and Nielsen (C&N) of Hamburg and constructed between 1988 and 1991 and occupied since 1992. The station consists of three rectangular buildings situated on top of steel platforms raised approximately 4 m above the snow, as shown in figure 1.4.



Figure 1.4. Halley 5 (75°S , 27°W) on the Brunt Ice Shelf, Antarctica. (Picture from www.antarctica.ac.uk)

The Accommodation Building (ACB) is 60 meters long by 15 meter wide and 3 meters high. The other two buildings, Ice and Climate Building (ICB) and Space Science Building (SSB), have identical cross sections but are 10 meters and 12 meters in length respectively. The building platforms can be raised with manual jacks along steel columns to accommodate an annual average snow accumulation of approximately 1.2 meters, Moore (1995). Each of these buildings has caused significant leeward snow accumulations, Bateman (2003). These snow drifts are periodically removed by bull dozer, requiring considerable effort due to the volume of accumulated snow. During the design of the station the formation and development of these snowdrifts were investigated with wind tunnel testing at the United States Army Cold Regions Research Engineering Laboratory (CRREL) and 3 meter high drifts were predicted. Drifts of 6 meters high have been measured at Halley 5. These snow drifts were also the focus of a two dimensional numerical analysis, Moore et al. (1994), Moore (1995). A project is underway for the conceptual design of Halley 6 and to replace Halley 5 by the 2009 season, Blake (2003).

1.1.4. Amundsen-Scott (United States of America)

The South Pole has been continuously occupied by America since 1956. The central facility at the Pole was rebuilt in 1974 as a geodesic dome 160 feet wide and 50 feet high. As a result of precipitation and snow drifting, the foundations of this surface mounted dome were eventually more than 20 feet underneath the snow placing excessive strain on the support beams of the structure. Snow removal became increasingly difficult and it was decided to replace this facility with a new station.

In the late nineties construction began on a new research and accommodation facility to replace the geodesic dome. The new station was designed by the company Ferrero and Choi of Hawaii, and consists of two C-shaped main elevated structures with a 12.0 m interconnecting section between them. The windward sections of the C-shaped buildings are approximately 27.4 m in length, 14.9 m wide with the two legs of the C-shape being 30.3 m in length and 11.6 m wide, Brooks (2000), Berry et al. (2000). The structure is raised approximately 3 m above the snow surface and can be elevated with hydraulic jacks to accommodate the annual snow accumulations as shown in figure 1.5 and 1.6. The mean

annual snow accumulation at the South Pole is less than two inches, Heacox (1998), considerably less than the 35 inches recorded on the northern tip of the Antarctic Peninsula, where the near vicinity of the coast increases the humidity which in turn increases the volume of precipitation.



Figure 1.5. The layout and view of the new South Pole station under construction at the south pole with the old geodesic dome pictured located to the left of the new station (Picture by D. McCarthy, NSF from <http://photolibrary.usap.gov>)

Although there are many similarities, the design of this structure differs somewhat in concept from SANAE IV, the main difference being that the peripheral edges are not rounded or otherwise aerodynamically shaped and the shape of the station is not symmetrical around its longitudinal axis, as is the case with SANAE IV. Instead, on the windward side, angled panels direct and accelerate wind flow and snow underneath the structure. The snow drift around this station was also evaluated by the Canadian company Rowan Williams Davies and Irwin Inc. with scale model tests conducted in a water flume with sand particles to represent the wind borne snow, Waechter and Williams (1999).



Figure 1.6. The new South Pole station, Amundsen-Scott station under construction at the south pole (Picture M. Connor, NSF from <http://photolibrary.usap.gov>)

1.1.5. Concordia (France / Italy)

The new Concordia station is a jointly run base operated by Italy and France. It is located at Dome C on the East Antarctic Plateau. This area sees minimal precipitation but significant wind blown snow drifting events occur. The station was also designed as an elevated construction mounted on 6 piles fitted with horizontal skids. The base can be periodically raised on these piles to minimise the effect of the snow drift. Figure 1.7 shows the layout of the base and its development during construction. Bottom figure shows the Concordia station during construction, top left shows the concept design and top right shows the station towards the end of construction.

Delpech et al. (1998) carried out snow wind tunnel tests at the Jules Verne cryospheric wind tunnel in Nantes, France to evaluate possible design modifications and remedial measures to minimise the accumulation of wind blown snow in the vicinity of the base. These tests showed that long snow drifts may be formed in the leeward wake of the station along with significant windward drifts. Wind deflection plates were tested to minimise the snow drift by streamlining the windward edges of the base.

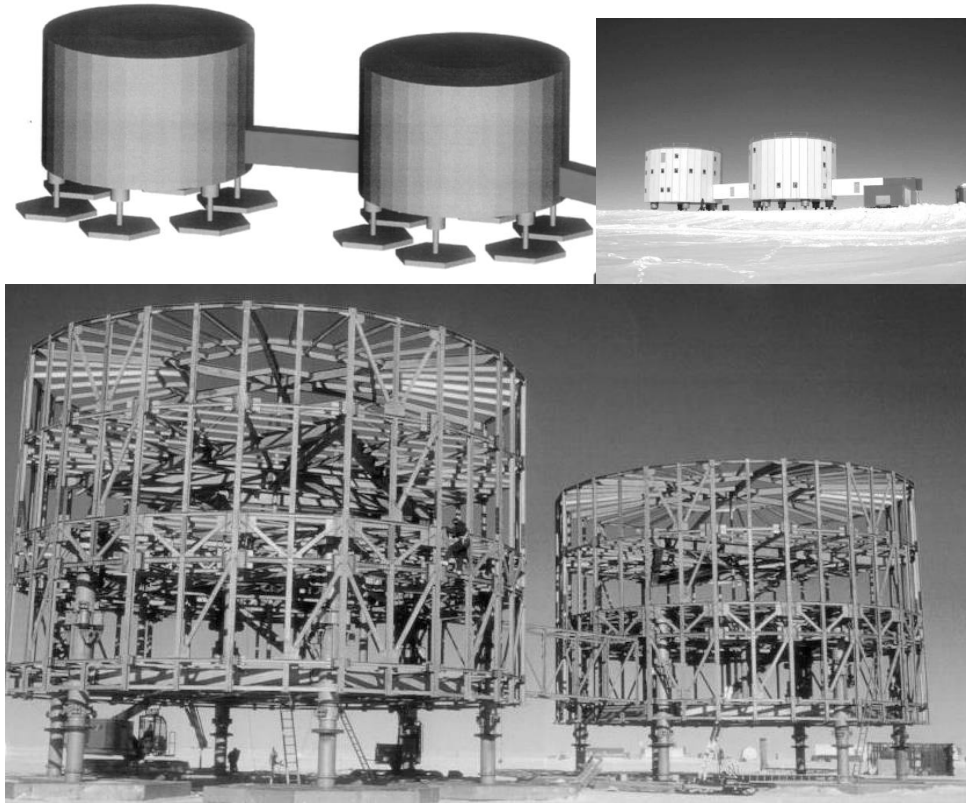


Figure 1.7. The jackable Concordia station (France / Italy) located at Dome C, East Antarctica

1.1.6. Summer base Kohnen (Germany)

The Kohnen summer base was built during the austral summer periods of 1999/2000 and 2000/2001 from which ice-core drilling operations could be carried out. The base location (75°00' S, 0°04' E) is also located in Dronning Maud Land. The eleven container units from the salvaged German base once situated at the Filchner-Ronne ice shelf, as mentioned earlier, were refurbished and placed on top of a 32 m by 8 m jackable steel platform. This platform is designed to house the working and living quarters 2 m above the snow surface and its long axis is aligned perpendicular to the prevailing easterly winds, Drücker et al. (2004). There are also three snowdrift units installed at Kohnen to measure drifting and blowing snow phenomena, a frequent phenomenon at the base, Van den Broeke et al. (2002).

The above examples illustrate that the elevation of research stations to minimise snow accumulation has been successful and has greatly improved the operation and snow management at these stations. However, the ever present wind driven snow accumulations

surrounding even the elevated structures indicate that these structures may also benefit from further detailed investigation and evaluation.

1.2. SNOW DRIFT ANALYSIS

1.2.1. Observation, experimental modelling and numerical simulation

The brief example of the elevated designs found in Antarctica, as given above, serves to illustrate that during the course of approximately half a century, snow drifting analysis developed considerably. Early observational and intuitive snow drift analysis methods lead to similarity methods for experimental field tests and the application of wind tunnels and water flumes and lately numerical simulations such as computational fluid dynamics (CFD) has been employed. Today all these methods are considered to be invaluable tools in the prediction of possible snow deposition locations and rates. Expertise with snow drifting phenomena in the field, as well as with experimental testing, for example using cryospheric wind tunnels, may remain in favour but they do however have the disadvantage of being either subjective (intuition of the experienced snow engineer) or, more importantly, too expensive for design optimisation studies. Here, numerical methods to simulate snow drifting may be very useful and, if properly validated, could be employed to optimise the design of structures before prototypes are built or to economically investigate the causes for snow drifts around existing structures. This thesis intends to contribute to this latter field in snow engineering, to provide a suitable engineering tool for the numerical simulation of snow drifting around structures. The thesis does however also include field experimental modelling work which was necessary to provide validation for numerical snow drift experiments.

The level of complexity of a numerical analysis of the snow drift process can be evaluated as indicated in the diagram in figure 1.8. Firstly, the dimension for the simulation depends on the type of analysis required. One-dimensional analysis may provide information regarding snow drift fluxes and perhaps the rate of sublimation of snow particles within the atmospheric boundary layer. Two-dimensional analyses give information regarding a snow concentration development along a fetch in the atmospheric boundary layer and may also determine drift developments over two-dimensional objects. Quasi three-dimensional analysis may give snow drift development over topographical terrain where the wind flow over the terrain is solved on a two-dimensional grid using the topographical depth information. Real flow is almost

always three-dimensional and for evaluation of drift developments over obstacles a three-dimensional approach is almost always required. For this work a fully three-dimensional approach is employed to study local snow drift over arbitrary obstacles. The dimension relies heavily on the available computer processor power as well as the efficiency of the software architecture. This therefore also determines the level of resolution and realism required that may be used to solve the flow within suitable time frames.

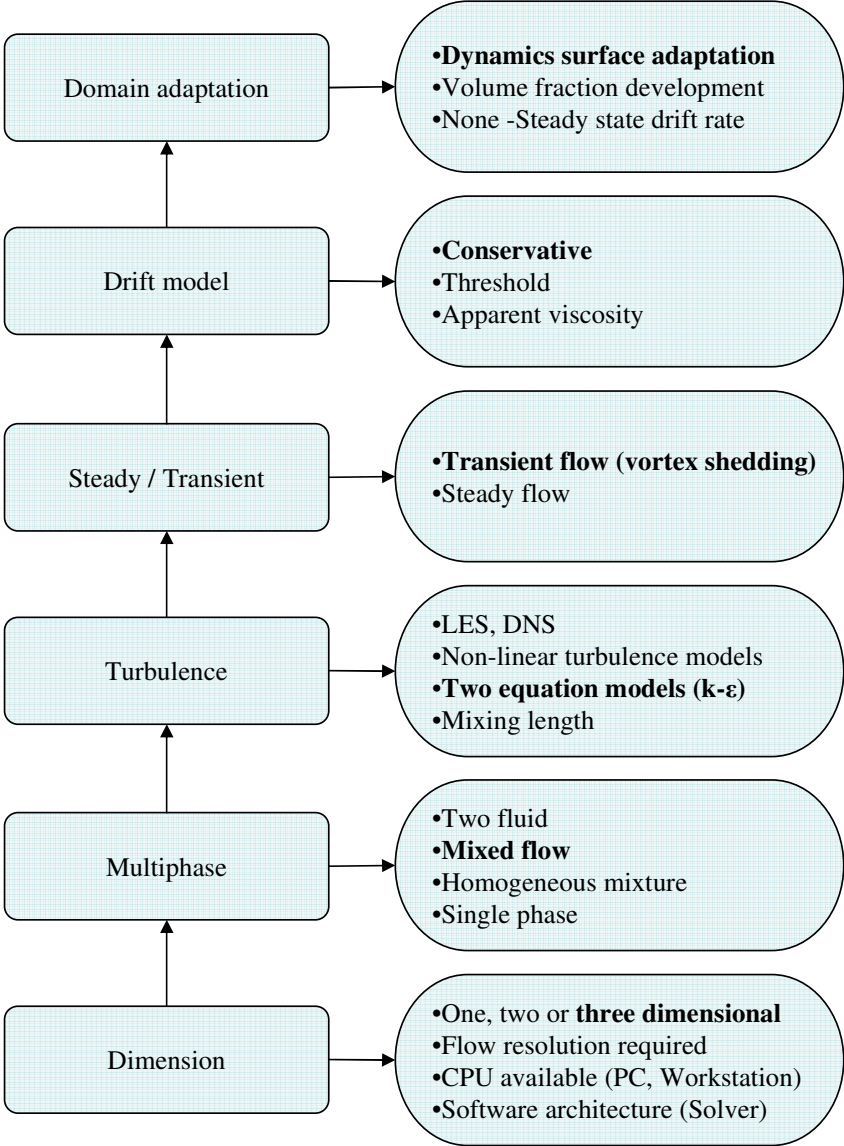


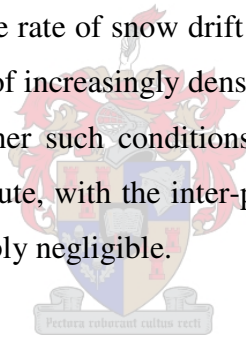
Figure 1.8. Snow drift numerical analysis specifications.

The drifting snow process may be approximated by some multiphase treatment of the mixed flow continuum. For an Eulerian approach a single phase analysis will only determine wind flow and surface shear velocity to be used as an estimate of regions of likely snow drift. A homogenous flow approach assumes that a discrete snow phase follows the flow phase exactly, without any slip velocity between phases, while the mixed flow approach does the same but incorporates some slip velocity between the discrete and continuous phase. Both solve a discrete phase particle advection equation to provide information in the particle concentrations. The two fluid models resolve the flow field velocity for both the continuous phase and the discrete phase and require a solution of all the turbulent transport equations for both phases.

The flow associated with the snow drifting process is always highly turbulent. To model such turbulence characteristics, a mixing length theory may be applied or alternatively two-equation turbulence models that determine the rate of turbulence production as well as dissipation. Most two-equation models assume the turbulence is isotropic which is unlikely, especially in regions of strong flow curvature or flow separation. A few modified two equation turbulence models as well as non-linear two equation models provide some information regarding the anisotropic nature of such flows and have been applied with great success for atmospheric boundary layer flow modelling. Advanced models such as large eddy simulation (LES) or direct numerical simulation (DNS) resolves the full three-dimensional characteristics of the turbulent flow but remains computationally expensive to apply, especially in flow domains with complicated grid geometries.

Flows around real obstacles are usually transient and steady state conditions rarely exist. Seemingly steady state separation regions surrounding three-dimensional obstacles are usually highly intermittent with coherent vortex structures being shed and convected along with the flow at regular intervals i.e. vortex shedding around a surface mounted obstacle. A developing snow surface due to erosion or deposition generates a new surface position continuously. This requires a transient analysis in order to attempt to predict the formation of equilibrium drift profiles or in other words, the drift profile that develops until a deposition region has grown sufficiently large to the point where erosion forces again become dominant and the drift stabilises.

The mechanisms that govern the deposition and erosion are many, varied and interconnected. The threshold of snow transport in wind is often termed the threshold shear velocity or the surface shear stress generated by the flow on the snow pack when the particles start to roll, jump and eventually entrain into the flow. This threshold condition is a function of the weight of the snow particles and the strength of the inter-particle bonds or cohesion, among other parameters. Thus, in drift models, one may predict either the onset of erosion or deposition when the aerodynamic surface shear velocity increases above or decreases below the threshold friction velocities. Such models are referred to in this work as threshold based models. These models may not always be adequate since additional phenomena are present that influence the drift rate. This may include the flow field velocity and snow concentration gradients in the flow i.e. the deposition of particles in strong shear regions but where the flow is strongly decelerating or where strong particle concentration gradients exists. The drift rate for such conditions may be estimated from the snow mass conservation within a control domain near the surface and such models are named in this work as conservative models. Other models have also estimated the rate of snow drift formation by modifying the effective flow viscosity to include the effects of increasingly dense snow concentrations where the flow is decelerated. It is uncertain whether such conditions exist physically since the naturally occurring drifting snow is highly dilute, with the inter-particle forces, along with their effect on the flow mixture viscosity, probably negligible.



From either the steady or transient state analysis one may determine an instantaneous erosion or deposition drift rate. This will estimate, for instance, the amount of snow that deposits at a particular instant with a particular flow field. This drift rate will change continuously since the developing snow drift surface changes the flow domain and thereby influencing the flow phenomena. This in turn changes the rate of the deposition based on the new flow characteristics. A snow drift model may not necessarily include the adaptation of an original snow pack and therefore only provide information regarding the rate of drift flux onto or from the snow pack. In order to predict a developing snow drift profile some computational domain adaptation strategy may be necessary that modifies the shape and position of an original surface at a given time step and in proportion to the instantaneous or time step averaged drift flux.

The present models aim to provide a snow drift simulation using a three-dimensional flow domain, employing a multiphase mixed flow approach with a standard two-equation turbulence model and including a transient adaptation of the surface geometry based on a conservative drift model. The details of each of these aspects of the simulation (as highlighted in figure 1.8) will be described in detail in this thesis as well as their alternatives.

1.3. RESEARCH OBJECTIVE AND CONTRIBUTION

This study originated from an initiative by the Department of Environmental Affairs and Tourism (DEA&T), directorate Antarctica and Islands of the South African Government, to incorporate and fund engineering sciences as an additional research field in the South African National Antarctic Program (SANAP).

The objectives of this research work are as follows. Firstly to establish a suitable and generic numerical method to simulate, predict and evaluate transient three-dimensional snowdrift formation due wind driven snow around obstacles using computational fluid dynamic methodologies. This can only be achieved by a thorough theoretical understanding of the aeolian snow transportation process as well as the mechanisms responsible for the erosion and settling of the snow particles at the snow pack. This method is validated by comparing its results against results from experimental and observed snow drift studies. Secondly to apply the method to numerically simulate three-dimensional snow drifting and snow accumulation in the near vicinity of the SANAE IV research station. It is necessary to understand the wind driven snow flow phenomena and the primary reasons for the accumulation patterns observed at the SANAE IV research station. This may enable one to propose, numerically evaluate and recommend possible and suitable remedial design concepts in order to reduce or eliminate the formation of local snow accumulation behind the station.

During the progress of this research contributions to the snow engineering field were made towards the analysis of snow drifting. Successful experimental work was undertaken at the SANAE IV research station in Antarctica to investigate snow drift phenomena around large scale obstacles and scale models. This experimental work included wind profile measurements and analyses at different locations around SANAE IV and snow drift tests with large scale structures and scale models requiring similarity analysis techniques.

A numerical method using computational fluid dynamic methodology was developed and implemented in the commercial CFD software code FLOW3D, to predict snow drifts around three-dimensional structures. During the course of the development of this method, parts of these research results were published in two international journal papers and two papers presented at international conferences, Beyers et al. (2003a), (2003b), (2004a) and (2004b).

During the model development a suitable method was investigated and successfully implemented to describe and predict the snow drift process under high shear conditions where the wind shear velocity exceeds the threshold conditions for snow saltation considerably. This is believed to be necessary to predict, for one, snow deposition around elevated obstacles where flow speeds are high due to acceleration underneath the structures. Observations almost always indicate drifting to occur at the same time even though threshold conditions may have been exceeded. These snow drifts seem to be strongly influenced by the flow divergence rather than only the threshold condition required for entrainment.

A three-dimensional snow drifting simulation was successfully carried out for the SANAE IV research station and results showed good agreement with the observed snow drift locations and its characteristic shape. It also highlighted the mechanisms causing the buildup patterns and possible remedial design concepts were evaluated. A concept to reduce the snow drifting is proposed that may possibly be a first for elevated structures and with possible application to many other similarly designed and constructed buildings in such environments.

Experimental and numerical research was conducted at the Narvik Institute of Technology, Norway and ongoing research collaboration established.

The content of the thesis is briefly outlined below. Chapter 2 describes the theory relevant to the numerical simulation of a general dilute multiphase mixture and the assumptions made to treat the drifting snow process as such a dilute mixture. The descriptions of the governing equations for the mixture continuity, momentum conservation, discrete phase advection and turbulence production and dissipation are provided. This is followed by the application of the theory to describe the snow drifting process i.e. the determination of the deposition or erosive snow flux within the near surface control volume. Here two approaches are described, namely a threshold based approach and a conservative based approach. The threshold based approach

describes snow drifting as a phenomenon where the deposition and erosion of snow is largely determined by the shear velocity field and the level of this shear field above or below the threshold shear velocity required to initiate the aeolian transportation of snow. The conservative based approach determines the deposition or erosive flux from the snow pack as a function of the snow mass conservation in the near surface control volume. The advantages and disadvantages of the two approaches are briefly discussed. To describe the snow drift models as well as providing boundary conditions of the snow concentrations, one requires information regarding the saltating and suspended snow volume fractions. The theory describing these upstream conditions is given. This numerical procedure uses the FLOW3D commercial software suite which employs a FAVOR (Fractional Area Volume Obstacle Representation) technique to describe solid obstacles within the computational domain. This powerful technique allows one to create and destroy obstacles during the transient simulations to represent the development of a snow surface as a function of the snow drift routine. The FAVOR method is described to illustrate how the snow drift routine implemented in the FLOW3D code is translated into the development of a new snow surface. Chapter 2 also references most of the literature reviewed during the course of the work.

Chapter 3 includes the first snow drift numerical validation by comparing results from a simulation of the wind driven snow flow around a three-dimensional cube with the observed results of the same flow for a test carried out in Antarctica. The drift development is predicted by both the threshold method and the conservative method and both indicated good agreement with the observed results. It is also shown that the results found by using the conservative approach is superior to those obtained by using a threshold approach.

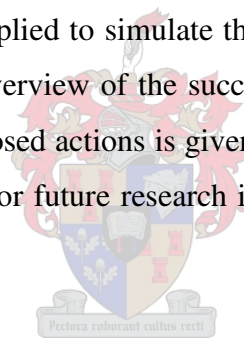
Chapter 4 gives results of the numerical validation of the snow drift prediction around two- and three-dimensional porous snow fences. The simulations employ the conservative based approach and the results for different wind speeds compares favourably with experimental and other numerical results.

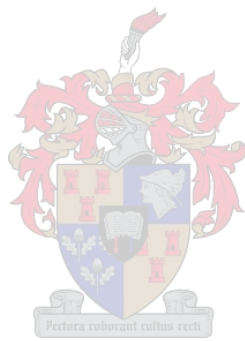
Chapter 5 presents the results of an additional validation simulation using the conservative based approach. This is for the evaluation of the snow drift prediction around two adjacent three-dimensional cubical buildings as experimentally measured by Thiis (2003). The simulation shows that the snow drift predictions are in good agreement with the measured

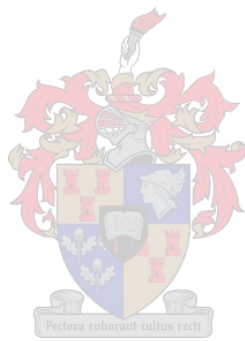
drifts. These results are significant mainly because some of the drift formations simulated here are also located in or near high shear areas which would not have been resolved with the threshold based drift model.

In chapter 6 the snow drift simulations using only the conservative based model are carried out to evaluate the mechanisms responsible for the snow drift development surrounding the interconnecting links at the SANAE IV research station in Antarctica. The results are evaluated and the drifts predicted are compared with the observation made at SANAE IV and show very good agreement. The numerical simulations indicate that the drift formation is largely determined by the flow divergence in the area leeward of the interconnecting links where strong swirling flows are present. The simulations are repeated but with a modified geometry to establish whether the proposed modification may minimise the drift formations. The numerical work suggests that the proposed modifications may be successful.

Chapter 7 summarises the theory applied to simulate the snow drifting process around three-dimensional objects and gives an overview of the successes as well as the limitations of the present method. A short list of proposed actions is given relevant to the snow drifting issue at SANAE IV as well as suggestions for future research into the numerical simulation of snow drift.



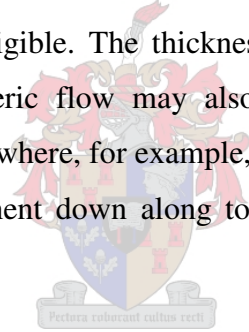




2. NUMERICAL SIMULATION OF WIND-BORNE SNOW AND SNOW DRIFTING

2.1. INTRODUCTION

Wind borne snow transport is a phenomenon that occurs in the atmospheric boundary layers and a brief description of the physics pertaining to this process is given below. This process, as well as most other applications where snow drifting are evaluated, deals with flows in the atmospheric boundary layer and more so the flow in the surface layer, i.e. the first tens of meters above the surface. Our research is interested in flow in the surface layer where the characteristics of the surface boundary layer have great influence on the flow along the surface and importantly, around and near obstacles on or near the surface. Within this surface layer the flow behaves as a Newtonian fluid, is highly turbulent and is considered incompressible although density fluctuations due to temperature differences are present. In the lower regions, fluid stresses and turbulent fluxes remain close to their surface values and Coriolis forces are considered negligible. The thickness of this region varies from tens to hundreds of meters. The atmospheric flow may also be subjected to large temperature gradients especially in the Antarctic where, for example, katabatic winds are driven by gravity from the central parts of the continent down along topographical features due to the cold surface layer.



Atmospheric boundary layer flows are, as with all real flows, transient and fully three-dimensional. A three-dimensional transient analysis allows one to evaluate effects such as three-dimensional vortex shedding and coherent secondary flow structures around obstacles in an atmospheric boundary layer. These important effects will be discussed in greater detail in this thesis. Although the time scales for atmospheric phenomena may be of the order of hours, the time scale for small scale effects such as vortex shedding around structures may be of the order of seconds. Therefore, even though one obtains valuable information from an analytical steady state analysis, it is vital to evaluate the transient two- and three-dimensional nature of the flow phenomena.

The near surface layer will, once the available shear energy at the surface is sufficient, start to entrain snow or ice particles. Depending on the available turbulence kinetic energy, the snow ejected into the wind stream may also be suspended to higher elevations by means of

turbulent eddies. Thus the introduction of such particulate matter into the flow necessitates a multiphase flow evaluation. These particles will interact with the carrier fluid and the flow domain boundaries and modify the turbulent flow characteristics.

The physical description of the aeolian process of drifting snow in the atmospheric boundary layer indicates some highly complex flow phenomena. Most of these environmental flow processes are truly three-dimensional with many associated complexities such as strong streamline curvature, flow vorticity and separation as well as a highly anisotropic turbulence distribution. These already present a challenging task from a numerical modelling perspective without even addressing the additional complexities arising from the multiphase or particulate effects relevant to snow drifting. The introduction of particulate matter into the flow domain implicitly affects the fluid mass and momentum conservation as well as the production and dissipation of turbulence. In addition, the temporal snow accumulation or erosion that dynamically alters the flow domain boundaries would require some form of an adaptive computational strategy. For such a numerical analysis to succeed as a suitable engineering tool one invariably needs to make a few sacrifices in the form of modelling assumptions.

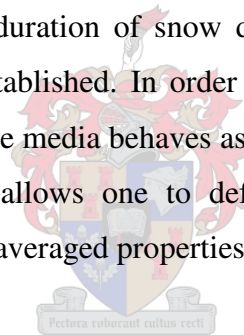
In the next section the governing equations for the multiphase flow are presented as well as other relevant analytical formulations and the underlying assumptions of these equations. The theory behind the numerical analysis and the experimental modelling applied in this work is also presented.

2.2. MULTIPHASE FLOW IN THE ATMOSPHERIC SURFACE LAYER

2.2.1. The multiphase continuum

The transport characteristics of a fluid parcel or particle in a multiphase fluid system can be described in terms of an Eulerian or a Lagrangian coordinate transformation. The Lagrangian approach employs a fixed spatial origin for the coordinate system and treats the fluid system as a continuum and predicts the trajectories of a single particle or a cloud of particles as a result of various forces acting on the particles. The Eulerian approach considers a moving continuum and treats both the fluid and the discrete particles as a continuum i.e. solving the appropriate transport equations for each phase in terms of volume fractions, Durst et al (1984). The numerical analysis of dilute multiphase flows may be accomplished by

employing an Euler-Euler or an Euler-Lagrangian coordinate frame or by employing kinetic gas theory. Kinetic gas theory is usually employed when considering particle-gas dynamics at a molecular level. There are numerous advantages inherent to each of these approaches. However, from a numerical analysis perspective the fully Eulerian approach greatly simplifies the modelling of the governing equations and is comparably more economical with computer processing power, Durst et al. (1984). A Lagrangian approach is applied when detailed information is required of the particle trajectories or residence times while the Eulerian approach delivers particle concentration distributions. For the present analysis it is important to determine deposition or entrainment fluxes and therefore the particle concentrations are required making the Eulerian approach very attractive. Various researchers have analysed snow drift processes with both fully Eulerian and the Euler-Lagrangian methods, Sundsbø (1997) and Alhajraf (2001) among others. The results from these works suggest that sufficient information is found from the fully Eulerian approach to adequately describe the snow drifting phenomena. Combined with a transient analysis such an approach even yields some time response information i.e. the duration of snow deposition before an aerodynamically equilibrium snow drift profile is established. In order to employ an Eulerian approach one needs to make the assumption that the media behaves as a continuum and that each phase may be considered a continuum. This allows one to define the governing equations of the multiphase fluid in terms of volume averaged properties and variables as discussed later.



Multiphase fluids may be described as either dilute or as dense. The dilute media assumption requires that the inter-particle collisions have negligible effect on the flow characteristics of the carrier fluid and the discrete phase, Ishii et al. (1989). Dense media however has strong inter-particle effects and these play an important role in the accurate description of the flow. A dilute multiphase flow entails that there is minimal coupling between the particles and the fluid i.e. the fluid mean velocity and turbulence characteristics are undisturbed by the particle phase, Johansen (1991). In the present analysis of wind driven snow, the air-snow system is considered highly dilute and only one-way coupling between the fluid and the dispersed phase exists i.e. the snow phase follows the continuous phase without influencing it. If the effects of fluid buoyancy on the fluid turbulence characteristics are included in the turbulence model, a degree of two-way coupling exists since mixture density affects the fluid turbulence while being a function of the particle concentration.

Considering the air-snow mixture as a dilute continuum seems acceptable considering that naturally occurring maximum snow volume fractions are typically $\phi \approx 0.001$, Pomeroy and Gray (1990), Bintanja (2000a). This would result in a particle mass loading of order smaller than unity which is one criterion for determining the diluteness of particle laden flows, Ishii et al. (1989). Or, in other words, as per Johansen (1991), diluteness is assured when particle bulk density is smaller than the density of the gas phase i.e.

$$\phi \rho_p < (1 - \phi) \rho_f \quad (2.1)$$

and since particle volume fractions are much smaller than unity, equation (2.1) limits dilute volume fractions to

$$\phi < \frac{\rho_f}{\rho_p + \rho_f} \quad (2.2)$$

Throughout this work the density of the wind blown snow particles are assumed constant at $\rho_s = \rho_p = 900 \text{ kg}\cdot\text{m}^{-3}$, the density of ice particles, Bintanja (2000b).

Furthermore, particle dimensions need to be small compared to the relevant Kolmogorov length scales associated with turbulent atmospheric flows, Bintanja (2000a). Although this is strictly not valid for all particle sizes found in wind driven snow it allows one to neglect particle inertia which greatly simplifies the analysis. The particle Stokes number or particle relaxation time is a measure of particle inertia relative to the viscous forces acting on it. The Stokes number is, as given by Kallio and Reeks (1989),

$$\tau^+ = \frac{\rho_p d^2 u_*^2}{\rho_f 18 \nu^2} \quad (2.3)$$

The preferential concentration of particles in large scale coherent vortex structures in turbulent flows and the influence of shear induced forces are non-negligible for particle Stokes numbers of the order of unity, Kallio and Reeks (1989), Eaton and Fesler (1994), Wang et al. (1997), and Wang and Squires (1996). Higher particle Stokes numbers imply that the high inertia of particles ensure that they travel relatively undisturbed through turbulent eddies. The particle size classes relevant to the present application of drifting snow have diameters of the order of $80\mu\text{m}$ to $300\mu\text{m}$, Budd (1966), Schmidt (1982). Therefore the Stokes numbers are of an order of one hundred and therefore the particle trajectories are largely governed by inertial and convective forces. To simplify the analysis, the present work

simulates a mono-dispersed particle size distribution where particle diffusivity is assumed constant and equal to the fluid diffusivity i.e a particle Schmidt number of unity.

The underlying theory and notation describing the conservation equations for a multiphase fluid generally follows that given in Ishii (1975) and Soo (1990). A multiphase fluid description consists of a set of mass, momentum and energy conservation equations for each phase present in the continuum. The present work excludes the energy equation and it is therefore not included. The flow under consideration is highly turbulent and therefore requires time averaging of the governing conservation or transport equations while volume averaging is required to define the transport equations in the continuum. Comprehensive details of the averaging theorems and derivations are given in Ishii (1975) and the theorems employed in the derivation of the multiphase flow equations are summarised in Appendix A.

2.3. MULTIPHASE MODEL

2.3.1. Continuity equation for phase k

The general k^{th} -phase volume-time averaged mass conservation equation in the absence of any phase changes reads

$$\frac{\partial}{\partial t}(\alpha_k) + \frac{\partial}{\partial x_i}(\alpha_k \bar{u}_i) + \frac{\partial}{\partial x_i}(\alpha' u'_i) = 0 \quad (2.4)$$

The interested reader may refer to Appendix B for the derivation of equation (2.4). The fluctuating terms in equation (2.4) may be approximated by means of a transport coefficient or eddy viscosity, Boussinesq (1877). Assuming that density fluctuations are negligible the continuity equation then becomes

$$\frac{\partial}{\partial t}(\alpha_k) + \frac{\partial}{\partial x_i}(\alpha_k \bar{u}_i) + \frac{\partial}{\partial x_i} \left(\frac{\mu_{kt}}{\sigma} \frac{\partial \alpha_k}{\partial x_i} \right) = 0 \quad (2.5)$$

If the mass diffusion effects are ignored then equation (2.5) reads

$$\frac{\partial}{\partial t}(\alpha_k) + \frac{\partial}{\partial x_i}(\alpha_k \bar{u}_i) = 0 \quad (2.6)$$

2.3.2. Momentum conservation of phase k

The k^{th} -phase volume-time averaged momentum conservation equations, in the absence of phase changes and ignoring density fluctuations, is given by

$$\frac{\partial}{\partial t}(\alpha_k \bar{u}_{ki}) + \frac{\partial}{\partial x_j}(\alpha_k \bar{u}_{kj} \bar{u}_{ki}) = -\frac{1}{\rho_k} \frac{\partial \alpha_k p_k}{\partial x_i} + \frac{1}{\rho_k} \frac{\partial}{\partial x_j}(\alpha_k \tau_{kij}) + \alpha_k g_i + \frac{\Gamma_{\tau ki}}{\rho_k} \quad (2.7)$$

$$\tau_{kij} = \mu_k \left(\frac{\partial \bar{u}_{ki}}{\partial x_j} + \frac{\partial \bar{u}_{kj}}{\partial x_i} \right) - \rho_k \overline{u'_{ki} u'_{kj}} \quad (2.8)$$

where τ_{kij} groups the viscous and turbulent stresses and the momentum transfer due to stresses at the phase interface, the interfacial drag, is denoted by $\Gamma_{k\tau}$. The volume-time average derivation of equation (2.7) may be found in Appendix C. The fluctuating terms in equation (2.8) which arise from the time averaging of the instantaneous momentum equation, as per Appendix C, may be regarded as an apparent stress tensor although it does not physically represent fluid stresses. These terms require approximation which may be accomplished by a Boussinesq approach where turbulent fluxes are approximated by employing a turbulent transport coefficient, Boussinesq (1877). This so-called eddy viscosity model applied to the turbulent fluxes in equation (2.8) is given by

$$-\rho_k \overline{u'_{ki} u'_{kj}} = \mu_{kt} \left(\frac{\partial \bar{u}_{ki}}{\partial x_j} + \frac{\partial \bar{u}_{kj}}{\partial x_i} \right) - \frac{2}{3} \rho_k \delta_{ij} k \quad (2.9)$$

Employing equation (2.7) with equation (2.9) yields the simplified volume-time averaged momentum equation which reads

$$\begin{aligned} \frac{\partial}{\partial t}(\alpha_k \bar{u}_{ki}) + \bar{u}_{kj} \frac{\partial}{\partial x_j}(\alpha_k \bar{u}_{ki}) &= -\frac{1}{\rho_k} \frac{\partial}{\partial x_i}(\alpha_k \bar{p}_k) + g_i \\ + \frac{\partial}{\partial x_j} \left(\alpha_k (\nu_k + \nu_{kt}) \left(\frac{\partial \bar{u}_{ki}}{\partial x_j} + \frac{\partial \bar{u}_{kj}}{\partial x_i} \right) \right) &+ \frac{\Gamma_{\tau ki}}{\alpha_k \rho_k} \end{aligned} \quad (2.10)$$

2.4. MIXTURE MODEL (DIFFUSION MODEL)

2.4.1. Mixture model properties

A simplification of the multiphase fluid model may be achieved by considering the mixture as a whole instead of as separate phases. The assumption of one mixed flow continuum

alleviates the need to solve an additional set of particle momentum equations to obtain the particle velocity field. To attain the mixed flow model one needs to define a number of important mixture properties and constitutive equations, Ishii (1975), namely for n phases,

Volume fraction identity

$$\sum_{k=1}^n \alpha_k = 1 \quad (2.11)$$

Mixture density

$$\rho_m = \sum_{k=1}^n \alpha_k \rho_k \quad (2.12)$$

General mixture transport

$$\rho_m \Psi_m = \sum_{k=1}^n \alpha_k \rho_k \Psi_k \quad (2.13)$$

Mixture velocity

$$\rho_m \mathbf{u}_m = \sum_{k=1}^n \alpha_k \rho_k \mathbf{u}_k \quad (2.14)$$

$$\mathbf{u}_m = \sum_{k=1}^n \frac{\alpha_k \rho_k}{\rho_m} \mathbf{u}_k = \sum_{k=1}^n c_k \mathbf{u}_k \quad (2.15)$$



where c_k is the mass concentration of the k^{th} -phase.

Mixture viscosity

$$\mu_m = \sum_{k=1}^n \alpha_k \mu_k \quad (2.16)$$

Mixture pressure

$$p_m = \sum_{k=1}^n \alpha_k p_k \quad (2.17)$$

The diffusion or drift velocity is the velocity of the k^{th} -phase relative to the velocity of the centre of the mixture mass i.e.

$$\mathbf{u}_{Dk} = \mathbf{u}_k - \mathbf{u}_m \quad (2.18)$$

The relative velocity is the velocity of the k^{th} -phase relative to the continuous phase i.e.

$$\mathbf{u}_r = \mathbf{u}_k - \mathbf{u} \quad (2.19)$$

Mass concentration identity for a two fluid mixture

$$c_1 + c_2 = 1 \quad (2.20)$$

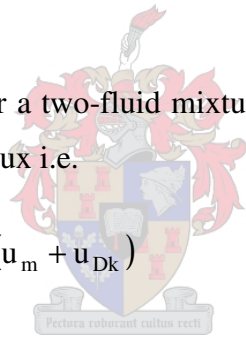
For a two-fluid mixture with the continuous phase denoted by 1 and the dispersed phase denoted by 2 one finds from equations (2.15) and (2.18) to (2.20)

$$\mathbf{u}_{D2} = c_1 \mathbf{u}_r \quad (2.21)$$

$$\mathbf{u}_{D1} = -c_2 \mathbf{u}_r \quad (2.22)$$

Defining the sum of phase fluxes for a two-fluid mixture in terms of the diffusion velocities gives a relationship for the mixture flux i.e.

$$\sum_{k=1}^n \alpha_k \rho_k \mathbf{u}_k \mathbf{u}_k = \sum_{k=1}^n \alpha_k \rho_k (\mathbf{u}_m + \mathbf{u}_{Dk})(\mathbf{u}_m + \mathbf{u}_{Dk}) \quad (2.23)$$



Substituting the diffusion velocities in equation (2.23) with the relative velocity relationships by means of equations (2.21) and (2.22) yields

$$\sum_{k=1}^n \alpha_k \rho_k \mathbf{u}_k \mathbf{u}_k = \rho_m \mathbf{u}_m \mathbf{u}_m + \sum_{k=1}^n \alpha_k \rho_k \mathbf{u}_{Dk} \mathbf{u}_{Dk} \quad (2.24)$$

2.4.2. Mixture continuity

For a two fluid mixture the mixture conservation equations can be found by summing the separate phase equations and rewriting the phase velocity terms in terms of the diffusion velocity. One can show that summing the continuity equations for each of the phases, equation (2.6), and using the mixture property relationships yields

$$\frac{\partial}{\partial t}(\rho_m) + \frac{\partial}{\partial x_i}(\rho_m \bar{u}_{mi}) = 0 \quad (2.25)$$

2.4.3. Mixture momentum conservation

Similarly the mixture momentum equation may be found from the balance of all the phases momentum equations and applying the relevant mixture property relationships. Summing equation (2.10) over all phases yields

$$\begin{aligned} \frac{\partial}{\partial t} \sum_{k=1}^{\infty} \alpha_k \rho_k \bar{u}_{k_i} + \frac{\partial}{\partial x_j} \sum_{k=1}^{\infty} \alpha_k \rho_k \bar{u}_{k_j} \bar{u}_{k_i} = & - \frac{\partial}{\partial x_i} \sum_{k=1}^{\infty} \alpha_k \bar{p}_k + \sum_{k=1}^{\infty} \alpha_k \rho_k g_i \\ & + \sum_{k=1}^{\infty} \frac{\partial}{\partial x_j} (\alpha_k \tau_{k_{ij}}) + \sum_{k=1}^{\infty} \Gamma_{k\tau_i} \end{aligned} \quad (2.26)$$

Rewriting equation (2.26) in terms of mixture relationships and diffusion velocities results in

$$\frac{\partial}{\partial t} \rho_m \bar{u}_{m_i} + \frac{\partial}{\partial x_j} \rho_m \bar{u}_{m_j} \bar{u}_{m_i} = - \frac{\partial \bar{p}_m}{\partial x_i} + \rho_m g_i + \frac{\partial}{\partial x_j} (\tau_{m_{ij}} + \tau_{Dm_{ij}}) + \Gamma_{\tau_{m_i}} \quad (2.27)$$

where the viscous and turbulent stresses are given by

$$\tau_{m_{ij}} = \mu_m \left(\frac{\partial \bar{u}_{m_i}}{\partial x_j} + \frac{\partial \bar{u}_{m_j}}{\partial x_i} \right) - \sum \alpha_k \rho_k \overline{u'_{k_i} u'_{k_j}} \quad (2.28)$$

and the diffusion stress is given by

$$\tau_{Dm_{ij}} = \sum_{k=1}^n \alpha_k \rho_k u_{Dk_i} u_{Dk_j} \quad (2.29)$$

The conservation of the mixture momentum requires, Ishii and Zuber (1979),

$$\Gamma_{\tau_{m_i}} = \sum_{k=1}^n \Gamma_{k\tau_i} = 0 \quad (2.30)$$

2.4.4. Relative velocity (one dimensional derivation)

For a two fluid mixture model it then remains necessary to define the relative velocity since this in turn may define the diffusion velocity of each phase and along with the other mixture properties and constitutive relationships close the set of equations. Detailed descriptions of the derivation of the relative velocity are given by Ishii (1975), Ishii and Zuber (1979), Alhajraf (2001), Sun et al. (2003). One method to determine an expression for the relative velocity is by multiplying the mixture momentum equation by the dispersed phase volume

fraction and subtracting this from the dispersed phase momentum equation, Alhajraf (2001), i.e.

$$\begin{aligned} \frac{\partial}{\partial t} \alpha (\rho_k \bar{u}_{ki} - \rho_m \bar{u}_{mi}) + \frac{\partial}{\partial x_j} (\alpha \rho_k \bar{u}_{kj} \bar{u}_{ki}) - \frac{\partial}{\partial x_j} (\alpha \rho_m \bar{u}_{mj} \bar{u}_{mi}) = -\alpha \left(\frac{\partial p_k}{\partial x_j} - \frac{\partial p_m}{\partial x_j} \right) \\ + \alpha (\rho_k - \rho_m) g_i + \frac{\partial}{\partial x_j} (\alpha \tau_{kij}) - \frac{\partial}{\partial x_j} \alpha (\tau_{mij} + \tau_{Dmij}) + \Gamma_{ki} \end{aligned} \quad (2.31)$$

Rewriting equation (2.31) in terms of the dispersed phase interfacial drag, using the definition of the diffusion velocity to replace the dispersed phase velocity and assuming that the mixture and the dispersed phase has the same pressure results in

$$\begin{aligned} \Gamma_k = \alpha \frac{\partial}{\partial t} \rho_k \bar{u}_{Dki} + \alpha \frac{\partial}{\partial t} (\rho_k - \rho_m) \bar{u}_{mi} + \alpha \frac{\partial}{\partial x_j} (\rho_k \bar{u}_{kj} \bar{u}_{ki} - \rho_m \bar{u}_{mj} \bar{u}_{mi}) \\ - \alpha (\rho_k - \rho_m) g_i - \alpha \frac{\partial}{\partial x_j} (\tau_{kij}) + \alpha \frac{\partial}{\partial x_j} (\tau_{mij} + \tau_{Dmij}) \end{aligned} \quad (2.32)$$

For an infinite medium under steady state conditions and far away from a wall the mixture is reduced to a one-dimensional, gravity dominated flow and equation (2.27) may be used to derive an expression for the gravity term, Ishii and Zuber (1979) i.e.

$$-\frac{\partial \bar{p}_m}{\partial z} + \rho_m g + \frac{\partial}{\partial z} (\tau_m + \tau_{Dm}) = 0 \quad (2.33)$$

$$g = \frac{1}{\rho_m} \left(\frac{\partial \bar{p}_m}{\partial z} - \frac{\partial}{\partial z} (\tau_m + \tau_{Dm}) \right) \quad (2.34)$$

Assuming steady state conditions and substituting the gravity term in equation (2.32) with equation (2.34) yields

$$\Gamma_k = -\alpha (\rho_k - \rho_m) \left(\frac{1}{\rho_m} \left(\frac{\partial p_m}{\partial z} - \frac{\partial}{\partial z} (\tau_m + \tau_{Dm}) \right) \right) - \alpha \frac{\partial}{\partial z} (\tau_k - \tau_m - \tau_{Dm}) \quad (2.35)$$

$$\Gamma_k = -\alpha \frac{(\rho_k - \rho_m)}{\rho_m} \frac{\partial p_m}{\partial z} + \alpha \frac{\rho_k}{\rho_m} \frac{\partial}{\partial z} (\tau_m + \tau_{Dm}) - \frac{\partial}{\partial z} (\alpha \tau_k) \quad (2.36)$$

The momentum transfer between the fluid and particles due to interfacial drag may be found from the general drag function for a sphere, given by Ishii and Mishima (1984),

$$\Gamma_k = -\alpha \frac{3}{8} \frac{1}{r_d} C_D \rho_f u_r |u_r| \quad (2.37)$$

where r_d is the drag radius of the particle. Combining equations (2.37) and (2.36) yields

$$u_{ri} |u_{ri}| = \left[\frac{(\rho_k - \rho_m)}{\rho_m} \frac{\partial p_m}{\partial x_i} - \frac{\rho_k}{\alpha \rho_m} \frac{\partial}{\partial x_j} (\tau_{mij} + \tau_{Dmij}) + \frac{\partial}{\partial x_j} (\tau_{kij}) \right] \frac{8}{3} \frac{r_d}{C_D \rho_f} \quad (2.38)$$

given in vector form. Equation (2.38) is employed by the CFD software FLOW3D and used in this work to calculate the general drift velocity of particles in a mixed flow medium. Ignoring viscous and diffusion stresses this equation yields,

$$u_{ri} = \frac{8r_d}{3|u_r|C_D} \frac{(\rho_k - \rho_m)}{\rho_m} \frac{\partial p}{\partial x_i} \frac{1}{\rho_f} = D_f \frac{(\rho_k - \rho_m)}{\rho_m} \frac{\partial p}{\partial x_i} \frac{1}{\rho_f} \quad (2.39)$$

where D_f is an inverse drag function used in FLOW3D that may be approximated by a Stokes flow assumption to give

$$D_f = \frac{8r_d}{3|u_r|C_D} = \frac{2r^2}{9\nu} \quad (2.40)$$

Alternatively the relative velocity can also be expressed in terms of gravity using equation (2.32) without replacing the gravity term and using equation (2.37)

$$u_{ri} |u_{ri}| = \left[\left(\frac{\rho_k - \rho_m}{\rho_m} \right) \rho_m g_i - \frac{1}{\alpha} \frac{\partial}{\partial x_j} (\tau_{mij} + \tau_{Dmij}) + \frac{\partial}{\partial x_j} (\tau_{kij}) \right] \frac{8}{3} \frac{r_d}{C_D \rho_f} \quad (2.41)$$

$$u_r = \frac{8r_d}{3|u_r|C_D} \frac{(\rho_k - \rho_m)}{\rho_f} g \quad (2.42)$$

The snow drift models employed in this work requires the vertical settling velocity to calculate some of the components of the erosion and deposition fluxes within the computational domain. By ignoring viscous and turbulent stresses and assuming that the flow around the spherical particle falls in the Stokes regime one may simplify equation (2.42) to yield

$$u_r = w_f = \frac{d_p^2 g \rho_k}{18\mu} \quad (2.43)$$

Baumeister and Marks (1958) in Budd (1966) determined from empirical measurements that particles in the size range, $1 \mu\text{m} < d < 50 \mu\text{m}$, obey the Stokes law with their fall velocities being proportional to d^2 as per equation (2.43). However, for particles with a size range of $100 \mu\text{m} < d < 1000 \mu\text{m}$, Baumeister and Marks (1958) showed that the fall velocity is in fact linearly proportional to the particle diameter i.e.

$$u_r = w_f = Cd \quad (2.44)$$

where the proportionality coefficient C depends on the shape of the particle where $C=3880 \text{ s}^{-1}$ for spherical particles and $C=2440 \text{ s}^{-1}$ for irregular shaped particles, Budd (1966). Budd (1966) eventually found good agreement with his blowing snow measurements by using $C=3100 \text{ s}^{-1}$. By employing a modified drag function for the flow around a sphere, as per Carrier (1953),

$$C_d = \frac{24}{\text{Re}} (1 + 0.0808 \text{Re}) \quad (2.45)$$

one may determine an alternative particle fall speed relationship from equation (2.41), similar to that presented in Moore (1995), Bintanja (2000a), namely

$$0.1612u_r^2 + \frac{v}{r}u_r - \frac{2r\rho_s g}{9\rho_a} = 0 \quad (2.46)$$

The positive root of equation (2.46) gives the particle fall velocity. Figure 2.1 compares the particle fall speeds determined from equations (2.43), (2.44) and (2.46). The fall velocity employed in this work is calculated according to equation (2.46). Figure 2.1 shows that the settling velocity relationship determined from equation (2.46) agrees favourably with the empirical relationship determined by Budd (1966) given by equation (2.44) for $C=3100 \text{ s}^{-1}$ for a wide range of size classes. The mixture model employed here requires the particle drag coefficient as an input parameter to determine the slip velocity between the discrete phase and the continuous phase as per equation (2.39). If it is assumed that the relative velocity is suitably approximated by equation (2.46), then the particle Reynolds number can be calculated which provides a measure of the particle drag coefficient. Figure 2.2 compares the drag coefficients calculated from assumption of the standard Stokes flow around a spherical particle as well as with the modified drag assumption of equation (2.45).

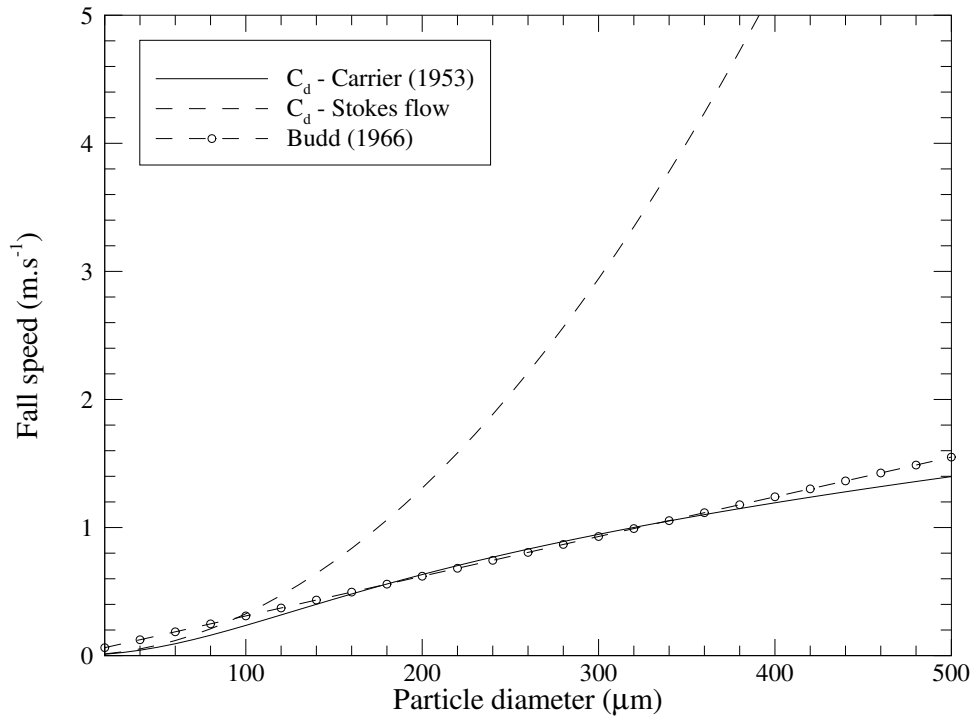


Figure 2.1. Particle fall speed as a function of particle diameter

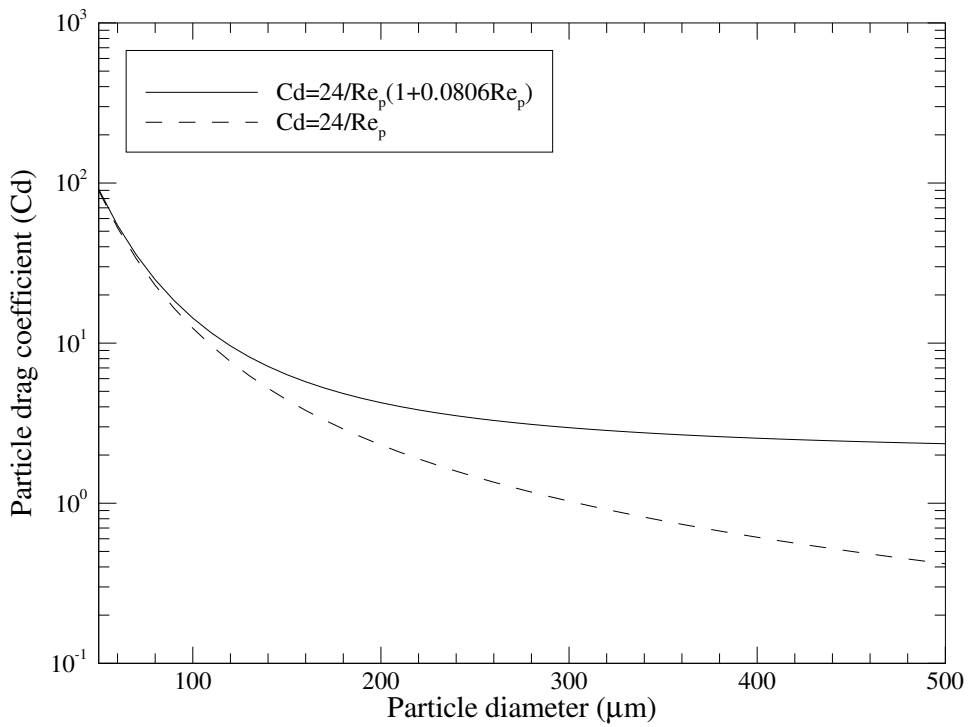


Figure 2.2. Particle drag coefficient vs. particle diameter

The particle fall speed may also be influenced by a shear field. A particle moving through a shear field may be subjected to a lift force proportional to the magnitude of a velocity gradient as well as the sign of the relative velocity between the particle and the fluid parcel, Saffman (1965). Thus a particle following the fluid in a shear field will experience lift in the same direction as the velocity gradient. Kallio and Reeks (1989), McLaughlin (1994), Wang and Maxey (1993) and Wang et al. (1997) among many researchers, found that the Saffman forces have a significant effect on the particle deposition velocity mainly in the viscous sublayer ($y^+ < 30$) and for particles settling by means of diffusional mechanisms i.e. particle relaxation times $2 < \tau_s < 10$. For the present work the computational cells near a wall are sufficiently far away from the wall to ensure that the law of the wall holds ($y^+ > 30$) and for our size classes and magnitude of shear fields the particle relaxation times are typically of the order of $\tau^+ > 100$. Thus the settling mechanisms are largely dominated by inertial and gravitational effects so that we may effectively ignore the influence of the Saffman forces.

The actual shear stress at the surface may also be influenced by the three-dimensionality of the boundary layer. The wall functions of the k- ϵ epsilon model employed here assume a fully developed two dimensional boundary layer at the wall in order to determine wall turbulence characteristics as well as the wall shear velocity. To include such three-dimensional effects one may include the streamwise gradient of the vertical velocity field to ensure a complete description of the shear stress. This has not been considered here but could be an interesting topic for future study where the effects of alternative or more advanced turbulence models on the modelling of deposition characteristics may be studied.

2.4.5. Particle size distribution

The particle size distribution under blowing snow conditions has been extensively investigated by numerous researchers including Budd et al. (1966), Budd (1966), Schmidt (1981), (1982), Pomeroy (1988), Dover (1993), Moore (1995), Mann (1998), Bintanja (2000a), (2000b) and Xiao et al. (2000). The earlier works aimed to provide a relationship for the particle size distribution at different heights above the surface in accordance with measurements taken during blowing snow occurrences, in particular those measurements taken by Budd et al. (1966) in Antarctica. It was found that the particle size distribution at the various measurement heights is best fitted by means of a two-parameter gamma distribution.

By employing the basic theory for the distribution of suspended snow, equation (F.5) in Appendix F, as well as employing the two-parameter gamma function for the frequency distribution of snow size classes, Budd (1966) derived functions for the variation of particle size and fall velocity as a function of height and shear velocity. Comprehensive details on the derivation and theory may be found in Budd (1966), Moore (1995) and Mann (1998) among others. The resultant function for the size distribution reads

$$\bar{d}_z = \frac{\bar{d}_{z_1}}{1 + \left(\frac{\beta_2}{\kappa u_*}\right) \ln\left(\frac{z}{z_1}\right)} \quad (2.47)$$

The subscripts 1 in equation (2.47) refer to the reference values of height, mean diameter and mean fall velocity. The gamma function parameters α and β are found from the measurement data and are related through

$$\alpha\beta = \text{Mean} \quad (2.48)$$

$$\alpha\beta^2 = \text{Variance} \quad (2.49)$$

and $\beta_2=C\beta$ in accordance with a linear relationship for the vertical particle fall velocity as a function of mean particle diameter for ice and drifting snow particles, equation (2.44).

In the present work this theory and results are mainly used to find an estimate of the mean diameter of the drifting particle at a particular height above the surface and its corresponding fall velocity. For this purpose the reference values used by Budd (1966) for a height of $z_1=50$ cm are evaluated. From the gamma distribution for $z_1=50$ cm in Budd (1966), one may determine that $\alpha=14.62$ and $\beta=0.0068$ which gives $\beta_2=21.09$. Using this reference height and the mean diameter at this reference height of $96 \mu\text{m}$, one finds the particle distribution with equation (2.47). To account for the particle shape variation Budd (1966) defined the projective diameter of the particle namely $d_p=4/\pi d_e$. Extrapolation of the projective diameter down to a height corresponding to the aerodynamics surface roughness $z_0=0.15$ mm gives a value of approximately $d_0=330 \mu\text{m}$. This value is assumed to represent the saltating or surface particle diameter. The particle diameter at the surface has been found to range between $200 \mu\text{m}$ and $500 \mu\text{m}$, as per Budd (1966) and for SANAE IV ranges from $100 \mu\text{m}$ to $500 \mu\text{m}$, Beyers and Harms (2003a). Schmidt (1982) carried out his own measurements of the particle size distribution during blowing snow events and determined empirical relationships for the

particle size as a function of height as well as for the shape parameter, α , as a function of height. Budd (1966) assumed that the shape parameter was constant at $\alpha \approx 15$ during his analysis. Again using a reference height of 50 cm but using the reference particle size and shape parameters of Schmidt (1982) one may find another vertical mean particle size distribution. Pomeroy (1988) averaged all the regression coefficients given by Schmidt (1982) for his particle size variation and shape parameter and determined respective expressions for these variables as

$$\bar{r} = 4.6 \cdot 10^{-5} z^{-0.258} \quad (2.50)$$

$$\alpha = 4.08 + 12.6z \quad (2.51)$$

Figure 2.3 compares the size variation as discussed above of Budd (1966), Schmidt (1982) and Pomeroy (1988). Moore (1995) and Mann (1998) indicate that the gamma function shape parameter should only be $\alpha=2$, a smaller value than given above. Pomeroy and Male (1992) also indicate that the focus height or the height where the particle size distribution starts to follow the gamma distribution as given by equation (2.47), is not equal to the saltation height, but is rather given by

$$h_f = 0.08436u_*^{1.27} \quad (2.52)$$

Using $\alpha=2$, a mean saltating particle diameter of 150 μm , as done by Bintanja (2000b) and Xiao et al. (2000), and taking the reference height as the focus height, one may determine another vertical size distribution as shown in figure 2.3. This is smaller due to the considerably smaller shape parameter employed.

In the computational domain the snow drift scheme used in this analysis requires the vertical fall velocity above the surface. This is dependent, inter alia, on the particle size in the layer above the surface. For this work it is assumed that the fall velocity to be used in the snow drift scheme should be calculated for particles near the saltation height or at the focus height. As shown, equation (2.47) determines the mean particle diameter versus height for a given reference height as well as shear velocity. Again, using $\alpha=2.0$, the vertical size distribution for different shear velocities can be determined, the fall velocities calculated from equation (2.44) and with the results shown in figure 2.4.

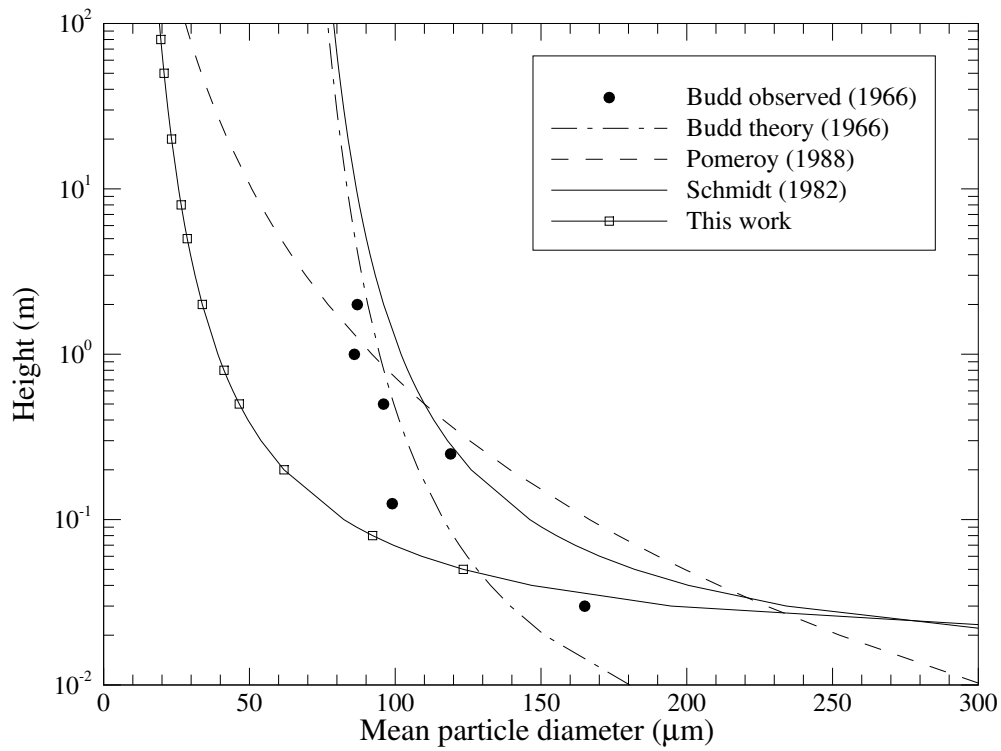


Figure 2.3: Height distribution of the mean particle diameter, reference height 0.5m

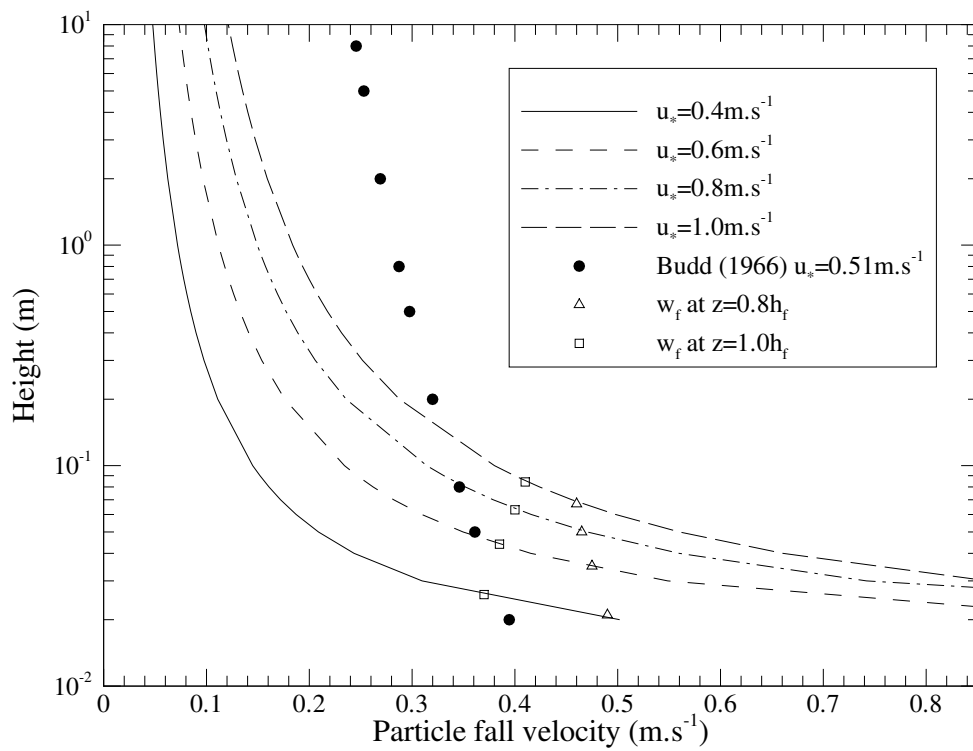


Figure 2.4: Height distribution of the particle mean fall velocity.

The fall velocity at the focus height and just below the focus height is also marked in figure 2.4. This suggests that in the region near the edge of the saltation layer, the fall velocity range is between $0.4 \text{ m}\cdot\text{s}^{-1}$ and $0.5 \text{ m}\cdot\text{s}^{-1}$ for the range of shear velocities evaluated. Therefore it is assumed for the present work that the particle fall velocity is constant and a value of $0.45 \text{ m}\cdot\text{s}^{-1}$ is used throughout the work.

2.4.6. Mixture diffusion equation

The concentration change in the mixture is governed by a turbulent convection-diffusion equation. The volume-time averaged diffusion equation for the dispersed phase is given by the general continuity equation for phase k

$$\frac{\partial}{\partial t}(\alpha_k \rho_k) + \frac{\partial}{\partial x_i}(\alpha_k \rho_k \bar{u}_{ki}) = \frac{\partial}{\partial x_i}(\alpha'_k \rho'_k u'_{ki}) \quad (2.53)$$

The derivation of equation (2.53) is given in Appendix B. Using the diffusion velocity, equation (2.18), to remove the phase velocity and employing the eddy viscosity concept to approximate the turbulent flux terms one finds

$$\frac{\partial \alpha_k \rho_k}{\partial t} + \frac{\partial}{\partial x_i}(\alpha_k \rho_k \bar{u}_{mi}) = \frac{\partial}{\partial x_i} \left(\frac{\mu_t}{\sigma^\eta} \frac{\partial}{\partial x_i}(\alpha_k \rho_k) \right) - \frac{\partial}{\partial x_i}(\alpha_k \rho_k \bar{u}_{Dki}) \quad (2.54)$$

Since the phase concentration is given by

$$\eta = \alpha_k \rho_k \quad (2.55)$$

then

$$\frac{\partial \eta}{\partial t} + \frac{\partial}{\partial x_i}(\eta \bar{u}_{mi}) = \frac{\partial}{\partial x_i} \left(\frac{\mu_t}{\sigma^\eta} \frac{\partial \eta}{\partial x_i} \right) - \frac{\partial}{\partial x_i}(\eta \bar{u}_{Dki}) \quad (2.56)$$

If the second phase represents the dispersed phase then equation (2.56) can be written in terms of the relative velocity, equation (2.21), i.e.

$$\frac{\partial \eta}{\partial t} + \frac{\partial}{\partial x_i} \eta (\bar{u}_{mi} + c_1 \bar{u}_{ri}) = \frac{\partial}{\partial x_i} \left(\frac{\mu_t}{\sigma^\eta} \frac{\partial \eta}{\partial x_i} \right) \quad (2.57)$$

where the continuous phase suspended mass loading, c_1 , for this dilute flow is of the order of unity. Appendix D gives the derivation of equation (2.57) in terms of the vertical fall velocity.

2.5. TURBULENCE MODELLING

2.5.1. Reynolds averaged Navier Stokes equations (RANS)

The time averaging of the instantaneous Navier Stokes equations, as highlighted earlier in the chapter, resulted in what is known as the Reynolds Averaged Navier Stokes (RANS) equations, equation (2.10), given in volume averaged form applicable to the multiphase continuum. This time averaging process yields momentum equations similar to the instantaneous equations except for the addition of new terms consisting of fluctuating components. These additional terms may be grouped in an apparent stress tensor, as given above, and are also known as the Reynolds stresses. These stresses require modelling to close the set of governing equations. Various methods exist to achieve such closure for the RANS equations including eddy viscosity modelling, where the enhanced turbulent momentum transfer is facilitated by an increased viscosity, or second moment closure schemes where each Reynolds stress term is modelled individually. According to the eddy viscosity concept the Reynolds stresses should be proportional to the mean strain rate, similar to viscous stresses being proportional to the fluid deformation, while experimental works has shown that turbulence decays in diminishing shear fields. Boussinesq (1877) proposed a linear relationship between the Reynolds stress and the rate of deformation i.e.

$$\overline{\rho u'_i u'_j} = \mu_t \left(\frac{\partial \bar{u}_i}{\partial x_j} + \frac{\partial \bar{u}_j}{\partial x_i} \right) \quad (2.58)$$

This models the effects of turbulence through an enhanced viscosity by means of the parameter μ_t , proportional to the turbulence level. Thus closure of the governing equations can be achieved if an approximation of the so-called turbulence viscosity can be found. Various methods exist to achieve this including mixing length, one-equation and two-equation models. This work employs the two-equation k- ϵ turbulence model which requires the solution of a turbulence kinetic energy (k) transport equation as well as a rate of turbulent energy dissipation (ϵ) equation, Launder and Spalding (1974).

2.5.2. Turbulence kinetic energy equation

The turbulence kinetic energy and rate of dissipation of turbulent energy provides a measure of the velocity and length scale associated with a turbulent eddy from which a turbulent viscosity may be approximated i.e.

$$\mu_t = \rho C_\mu \frac{k^2}{\varepsilon} \quad (2.59)$$

Details of the derivation of the k and ε equations are given by Wilcox (1993). The volume-time averaged turbulence kinetic energy of the flow field is found from the solution of

$$\rho \frac{\partial k}{\partial t} + \rho \bar{u}_j \frac{\partial k}{\partial x_j} = \frac{\partial}{\partial x_j} \left(\mu \frac{\partial k}{\partial x_j} \right) - \frac{\partial}{\partial x_j} \left(\frac{\rho}{2} \overline{u'_j u'_i u'_i} + \overline{\rho u'_j} \right) - \rho \overline{u'_i u'_j} \frac{\partial \bar{u}_i}{\partial x_j} - \mu \frac{\partial \overline{u'_i}}{\partial x_j} \frac{\partial \overline{u'_i}}{\partial x_j} \quad (2.60)$$

as given in Ferziger and Perić (2002). The second term on the right hand side of equation (2.60) represents the turbulent diffusion of turbulence kinetic energy and may be approximated by

$$- \frac{\partial}{\partial x_j} \left(\frac{\rho}{2} \overline{u'_j u'_i u'_i} + \overline{\rho u'_j} \right) = \frac{\mu_t}{\sigma_t^k} \frac{\partial k}{\partial x_j} \quad (2.61)$$

The third term represents the rate of turbulence kinetic energy production which may be approximated by the eddy viscosity model to yield

$$- \rho \overline{u'_i u'_j} \frac{\partial \bar{u}_i}{\partial x_j} = \mu_t \left(\frac{\partial \bar{u}_i}{\partial x_j} + \frac{\partial \bar{u}_j}{\partial x_i} \right) \frac{\partial \bar{u}_i}{\partial x_j} - \frac{2}{3} \rho k \delta_{ij} \quad (2.62)$$

The right hand side of equation (2.62) consists of the eddy viscosity and a strain rate scale, Murakami (1998),

$$\mu_t \left(\frac{\partial \bar{u}_i}{\partial x_j} + \frac{\partial \bar{u}_j}{\partial x_i} \right) \frac{\partial \bar{u}_i}{\partial x_j} = \mu_t S^2 \quad (2.63)$$

where

$$S = \sqrt{\frac{1}{2} \left(\frac{\partial \bar{u}_i}{\partial x_j} + \frac{\partial \bar{u}_j}{\partial x_i} \right)^2} \quad (2.64)$$

The fourth term on the right hand side of equation (2.60) is often approximated by the product of density and dissipation, $\rho\varepsilon$. Thus equation (2.60) simplifies to

$$\frac{\partial k}{\partial t} + \bar{u}_j \frac{\partial k}{\partial x_j} = \frac{\partial}{\partial x_j} \left(\left(v + \frac{v_t}{\sigma_t^k} \right) \frac{\partial k}{\partial x_j} \right) - v_t \left(\frac{\partial \bar{u}_i}{\partial x_j} + \frac{\partial \bar{u}_j}{\partial x_i} \right) \frac{\partial \bar{u}_i}{\partial x_j} - \varepsilon \quad (2.65)$$

2.5.3. Rate of turbulent energy dissipation equation

The rate of turbulent dissipation is found from the solution of

$$\frac{\partial \varepsilon}{\partial t} + \bar{u}_j \frac{\partial \varepsilon}{\partial x_j} = \frac{\partial}{\partial x_j} \left(\left(\frac{v + v_t}{\sigma_t^\varepsilon} \right) \frac{\partial \varepsilon}{\partial x_j} \right) + \frac{\varepsilon}{k} \left(C_{\varepsilon 1} v_t \left(\frac{\partial \bar{u}_i}{\partial x_j} + \frac{\partial \bar{u}_j}{\partial x_i} \right) \frac{\partial \bar{u}_i}{\partial x_j} - C_{\varepsilon 2} \varepsilon \right) \quad (2.66)$$

as given in Ferziger and Perić (2002). Modelling constants for the turbulence model applied to confined flows such as within wind tunnels are given by Jones and Launder (1972) as

$$C_{\varepsilon 1} = 1.44 \quad C_{\varepsilon 2} = 1.92 \quad C_\mu = 0.09 \quad \sigma_t^k = 1.0 \quad \sigma_t^\varepsilon = 1.3 \quad (2.67)$$

However, for environmental flows the model constants need to be consistent with a homogeneous atmospheric boundary layer, i.e. from Richards and Hoxey (1993), Huser et al. (1997). For $\kappa = 0.41$ the model constants are

$$C_{\varepsilon 1} = 1.44 \quad C_{\varepsilon 2} = 1.92 \quad C_\mu = 0.09 \quad \sigma_t^k = 1.0 \quad \sigma_t^\varepsilon = 1.16 \quad (2.68)$$

Richards and Hoxey (1993) calculated new constants for an atmospheric boundary layer simulation from measurements in the surface layer and reported values for $\kappa = 0.42$ of

$$C_\mu = 0.013 \quad \sigma_t^\varepsilon = 3.22 \quad (2.69)$$

The values used in this thesis follow those given in equation (2.68) but the additional values given by equation (2.69) are presented as an example to stress the need for turbulence measurements during the analysis of environmental flows. Although this is a costly exercise, it is important to establish the correct upstream turbulent properties for the numerical analysis.

The particle effects on turbulence are not considered for the present analysis. The simulated turbulence will be influenced indirectly by the particles through the modified wall function

which includes a momentum sink due to saltation. In addition, the turbulence may be strongly affected by particle suspension which may cause expenditure of turbulent energy. Such effects may not be insignificant or negligible but are not included in the present model.

The three-dimensional turbulent flow field surrounding obstacles is characterized by a highly anisotropic strain rate tensor. The original k-ε turbulence model is based on the underlying assumption of isotropic turbulence in order to approximate the eddy viscosity. Therefore it can not reproduce anisotropic turbulent features in the flow to any degree of accuracy. This results in inaccuracies in the prediction of the flow field especially in regions of flow separation or impinging flows. Various modifications to the standard k-ε turbulence model or alternative and more advanced turbulence models would greatly improve the accuracy of the flow field simulations. Some brief comments to this end are given in Appendix I. However, the k-ε turbulence model has proven for the present work to be a simple and also an effective model for the turbulent flow field analysis.

2.5.4. Wall functions

The boundary conditions for the k-ε turbulence model require careful consideration. For high Reynolds number flows the sublayer of the boundary layer may be very thin which will require many grid points to resolve. Instead one may employ wall functions to approximate the logarithmic region of the turbulent boundary layer. The turbulent velocity profile of the inner turbulent layer is given by the well known logarithmic function

$$u^+ = \frac{1}{\kappa} \ln(z^+) + B \quad (2.70)$$

where

$$u^+ = \frac{u}{u_*} \quad (2.71)$$

and

$$z^+ = \frac{z_w u_*}{\nu} \quad (2.72)$$

is the dimensionless horizontal velocity and normal distance from the wall respectively, while $B=5.0$ is an empirical constant. By assuming that the rate of dissipation of turbulence kinetic energy equals the rate of production at the first near wall node one may find wall boundary conditions for the turbulence properties. It is furthermore assumed that all mean velocity gradients, except for the vertical gradient of the tangential velocity, are zero. It can be shown that these assumptions lead to

$$\mu_t \left(\frac{\partial u}{\partial n} \right)^2 = \frac{\tau^2}{\mu} = \frac{u_*^4}{C_\mu k^2} \rho \epsilon \quad (2.73)$$

where the shear velocity is a measure of the surface shear stress as per equation (E.7) i.e.

$$u_* = \sqrt{\frac{\tau}{\rho}} \quad (2.74)$$

Rewriting this yields the turbulence kinetic energy at the first node away from the wall

$$k = \frac{u_*^2}{\sqrt{C_\mu}} \quad (2.75)$$

By differentiating equation (2.70) in terms of the normal distance from the wall for the first node, z_w , gives the vertical velocity gradient at the wall

$$\frac{\partial u}{\partial n} = \frac{u_*}{\kappa z_w} \quad (2.76)$$

Combining this with equations (2.73) and (2.75) yields the boundary condition for the rate of turbulent dissipation at the first node away from the wall

$$\epsilon = \frac{u_*^3}{\kappa n} \quad (2.77)$$

The shear velocity is required for the calculation of equations (2.75) and (2.77). This is found from an iterative solution of equation (2.70).

Atmospheric flows over real surfaces with varying roughness require additional modelling, if one does not model the roughness elements explicitly. This may be accomplished by means of

modification of the empirical constant B. A dimensionless wall roughness length may be formed, White (1991),

$$k_s^+ = \frac{k_s u_*}{\nu} \quad (2.78)$$

where k_s is an effective roughness length not necessarily equal to the physical size of the roughness elements. Equation (2.78) may be incorporated into equation (2.70) for fully rough flows, as per White (1991),

$$u^+ = \frac{1}{\kappa} \ln\left(\frac{zu_*}{\nu}\right) + B - \Delta B(k_s^+) \quad (2.79)$$

where

$$\Delta B(k_s^+) = \frac{1}{\kappa} \ln(1 + 0.3k_s^+) \quad (2.80)$$

Additional background and details of transitional roughness regimes formulations are given by Beyers (2000). The atmospheric boundary layer flow is considered fully rough in this work. Beyers and Harms (2003a) extended equation (2.79) to include the additional effective roughness induced by saltating particles i.e.

$$\Delta B(k_s^+) = \frac{1}{\kappa} \ln(1 + 0.3k_s^+ + 9.53s^+) \quad (2.81)$$

$$s^+ = \frac{c_1 u_*^*}{2g\nu} \quad (2.82)$$

Details and background to this formulation is given in Appendix G.

2.6. SNOW DRIFTING MODELLING

2.6.1. Saltation and suspension of snow

Saltation threshold

The general description of the snow drifting process, in the absence of precipitating snow, is briefly given as follows. Wind-borne snow transport is initiated in the atmospheric surface layer when the aerodynamic surface shear stress is large enough to overcome the inertia,

immersed weight and cohesive bonds of snow or ice particles on the surface layer of the snow pack, Schmidt (1980). Particles then start rolling and sliding along the surface (creep) and will eventually, if the available viscous shear energy is sufficient, overcome gravity and eject from the snow pack, jumping along the surface (saltation). The term saltation was first coined by Gilbert (1941), in Kim et al. (1991), for the study of underwater sand bed motion and originates from the Latin verb 'saltare', which means 'to leap or dance'. The initiation of saltation is generally defined by a threshold wind velocity scale such as the shear velocity, u_{*t} , a measure of the surface shear stress. Bagnold (1941) defined the "fluid" threshold speed for sand transport as the wind speed to initiate movement of a specific size of particle and the "impact" threshold speed as the wind speed required to maintain saltation, usually lower than the "fluid" threshold due to the presence of the impacting particles. The fluid and impact threshold velocity is also referred to as the static and dynamic threshold velocity respectively, Li and Pomeroy (1997). The impact threshold may not always be lower than the fluid threshold, especially for the case of inelastic grains of fresh snow, as suggested by Doorschot and Lehning (2002). These saltating particles impact with the snow pack and dislodge more particles from the surface. Typical fluid threshold shear velocities are $u_{*t} < 0.25 \text{ m}\cdot\text{s}^{-1}$ for fresh snow and $0.25 \leq u_{*t} \leq 1.0$ for old and wind hardened snow surfaces, Pomeroy and Gray (1990), Tabler (1980a). This present work regards threshold conditions as conditions or wind speeds found at the cessation of saltation since all impacts and rebounding processes are present as saltation ceases and not necessarily when it starts, Pomeroy (1989). Threshold shear velocities of $u_{*t} = 0.28 \text{ m}\cdot\text{s}^{-1}$ were measured by Budd et al. (1966) and Liljequist (1957) for Antarctic conditions. Similar observations were made at SANAE IV as given by Beyers and Harms (2003a) and described in Appendix G. If the turbulent energy of the flow field is sufficiently large, then the saltating particles are entrained further upwards by turbulent eddies (suspension). The sustained saltation and suspension of snow particles expends turbulent energy of the carrier fluid, which means this process is 'self limiting' i.e. steady state concentrations may exist under ideal circumstances, Kind (1976), Bintanja (1998), (2000a). Therefore snow transported over a uniform surface or fetch under ideal conditions would eventually develop to an equilibrium snow concentration distribution or profile. Early research, Kobayashi (1973) in Kind (1976), (1986), indicated that saltation is the primary mode of sediment transport for environmental flows for $u_{10} < 15 \text{ m}\cdot\text{s}^{-1}$. For higher wind

velocities suspension becomes the dominant mode of snow transport, Pomeroy and Male (1992).

The snow drifting process is often compared to aeolian sand transport and the extensive work by Bagnold (1941) is often quoted. Although the transport mechanisms are essentially the same, sand is affected little, if any, by temperature, pressure loads or metamorphic processes. Such effects may change the size, structure or cohesion characteristics of the snow grains which in turn influences its response to wind forces. The effect of this difference is shown, for example, by a Barchan sand dune with its gentle slope on the windward side while the steep slope is on the leeward side. Sastrugi, on the other hand, has its gentle slope on the leeward side with a steep, vertical or even undercut slope on the windward side, Gerdel (1960). Interestingly Schmidt (1986a) sampled the forces required to fracture grains from a snow surface and showed that the upwind and eroding face of a moving snow dune required less force to fracture than the top deposition face of the dune.

For temperatures higher than -10°C , Gerdel (1960) suggests favourable conditions for cornice formation. Due to these strong cohesive forces between the surface particles and the dependence of the intergranular bonds on particle size, temperature and pressure, there exist large differences between the “fluid” and “impact” thresholds as explained above. Schmidt (1980), (1986b) shows and concludes that the threshold force required to break the cohesive bonds between particles is at least an order of magnitude larger than the force required to overcome the immersed weight of the particles. In his work it is shown that cohesion increases rapidly with snow particle size while cohesion strength on contact decreases exponentially with decreasing temperature. He also found that initial cohesive forces are less, at a given temperature, the lower the humidity with respect to saturation over ice and that threshold strength will increase in time after deposition. This last characteristic is clear from the stability of snowdrifts almost immediately after deposition and thus, even slight changes in gusting or local flow velocity may result in longer average rests between moves and greater resistance to subsequent moves. It is evident that the onset of saltation is a complicated process that can not be easily generalised. Various researchers have derived empirical functions for the threshold velocity, Bagnold (1941), Schmidt (1981), Li and Pomeroy (1997) and Sugiura et al. (1998), as functions of among other parameters, the fluid and particle density, particle diameter, temperature and bond strengths. For the present work the threshold

value observed at SANAE IV of $u_{*t} = 0.28 \text{ m}\cdot\text{s}^{-1}$ as mentioned above is considered most appropriate and is therefore used throughout the numerical analysis.

Saltation concentration profile

For a numerical flow analysis of the aeolian snow transport process it is necessary to define approaching flow boundary conditions that establish a realistic upstream snow concentration or snow volume fraction distribution. The wind driven snow concentration distribution is divided into mainly two regions (ignoring the surface creep transport region) namely the saltation region at the surface and the suspension region above the saltation region. Thus one needs relationships that define the vertical extent of the region as well as the snow concentration distribution within the region under consideration.

The snow concentration profile during blowing snow conditions have been extensively studied with diverse results. Sommerfield and Businger (1965) measured snow concentration profiles and tried to fit these results to the theoretical steady state particle concentration profile derived by Shiotani and Arai (1953), see Appendix F. The discrepancy between their measured values and the theoretical results led them to deduce that the eddy diffusivity for snow transport is of the order of ten times larger than the eddy diffusivity of the air transport, Businger (1965).

Budd et al. (1966) and Budd (1966) studied the drifting of non-uniform snow particles and stated that the difficult nature of snow drift measurements has made it difficult to evaluate the theory and the deviation of the measurements from the theory, as mentioned above. They considered their measurements extensive enough to explain these deviations from the predictions based on the turbulent exchange theory as done by Shiotani and Arai (1953). The discrepancy is explained by dropping either of two simplifying assumptions in the measured concentration profile analysis i.e. the constant fall velocity and the existence of a steady state. The erroneous particle eddy viscosity of Sommerfield and Businger (1965) comes from the estimation of too high particle fall velocities for the size ranges involved in snow drifting, Schmidt (1982).

Bagnold (1941) postulated that the difference in momentum of sand particles rising from the surface and the momentum of sand dropping to the surface during saltation is proportional to the shear stress working on the surface, in Takeuchi (1980). He subsequently concluded that the total sand flux during saltation is

$$Q_{\text{salt}} = \frac{C_p u_*^3}{g} \quad (2.83)$$

Dyunin (1963) applied dimensional analysis of fluid and granular material transport to snow bearing air flow (dynamic theory in Radok (1977)). He defines the snow flux (q) as the weight of snow carried through a unit of area of transverse section per unit of time ($\text{kg}\cdot\text{m}^{-2}\cdot\text{s}^{-1}$). The total snow flux (Q) is defined as the height integrated snow flux or the weight of snow per unit width per unit time ($\text{kg}\cdot\text{m}^{-1}\cdot\text{s}^{-1}$). His work presented the results of various researchers in describing the total snow flux, and converted these formulae to 1 meter reference velocity. This is summarised in table 2.1 as per Takeuchi (1980) and shows a diverse range of results.

Table 2.1. Total snow transport ($\text{g}\cdot\text{m}^{-1}\cdot\text{s}^{-1}$) from 1 meter horizontal velocity data

Researcher	Total snow flux formulae	Remarks
Khrgian (Dyunin 1963)	$Q = -5.8 + 0.267U_1 + 0.123U_1^2$	
Ivanov (Dyunin 1963)	$Q = 0.0295U_1^3$	
Mel'nik (Dyunin 1963)	$Q = 0.092U_1^3$	
Dyunin (1963)	$Q = 0.0334(1 - (4/U_1))U_1^3$	
Komarov in Takeuchi (1980)	$Q = 0.011U_1^{3.5} - 0.67$	
Budd et al. (1966)	$\ln(Q) = 1.18 + 0.1080U_1$	2m drift height
Kobayashi in Takeuchi (1980)	$Q = 0.03U_1^3$	
Takeuchi (1980)	$Q = 0.02U_1^{2.7}$	2m drift:old firm snow
Takeuchi (1980)	$Q = 0.0029U_1^{4.16}$	2m drift:settled dry now

Takeuchi (1980) argued that the vertical density of drifting snow could not be uniquely defined unless the drift was saturated or fully developed. The drift was considered to develop towards a fully developed state within a fetch length of approximately 350 meter and that

suspended snow would gradually take over as the dominant mode of transport as the drift develops.

Kobayashi et al. (1985) carried out snow drift measurements on a strong katabatic wind slope in East Antarctica and concluded that vertical snow fall density during blowing snow conditions may be found from the measured snow mass flux vertical profile asymptotes. This is described in Appendix F.

Takahashi (1985) measured total snow drift fluxes in Antarctica and found that above 1 meter height the drift flux is proportional to the 8th power of wind velocity. Below 0.1 meter a 4th power of wind velocity was determined. This supported the theoretical 3rd power relationship given by Bagnold (1941), equation (2.83), for saltation dominated flux. The large power factor was attributed to suspension dominated flows in strong wind conditions. Their measured threshold wind velocity was 6 m·s⁻¹. They also found small snow repose angles for high temperatures and attributed this to rounding of the snow crystals. The low temperature snow crystals showed high repose angles.

The total saltation snow transport is given by

$$Q_{\text{salt}} = u_p \frac{W_p}{g} \quad (2.84)$$

where u_p is the mean saltating particle velocity which is proportional to the threshold shear velocity, Pomeroy (1989) and Pomeroy and Gray (1990),

$$u_p = cu_{*t} \quad (2.85)$$

with $c=2.3$, and that this velocity remains constant during saltation. W_p is the weight of the saltating snow particles over a unit area of snow cover. Following Owen (1964) and Schmidt (1986b), Pomeroy (1989) indicate that the weight of saltating snow is related to the flow shear experienced by the particles i.e.

$$W_p = e(\tau - \tau_n - \tau_t) \quad (2.86)$$

where the proportionality coefficient, e , is the saltation efficiency. The immersed weight of the particles is balanced by the excess shear stress that consists of the total atmospheric shear

stress less the shear stress applied to non-erodible surface elements, τ_n , and less the threshold shear stress applied to the erodible surface, τ_t . The saltation efficiency is inversely related to surface friction resulting from particle impact and ejection i.e. harder surfaces show greater saltation transport since less kinetic energy is lost through particle impacts as opposed to soft surfaces, Schmidt (1986b). Measurements of mass fluxes resulted in a relationship for the saltation efficiency by Pomeroy and Gray (1990) namely

$$e = \frac{1}{4.2u_*} \quad (2.87)$$

Thus the total saltation snow transport is given by a combination of equations (2.84) to (2.87), as per Pomeroy and Gray (1990),

$$Q_{\text{salt}} = \frac{0.68\rho}{u_*g} u_{*t} (u_*^2 - u_{*n}^2 - u_{*t}^2) \quad (2.88)$$

This indicates that total saltation flux varies linearly with friction velocity and thus also with wind velocity as opposed to the cubic relationship given by equation (2.83). The saltating snow particles are a mass source for possible suspension of particles from the lower near surface layer to upper regions through turbulent diffusion. The height of the interface between the saltation and the suspension layer is defined as per Greeley and Iversen (1985) as the ratio between the measured total snow transport and the mean snow mass flux and is given by,

$$h_s = \frac{1.6}{2g} u_*^2 \quad (2.89)$$

The mean saltation density or reference saltation density is given by Pomeroy and Gray (1990) and Déry and Taylor (1996), Déry et al. (1998) as

$$\eta_r = \frac{Q_{\text{salt}}}{h_s u_p} \quad (2.90)$$

Equation (2.90) is used in the present analysis as the inlet snow concentration for the saltation layer, the vertical extent of which is defined by equation (2.89). Doorschot and Lehning (2002) have suggested that the saltation flux given by equation (2.88) may underestimate the total saltation flux since the effects of aerodynamic entrainment (turbulent diffusion) are

usually ignored but may also contribute to the flux in the saltation layer. This is not investigated any further in this study.

Suspended snow concentration profile

The saltation layer acts as a snow source for turbulent entrainment. If the turbulence kinetic energy in the surface layer is sufficient, snow particles will be entrained vertically into the suspension layer. The suspended snow flux can be represented by the general relationship

$$q_{\text{susp}} = \eta(z)u(z) \quad (2.91)$$

and the total suspended snow transport is then given by the general mass flux description

$$Q_{\text{susp}} = \int_{h_s}^{\infty} \eta(z)u(z)dz \quad (2.92)$$

The suspended snow concentration profile required in equation (2.91) may be found from a one-dimensional steady state equation for settling diffusion in turbulent flows as described in Appendix F. The vertical velocity distribution is given by equation (E.7), Appendix E, for a fully developed profile for a turbulent atmospheric boundary layer. Pomeroy and Male (1992) used these functions to ultimately derive a vertical suspended snow concentration profile namely

$$\eta_{\text{susp}}(z) = 0.8 \exp\left(-1.55\left(4.78u_*^{-0.544} - z^{-0.544}\right)\right) \quad (2.93)$$

Mellor and Fellers (1986) provided an earlier empirical relationship for the snow concentration (in $\text{g}\cdot\text{m}^{-3}$) and snow flux (in $\text{g}\cdot\text{m}^{-2}\cdot\text{s}^{-1}$) found through regression analysis of snow flux and wind velocity measurements

$$\begin{aligned} \eta(u_{10}, z) = & \exp\left(4.8679 - 0.42209 \ln(z) - 34.369(1/u_{10}) - 0.13265(\ln(z))^2 \right. \\ & - 17.427(\ln(z))(1/u_{10}) - 972.01(1/u_{10})^2 - 0.0070277(\ln(z))^3 \\ & \left. + 3.2692(\ln(z))^2(1/u_{10}) + 135.54(\ln(z))(1/u_{10})^2 + 6430.2(1/u_{10})^3 \right) \end{aligned} \quad (2.94)$$

$$\begin{aligned} q_{\text{susp}}(u_{10}, z) = & \exp\left(10.089 - 0.41049 \ln(z) - 122.03(1/u_{10}) - 0.13856(\ln(z))^2 \right. \\ & - 14.446 \ln(z)(1/u_{10}) - 0.0059773(\ln(z))^3 + 3.2682(\ln(z))^2(1/u_{10}) \\ & \left. + 114.13 \ln(z)(1/u_{10})^2 + 2290.0(1/u_{10})^3 \right) \end{aligned} \quad (2.95)$$

They established that very close to the ground the snow concentration curves converge, indicating that a maximum snow concentration may exist independent of wind speed, $\eta \approx 1.4 \text{ kg}\cdot\text{m}^{-3}$, as noted by Owen (1964), Budd (1966), Greeley and Iversen (1985) and Tabler (1991a). Such a maximum snow concentration yields a typical maximum snow volume fraction of $\alpha_s = \eta/\rho_s = 0.0016$ as mentioned by Bintanja (2000a) and mentioned earlier in this chapter.

The total saltation flux given by equation (2.88) added to the total suspended flux given by equation (2.92), gives the total snow flux for a given wind condition. This is given by Pomeroy and Male (1992) as per their Prairie Blowing Snow Model (PSBM) to be

$$Q_{0-5} = \frac{u_{10}^{4.04}}{458800} \quad (2.96)$$

for the first five meters above the surface. This agrees well with the relationship given by Tabler (1991a) for the first ten meters above the surface and found by using the concentration relationship given by equation (2.94)

$$Q_{0-10} = \frac{u_{10}^{3.93}}{290951} \quad (2.97)$$

The total suspension mass flux found by integrating equation (2.92) from the saltation height to a height of 20 m results in the total mass flux that follows the curve

$$Q_{0-20} = 0.8065u_*^{3.118} = \frac{u_{10}^{3.83}}{139282} \quad (2.98)$$

given by Beyers and Harms (2003a) and described in Appendix G.

Equations (2.90) and (2.93) are subsequently used in the numerical analysis to provide inlet snow concentration profiles for a given inlet wind profile and for the saltation and suspension regions respectively. The total snow mass flux given by equation (2.98) is employed in this work in a similarity theory analysis applied to the outdoors modelling of snow drifting around a scale model of the SANAE IV station, presented later in this thesis and in Appendix G.

2.6.2. Erosion / Deposition scheme

Two different models are employed in this work to determine the flux of snow either depositing or eroding from the snow pack. The first model, called Model I - the threshold model, is based mainly on saltation threshold shear velocity or shear stress conditions to determine either the onset of erosion or deposition. The second model, called Model II – the conservation based model, is based on the conservation of the convected and diffused snow concentration near the surface boundary in order to determine the balance between erosion and deposition fluxes. These two models are used to simulate the snow drift surrounding verification test cases in order to evaluate their accuracy as presented later in this thesis.

Model I –the threshold model

Snow or ice particles may accumulate when the flow conditions cease to supply sufficient shear energy for suspension, saltation and creep of particles. Then the particles drop out of the flow domain at their respective fall velocities. Presently the deposition flux is calculated as a function of the available snow concentration and the particle fall velocity and is assumed to reach its minimum value when the calculated shear stress is equal to the threshold shear stress i.e.

$$q_{\text{depshear}} = \eta w_f \left\| \left\| \frac{u_{*t}^2 - u_*^2}{u_{*t}^2}; 0.0 \right\| \right\| \quad (2.99)$$

as per Naaim et al. (1998). Sundsbø (1997), (1998) employed a similar formula to simulate the snow deposition flux except that the shear and threshold shear velocities were raised to the third power instead of the second power as per equation (2.99). Alhajraf (2001) used the same numerical approach as Sundsbø (1997) and evaluated several functions similar to equation (2.99) to predict the flux of depositing particles around fences and other obstacles. The brackets, $\| \|$, in equation (2.99) represent the Fortran function DMAX1. The fall velocity is assumed constant for the present analysis and described earlier in this chapter.

The shear erosion of the snow pack occurs when the available shear stress in the surface layer exceeds the inter-particle bonds and inertia and particles start to creep and saltate. The erosive flux due to aerodynamic shear should therefore be a function of the available surface shear stress and the bonding strength of the snow pack, Kind (1976), Anderson and Haff (1991).

One may deduce that this erosive flux may be given by, Naaim et al. (1998) and similar to Kind (1992) and Gauer (1998),

$$q_{\text{eroshear}} = -A \left\| \rho u_*^2 - \rho u_{*t}^2; 0.0 \right\| \quad (2.100)$$

where A is a proportionality coefficient representing the snow pack bonding strength. For the present analysis a value of $\rho A = 7.0E - 4$ was used as determined by Naaim et al. (1998). Equation (2.100) was further modified by Naaim et al. (1998) to incorporate the effects of the equilibrium snow concentration profile along a length of fetch.

The normal component of the erosive flux i.e. the flux due to impinging particles, is assumed to be proportional to the snow concentration, the incident angle and the velocity of the mixed flow, similar to the descriptions by Lee et al. (2002a), Humphrey (1990) and Tu et al. (1997), Nøkleberg and Sørentvedt (1998) among others,

$$q_{\text{eroimp}} = -KV^n \eta f(\alpha) \quad (2.101)$$

Here K is a proportionality coefficient accounting for particle and snowpack material properties, V is the near surface impinging flow velocity, $2 < n < 4$ for erosion of brittle materials, as per Humphrey (1990), and $f(\alpha)$ is a function dependent on the incident angle of the flow given for the present model by

$$f(\alpha) = \frac{16}{\pi^2} \alpha^2 - \frac{8}{\pi} \alpha + 1.0 \quad (2.102)$$

Here the incident angle, α , is aligned with the surface normal vector pointing into the surface. The impingement erosion equation allows erosion even if the local wall shear stress is below the threshold shear stress, a condition which would alternatively only provide snow deposition according to equation (2.99). These conditions may exist at the snow surface near an upstream corner of a surface mounted obstacle, for example, where flow travels downwards and away from the side walls of a surface mounted cube. This region has low tangential stress due to a small tangential flow component above the snow surface which would allow deposition but which should be balanced by erosion from impinging snow.

As a point of interest, the deposition mechanisms may also be influenced by an electrostatic charge generated between interacting particles which is discharged upon impact with other

particles or with the snow surface. Maeno et al. (1985) found that drifting particles have negative charge and the surface of the snow pack have variable positive or negative charge that may correspond to local erosion or deposition patterns. This interesting effect of the electrostatic charge on surface erosion has not been considered in the present work.

The resultant erosion and deposition flux contribution at a snow surface is then found from the function

$$q_{\text{ero/dep}} = q_{\text{depshear}} + q_{\text{eroshear}} + q_{\text{eroimp}} \quad (2.103)$$

This method depends primarily, perhaps rather simplistically, on the definition of the threshold shear velocity and a scaling function such as found in equation (2.99) to determine the proportion of depositing particles. Such a formulation of the deposition flux somewhat contradicts the notion of the threshold shear velocity, i.e. where the threshold velocity is defined as the condition where saltation ceases. These methods have been used with success as indicated below but it is believed that a more complete description should include a balance between all fluxes near the surface including convection, diffusion, erosion and deposition fluxes. Such a model is described below.

Model II – the conservation based model

The above procedure works well where the snow accumulation regions are dominated by either below threshold deposition or above threshold erosion and very realistic snow drift and sand drift predictions have been simulated by Sundsbø (1997), (1998) and Alhajraf (2001), (2003). It does not account for snow accumulation in regions of strong flow deceleration as mentioned in Kind and Murray (1982) or where the flow turbulence levels are too low to support the carried mass of the snow. Interestingly and in contradiction to this, Tsuchiya et al. (2002) suggest that the region where snow accumulation occurs around obstacles is associated with flow acceleration instead.

In order to evaluate the total erosive or accumulative snow flux one may evaluate the snow transport equation in the first near surface cell, similar to the approach followed by Moore (1995), Liston and Sturm (1998), Gauer (1998), Lehning et al. (2000) and Raupach and Lu (2004). The total snow flux in the first near surface cell is shown in figure 2.5. The control

volume is separated into two regions being the saltation and turbulent suspension region. The height of the saltation layer is defined by equation (2.89) while the height of the turbulent region is arbitrary but should be at a sufficient level above the saltation layer. The drifting snow processes occurring in this near surface control volume include, as indicated in figure 2.5, the horizontal turbulent convection and diffusion of snow, the near surface saltation mass transport, the ejection of new saltating snow due to excess shear at the snow pack, the vertical turbulent entrainment or diffusion of snow and the vertical settling of snow towards the surface. The present model does not account for the changing mass of snow in the control volume due to sublimation. Thus the transient change in the mass conservation of snow in the near surface control volume is given by the balance of the mass contribution of the above mentioned processes. Physically this balance represents the snow carrying capacity of the wind flow at a specific point in the flow domain. In other words, once the mass conservation contributions from the convected, diffusive, saltating and settling snow has been accounted for, any the remaining snow fraction exceeds the carrying capacity of the wind flow, in which case deposition will occur. If there is insufficient snow within the control volume the balance of the abovementioned flow processes will yield the amount of snow fraction to be added to the wind flow in the control volume due to the process of erosion.

For the purpose of this description the particle phase eddy diffusivity is assumed to be equal to the continuous phase eddy diffusivity. This is a subject of much debate as briefly summarised in Xiao et al. (2000) but a turbulent Schmidt number of unity seems to be common practice. The snow mass conservation equation for the control volume given in figure 2.5 is given by

$$\begin{aligned}
& \iint \frac{\partial}{\partial x} \left(\eta u - v_t \frac{\partial \eta}{\partial x} \right) dy dz \Delta x + \iint \frac{\partial}{\partial y} \left(\eta v - v_t \frac{\partial \eta}{\partial y} \right) dx dz \Delta y + \\
& \iint \frac{\partial}{\partial x} \eta_s u_s dy dz_s \Delta x + \iint \frac{\partial}{\partial y} \eta_s v_s dx dz_s \Delta y - \iint \eta w_f dx dy + \\
& \iint \left(\eta w - v_t \frac{\partial \eta}{\partial z} \right) dx dy + \dot{m}_{\text{salt}} = - \iiint \frac{\partial \eta}{\partial t} dx dy dz = - \iiint \frac{\partial \alpha_s \rho_s}{\partial t} dx dy dz
\end{aligned} \tag{2.104}$$

where \dot{m}_{salt} is an ejected mass flux of snow due to saltation at the surface.

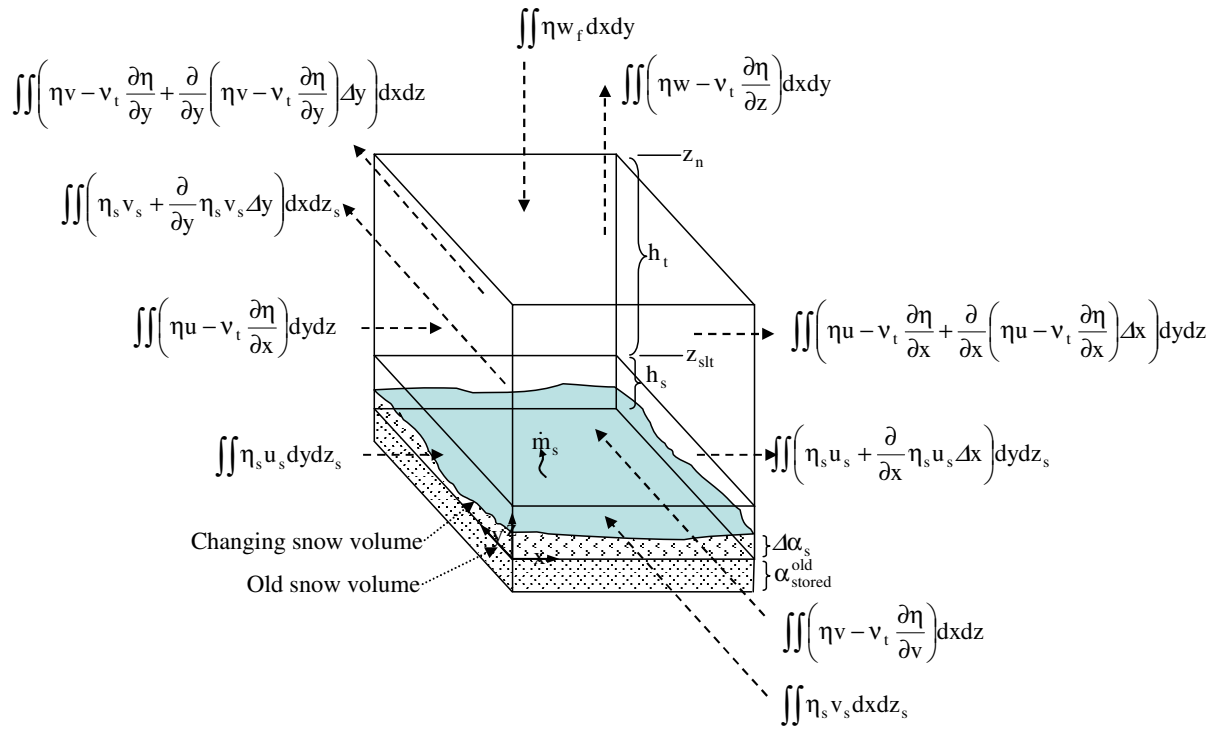


Figure 2.5 Control volume with the near surface snow mass conservation

In this conservation based model as per equation (2.104) the snow particles are assumed to travel at the same horizontal velocity as the flow and that there is a constant vertical slip velocity due to the particle gravitational settling. This is based on the assumption of negligible inertia, Bintanja (2000a), Xiao et al. (2000).

Equation (2.104) can be simplified by performing the x- and y-direction integration to give

$$\begin{aligned}
 & \frac{\partial}{\partial x} \int \left(\eta u - v_t \frac{\partial \eta}{\partial x} \right) dz \Delta x \Delta y + \frac{\partial}{\partial y} \int \left(\eta v - v_t \frac{\partial \eta}{\partial y} \right) dz \Delta x \Delta y + \\
 & \frac{\partial}{\partial x} \int \eta_s u_s dz_s \Delta x \Delta y + \frac{\partial}{\partial y} \int \eta_s v_s dz_s \Delta x \Delta y - \eta w_f \Delta x \Delta y + \\
 & \left(\eta w - v_t \frac{\partial \eta}{\partial z} \right) \Delta x \Delta y + \dot{m}_{\text{salt}} = -\rho_s \Delta x \Delta y \Delta z \frac{\partial \alpha_s}{\partial t}
 \end{aligned} \tag{2.105}$$

This can be further simplified to yield

$$\begin{aligned}
-(\alpha_s^{\text{new}} - \alpha_s^{\text{old}}) = & \left[\frac{\partial}{\partial x} \int \overbrace{\left(\eta u - v_t \frac{\partial \eta}{\partial x} \right)}^{q_{x-\text{susp}}} dz + \frac{\partial}{\partial y} \int \overbrace{\left(\eta v - v_t \frac{\partial \eta}{\partial y} \right)}^{q_{y-\text{susp}}} dz + \right. \\
& \frac{\partial}{\partial x} \int \overbrace{\eta_s u_s}^{q_{x-\text{salt}}} dz_s + \frac{\partial}{\partial y} \int \overbrace{\eta_s v_s}^{q_{y-\text{salt}}} dz_s + \\
& \left. \overbrace{\left(\eta w - \eta w_f - v_t \frac{\partial \eta}{\partial z} \right)}^{q_{z-\text{susp}}} + q_{\text{salt}} \right] \frac{\Delta t}{\rho_s \Delta z}
\end{aligned} \tag{2.106}$$

If the right hand side of equation (2.106) is positive then more snow leaves the control volume than available and erosion adds an additional snow fraction to the flow. Should the right hand side of equation (2.106) be negative then more snow enters the control volume than the carrying capacity of the wind can maintain and snow deposition removes the excess snow from the control volume. Thus the right hand side of equation (2.106) represents the mass of snow depositing or eroding at the snow pack.

The first and second terms on the right hand side of equation (2.106) represents the horizontal flux of the suspended snow. The x-direction flux (with the y-direction being similar) is given by

$$q_{x-\text{susp}} = u\eta - v_t \frac{\partial \eta}{\partial x} \tag{2.107}$$

By assuming that the vertical velocity and concentration profiles follow equations (E.7) and (F.9) respectively, and using K-theory or equation (E.5) to approximate the turbulent viscosity, we find in the first near surface cell (in terms of the reference velocity and snow concentration at the centre node P)

$$q_{x-\text{susp}} = u_P \frac{\ln\left(\frac{z}{z_0}\right)}{\ln\left(\frac{z_P}{z_0}\right)} \eta_P \left(\frac{z}{z_P}\right)^\beta - \kappa u_* z \frac{\partial \eta}{\partial x} \tag{2.108}$$

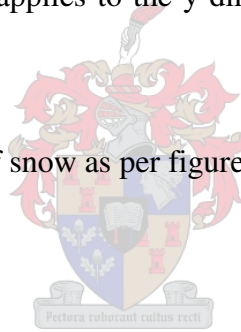
The total horizontal snow flux that crosses the height of the first cell is found, as per Moore (1995), from the vertical integration of equation (2.108) from the saltation height to the top of the control volume, and can be shown to yield

$$\begin{aligned}
Q_{x-susp} &= \int_{z_{slt}}^{z_n} q_{x-susp} dz \\
&= \frac{\eta_p u_p Z_P^\beta}{\ln\left(\frac{Z_P}{Z_0}\right)} \int_{z_{slt}}^{z_n} z^{-\beta} \ln\left(\frac{z}{Z_0}\right) dz - \kappa u_* z_P^\beta \frac{\partial \eta}{\partial x} \int_{z_{slt}}^{z_n} z^{1-\beta} dz \\
&= \frac{\eta_p u_p Z_P^\beta}{\ln\left(\frac{Z_P}{Z_0}\right)} \left(\ln\left(\frac{z}{Z_0}\right) \frac{z^{1-\beta}}{1-\beta} - \frac{z^{1-\beta}}{(1-\beta)^2} \right)_{z_{slt}}^{z_n} - \kappa u_* z_P^\beta \frac{\partial \eta}{\partial x} \left(\frac{z^{2-\beta}}{(2-\beta)^2} \right)_{z_{slt}}^{z_n} \quad (2.109)
\end{aligned}$$

where subscripts z_n and z_{slt} refer to the top cell interface and the saltation heights respectively. The same formulation applies to the y-direction suspended flux except that the u-velocity is replaced by v-velocity.

The flux of the vertical suspension of snow as per figure 2.5 is given by

$$q_{z-susp} = (w - w_f) \eta - v_t \frac{\partial \eta}{\partial z} \quad (2.110)$$



For a steady state fully developed atmospheric boundary layer the suspension of particles may be approximated by equation (F.5) which allows one to define the concentration gradient required in equation (2.110) which yields

$$q_{z-susp} = \left((w - w_f) \eta_n - v_{tn} \eta_P \beta \left(\frac{z_n}{Z_P} \right)^\beta \right) \quad (2.111)$$

This equation is only valid for the steady state fully developed atmospheric boundary layer and is specifically not valid for regions where the flow separates such as around obstacles. Alternatively, the turbulent diffusion flux in equation (2.110) may be approximated by assuming a fully developed turbulent atmospheric boundary layer where the snow concentration gradient is always negative in the direction of the wall normal vector and that

subsequently the turbulent diffusion cause snow particles to leave the control volume at a diffusion velocity i.e.

$$-v_t \frac{\partial \eta}{\partial z} = w_t \eta \quad (2.112)$$

where w_t is the velocity of vertical entrainment due to the turbulent suspension. The turbulent diffusion velocity for the atmospheric boundary layer may be approximated from the turbulent eddy diffusivity and Britter et al. (2003) give the turbulent diffusion velocity or mean drift velocity as being proportional to the shear velocity

$$w_t = \alpha_1 u_* \quad (2.113)$$

based on the vertical gradient of the turbulent eddy diffusivity where $\alpha_1 \approx 0.65$. Raupach and Lu (2004) present the same model but with $\alpha_1 \approx \kappa = 0.41$. Assuming the k- ϵ turbulence model law of the wall is applicable, equation (2.113) can be shown to be

$$w_t = \alpha_1 \sqrt{1.5 C_\mu^{0.5}} \sqrt{w'^2} \quad (2.114)$$

which gives for the values of Raupach and Lu (2004)

$$w_t = 0.275 w' \quad (2.115)$$

and for Britter et al. (2003)

$$w_t = 0.436 w' \quad (2.116)$$

The formulation given by equation (2.114) is based on a fully developed turbulent atmospheric boundary layer and does not apply to regions of local flow disturbances such as recirculation regions with strong turbulent mixing.

Binder and Hanratty (1992), Mols and Oliemans (1998) and Mols et al. (2000) used another approach to approximate the depositional velocity within a thin boundary layer for turbulent flows, the so-called diffusion/free-flight models. The particles are assumed to reach a perfectly absorbing wall from a high concentration gradient in a tube by coasting into the boundary layer to the wall at a diffusion velocity. Their diffusion process is the reverse of the snow suspension process since the concentration gradients are reversed but the diffusion flux

principles are considered similar for the present study. Their diffusion flux velocity is based on that given by Binder and Hanratty (1992) i.e.

$$w_t = \frac{1}{2} \sqrt{\frac{2}{\pi}} \sqrt{w'^2} = 0.398w' \quad (2.117)$$

Gauer (1998) and Lehning et al. (2000) also used a turbulent diffusion flux velocity approximated by the vertical velocity fluctuations in the atmospheric boundary layer namely

$$w_t = w' \quad (2.118)$$

The diffusion velocity given by equation (2.118) is clearly larger than that given by equations (2.115), (2.116) or (2.117) and may overestimate the actual diffusion flux since for particles with large relaxation times the particle velocity fluctuations do not follow the fluid velocity fluctuations exactly, Kallio and Reeks (1989), due to the inertial effects. In fact Kallio and Reeks (1989) present results to show that for high particle relaxation times, $\tau_s^+ = 100$, the particle velocity fluctuations are approximately half of that of the fluid i.e

$$w'_p \approx 0.4w' \quad (2.119)$$

This seems to indicate that the diffusion velocity given by equations (2.116) or (2.117) may be more appropriate. However the numerical simulations carried out in this work employed coefficient values of between 0.7 and 1.0 which gave realistic predictions of snow drift developments. Assuming an isotropic turbulence field, one finds the fluid velocity fluctuations as proportional to the turbulence kinetic energy of the fluid i.e.

$$\sqrt{w'^2} = \sqrt{\frac{2}{3}k} \quad (2.120)$$

The benefit of the diffusion velocity formulation in equation (2.110) is that it allows us to simply modify the vertical gravitation settling in equation (2.110), i.e. using equation (2.112)

$$q_{z-susp} = (w - w_f + w_t)\eta \quad (2.121)$$

This eliminates the need to calculate the vertical concentration gradient required in equation (2.110).

The saltation snow flux in equation (2.106) is

$$q_{x-salt} = \eta_s u_s \quad (2.122)$$

where the subscript s denotes properties within the saltation layer only. The total saltation flux is given by the general formulation

$$Q_{x-salt} = \int_{z_0}^{z_{slt}} \eta_s u_s dz_s \quad (2.123)$$

This total saltation snow flux is determined by Pomeroy and Gray (1990), equation (2.88), and is used in this model instead, i.e.

$$Q_{x-salt} = \frac{0.68\rho}{u_* g} u_{*t} (u_*^2 - u_{*n}^2 - u_{*t}^2) \quad u_* \geq u_{*t} \quad (2.124)$$

If conditions change so that saltation ceases, the available or remaining snow in the saltation layer within the control volume should deposit. Assuming that this snow will deposit at the settling velocity undisturbed by turbulence gives

$$q_{saltdep} = \eta_s w_f \quad u_* < u_{*t} \quad (2.125)$$

For conditions above threshold the erosion of particles at the surface is given by equation (2.100). Combining equations (2.106), (2.109), (2.100), (2.121), (2.124) and (2.125) gives the total advected snow flux balance in the near surface control volume

$$q_{acc/ero} = \frac{\partial}{\partial x} Q_{x-susp} + \frac{\partial}{\partial y} Q_{y-susp} + \frac{\partial}{\partial x} Q_{x-salt} + \frac{\partial}{\partial y} Q_{y-salt} + q_{z-susp} + q_{saltdep} - q_{eroshear} \quad (2.126)$$

or

$$-(\alpha_s^{new} - \alpha_s^{old}) = q_{acc/ero} \frac{\Delta t}{\Delta z \rho_s} \quad (2.127)$$

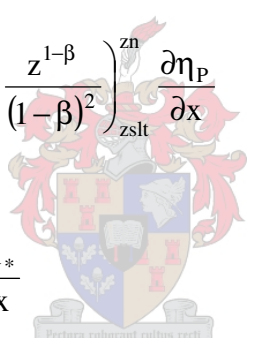
Assuming that the shear component due to surface obstacles is negligible we find the change of total saltation flux, as required in equation (2.126), along the x-direction as

$$\frac{\partial}{\partial x} Q_{x-salt} = \frac{0.68\rho}{g} u_{*t} \left(\frac{\partial u_*}{\partial x} - u_{*t}^2 \frac{\partial}{\partial x} \left(\frac{1}{u_*} \right) \right) \quad u_* \geq u_{*t}$$

$$= \frac{0.68\rho}{g} u_{*t} \frac{\partial u_*}{\partial x} \left(1 + \frac{u_{*t}^2}{u_*^2} \right) \quad (2.128)$$

This ensures that decelerating flows may deposit excess snow if saltation is present.

Lastly, equation (2.126) requires the horizontal change of the total suspended flux. This may be found from the partial differentiation of equation (2.109) where it has been assumed that the only variables that have a significant first derivative are the local velocity, the local snow concentration and the local shear velocity i.e.

$$\begin{aligned} \frac{\partial}{\partial x} Q_{x-susp} &= \frac{\partial Q}{\partial u_P} \frac{\partial u_P}{\partial x} + \frac{\partial Q}{\partial \eta_P} \frac{\partial \eta_P}{\partial x} + \frac{\partial Q}{\partial u_*} \frac{\partial u_*}{\partial x} \\ &= \frac{\eta_P z_P^\beta}{\ln\left(\frac{z_P}{z_0}\right)} \left(\ln\left(\frac{z}{z_0}\right) \frac{z^{1-\beta}}{1-\beta} - \frac{z^{1-\beta}}{(1-\beta)^2} \right)_{zslt}^{zn} \frac{\partial u_P}{\partial x} \\ &\quad + \frac{u_P z_P^\beta}{\ln\left(\frac{z_P}{z_0}\right)} \left(\ln\left(\frac{z}{z_0}\right) \frac{z^{1-\beta}}{1-\beta} - \frac{z^{1-\beta}}{(1-\beta)^2} \right)_{zslt}^{zn} \frac{\partial \eta_P}{\partial x} \\ &\quad - \kappa z_P^\beta \frac{\partial \eta}{\partial x} \left(\frac{z^{2-\beta}}{(2-\beta)^2} \right)_{zslt}^{zn} \frac{\partial u_*}{\partial x} \end{aligned} \quad (2.129)$$


The same applies to the change of the total snow flux in the y-direction. Thus at each near surface control volume, the first derivatives of local velocity, snow concentration and shear velocity along with the local flow properties give the suspended snow change according to equation (2.129).

The instantaneous erosion or accumulation flux, $q_{acc}(t)$, is given by equation (2.126). In order to simulate snow drift development within reasonable simulation times it is necessary to artificially increase the deposition flux by multiplying it by a scaling factor. However, to ensure that the simulation remains stable and that drift patterns follow the artificially high local deposition fluxes, a relaxation factor is used. Firstly an average accumulation flux is calculated at time t during the simulation according to

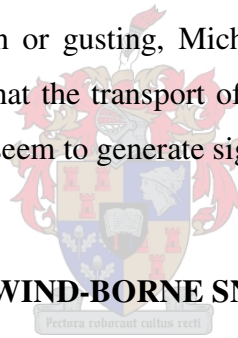
$$\bar{q}_{acc} = \frac{\int_0^T q_{acc}(t) dt}{\int_0^T t dt} \quad (2.130)$$

where T is the total simulation time at time t . The applied accumulation flux to determine the drift development in the model is then given by

$$q_{acc} = \bar{q}_{acc} \alpha_{22} + q_{acc}(t)(1 - \alpha_{22})$$

where α_{22} is a relaxation factor. For the present work a value of $\alpha_{22}=0.5$ has consistently given realistic results with stable simulations.

This instantaneous snow drift flux used in this analysis relies partially on the empirical relationships for saltation and suspension phenomena, relationships that assume equilibrium conditions (fully developed and steady state) for its derivation. It should be noted here that these assumptions are under investigation to evaluate their relevance under unsteady conditions such as flow acceleration or gusting, Michaux et al. (2002). These preliminary investigations do however suggest that the transport of snow does indeed closely follow the wind field and that gusting does not seem to generate significant increases in mass fluxes.



2.7. NUMERICAL MODEL OF WIND-BORNE SNOW DRIFT

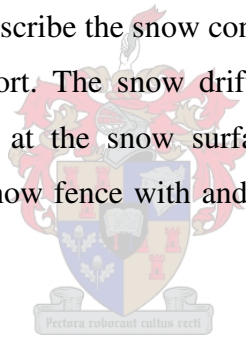
2.7.1. The modelling technique

In both the numerical and the experimental analysis one needs to capture the characteristic behaviour inherent to the complex three-dimensional flow domain and include the effects of the accompanying snow transport processes. Most of the flow processes found in the environment are truly three-dimensional with many associated complexities such as strong streamline curvature, flow vorticity and separation as well as highly anisotropic turbulence distribution. These already present a challenging task from a numerical analysis perspective without even addressing the additional complexities arising from the multiphase or particulate effects, such as relevant to snow drifting. The introduction of particulate matter in a flow domain implicitly affects the fluid mass and momentum conservation and turbulent energy production and dissipation. Furthermore, temporal snow accumulation or erosion dynamically alters the boundaries of the flow domain, thereby requiring a solution adaptive computational

domain. For this present numerical analysis to succeed as a suitable engineering tool one invariably needs to make a few sacrifices in the form of modelling assumptions. Additional valuable comments are made by Leschziner (1993) regarding the effectiveness of CFD as an engineering tool in the wind engineering field. For the present it is necessary to give an account of some of the earlier work regarding the numerical simulation of aeolian processes and in particular the wind driven snow phenomenon.

Decker (1990) applied continuum mixture theory to derive the two-phase transport equations for wind blown snow in a two-dimensional turbulent flow field. The simulation was applied to calculate the accumulation rate in the lee of a two-dimensional wedge.

Sato et al. (1993) developed a three-dimensional numerical model from the Navier Stokes equations with a Prandtl mixing length turbulence model to predict wind driven snow fields and to calculate snow concentration fields as well as snow accumulation and erosion rates. Diffusion theory was employed to describe the snow concentration distribution with empirical functions for the inlet snow transport. The snow drift rate was calculated as the balance between erosion and accumulation at the snow surface. Results were presented for the accumulation rates around a solid snow fence with and without bottom gap, around a three-dimensional hut and around a hill.



Liston et al. (1993) employed the RANS equations with the $k-\epsilon$ turbulence model to simulate the single phase airflow around a solid fence and applied saltation theory to simulate snow drift near the surface boundary. Thus no particle suspension was modelled. Boundary conditions for turbulence quantities at the inlet and walls were similar to those given by Hoxey and Richards (1993) and described elsewhere in this thesis. More importantly, their model included an algorithm to gradually count the filled fraction of each control volume when deposition occurs below threshold friction velocity and blocked the cells when the control volume was fully packed. No details were given for the accumulation rate function.

Moore et al. (1994) and Moore (1995) developed a numerical scheme based on the steady state RANS equations with a mixing length turbulence model to study snow drift development around elevated structures. This included the snow drift evaluation around a two-dimensional model of the raised Halley 5 station, Antarctica. A snow concentration field

was found from the solution of an advection-diffusion equation after the steady state flow field solution was found. A snow accumulation or erosion rate was found from the balance of vertical and horizontal snow mass fluxes in the first above surface control volume. The boundary position was updated to account for the changing deposition of snow and the flow field recalculated until an equilibrium profile was established.

Sundsbø (1997), (1998) used the Euler-Euler approach with the mixing length turbulence model to simulate two-dimensional snow drift and included temporal snow surface changes. The computational domain was dynamically divided into four regions for saltation, saltation erosion, saltation accumulation and suspension, based on the simulated surface shear stress or shear velocity. An accumulation source term was added when the shear velocity decreased below the threshold shear stress and was given by

$$Q_s = \eta w_f \frac{u_*^3 - u_{*t}^3}{u_{*t}^3} \quad (2.131)$$

Sundsbø and Bang (2000) also used this snow drift analysis to evaluate the wind conditions and the snow drift potential over a large topographical terrain at Hammerfest in northern Norway.

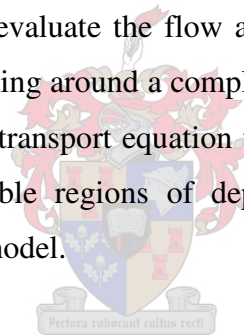
Liston and Sturm (1998) developed a numerical model, SnowTran-3D to simulate snow drift or redistribution over large scale topographical areas. The model included temporal snow surface changes due to snow drifting. Their erosion and accumulation scheme is based on the snow flux balance near the snow surface i.e. the snow flux eroded or deposited is a function of the balance between saltating, suspended, sublimating and precipitation snow. Details are given in Liston and Sturm (1998) and Greene et al. (1999). This approach is superior to those that only rely on threshold shear velocity to determine whether erosion or accumulation will occur since it will allow suspended and saltating snow to accumulate even at high shear stress levels when either the carrying capacity of the air is exceeded or in strongly decelerating flows. The present model uses a similar approach to derive the snow accumulation mass flux.

Naaïm et al. (1998) applied a two-dimensional finite volume technique with a Chen Wood modified k-ε turbulence model to simulate snow drifting around a solid wall with a bottom gap. Their model allowed for temporal snow surface changes and employed the mixture

momentum equation. The erosion flux was based on the available or excess shear stress above the surface as per Anderson and Haff (1991) and also included a modification to account for dependency on the available snow concentration. The deposition flux was calculated according to equation (2.99). Their simulations for snow drift around a solid wall with a bottom gap showed good agreement with experimental results.

Gauer (1998) employed a finite volume method to simulate topographical snow drifts. The erosion / deposition scheme is based on a mass and momentum balance in the surface layer similar to that applied by Liston and Sturm (1998). Lehning et al. (2000), (2002a), (2002b), Bartelt and Lehning (2002) used a similar approach to simulate the saltating and suspended snow transport over a large topographical terrain as part of the modelling and prediction of the condition of the snow pack in high alpine terrains for avalanche warning forecasting.

Tominaga and Mochida (1999) employed a finite volume method with a modified Launder-Kato type $k-\varepsilon$ turbulence model to evaluate the flow around a surface mounted cube. They applied this work to study snow drifting around a complex three-dimensional building terrain. Their model solved a snow particle transport equation to determine areas of high local snow concentration which indicate possible regions of deposition. No temporal snow surface modifications were included in the model.



Chopard and Masselot (1999), Masselot (2000) proposed an alternative approach to the CFD modelling of snow drifting processes as described above. Their novel approach is based on Cellular Automata and Lattice Boltzmann methods. The work seems to successfully predict snow drift development around fences, tents, roads and over mountain crests but seems to be computationally expensive requiring parallel processor architectures.

Thiis (2000) carried out a numerical analysis employing the multiphase mixture model to simulate the transient drifting snow around three-dimensional buildings. A similar procedure seems to have been followed by Olowson (2004) to simulate snow drift development surrounding a mountain hut. In the model the mixture viscosity is modified proportionally to the concentration of snow which then causes regions with high concentrations of snow to slow down the air flow. It is uncertain if the apparent viscosity methods as per Thiis (2000) and Olowson (2004) simulate realistic drifting snow behaviour since the actual snow volume

fractions typically found are of the order of 0.001 and even much smaller, Bintanja (2000a). Thus being such a highly dilute flow process the particle concentrations should have a negligible impact on the effective viscosity of the mixture and should therefore not dramatically change the wind velocity where snow concentrations increase. However, the results indicate that the predicted drifts compares favourably with observed drift formations. Although the methods simulate a transient developing snow drift visualised by showing surfaces of constant volume fraction, it does not modify the computational domain to adapt to the changing surface. Therefore the original snow surface boundary condition with the associated boundary conditions such as no-slip walls and law of the wall turbulence approximations are not updated to be applicable at the new snow surface interface. The benefit of their method is its simple implementation in existing and powerful commercially available software without intensive user programming.

Alhajaraf (2003), (2002), (2001) applied the volume of fluid method to simulate the multiphase flow of sand and snow around three-dimensional obstacles such as walls and porous fences. He applied the standard $k-\epsilon$ turbulence model and included saltation and suspension source terms in the particle transport equation to simulated the near surface erosion and deposition. The simulation includes the transient modification of the surface proportional to the erosion/deposition flux. The source terms in the particle transport equations allows the near surface concentrations to gradually increase up to a maximum packing fraction after which the control volume is completely blocked and the flow ceases.

In addition to the snow drift studies around obstacles and over terrains, drifting snow is also investigated in meteorological research and to evaluate, in particular, the phenomema of snow sublimation and its influence on the vapour budget of the earth. During strong winds snow sublimation is believed to be the major contributor to the total surface to atmosphere moisture flux. In the process, the meteorological research makes valuable contributions to the understanding of the physical processes such as saltation and suspension that may assist and refine the drift modelling around structures, such as works by Schmidt (1986b), Mann (1998), Déry (1998), Xiao et al. (2000), Bintanja (2001b) and Doorschot and Lehning (2002) among many others.

Most of the above mentioned methods use a finite volume approach with some form of turbulence closure to simulate the simplified two-phase flow phenomena of blowing snow. In order to determine the erosion or deposition patterns one may differentiate between methods that have some form of snow surface modification and those that do not. The latter usually provides an estimate of the likely snow drift locations based on deposition and erosion fluxes and local snow concentrations only. These models then typically give snow drifts in terms of the rate of accumulation based on a steady state flow field solution. An alternative method, considered to be more complete, use erosion and deposition flux information to modify a surface either once off at the end of a steady state simulation or temporally during the course of a transient analysis. For these methods some form of a computationally adaptive strategy is required since the snow surface represents a wall boundary condition that dynamically changes during the course of a simulation. Both methods also require knowledge of the mass rate of snow that is eroded from or deposited on the surface. Here again, one differentiates between methods that largely depend on the threshold shear velocity to determine the onset of either erosion or deposition and those methods that determine the erosion or deposition flux from a volume averaged mass balance in the near surface control volume. This was described earlier in the chapter.

Two methods have been applied in this thesis, both using a dynamically changing surface condition. Initially the threshold method was used and evaluated and shown to provide good results, shown later, for surface mounted obstacles. It was found that these methods were inadequate when required to simulate snow drifts in regions of high shear. Here deposition is dependent, among other things, on the divergence of the velocity field. Therefore snow may also deposit even if the threshold shear velocity is considerably exceeded. In such instances a method based on the mass balance of the near surface control volumes is preferred since it may indicate more deposition flux due to a decelerating fluid in a high shear area. Simply put, the deposition flux is a function of the balance between erosion and deposition which in turn may be found from the conservation of the mass of snow transported in the surface control volume.

FLOW3D was selected as the computational fluid dynamics software since it includes the FAVOR algorithm which allows the simulation of the gradual filling of open fluid cells. This commercially available software has been used with great success in predicting snow drifting

phenomena, Sundsbø (1997), who employed a threshold based model. Alhajraf (2001), (2004) similarly and successfully used the FAVOR technique in the development of an in-house code to simulate sand and snow drifts.

The governing equations presented earlier in this chapter are suitable for finite volume or finite difference discretisation. Such discretisation requires a computational grid which invariably necessitates the use of a boundary fitted mesh which may complicate matters when dealing with boundaries of large and complicated flow geometries such as those found in environmental and wind engineering applications. The Fractional Area Volume Obstacle Representation (FAVOR) technique was developed originally as a means to define general geometrical objects in a grid of block elements. This method was extended as a computational model for compressible Euler equations for two-dimensional block structured grids, Hirt (1993). A brief explanation of the FAVOR method employed in FLOW3D is given below to facilitate the description of the temporal surface adaptation method used in this research.

Essentially the FAVOR technique formulates all governing equations in terms of open area and volume fractions. Thus the governing conservation equations for each computational cell are re-written in terms of the available flow area at cell interfaces and the available flow volume of the cells. One of the more powerful advantages of this scheme is the simple treatment of moving obstacles i.e. moving obstacles simply result in a fluid mass source or sink in the continuity equation when an obstacle exits or enters a control volume respectively. This ignores the inertia effects that are assumed negligible for the relatively slow moving accumulating or eroding snow surface.

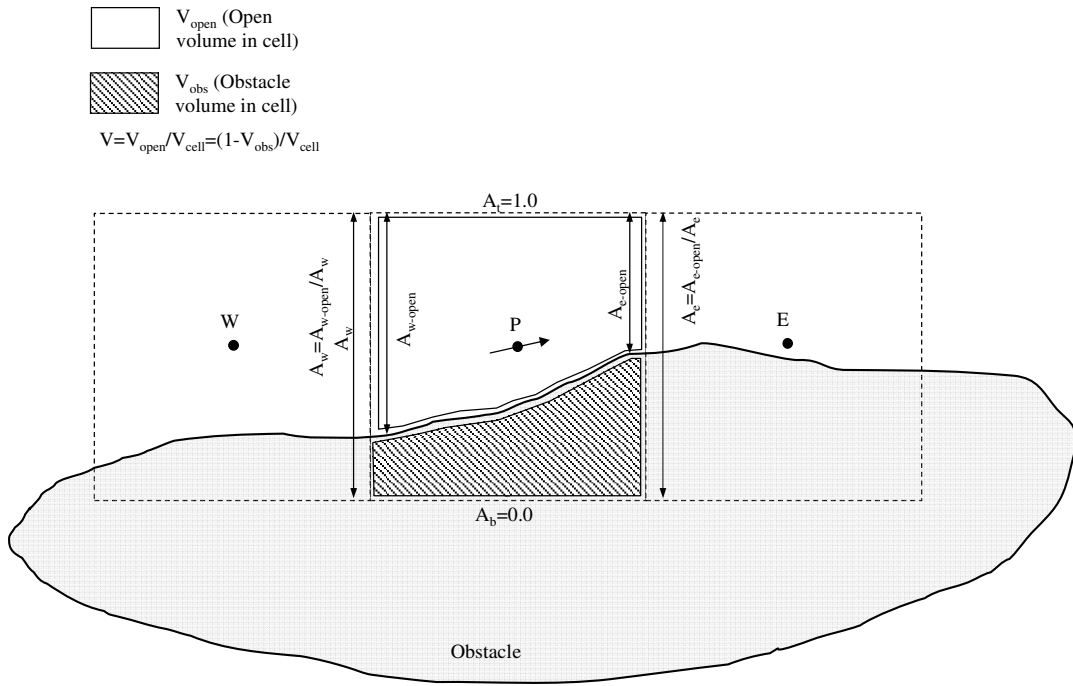


Figure 2.6. FAVOR description of the fractional area and volume

The computational cell interfacial area and volume fractions are defined in terms of the available area and volume fractions, as shown in figure 2.6, or the fractional area and volume open for fluid transport i.e.

$$\text{Area fraction: } A_i = \frac{A_{\text{open}}}{A_{\text{face}}} \quad (2.132)$$

$$\text{Volume fraction: } V = \frac{V_{\text{open}}}{V_{\text{cell}}} \quad (2.133)$$

For example, the FAVOR mass conservation equation for incompressible flow with moving obstacles can then be shown to be, as per Hirt (1993) and Tsukiyama et al. (1993),

$$\frac{\partial V}{\partial t} + \nabla(A_i \bar{u}_i) = 0 \quad (2.134)$$

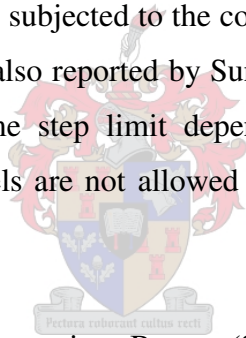
where the first term in equation (2.134) account for the rate of change of the volume i.e. for moving obstacles. The FAVOR momentum conservation equation is

$$\frac{\partial \bar{u}}{\partial t} + \frac{A_i}{V} \bar{u}_i \nabla \bar{u}_j = -\frac{1}{\rho} \nabla p + \frac{1}{\rho V} \nabla(A_i \tau_{ij}) \quad (2.135)$$

Some of the earlier problems of the extension of the FAVOR technique to flow modelling were convection instabilities due to small area fractions and the treatment of flow cells intersected by obstacles. The first of these problems are due to the maximum time step dependency on advection which for the FAVOR technique yields

$$\delta t < \frac{\delta x V}{A_i \bar{u}_i} \quad (2.136)$$

This restriction is suitably resolved by artificially modifying the volume fraction to equal a tolerance value which allows larger time step values. Since the area fraction remains unchanged, the boundary remains the same but the cell may absorb volume changes, Hirt (1993). Even with this artificial modification it was necessary to force cells to be completely blocked once a tolerance value of volume fraction is reached. Presently every cell that is gradually being filled with snow is blocked completely once the volume fraction value exceeds 80% of the maximum packing fraction of solid particles. This ensures that the maximum allowable time step that is subjected to the constraints of equation (2.136) does not tend to infinity. This condition was also reported by Sundsbø (2003). The solution scheme is also subjected to an additional time step limit dependent on the dynamics or effective viscosity of the fluid i.e. fluid parcels are not allowed to diffuse through more than one cell width within a time step.



A general form of the conservation equation, Beyers (2000), for any transported variable is commonly given in the form

$$\frac{\partial}{\partial t}(\rho\phi) + \nabla \cdot \bar{J}(\phi) = S(\phi) \quad (2.137)$$

where the flux vector consists of convection and diffusion components and is given by

$$\bar{J}(\phi) = \rho \bar{U}\phi - I\nabla\phi \quad (2.138)$$

When discretising this transport equation within a computational domain, the terms on the left hand of this equation may be grouped as the influence coefficients in a solution matrix and the terms on the right hand side will determine the source terms. Influence coefficients arise from information at the interfacial position between control volumes and are multiplied by the respective interfacial areas of the control volume. The source terms on the other hand are

calculated using information at control volume centres and are multiplied by the volume of the control volume. In terms of the FAVOR treatment equation (2.137) becomes

$$\frac{\partial}{\partial t}(\rho\phi) + \frac{A_i}{V} \nabla \cdot \bar{J}(\phi) = S(\phi) \quad (2.139)$$

Thus, for the present work, the mixture momentum conservation, turbulence kinetic energy, turbulent dissipation and particle advection-diffusion equations, as given at the beginning of this chapter, may all be re-written in a similar form of equation (2.139) i.e. in terms of the available interfacial area fractions and open volume fraction.

2.7.2. Surface adaptation

After each time step during the simulation the near surface erosion and deposition flux is calculated in accordance with equation (2.106). Thus each control volume where there exists an intersecting snow surface (obstacle) as well as an available volume fraction for flow, the fraction of snow eroding or depositing is calculated. This is added and stored in a scalar calculated for each control volume that determines the change in the interfacial area fractions and volume fraction. This scalar represents the stored snow within the first near surface control volume.

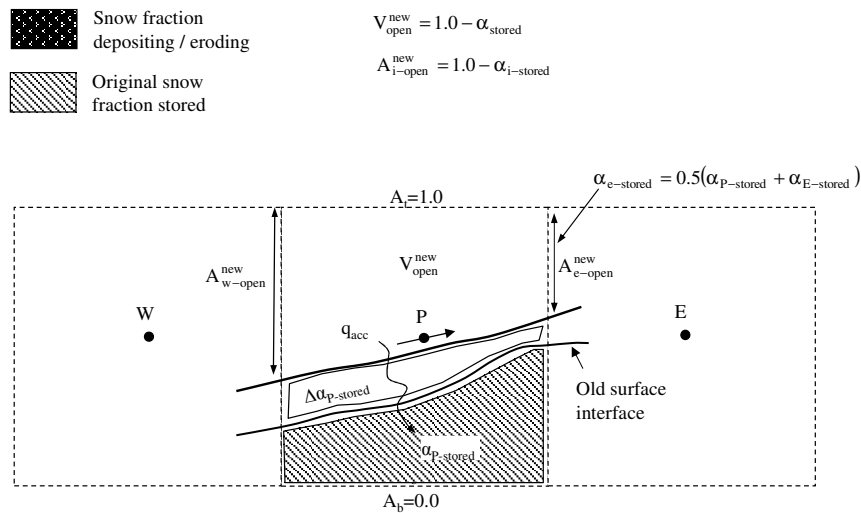


Figure 2.7. Surface adaptation and area and volume fraction modification.

The new control volume area and volume fractions are then updated at each time step once the new stored snow counter was calculated. The snow fraction calculated as per equation

(2.106) that leaves a control volume to deposit, is assumed to deposit and be packed at the surface according to a packing ratio. Thus the stored snow is divided by the packing fraction to ensure that the change in the control volume accommodates the bulk snow density and not the snow particle density as employed in equation (2.106) i.e.

$$\alpha_{\text{stored}}^{\text{new}} = \alpha_{\text{stored}}^{\text{old}} + \Delta\alpha_{\text{stored}} \quad (2.140)$$

$$\Delta\alpha_{\text{stored}} = \frac{q_{\text{acc}}\Delta t}{\Delta z\rho_s\phi} \quad (2.141)$$

This will ensure that the bulk snow density of the snow pack is maintained. The new volume fraction for each control volume is calculated as

$$V_{\text{open}}^{\text{new}} = 1.0 - \alpha_{\text{stored}} \quad (2.142)$$

and the area fractions for each face of the control volume is calculated according to

$$A_{i\text{-open}}^{\text{new}} = 1.0 - \alpha_{i\text{-stored}} \quad (2.143)$$

where the interfacial stored snow fraction on the right hand side of equation (2.143) is the average of the stored fraction in the control volume and the nearest neighbour. For example, at the eastern control volume interface as per figure 2.7 this is given by

$$\alpha_{e\text{-stored}} = 0.5(\alpha_{P\text{-stored}} + \alpha_{E\text{-stored}}) \quad (2.144)$$

For the present work a constant snow packing ratio in the surface layer is employed namely $\phi=0.2$ which implies a bulk snow density of $\rho_b = \phi\rho_s \approx 180 \text{ kg.m}^{-3}$, a value typically associated with a snow pack consisting of freshly fallen snow. The free control volume snow fraction is also updated by the change in the snow fraction calculated by means of equation (2.106).

2.7.3. Boundary conditions

The boundary conditions or approximations which are required for the transported variables are inlet, outflow, symmetry and wall boundary conditions.

Inlet

The boundary values for all inlet variables are given according to Dirichlet type boundaries. Numerical simulation of the atmospheric boundary layer requires a homogeneous approach flow which necessitates the correct specification of the inlet or approach turbulent velocity profile and its turbulence characteristics. This should maintain the homogeneous flow in the surface layer which implies that the streamwise gradients of all variables should be zero. This is achieved with an inlet profile that follows the general logarithmic profile for the atmospheric boundary layer i.e.

$$u = \frac{u_*}{\kappa} \ln\left(\frac{z}{z_0}\right) \quad (2.145)$$

The inlet velocity profile is determined from an equation for the fully developed turbulent velocity profile for an atmospheric boundary layer. This is described in Appendix G with the inlet velocity profile employed in this work given by equation (G.15). This profile includes the effects of the surface roughness as well as the aerodynamic roughness contribution due to the saltation of snow particles near the surface. The profile function as per Appendix G is given below namely

$$\frac{u(z)}{u_*} = \frac{1}{\kappa} \ln\left(\frac{zu_*}{v}\right) + B - \Delta B(k^+, s^+) \quad (2.146)$$



where $B=5.5$ and, for fully developed turbulent flow with surface roughness,

$$\Delta B(k^+, s^+) = \frac{1}{\kappa} \ln(1 + 0.3k^+ + 9.53s^+) \quad (2.147)$$

and

$$k^+ = \frac{\kappa u_*}{v} \quad (2.148)$$

Employing an additional parameter to account for the effects of saltating snow particles on the velocity profile

$$s^+ = \frac{c_1 u_*^3}{2gv} \quad (2.149)$$

This is employed along with a constant turbulence kinetic energy profile of

$$k = \frac{u_*^2}{\sqrt{C_\mu}} \quad (2.150)$$

and a turbulent dissipation profile determined from

$$\varepsilon = \frac{u_*^3}{\kappa(z + z_0)} \quad (2.151)$$

A concise description of the conservation theory behind this is given by Richards and Hoxey (1993). Similar descriptions are given by Miles and Westbury (2003) and Liston et al. (1993).

The flow in the surface layer is partially maintained by the interaction with flow at higher layers and the surface layer shear stress remains essentially constant. Near the ground the k - ε turbulence model requires specification of the turbulence kinetic energy and dissipation. To find near wall turbulence characteristics it is assumed that there exists equilibrium between turbulence production and dissipation, Ferziger and Péric (2002). For a homogenous surface layer this assumption results in the near wall turbulence production and dissipation rate given by, as presented in Richards and Hoxey (1993) among others,

$$k = \frac{u_*^2}{\sqrt{C_\mu}} \quad (2.152)$$

$$\varepsilon = \frac{u_*^3}{\kappa(z + z_0)} \quad (2.153)$$

Inlet snow fractions is determined from equations (2.90) and (2.93).

Outlet and symmetry boundaries

All variables at the outflow of the computational domain and at symmetry boundaries are forced to comply to zero normal derivatives.

Walls

Zero normal derivatives are applied for all variables except for turbulence quantities. The turbulent quantities are found from the well-known law of the wall approximations. This model assumes that the rate of turbulent production of kinetic energy equals the rate of

dissipation at the first node away from the wall. This yields the following two equations for the turbulence kinetic energy and dissipation at the first node above a wall

$$k_w = \frac{u_*^2}{\sqrt{C_\mu}} \quad (2.154)$$

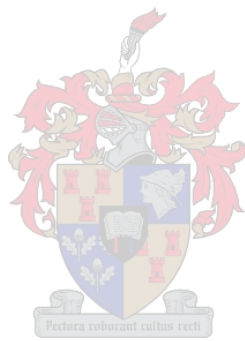
and

$$\epsilon_w = \frac{u_*^3}{\kappa n} \quad (2.155)$$

where n is the normal distance away from the wall. It is evident that in order to find the turbulent quantities near the wall, the shear velocity needs to be calculated. This is found from an iterative solution of the velocity profile equation.

2.7.4. Implementation of the snow drift model in FLOW3D

The method described above is implemented by means of new FORTRAN user subroutines added to the existing source code of the FLOW3D software suite. The subroutines calculate and update boundary conditions to provide the necessary upstream values for the profiles of the turbulent velocity profile as well as for the snow volume fraction distribution. During the course of the simulations further subroutines calculate the flux of depositing or eroding snow fractions according to equation (2.106). Before the simulation proceeds to the next time step, the near-surface control volume changes to the free area and volume fractions are calculated, and the old area and volume fraction updated. To calculate the changing volume fraction of snow, a number of first derivatives is required namely the derivative of local flow velocity, shear velocity and snow concentration. All these derivatives are found by means of central difference approximations using their respective interfacial values.



3. SIMULATION OF SNOW DRIFT AROUND A THREE-DIMENSIONAL CUBE

3.1. EXPERIMENTAL WORK AT SANAE IV, ANTARCTICA

A 2 m cube was constructed near the SANAE IV (72°S, 2°W) research station in Dronning Maud Land in Antarctica and wind driven snow build-up measured for comparison with and verification of the numerical simulation results. This experimental work and some of the subsequent numerical simulations given below were also reported in Beyers and Harms (2003a). The selected study area near SANAE IV lies 2 km upwind of the nunatak on which the research station is built and the snow surface in this area consists mainly of old and compacted snow covered with small sastrugi present at the start of the test period. The prevailing winds experienced in this area are north-eastern, eastern or south-eastern winds with rare katabatic winds approaching from the south. A Finnish Antarctic geophysical research group from Helsinki University, Finland, measured the snow properties in the testing area during the FINNARP-2000 and 2001 summer seasons. The measured bulk snow density of the surface layers ranged between 450kg/m³ and 550kg/m³, Rasmus (2000). Precipitating snow particles as well as older surface snow particles, sampled at the Aboa research station, 72°S, 10°W by Karkas (2001), measured approximately 100 µm and 500 µm respectively. For the present work the snow properties at the SANAE IV test location are assumed to be similar to those measured at Aboa. This assumed particle diameter is rather large compared to the particles usually present in blowing snow where the mean particle diameter is typically in the range of 80 µm to 160 µm instead, Budd et al. (1966). The effects of introducing particles of different and probably more realistic size classes are not presently evaluated. The particle size will however influence, among other properties, the drag coefficient and particle fall velocity and thereby affect the simulated results. For one, smaller particles may have a smaller settling velocity which means the simulation may predict longer and less pronounced snowdrifts due to longer particle settling trajectories.

The wind profiles were measured in the test area with four MCS 7 aluminium cup type anemometers mounted on a 6m mast and positioned 0.5 m, 1.4 m, 2.7 m and 5.5 m above the snow surface. The sensors were mounted on horizontal arms 0.5 m in length and orientated in a north-south direction to minimise interference from the weather mast. The wind velocities were logged at 5-minute intervals on a MCS 120 RS232 digital logger. The time of initiation

of blowing snow was also logged through visual observation to determine the threshold wind speed for snow saltation.

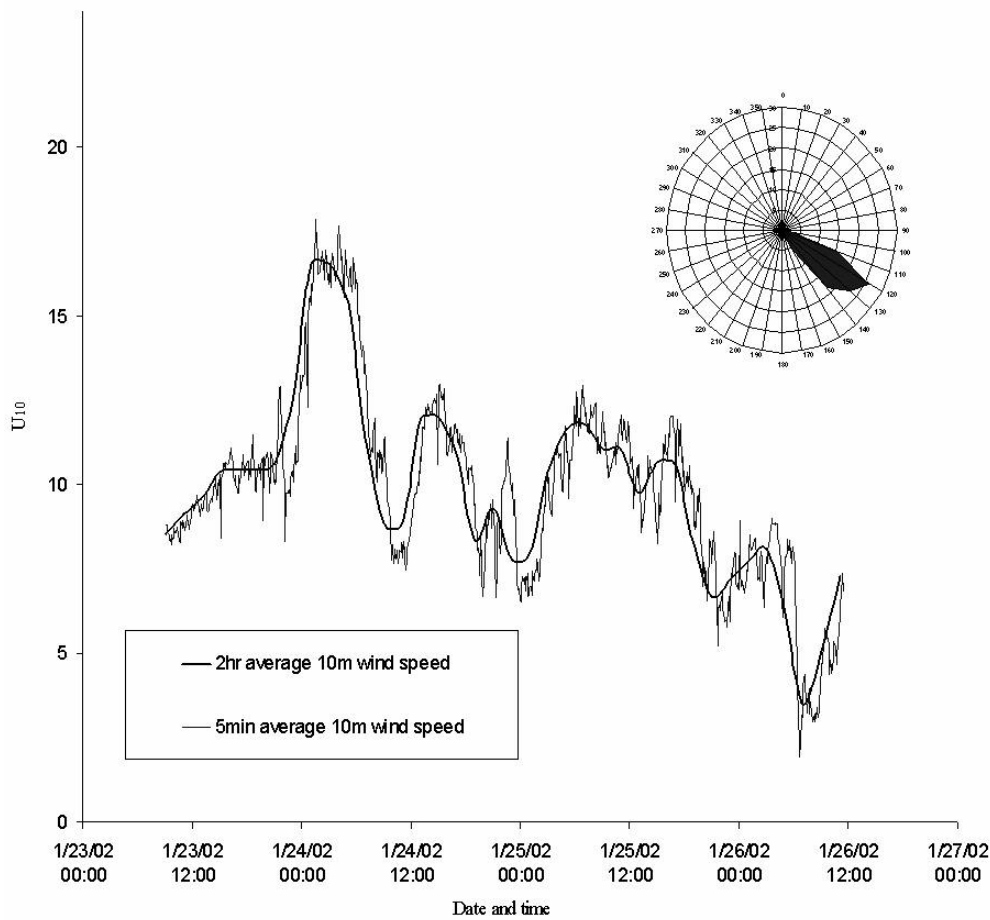


Figure 3.1. Extrapolated 10 m wind speeds, average wind speed and wind direction for the period 23/01/2002 – 26/01/2002

Since very little snow precipitation occurs in the area it is assumed that the snow is old and wind hardened with corresponding high threshold velocity characteristics. A large area surrounding the cube was cleared of accumulated snow on 22/01/2002 prior to the start of a test period from 23/01/2002 to 25/01/2002. The snow surface is therefore considered flat and compacted and snow entrainment considered only originating far upwind of the cube. The extrapolated 10m wind speeds, the 2-hourly 10 m average wind speeds and wind direction for the duration of the relevant test period pertaining to the cube experiments are shown in figure 3.1. The threshold 10m wind speed was found from field observations to be approximately $8 \text{ m}\cdot\text{s}^{-1}$. This gives a threshold shear velocity of $u_* = 0.28 \text{ m}\cdot\text{s}^{-1}$, Beyers and Harms (2003a). The snow build-up was measured on 26/01/2002 and the observed results are shown in figure

3.2. The average approach ten meter wind velocity for the duration of the test was $u_{10}=9.88 \text{ m}\cdot\text{s}^{-1}$. This value was used as the upstream wind velocity in the numerical simulation.

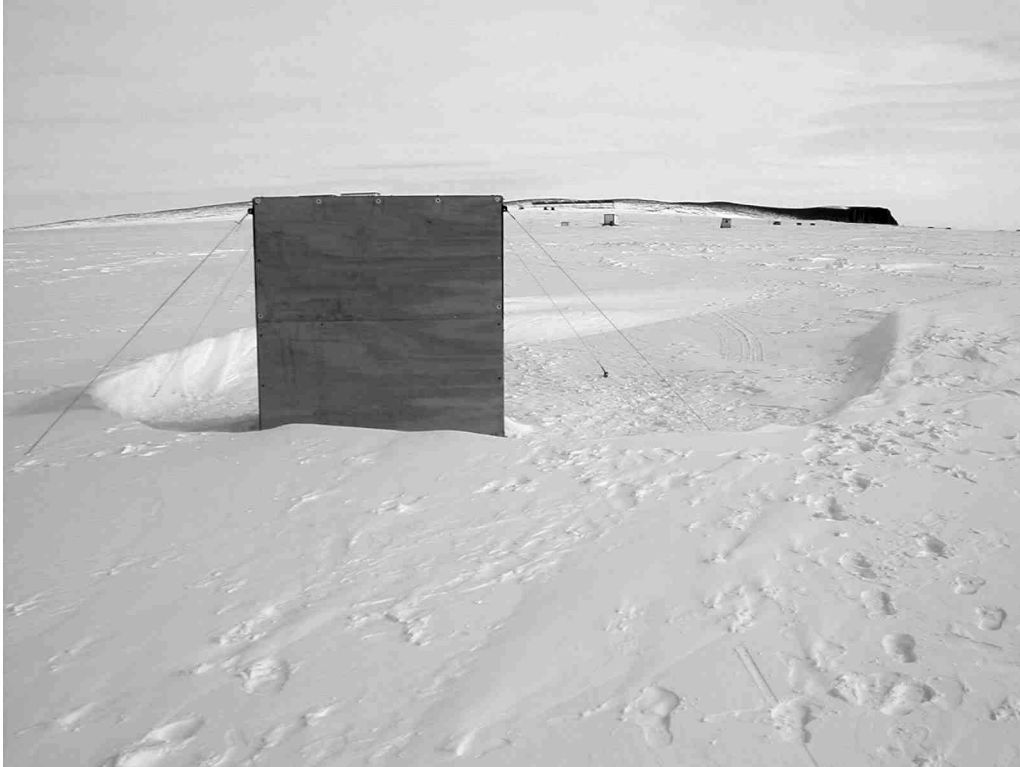


Figure 3.2. Observed snow build-up behind the 2 m cube, near SANAE IV, on 26/01/2002. Observer is looking west with Vesleskarvet and SANAE IV in the background

3.2. THE NUMERICAL MODEL

The computational domain employed for the present simulation is shown in figure 3.3. A $91 \times 80 \times 41$ grid was employed for the final simulation presented here. This final grid, as shown in figure 3.4, was selected after several tests with coarser grids ensuring that a grid independent solution is presented. This grid required local refinement at the cube corners to resolve important secondary flow effects without becoming too computationally expensive. Since the present scheme gradually fills and solidifies open surface cells with snow, it was also necessary to keep the first few cells above the surface sufficiently small and similar in size. Only the results for the final grid are discussed here.

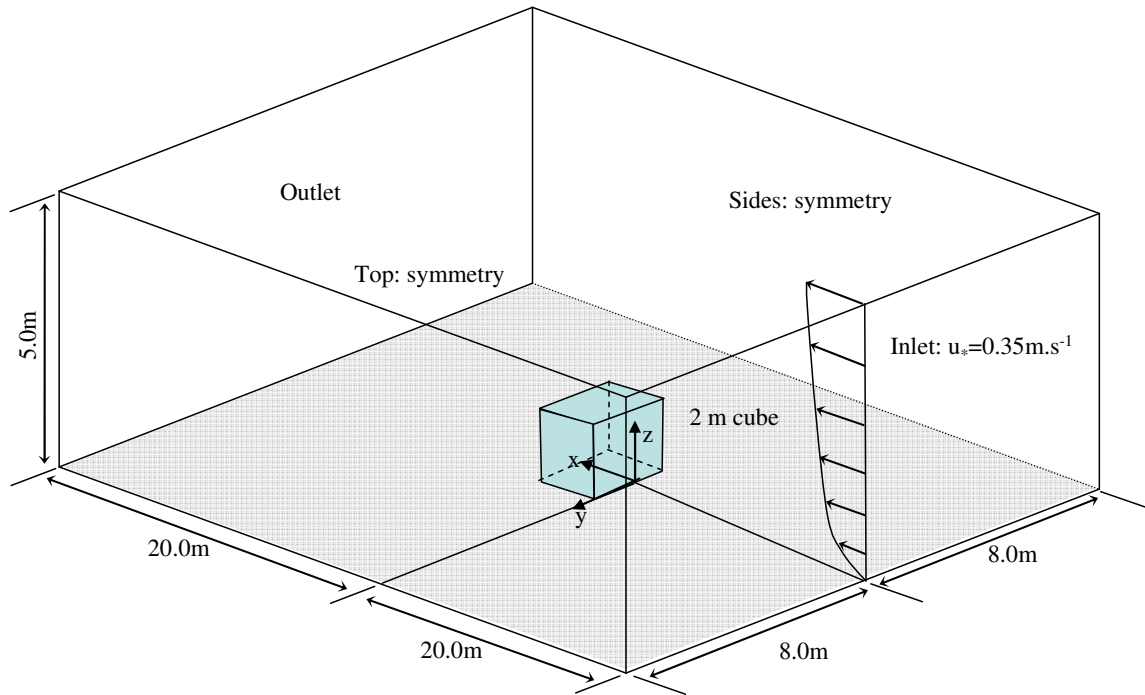


Figure 3.3. Computational domain for the three-dimensional cube simulation

Table 3.1. Simulation parameters for the three-dimensional cube simulation for Model I.

Total simulation time	T	40 s
Drift initiation time	T_{acc}	20 s
Shear velocity	u_*	$0.35 \text{ m}\cdot\text{s}^{-1}$
Saltation roughness parameter	C_1	0.0035
Surface roughness parameter	k	0.0001
Suspended snow multiplier	K_s	1000.0
Snow erosion multiplier	α_{ero}	10.0
Snow accumulation multiplier	α_{acc}	24.0
Saltation proportionality factor	ρA	$7.0\text{E-}4$
Erosion proportionality	E_r	$1.0\text{E-}6$
Interpolation scheme	Second order	
Turbulent Schmidt number	Sc	1.0
Snow drift model	Model I	
Mean particle size	d_m	$110 \mu\text{m}$
Mean particle settling velocity	w_f	$0.45 \text{ m}\cdot\text{s}^{-1}$
Drift coefficient	D_f	20.0

A second order interpolation scheme was selected as opposed to the upwind interpolation scheme since the latter showed severe inaccuracies in predicting the expected horseshoe vortex. A turbulent Schmidt number of 1.0 was selected for the present solution of the snow advection equation. This is not given any further consideration in the present analysis. Although the measured snow build-up was accompanied by a wind approaching the windward cube face at an angle of approximately 35° , see figure 3.2, this simulation evaluates only an approach wind direction normal to the front cube face. Subsequent research will investigate the snow build-up predictions with different approaching wind directions. The inlet u-velocity profile is described by equation (2.146) with the effective surface roughness and shear velocity parameters given in table 3.1. The inlet shear velocity was found from averaging the measured shear velocity over the duration of the test as given in figure 3.1. The inlet snow concentration profile is determined from equations (2.90) and (2.93) with the shear velocity as given per table 3.1.

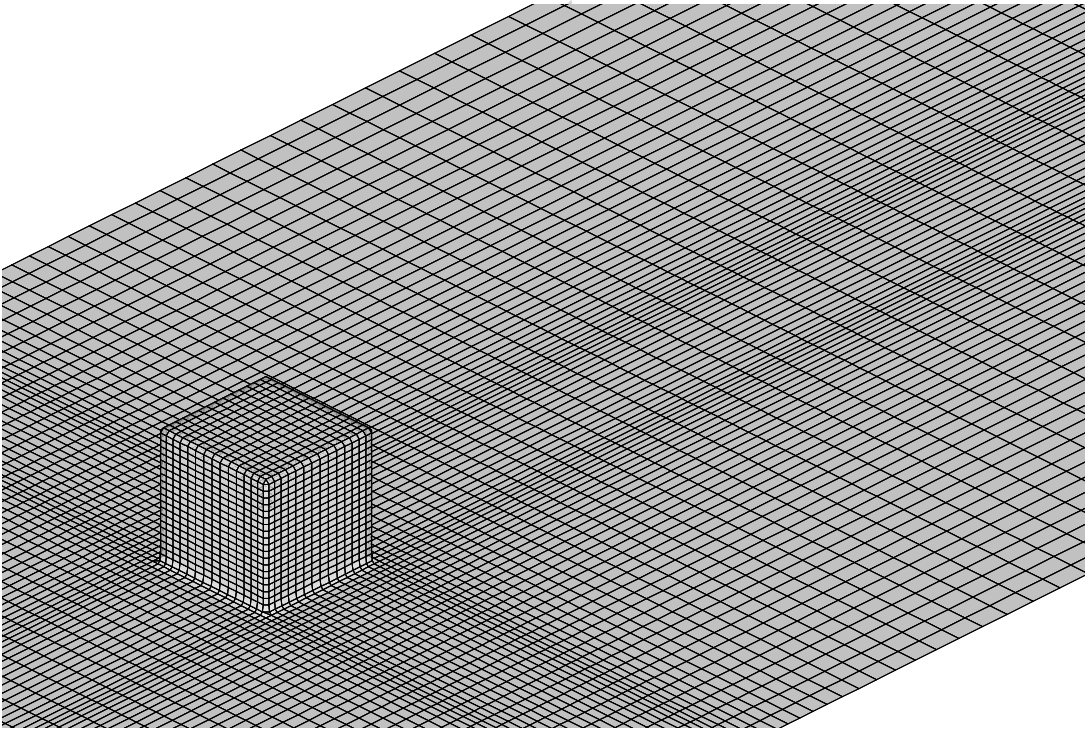


Figure 3.4. Computational mesh for the fine grid for the cube snow drift simulation

During the course of all simulations presented here and also in other simulations presented in subsequent chapters the time step used in the simulation is automatically calculated by the

FLOW3D solver to ensure that the constraints on the time step limit as, mentioned in chapter 2, are met. This ensures that the simulations are stable but also means that simulation times may be prolonged when solutions reach near steady state conditions where the constraints on the time step size could be relaxed. During each time step the solver iterations are continued until all cells have reached mass residuals smaller than some small number, typically of the order of 0.01 times the volume of that cell.

3.2.1. The turbulent flow field

The three-dimensional turbulent flow around a surface mounted cube has been extensively investigated numerically as well experimentally. These studies include works by Paterson and Apelt (1986), (1990), Castro and Robins (1977), Murakami et al. (1987), (1992), Murakami (1998), Sakamoto and Arie (1982) and Delaunay et al. (1995) among others. Although the results presented in these works are not all strictly applicable to the present flow conditions they do provide invaluable information for a qualitative evaluation of the numerical analysis in capturing the main flow phenomena. Castro and Robins (1977) provided the first experimental data for a cube fully immersed in a turbulent boundary layer where $50000 < Re_h < 100000$. Paterson and Apelt (1990) compared these measured data with their numerical simulation results employing the $k-\epsilon$ turbulence model. Their work also examined the influence of the surface roughness and upstream boundary layer thickness on the flow field surrounding the cube. Murakami et al. (1987), (1992) and Murakami (1993), (1998) extensively investigated the accuracy of different numerical schemes and turbulent models to predict flow around a three-dimensional cube. Murakami et al. (1987) applied large eddy simulation (LES) to resolve the turbulent flow field surrounding a cube and evaluated the effect of varying Smagorinski constants. Murakami et al. (1992) compared the results for this flow when employing LES, the modified $k-\epsilon$ turbulence model and an algebraic stress model (ASM). They concluded that the modified $k-\epsilon$ turbulence model could not reproduce the measured recirculation region on top of the cube roof and that the magnitude of the leeward reverse flow was too large compared to experimental values. The isotropic $k-\epsilon$ turbulence model overestimates the turbulence kinetic energy at the frontal top roof corner which in turn produces a too large eddy viscosity. This results in a strong mixing effect which subsequently removes the separation region from the roof top. This overestimation was caused by overestimation of the turbulent production source term. Shah and Ferziger (1997) also used

LES to compute the flow around the cube and compared the results against those of Martunuzzi and Tropea (1996). In order to evaluate the accuracy of the simulation in capturing the important mixed flow phenomena we first compare the results of this simulation with some of these earlier works. The first results were taken shortly after the start of the transient run, i.e. when “pseudo” steady state conditions still prevailed after the start and snow build-up was still insignificant. Figure 3.5 shows the results of the cube wall pressure coefficient calculations from the present simulation compared to the results from the Castro and Robins (1977) and Paterson and Apelt (1986). The pressure coefficients are calculated from

$$C_p = \frac{p - p_r - 2/3k^2}{0.5\rho u_r^2} \quad (3.1)$$

The reference properties are taken from the flow field at cube height and at the inlet boundary and also neglect the hydrostatic pressure field due to buoyancy effects. The discrepancy along line A may be attributed to the much thinner boundary layer for a smooth surface as in the present simulation ($Re_h \approx 1377000$). Paterson and Apelt (1990) made similar observations. The discrepancy in the prediction of the negative pressures on the windward corner of the top face could be somewhat limited with more mesh refinement. The downstream effect of this seems small and it is ignored in this analysis. The negative pressure on the top surface, i.e. the size of the top separation layer, may be attributed to the thin upstream boundary layer, Paterson and Apelt (1990), and the inaccuracy of the k- ϵ turbulence model in capturing that separation layer, Murakami et al. (1992). Figure 3.5 indicates that the present pressure field compares favourably with the earlier research work. Figure 3.6 shows the distribution of the horizontal velocity in the x/z plane at y/h=0. This indicates favourable agreement between results from this simulation and those from Paterson and Apelt (1990) and Castro and Robins (1977). Figure 3.7(a)-(c) shows the vector field plots for three different planes. The lengths, heights and location of different separation and recirculation zones are taken from these plots and compared with results from Paterson and Apelt (1990) in table 3.2. This comparison suggests that the important flow phenomena are captured and its characteristics compare favourably with those from Paterson and Apelt (1990) for smooth surface flows. Figure 3.7(a)-(c) indicates a few characteristic flow phenomena around surface mounted obstacles. Such flows around three-dimensional surface obstacles are typically characterised by a horseshoe vortex which travel around and downstream from the obstacle (A). These streamwise vortices

convect fluid into the wake resulting in shorter wake separation regions than those associated with two-dimensional obstacles, AbuOmar and Martinuzzi (2000). As the flow approach the cube the boundary layer separates at a saddle point (B) due to the adverse pressure gradient windward of the cube. The flow separates here and this separating streamline impinges on the windward cube face at a stagnation point (C).

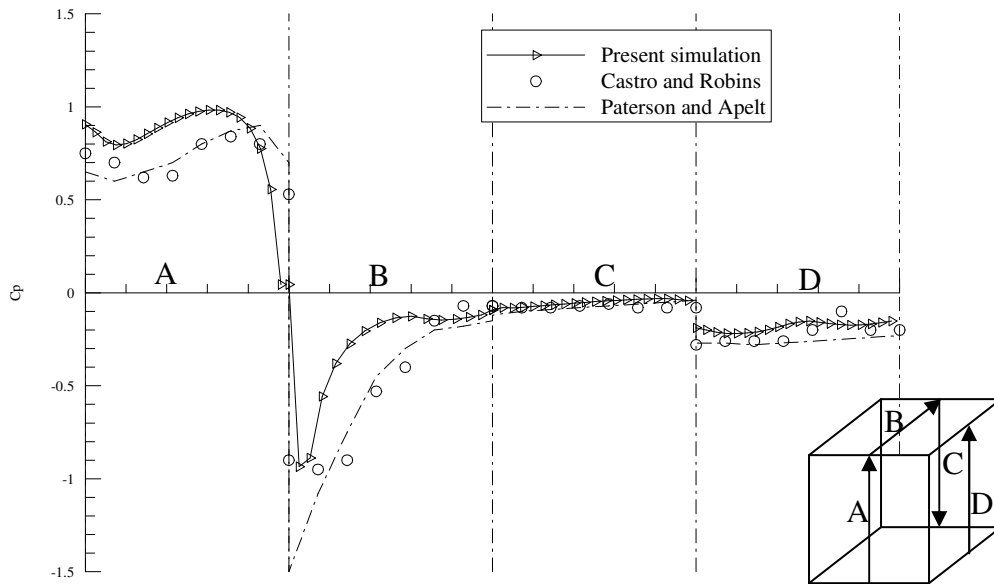


Figure 3.5. Pressure coefficient calculation on the cube surfaces

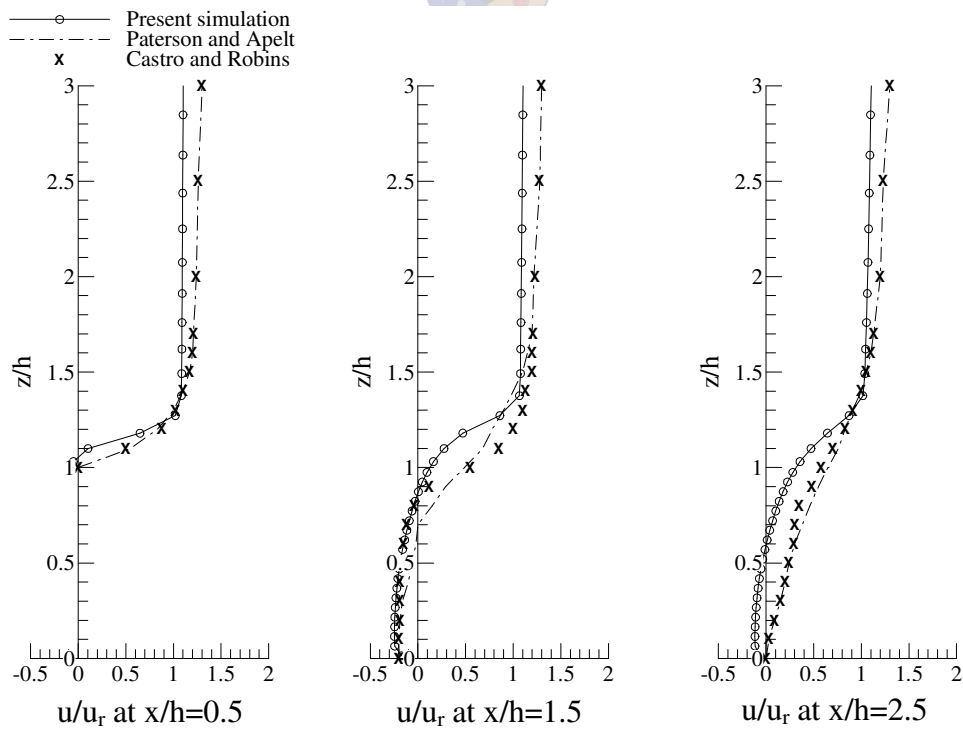


Figure 3.6. Velocity distribution results in the x/z plane at $y/h=0.0$

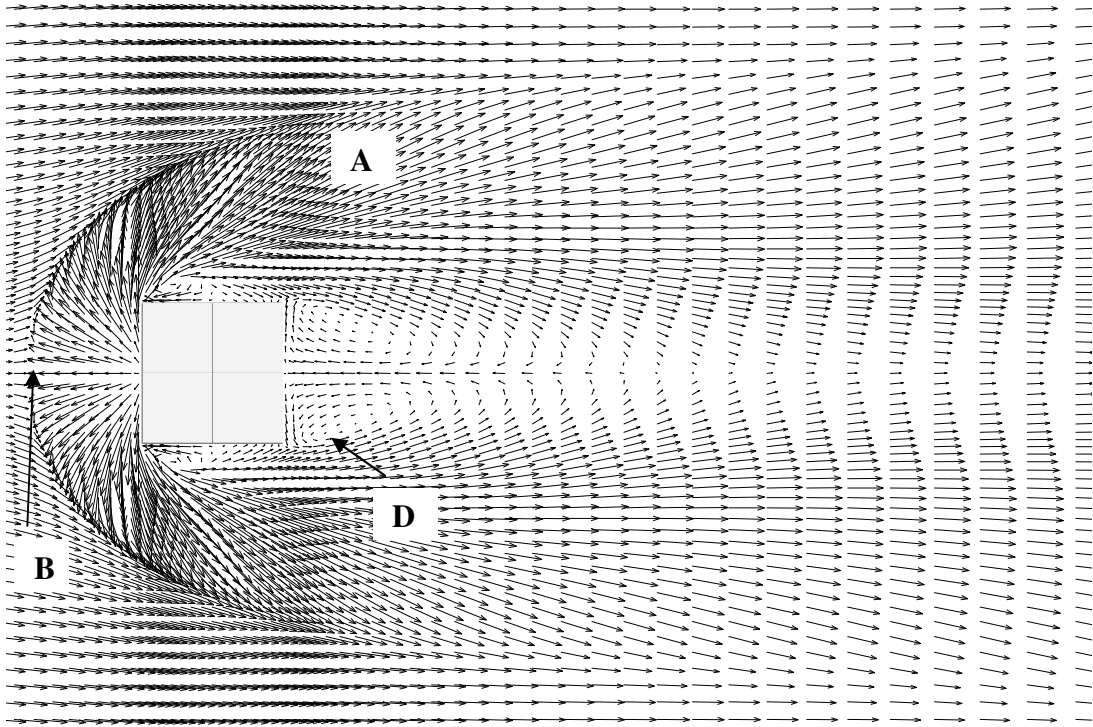


Figure 3.7(a). Vector field plot for x/y plane at $z/h=0.055$

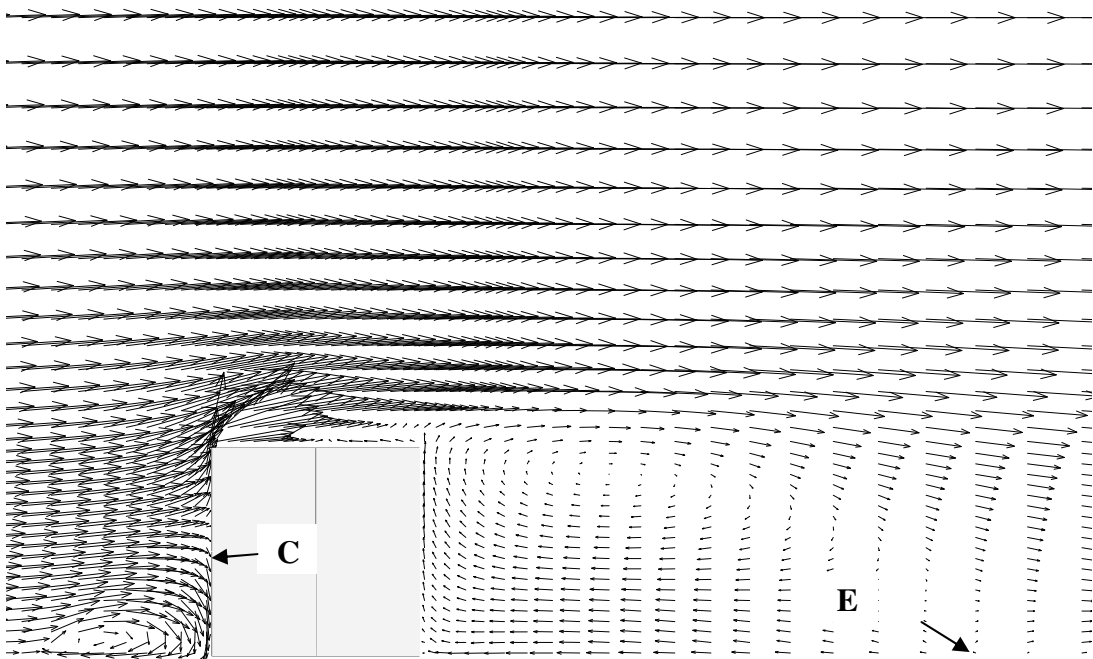


Figure 3.7(b). Vector field plot for x/z plane at $y/h = 0.0$

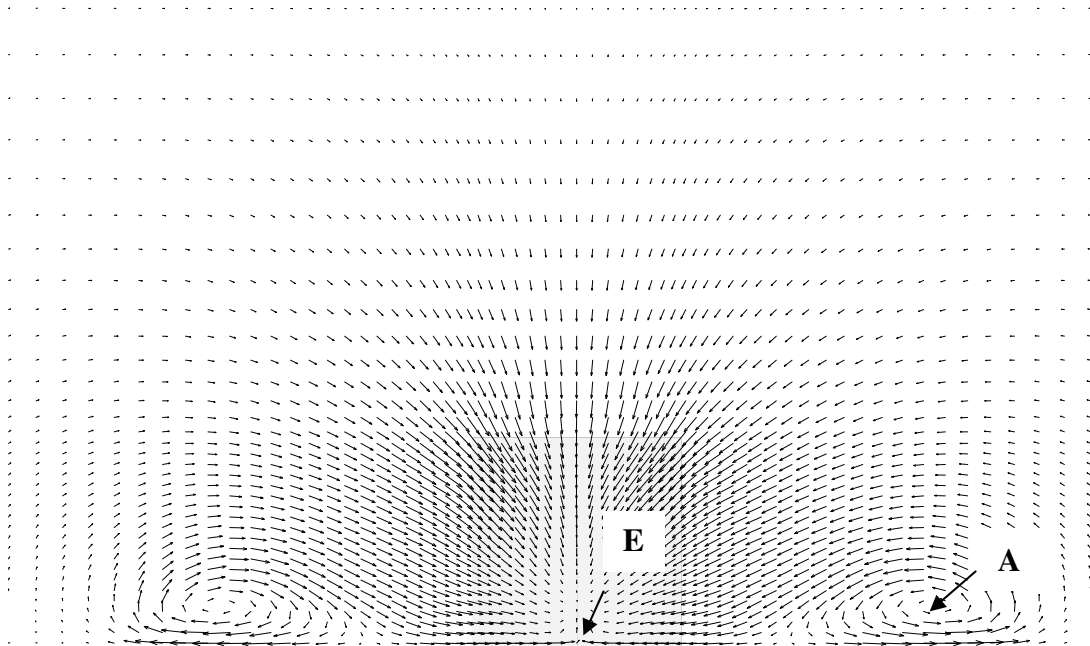


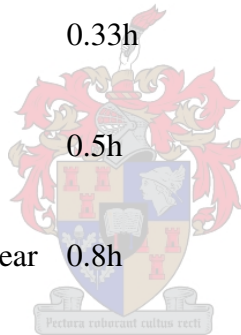
Figure 3.7(c). Vector field plot for y/z plane at $x/h=2.595$

The lower part of the impinging flow is swept downward and around the obstacle in the horseshoe vortex. The low pressure in the leeward wake of the obstacle contains another recirculation region, the arch vortex extending upward and away from the ground (D). This separation reattaches to the ground at a downstream stagnation point (E) and thereafter the wake expands due to the increased mass flow.

Experimental work has shown for flows around a three-dimensional cube that there should be very little, if any, reattachment on the roof, Lakehal and Rodi (1997) among others. The $k-\varepsilon$ model is known to produce very little roof separation due to the overestimation of the turbulence kinetic energy in the impingement region and subsequently high prediction of eddy viscosity. This in turn leads to an enhanced mixing effect which effectively destroys the separation layer. The MMK model proposed by Tsuchiya et al. (1997) and Murakami (1998) seems to overcome this inaccuracy quite efficiently showing a much stronger recirculation region.

Table 3.2. Cube separation zones characteristic dimension comparison.

	Present $Re_h=1377000$	Paterson and Apelt (1990), Case (d)
z_0/h	0.0000025	0.000005
$k^{0.5}/U_r$	0.01	0.08
<u>Vertical plane $y/h=0.0$:</u>		
Length of rear recirc. region	2.2h	2.0h
Length of top recirc. region	-	0.65h
Height of centre of top	-	0.05h
Height of front recirc. region	0.6h	0.55h
Length of front recirc. region	1.0h	0.3h
<u>Horizontal plane $z/h=0.055h$:</u>		
Lateral location of centre of side recirc. region	0.1h	0.14h
Longitudinal location of centre of side recirc. region	0.33h	0.41h
Lateral location of centre of rear recirculation region	0.5h	0.65h
Longitudinal location of centre of rear recirc. region	0.8h	0.77



One noteworthy observation may be made regarding possible snow accumulation areas based on these flow field results. Figure 3.8(a) shows a contour plot of the near surface friction velocity in the x/y plane. The maximum contour value was set at u_* . This indicates three shear stress zones where deposition may occur first. The first is at the edge of the windward recirculation zone, the second occurs in the leeward recirculation zone behind the cube and the third zone occurs downstream from the cube and lateral to the main flow direction. This third region starts at approximately $2.5H$ downstream of the cube, which corresponds with the reattachment length of the leeward recirculation zone, and follows the converging streamlines travelling around the cube.

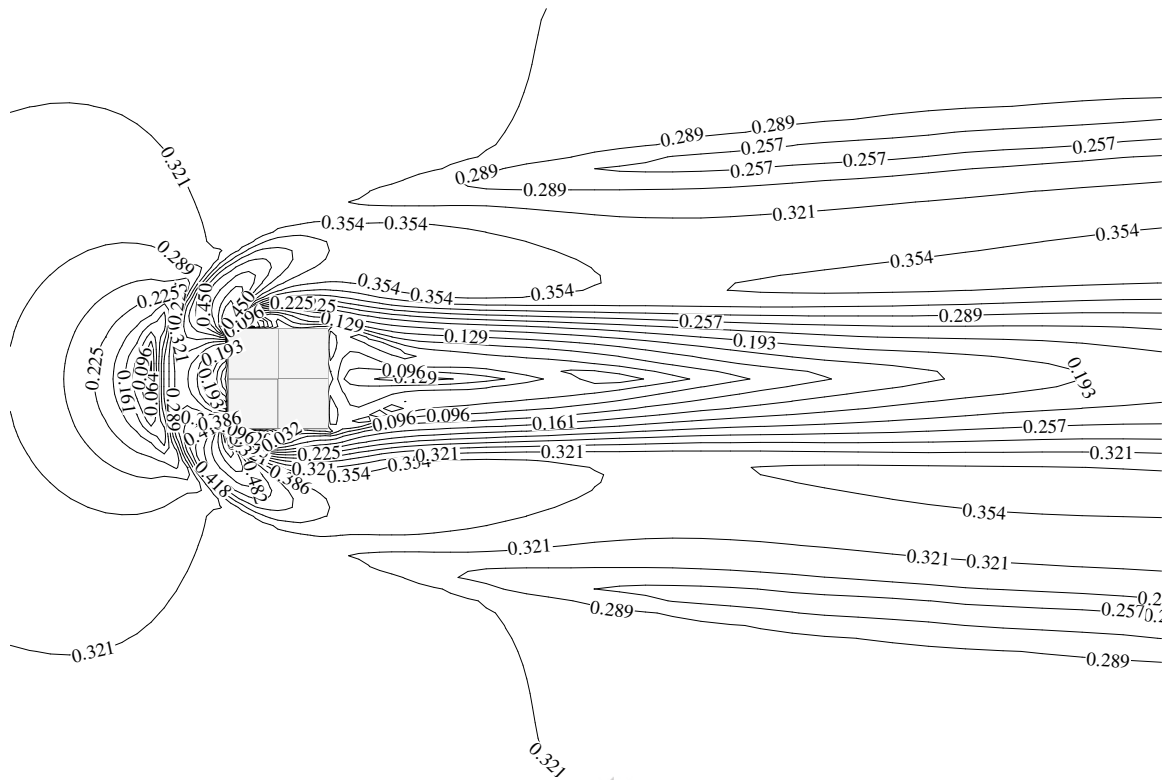


Figure 3.8(a). Contour plot of the near surface friction velocity in the x/y plane at $z/h=0.01$.

In this area the flow is returning towards its original upstream magnitude although the horseshoe vortex is still present. Thus, the swirling motion of the vortex causes a slight drop in tangential momentum in order to support the upward directed velocity which manifests itself as a low shear stress area at the outer edge of the vortex, see figure 3.8(a). This (1999) also observed that the lateral snowdrifts form at the reattachment length as found here. This implies that the initiation of these lateral drifts is a function of the flow pattern surrounding the cube and not necessarily as a function of initial build-up near the windward recirculation zone. Possible snow accumulation could occur in zone 2, directly behind the cube, if significant snow concentrations were present, which is not the case for this analysis, see figure 3.8(b) showing the ratio of the snow fraction and the upstream snow fraction at the same height. The observed accumulation did show reasonable accumulation directly behind the cube which suggests that some precipitation occurred during the test period. This may have introduced snow in this recirculation area. This contribution to drift formation is not presented or discussed further here since it is the focus of further ongoing research evaluating the effects of precipitation.

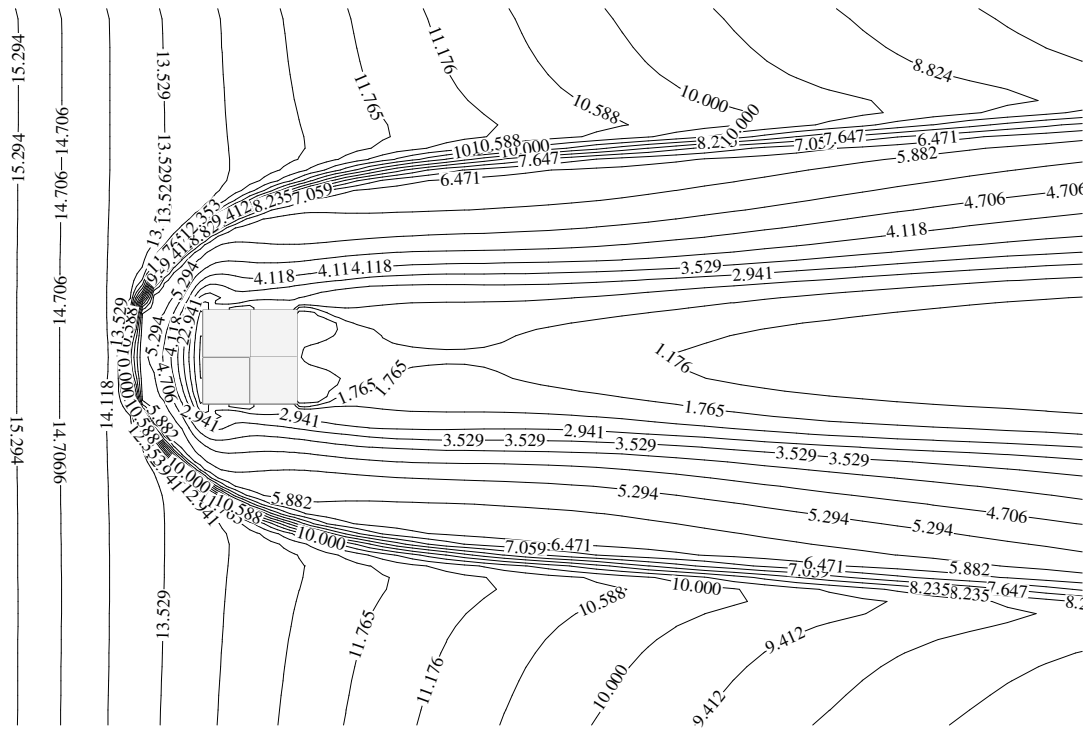


Figure 3.8(b). Contour plot of the near surface snow fraction ratio in the x/y plane at $z/h=0.055$

3.3. SNOW DRIFT SIMULATION MODEL I

The first simulation is carried out with the snow drift Model I – the threshold model - activated. This model is described in chapter 2. The three-dimensional snowdrift surface at the end of the simulation is shown in figure 3.9. Although the observed snow accumulation shows some differences to the predicted snow build up it does seem that the model satisfactorily predicts the accumulation location and scales, especially when compared to the time dependant predicted buildup as shown in figure 3.10(a)-(c). The predominant snow accumulation zones follow the description of their locations given above. The windward accumulation gradually grows larger and tends to grow towards the downstream accumulation in zone three. The second region accumulation is initially smaller than zone 1 and 3 but eventually grows to a similar height. This may be attributed to a too small impingement erosion factor K and could diminish to within observed values with increasing K . It seems that all three regions grew to approximately the same height but zone 1 and 3 showed large initial growth rates as expected from the greater snow fraction in their vicinity. The drifts in zone 1 and 3 did not meet, as compared to the observed snowdrift in figure 3.2. This however

was also observed by Thiis (1999) and suggests that the observed drift formation may have been associated with some precipitation of snow, as suggested above. The predicted snow accumulation heights compared to the observed values are summarised in table 3.3.

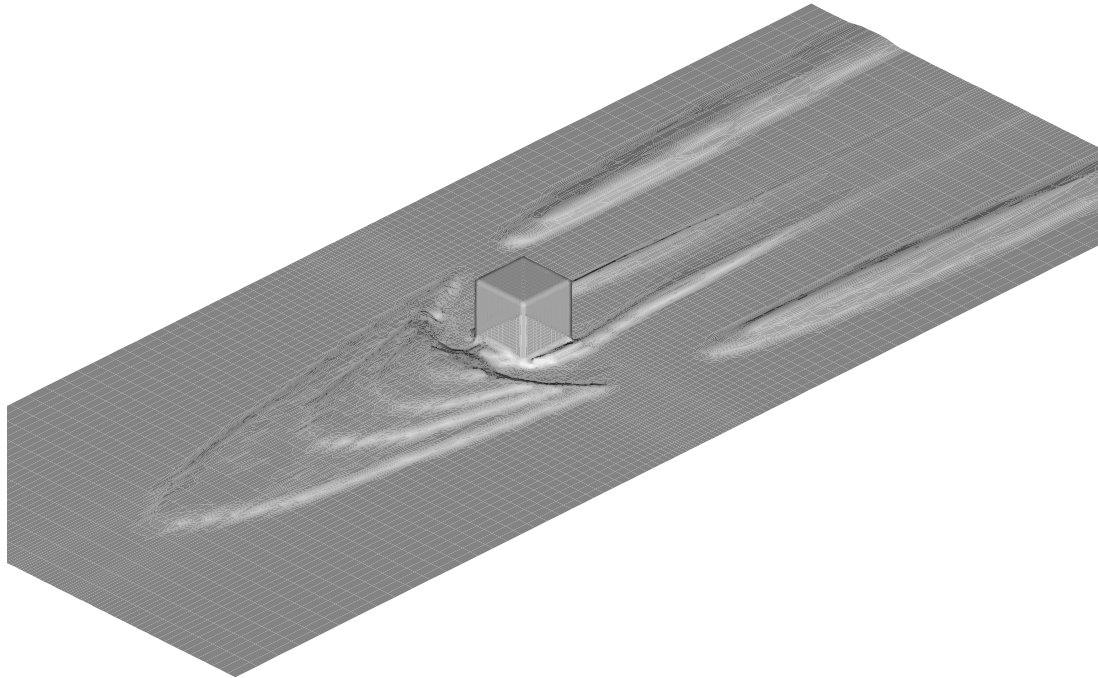


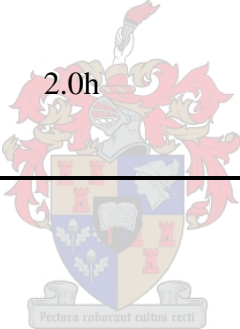
Figure 3.9. Three-dimensional snow drift prediction at the end of the simulation (Model I)

The results seem to indicate that the snow drift predicted by employing Model I, gives realistic results that compare well with the observed snow drift surrounding the surface mounted cube. The model did however predict a drift formation on the windward face of the cube which is not considered realistic based on observations. Furthermore it is believed that the deposition should generally follow the edge of the horseshoe vortex and that the lateral region should grow from the upwind drift formation or that they should eventually meet, something not predicted in this model. The snow drift prediction also shows a significant drift adjacent to the cube side wall. This is a recirculation region with low shear velocity since the flow separates around the windward corners. However, this is also a region with low snow concentration and with high turbulence kinetic energy due to the flow separation. These two factors, the low snow fraction and the high turbulent entrainment should ensure minimal snow deposition here. The next section in this chapter deals with exactly the same model,

computational parameters and flow conditions, but employs the alternative snow drift model described in chapter 2, Model II – the conservation based model.

Table 3.3. Snow accumulation heights comparison between predicted and measured values

	Present simulation	Observed at SANA E IV
<i>Snow accumulation maximum height:</i>		
Windward accumulation, zone 1	0.36	0.4
Leeward accumulation, zone 2	0.18	0.0
Lateral accumulation, zone 3	0.205	0.4
<i>Snow accumulation location:</i>		
Longitudinal location of maximum windward drift	1.04H	0.5H – 0.8H
Longitudinal location of maximum lateral drift	3.44H	1.5H – 3.5H
Lateral location of maximum lateral drift	2.0h	2.0h



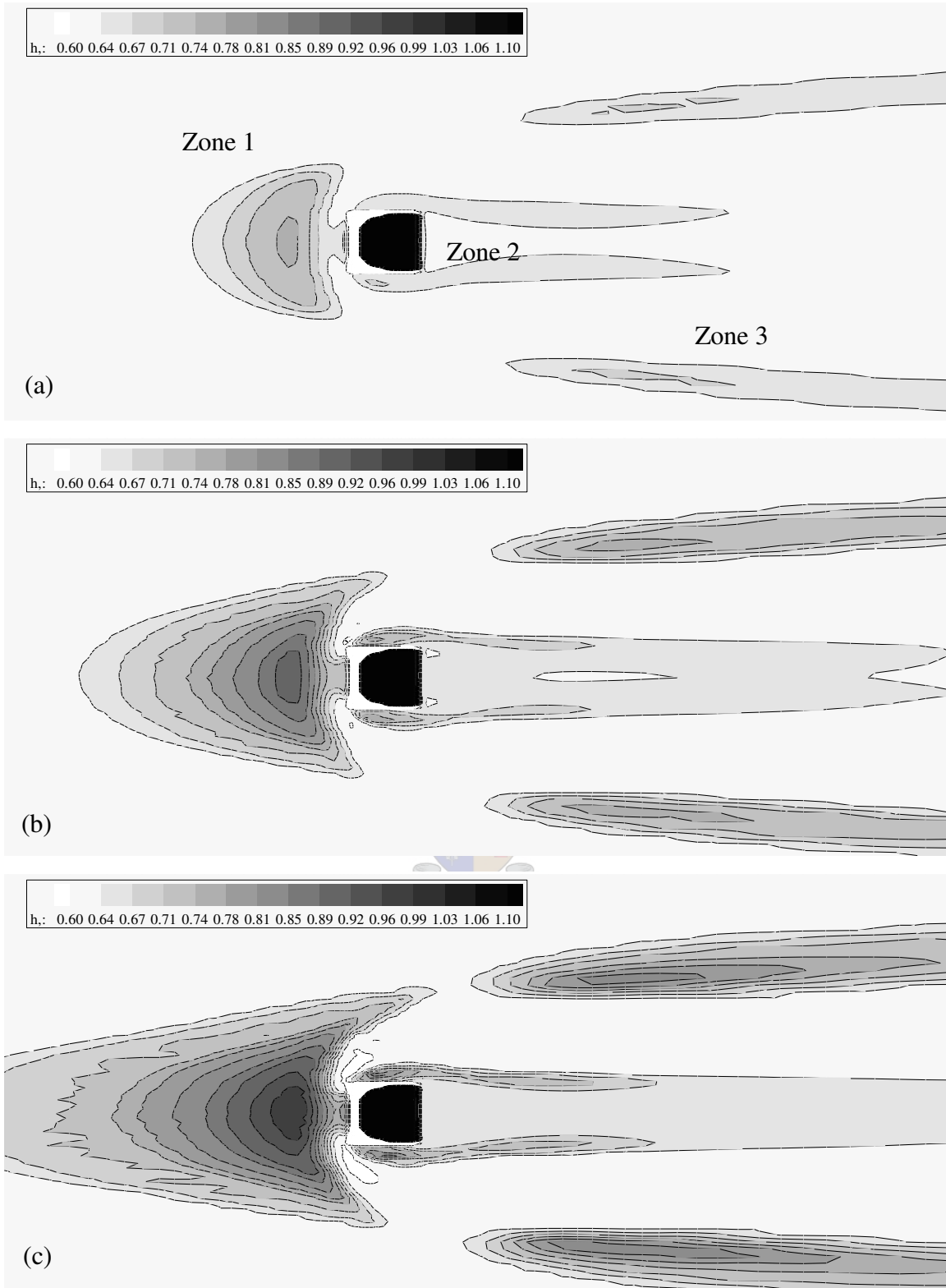


Figure 3.10. Snow drift height contours results from Model I simulation at the (a) beginning, (b) halfway through and (c) at the end of the simulation

3.4. SNOW DRIFT SIMULATION MODEL II

The snow drift development simulated by means of Model II is evaluated by a second simulation run with exactly the same computational domain and simulation parameters as before. Thus the flow field prior to the start of deposition is the same as before and only the deposition flux is calculated differently as described in chapter 2 for Model II. The simulation parameters for the analysis with snow drift Model II are given in table 3.4.

Table 3.4. Simulation parameters for the three-dimensional cube simulation for Model II.

Total simulation time	T	40 s
Drift initiation time	T_{acc}	20 s
Shear velocity	u^*	$0.35 \text{ m}\cdot\text{s}^{-1}$
Saltation roughness parameter	C_1	0.0035
Surface roughness parameter	k	0.0001
Turbulent entrainment factor	α_1	0.8
Drift relaxation factor	α_{22}	0.8
Snow erosion multiplier	α_{ero}	0.0
Snow accumulation multiplier	α_{acc}	100.0
Erosion proportionality	E_r	1.0E-6
Interpolation scheme	Second order	
Turbulent Schmidt number	Sc	1.0
Snow drift model	Model I	
Mean particle size	d_m	110 μm
Mean particle settling velocity	w_f	$0.45 \text{ m}\cdot\text{s}^{-1}$
Drift coefficient	D_f	20.0

The three-dimensional drift at the end of the simulation is shown in figure 3.11. The drift development at three stages during the simulation is shown in figure 3.12(a)-(c). This indicates that the drifts form at similar locations as predicted by Model I but that the windward drift is more pronounced, the downstream lateral drift is less pronounced and the drift next to the cube is eliminated. The deposition of snow next to the wall on the windward side of the cube has also disappeared. It was found during trial simulations that the drift surface becomes more irregular for snow accumulation scale factors larger than 100.0. The reason is that the deposition flux calculated in Model II relies on the first derivatives of the

wall tangential velocity as well as the snow concentration. Since the present model employs a regular Cartesian grid and not a boundary fitted grid the newly formed surfaces may create locally inaccurate gradients causing these local surface discontinuities. However, this effect is negligible for a small scale factor as employed in the present simulations and as shown by the results.

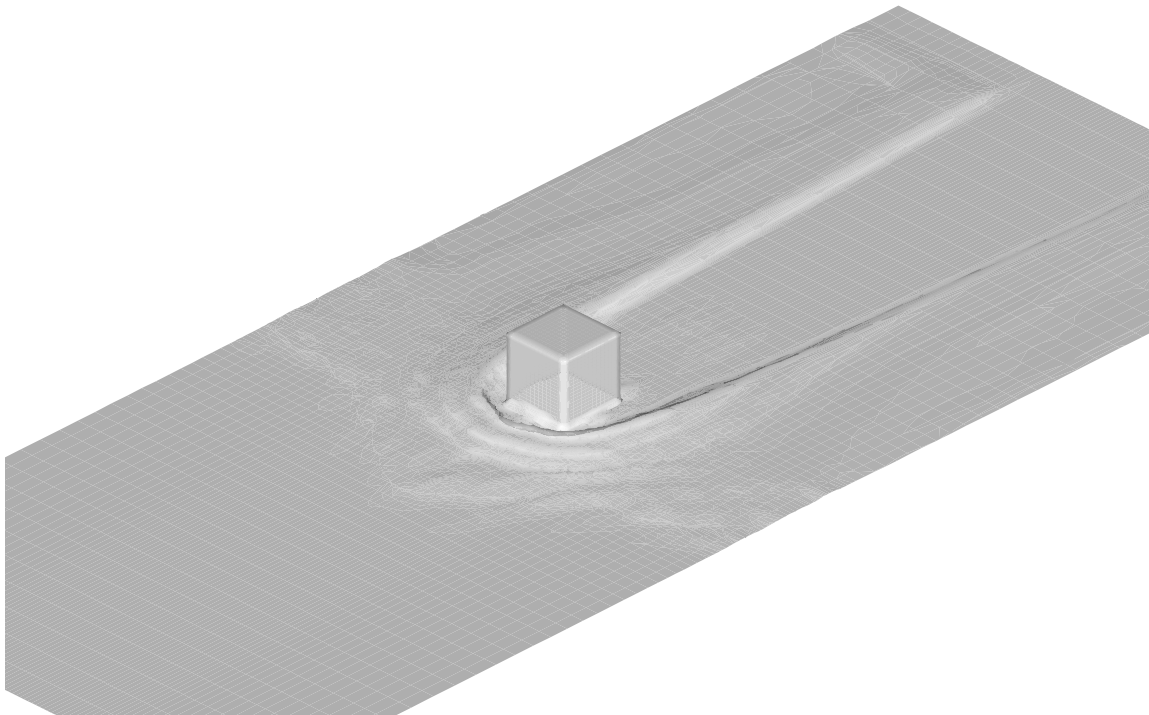


Figure 3.11. Three-dimensional snow drift prediction at the end of the simulation for Model II

The results of the snow drift predicted by Model II give very realistic drifts compared to our original observations, Beyers and Harms (2003a), made during the field tests in Antarctica as described earlier in this chapter. The results are in some ways similar to those predicted by Model I but improve the drift prediction in important areas. The near wall drift at the windward edge of the cube is eliminated by Model II, as shown in figure 3.13, primarily due to the effect of the strong mixing caused by high turbulent diffusion in this region. This vertical entrainment of particles due to flow turbulence is not modelled by the threshold based models as per Model I.

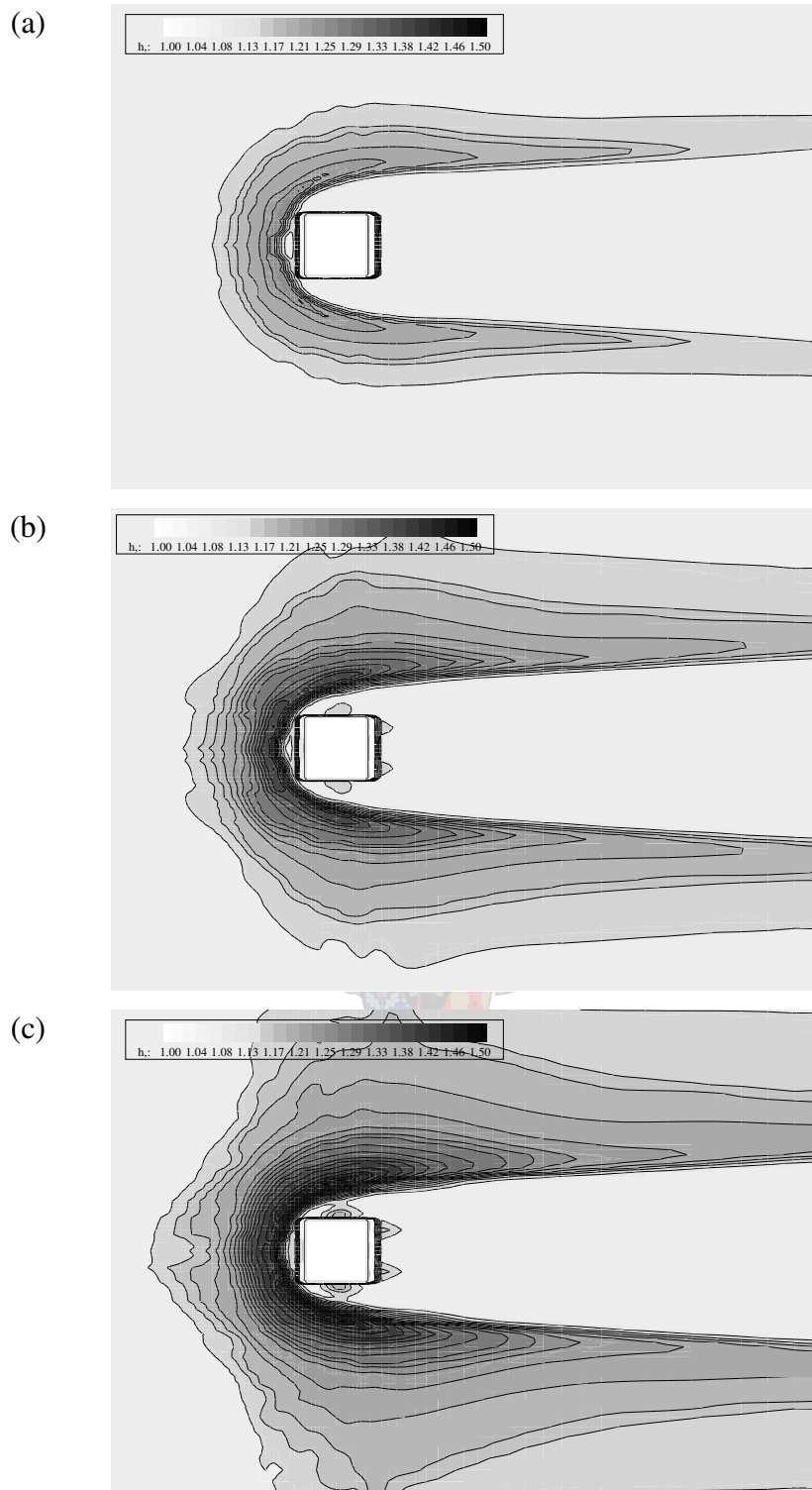


Figure 3.12. Snow drift height contour results from Model II simulation at the (a) beginning, (b) halfway through and (c) at the end of the simulation

The deposition mechanisms leading to the drift development as predicted by Model II are as follows. Firstly the windward deposition that curves around the cube follows the horseshoe vortex. Here the drifts are caused by strong velocity and concentration gradients in the flow i.e. the deposition rate is highly dependent on the divergence of the snow mass flux vector as given in chapter 2.

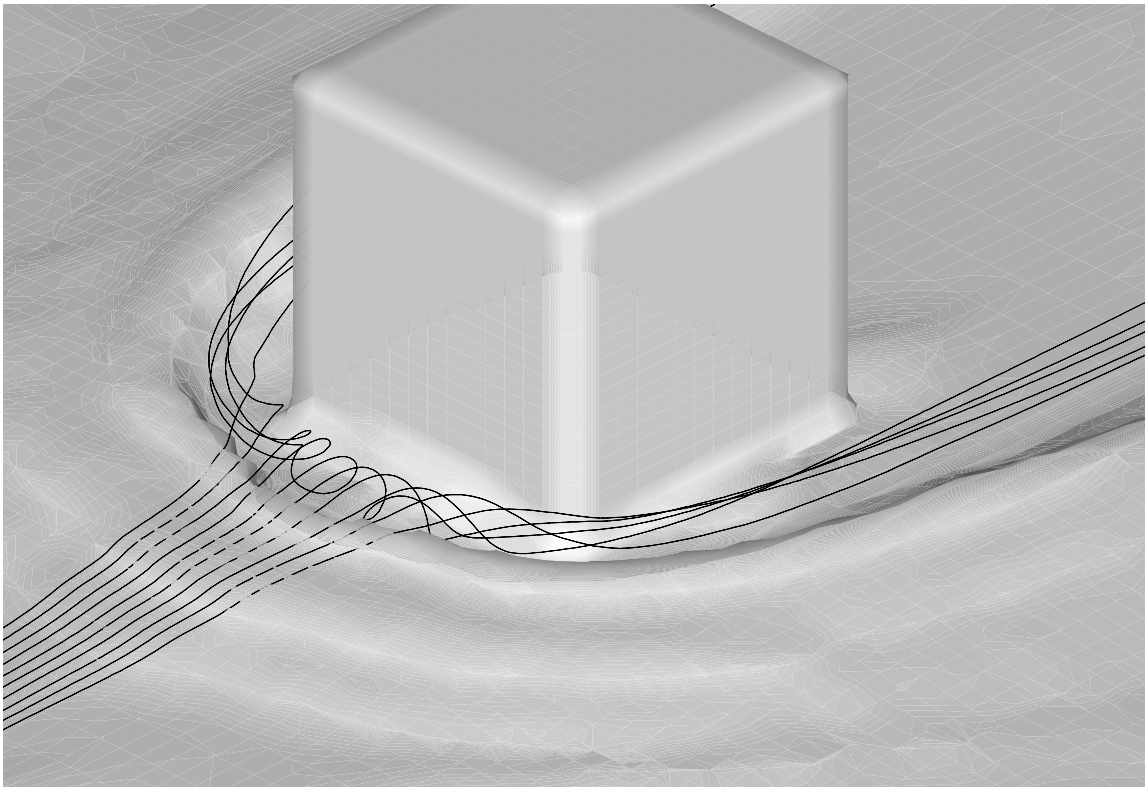


Figure 3.13. Detailed view of windward accumulation at the end of the simulation (Model II).

Secondly the low velocity near the cube windward wall and in the recirculation regions near the surface at the sides of the cube caused deposition in Model I due to the lower than threshold conditions, but in Model II these unrealistic drifts are removed by the strong turbulent diffusion in the same areas. This simulation shows that the snow drift is continuously formed around the cube with the windward drift more pronounced than the lateral drifts. Model I simulations showed that the lateral drifts are not continuous with the windward drift but grow towards each other. However, the Model I prediction relied on the lateral drifts to form only in an area where the shear velocity decreased below the threshold

condition. In the Model II prediction this is not the case and the lateral drifts are formed as a function of the vertical settling and the local flow divergence. It is worth noting that the present simulations employ the standard $k-\varepsilon$ turbulence model which typically does not correctly simulate the wake region behind the cube as described by Shah and Ferziger (1997) as well as Lakehal and Rodi (1997). The present simulation shows a lateral drift that follows the edge of the downstream horseshoe vortex. Since this vortex is expected to expand or diffuse (and not simulated by the standard $k-\varepsilon$ turbulence model) it may cause a stronger cross-streamwise flow gradient and may result in a lateral drift pattern that gradually widens and flattens downstream. This may be a worthwhile research topic for future studies.

These simulations do not predict any drift at the leeward walls of the cube, a phenomenon that was sometimes observed during field observations at SANAE IV. Thiis (1999), (2003) also suggests that during strong storms, suspension dominates and more suspended material is allowed to be entrained in the wake of the obstacle leading to build-up directly behind the obstacle. Saltation dominated storms only allow the majority of snow to be entrained in the horseshoe vortex which leads to mostly windward and lateral build-up. Mavroidis et al. (2003) have shown with field and wind tunnel experiments that the horseshoe vortex found for flows around a surface cube is responsible for the transport of particles laterally round the obstacle and keeping it close to the surface. On the other hand, material that approaches the obstacle at higher levels ($z > 0.5H$) may travel over the obstacle and be entrained in the leeward recirculation region. In the context of snow drift around a cube, this may suggest that saltation dominated conditions ($U_{10} < 15 \text{ m}\cdot\text{s}^{-1}$) will present mainly a drift that follows the edge of the horseshoe vortex since most of the approaching snow travels laterally around the cube. Suspension dominated storms ($U_{10} > 15 \text{ m}\cdot\text{s}^{-1}$) may present a similar drift pattern but with the addition of more buildup in the leeward recirculation region adjacent to the cube wall. This buildup is due to a higher recirculation region snow concentration originating from suspended snow that passes over the cube. Another contributing factor to the absence of this leeward snow buildup may be the fact that the $k-\varepsilon$ turbulence model is known not to resolve a third counter-rotating vortex in the leeward corner between the leeward wall and the main leeward vertical recirculation region, Becker et al. (2002). This would assist the build-up of snow in this region even further.

Importantly for the present test case is that the continuous drift around the cube is predicted near areas of very high flow shear (around the windward corners). This phenomenon is the first glimpse into the more realistic behaviour of the Model II description since the aim of later simulations in this work is to develop drift in regions dominated by high shear velocities such as leeward of elevated obstacles. This simulation indicates that deposition is predicted even under high shear velocity conditions.

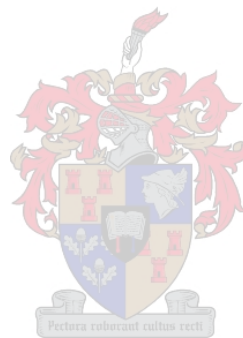
The horseshoe vortex is strongly influenced by the approaching boundary layer characteristics and the terrain surface roughness, Lun et al. (2003), Mavroidis et al. (2003). For the present analysis a very small effective surface roughness was used and therefore the flow recirculation windward of the cube is small and near the cube. The predicted snow drift therefore develops too close to the cube compared to the observed drifts. For a slightly larger effective surface roughness the vortex system will be more pronounced and will move further away from the cube. The subsequent snow drift will also move farther from the cube walls.

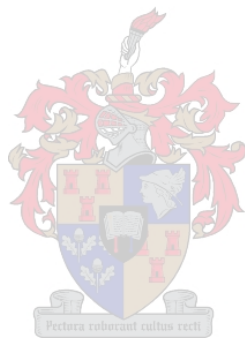
Table 3.5. Snow accumulation heights comparison between predicted (Model I and Model II) and observed values at SANAE IV field test.

	Model I	Model II	Observed
<i>Snow accumulation maximum height:</i>			
Windward accumulation, zone 1	0.36	0.35	0.4
Leeward accumulation, zone 2	0.18	0.0	0.0
Lateral accumulation, zone 3	0.205	0.33-0.15	0.4
<i>Snow accumulation location:</i>			
Longitudinal location of maximum windward drift	1.04H	0.5H	0.5H – 0.8H
Longitudinal location of maximum lateral drift	3.44H	-	1.5H – 3.5H
Lateral location of maximum lateral drift	2.0H	0.5H	2.0H

To conclude, both Model I and Model II predictions provide realistic drift patterns although the Model I deposition areas are wholly dependent on the regions where the shear velocity is lower than the threshold shear velocity. The Model II results clearly show superior drift

predictions where the near cube windward deposition is eliminated and a continuous drift is predicted around the cube, which is more in agreement with observations made during the Antarctica field tests and as indicated by figure 3.2. The Model I simulations could not predict the continuous drift since the windward corners of the cube generate high local shear velocities which then does not generate deposition according to Model I theory. Table 3.5 summarises the key drift characteristics for the Model I, Model II and the observed drift around the cube. The observed drift position in the lateral region is believed to be strongly influenced by the aligned wind condition for the observed drift. The Model II prediction is for a normal wind angle only.





4. SIMULATION OF SNOW DRIFT AROUND A POROUS SNOW FENCE

4.1. EARLIER EXPERIMENTAL AND NUMERICAL WORK

Snow fences are used to deliberately deposit drifting snow at specific locations to minimise its accumulation in other more sensitive or unwanted areas. They are typically found next to highways to keep the roads clear of snow drifts and also to improve visibility on the roadway. Snow fences may also be employed to deliberately move large volumes of snow for construction of elevated roadways and landing strips in polar areas. This reduces the volume of snow that needs to be moved by mechanical means. Such fences may also be employed to deposit snow away from areas sensitive to avalanching. Various different designs are used ranging from solid fences to highly porous fences, fences with vertical or horizontal wooden slats, fences from artificial materials or living fences such as shrubs or trees forming natural wind breaks. The different fence designs are usually named according to their origins and therefore one finds Wyoming, Canadian, Norwegian, Russian and Japanese snow fences, among others, Gurer et al. (2002). The basic characteristics of a porous fence is to reduce the wind velocity in the approaching flow as it passes over and through the fence allowing a proportion of the wind driven snow to deposit. The snow drift for snow fences are usually given in terms of fence height, bottom gap, fence porosity, fence vertical inclination and trapping efficiency among other characteristic parameters.

Another fence type, the blower fence, is similar in design but differs somewhat in its operation. These fences remove snow from unwanted areas by means of high velocity wind scour. Blower fences may be used to reduce snow deposition in regions of terrain curvature where eddies are formed due to the natural topography. Early blower fence research and design is described by Zhonglong and Yuan (1980). Anno (1986) gives results of model and prototype testing of a solid blower type fence used to prevent snow buildup as opposed to the porous fence application where preferential snow buildup is established. Sundsbø (2003) successfully used a blower type fence to remove snow from roads along a steep embankment. The drift free length of this deflecting type fence is given in terms of fence height, fence inclination, bottom gap space, terrain slope, wind direction and velocity and the approaching snow flux.

This work is interested in the simulation of the wind flow and subsequent snow drift surrounding a porous snow fence in order to further validate the snow drift Model II given earlier in this work. Extensive research has been done on the design and optimisation of particularly this type of snow fences. These works include studies of flows through general porous fences or screens to establish the characteristics of the wake flow leeward of the fence. Others studies were specifically involved with snow fences to determine their trapping efficiency and drift lengths as functions of the fence dimensions and wind conditions. A few of these studeis are summarised below.

Tabler (1980a), (1980b) presented results of years of snow drift measurements surrounding both Wyoming and Canadian type snow fences. These fences were installed next to Highway 80 in south-eastern Wyoming. The Wyoming snow fence consists of horizontal slats 15 cm wide with 15 cm gaps between the slats. For an efficient fence the total fence porosity should be approximately 50% when including a bottom gap of between 0.1H and 0.15H, where H is the fence height, similar to that given in Radok (1977). A successful snow fence must be designed with sufficient capacity to store the seasonal transported snow volume. Tabler (1980b) presents relationships for the empirical drift profile height as a function of the distance from the fence. For the leeward drift the relationship is

$$\frac{z}{H} = 0.20 - 0.377\left(\frac{x}{H}\right) - 0.0472\left(\frac{x}{H}\right)^2 + 0.002329\left(\frac{x}{H}\right)^3 - 5.392 \cdot 10^{-5}\left(\frac{x}{H}\right)^4 + 4.840 \cdot 10^5\left(\frac{x}{H}\right)^5 \quad \frac{x}{H} < 30.0 \quad (4.1)$$

and for the downwind drift the relationship reads

$$\frac{z}{H} = 0.5 - 0.04\left(\frac{x}{H}\right) \quad \frac{x}{H} < 12.5 \quad (4.2)$$

Figure 4.1 gives some of the characteristic dimensions of a snow drift associated with a Wyoming type fence, Tabler (1980b) of 50% porosity.

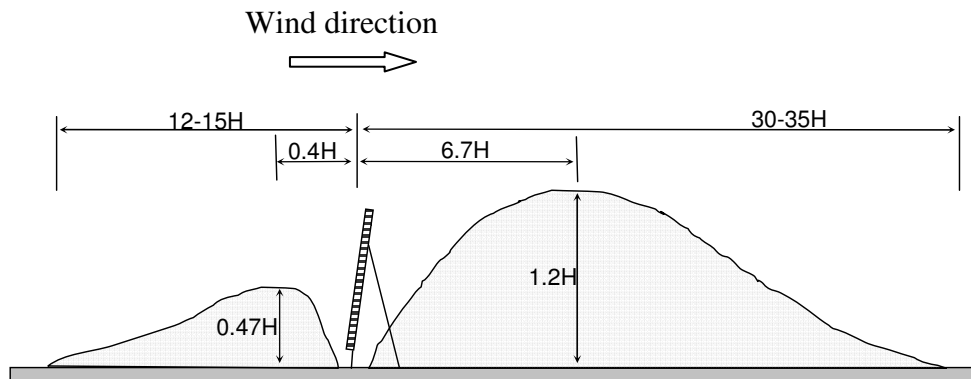


Figure 4.1. Characteristic snow drift dimension around a Wyoming type snow fence, Tabler (1980b, 1991b) - not drawn to scale

Tabler (1980b) carried out outdoor scale model tests of snow drifting around Wyoming snow fences and reported on some important scaling techniques and drift profile results. Iversen (1981) presents comparative wind tunnel scale model tests for a Wyoming snow fence and compared the measured snow drift development profiles with the results of Tabler (1980b) described above.

Perera (1981) carried out flow measurements with a pulsed wire anemometer to evaluate the wakes of two-dimensional solid and porous fences and provide profiles of normalized mean velocity behind the fences. The research indicated that the separation bubble behind the fence disappeared for fence porosities larger than 0.3. Bradley and Mulhearn (1983) also measured the flow behind a 50% porous fence and evaluated the wake profile downstream of the fence. They indicate that the wake region steadily increases in depth downstream and that the flow gradually accelerates until it recovers to the upstream logarithmic profile. However, the profile retains a deficit of approximately 4% even up to $50H$ downstream. Their report mentions that the separation bubble behind the fence gradually decreases up to 25% fence porosity and that no evidence of this separation is found for porosities of 50%, consistent with the results of Perera (1981). Ranga Raju et al. (1988) also measured the turbulent intensity along the flow field surrounding a two-dimensional fence with porosity of 38%. They show that the turbulent intensity, at any point downstream of the fence, decreases with decreasing porosity as the velocity gradients diminish. They also showed that the separation bubble disappear for porosity greater than 30%. Lee and Kim (1999) give the results of flow

measurements behind fences with different porosities. They found that an increase in porosity results in a decrease in both the height of the shear layer and the flow curvature and that for a porosity exceeding 40% the recirculation region disappears completely.

Norem (1985) gives general design guidelines for snow drift management along roadways by means of snow fences and gives design specifications for a typical Norwegian type snow fence. The fence height is determined by the quantity of seasonal snow to be trapped or stored, the snow drift rate, topography and depth of snow fall. A 50% porous fence seems to give the highest storage capacity. A bottom gap of between 0.1H-0.3H maintains an eroding wind close to the ground to eliminate build-up too close to the fence.

Wilson (1985) applied a numerical scheme based on the SIMPLE algorithm along with various turbulence models to study wind flows through porous barriers. The momentum loss through the porous barrier was modelled as a sink term in the windward momentum conservation equation namely

$$SU = -\frac{k_r}{2\delta x} u|u| \quad (4.3)$$

where k_r is a pressure loss coefficient through the fence with the cell width given by δx . The pressure drop through a 50% porous fence was measured during their experiments from which a pressure loss coefficient of $k_r=1.97$ was determined. Their numerical results showed reasonable agreement with the measured flow and also indicated that the $k-\epsilon$ turbulence model failed to accurately predict the speed-up across the top of the fence or the increased velocity in the outer layer and also underestimated the rate of return of the downwind flow to the upstream state.

Anno (1985) used activated clay particles to study snow accumulation around a model snow fence in a wind tunnel. The activated clay was used since it could simulate cohesive particle drifts and represented good geometrical similarity with snow particles. This measured result of the model fence was compared with observed results around a large scale fence in Hokkaido, Japan.

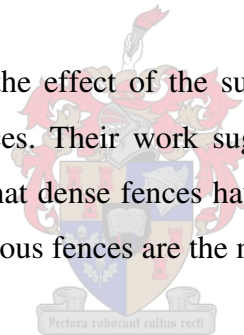
Sato et al. (1993) developed a three-dimensional numerical model to predict the snow drift rates in the vicinity of a solid fence with and without a bottom gap. Their model did not

update the snow flow field as a function of the changing surface geometry due to snow accumulation or erosion but gave an estimate of the rate of deposition from the steady state analysis.

Liston et al. (1993) applied a single phase airflow model with a saltation flux model to simulate the snow drift surrounding a solid fence. They found that the leeward recirculation eddy increased in length for decreasing surface roughness, consistent with a sharper velocity profile gradient near the surface.

Sundsbo (1997) carried out two-dimensional numerical simulations of the flow and snow drift through a 50% porous fence. The model employs a mixing length turbulence model and dynamic modification of the developing snow surface as deposition progresses. The prediction of the transient snow drift development compares favourably with the data given by Tabler (1980b).

Naaïm-Bouvet et al. (2002) tested the effect of the surface slope on the snow drift profile around solid and porous snow fences. Their work suggests that an increasing slope angle decreases the catch efficiency and that dense fences have higher efficiencies for steep slopes compared to porous fences while porous fences are the most efficient for flat terrains.



Gurer et al. (2002) tested eleven different types of snow fences in a cryospheric wind tunnel and gave comparative results for catch efficiency, drift area and volume, rate of collection and shape of drifts.

Alhajaraf (2003), (2002), (2001) applied the volume of fluid method, similar to Sundsbø (1997) with the standard k- ϵ turbulence model to study particle drifts around single and multiple rows of porous fences. The model allowed for the changing surface due to deposition by blocking the control volume if the particle volume fractions exceed a maximum packing fraction. Good agreement between the simulated equilibrium drift profiles and those measured by Tabler (1980b) and Iversen (1981) is achieved.

4.2. TWO-DIMENSIONAL NUMERICAL MODEL OF SNOW DRIFT AROUND A 50% POROUS FENCE

The present analysis models the Wyoming snow fence drift since the availability of the measured profiles and numerical results as described above, provides ample opportunity for numerical model verification. The numerical analysis of a snow fence is firstly done in two dimensions and the results compared with the available snow drift profiles from these earlier measurements and numerical simulations. The computational domain employed for the two-dimensional analysis is shown in figure 4.2. A 50% porous fence, 3.8 m high with a bottom gap of 0.5 m (0.13H) is modelled, in accordance with proper fence dimensions as given in Tabler (1991b). The fence is placed vertically to the oncoming flow although real fences are usually built with a downwind inclination of 15°, but this seems to have little influence in the final drift geometry, Tabler (1980b).

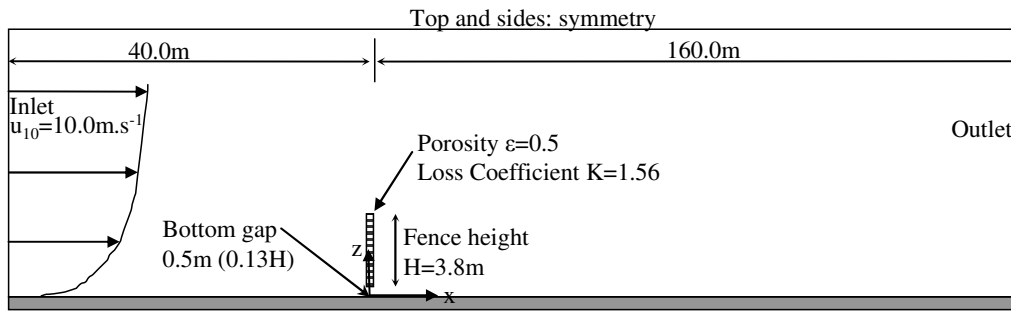


Figure 4.2. Two-dimensional computational domain for a snow drift simulation around a 50% porous fence

The fence itself is not modelled geometrically but rather by means of a porous baffle of zero volume but with a suitable area porosity and an appropriate pressure loss coefficient. Similar simulations using this technique are described by Wilson (1985). The effects of the fence is thus incorporated into the computational domain as a momentum sink or pressure loss term in the Navier Stokes equations. For the flow in the x-direction the momentum sink term is given for a typical vertical fence by equation (4.3). The pressure loss coefficient, k_r , for a porous baffle is given, as per Lee and Lim (2001), by

$$k_r = 0.52 \frac{(1 - \epsilon^2)}{\epsilon^2} \quad (4.4)$$

where ε is the fence area porosity. For $\varepsilon=0.5$, $k_f=1.56$. Packwood (2000) carried out numerical experiments to establish pressure loss coefficients for porous fences. This suggested for $\varepsilon=0.5$, $k_f \approx 1.00$.

Three different inlet wind shear velocities are considered here namely $u_*=0.30 \text{ m}\cdot\text{s}^{-1}$, $u_*=0.35 \text{ m}\cdot\text{s}^{-1}$ and $u_*=0.50 \text{ m}\cdot\text{s}^{-1}$ which corresponds to 10 meter wind speeds of $u_{10}=9.76 \text{ m}\cdot\text{s}^{-1}$, $u_{10}=11.12 \text{ m}\cdot\text{s}^{-1}$ and $u_{10}=15.0 \text{ m}\cdot\text{s}^{-1}$ respectively. The reason for this was to evaluate whether the snow drift model employed provides realistic drift profiles when the approaching bed shear velocity exceeds the threshold shear velocity considerably. Inlet snow concentrations are calculated according to equations (2.90) and (2.93). Inlet turbulence characteristics are given by equations (2.152) and (2.153). The standard k- ε turbulence model is applied. A 121 x 41 cell computational mesh was selected after grid independence tests were carried out. This computational mesh is show in figure 4.3. The porous baffle is located 40 m downstream of the inlet while the initial snow surface depth is 1.1 m. Local mesh refinement is applied in the horizontal direction in the vicinity of the fence and in the vertical direction across the top of the fence. The model parameters employed during the simulation is given in table 4.1. These fence simulations are carried out using only the Model II snow drift scheme to evaluate its success in predicting the drift profile development and compare those results with those of other researchers. Sundsbø (1997) and Alhajraf (2001) have shown that the threshold drift models can predict realistic drift profiles.

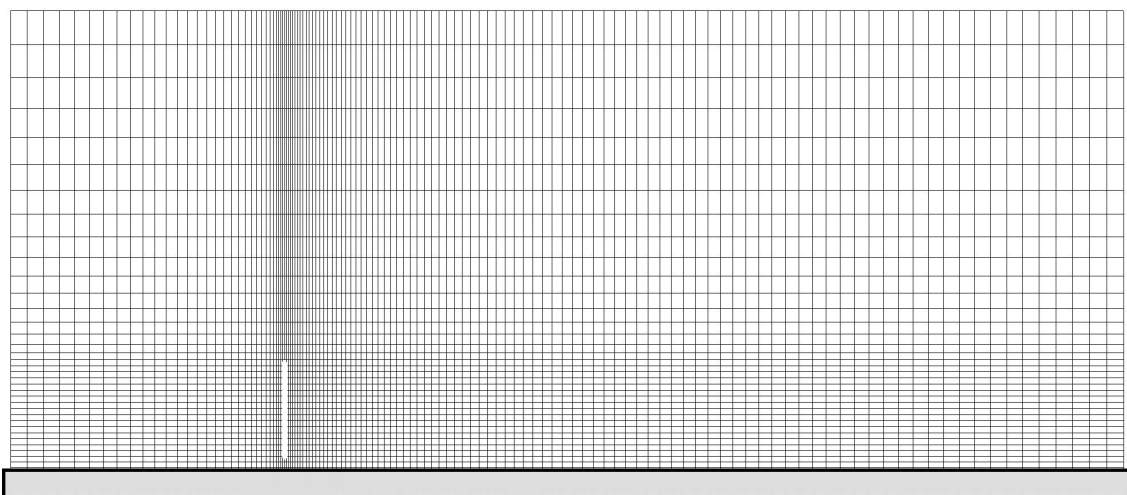


Figure 4.3. Computational domain for the snow fence simulation - not to scale

Table 4.1. Simulation parameters for the two-dimensional snow fence simulation using Model II

Total simulation time	T	200 s
Shear velocity	u^*	$0.30 \text{ m}\cdot\text{s}^{-1}$, $0.35 \text{ m}\cdot\text{s}^{-1}$, $0.50 \text{ m}\cdot\text{s}^{-1}$
Saltation roughness parameter	C_1	0.0035
Surface roughness parameter	k	0.0001
Turbulent entrainment factor	α_1	0.7-1.2
Drift relaxation factor	α_{22}	0.5
Snow erosion multiplier	α_{ero}	1.0
Snow accumulation multiplier	α_{acc}	500.0
Erosion proportionality	E_r	7.0E-4
Interpolation scheme	Second order	
Turbulent Schmidt number	Sc	1.0
Snow drift model	Model II	
Mean particle size	d_m	110 μm
Mean particle settling velocity	w_f	$0.45 \text{ m}\cdot\text{s}^{-1}$
Drift coefficient	D_f	20.0
Fence porosity	ε	0.50
Fence pressure loss coefficient	k_r	1.56

4.3. RESULTS AND DISCUSSION

All simulations were continued for 200 seconds with the initiation of snow deposition started after 20 seconds which allowed a steady state flow field to be established first. The resultant snow drift development, predicted during the course of the simulations, is shown in figures 4.4, 4.5 and 4.6. The snow drift profile with the accompanying velocity vectors for the second simulation is shown in figure 4.7(a) and (b) at the initiation of the snow deposition and at the end of the simulation. This serves to illustrate the modification of the flow field to accommodate the new and dynamically changing surface profile. The resultant characteristic dimensions of the drift profile at the end of the simulations are compared with the dimensions given by Tabler (1980b) and Iversen (1981) in figure 4.8 and summarised in table 4.2. The

results indicate that the simulated leeward drift profile compares favourably with the characteristic profile given by Tabler (1980b) and Iversen (1981) for the test cases. It must be said that the drift profile predicted at the end of these simulations still showed some minor changes in the tail of the leeward drift. The predicted windward drift as well as the largest part of the leeward drift closer to the fence reached an equilibrium profile halfway through the simulation and very few transient changes were observed thereafter.

For all three test cases the simulated windward drift is somewhat different than that predicted by Tabler (1980b). Iversen (1981) and Naaim et al. (1998) present results showing smaller or insignificant windward drifts obtained in wind tunnel tests and numerical simulations where the approaching wind friction velocity was kept constant and well above the threshold friction value. This contradicts the notion of Kind and Murray (1982) that the equilibrium drift profile is largely insensitive to the approach shear velocity ratio i.e. ratio of the upwind shear velocity to threshold shear velocity. Alhajraf (2001) carried out numerical simulations to test this influence and found that for a shear velocity 2% above the threshold the upwind drift compares well with that of Tabler (1980b) while for a shear velocity 20% above the threshold the upwind drift all but disappears, supporting the results of Iversen (1981).

The predicted leeward length, slope and height of the drifts are generally in good agreement with the measured results although the simulated drifts are closer to the fence with steeper upwind faces. This may be due to the small fence gap of 12% and may also explain why the windward drifts become larger than 0.5H. As the leeward drift develops closer to the fence the windward drift region experience lower velocity and more material is deposited. The drift for test 1 is still developing at the end of the simulations and therefore the leeward drift length is short and the slope still shallow.

These simulations are insensitive to the specific fence design and only use the porosity and pressure loss coefficient as a measure to modify the momentum as the flow passes through the fence. Various fence designs have very different characteristic dimensions as shown by Gurer et al. (2002) while a comparison is attempted here between Wyoming type (horizontal slat) fences with 'numerically' porous walls. Nevertheless the results indicate that fence snow drift characteristics are generally captured and realistically predicted.

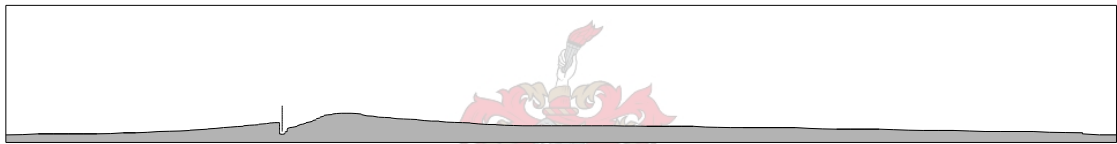
(a) $t=40$ s



(b) $t=80$ s



(c) $t=120$ s



(d) $t=160$ s



(e) $t=200$ s

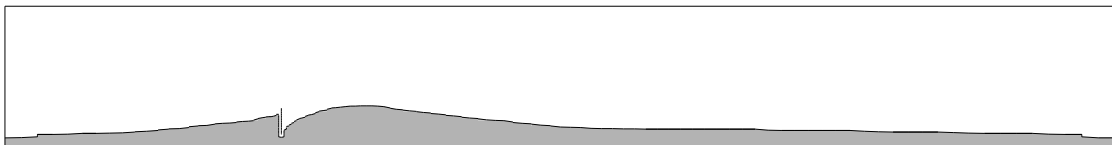
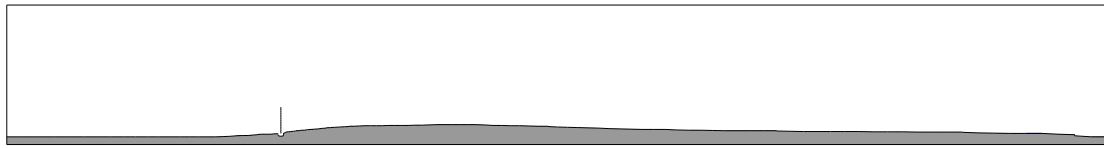


Figure 4.4. Snow drift development over time for $u_* = 0.30 \text{ m}\cdot\text{s}^{-1}$, (a) $t=40$ s, (b) $t=80$ s, (c) $t=120$ s, (d) $t=160$ s, (e) $t=200$ s

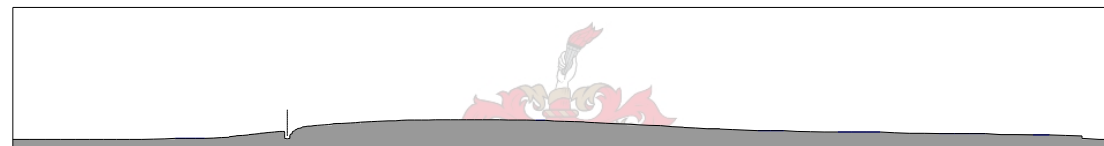
(a) $t=40$ s



(b) $t=80$ s



(c) $t=120$ s



(d) $t=160$ s



(e) $t=200$ s

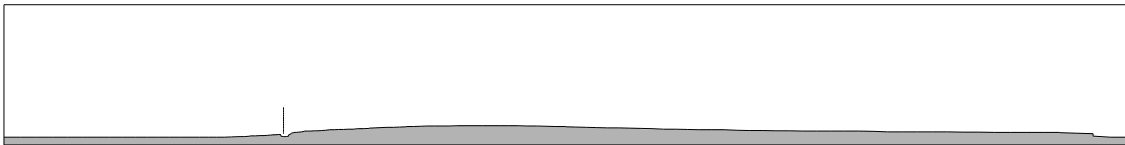


Figure 4.5. Snow drift development over time for $u_* = 0.35 \text{ m}\cdot\text{s}^{-1}$, (a) $t=40$ s, (b) $t=80$ s, (c) $t=120$ s, (d) $t=160$ s, (e) $t=200$ s

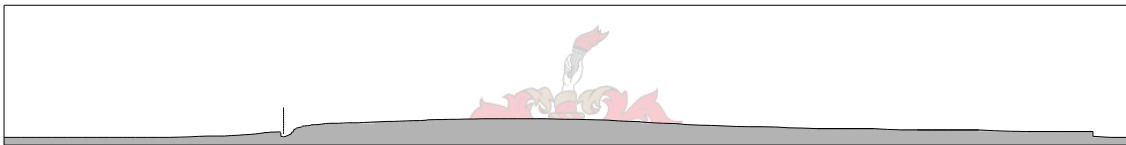
(a) $t=40$ s



(b) $t=80$ s



(c) $t=120$ s



(d) $t=160$ s



(e) $t=200$ s

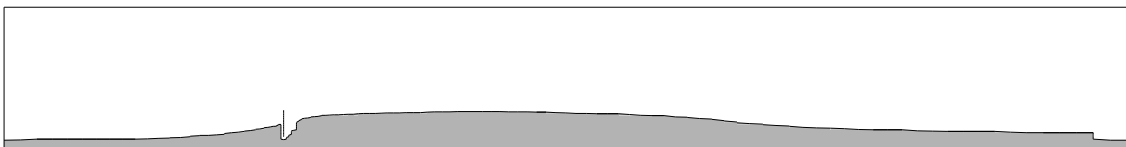
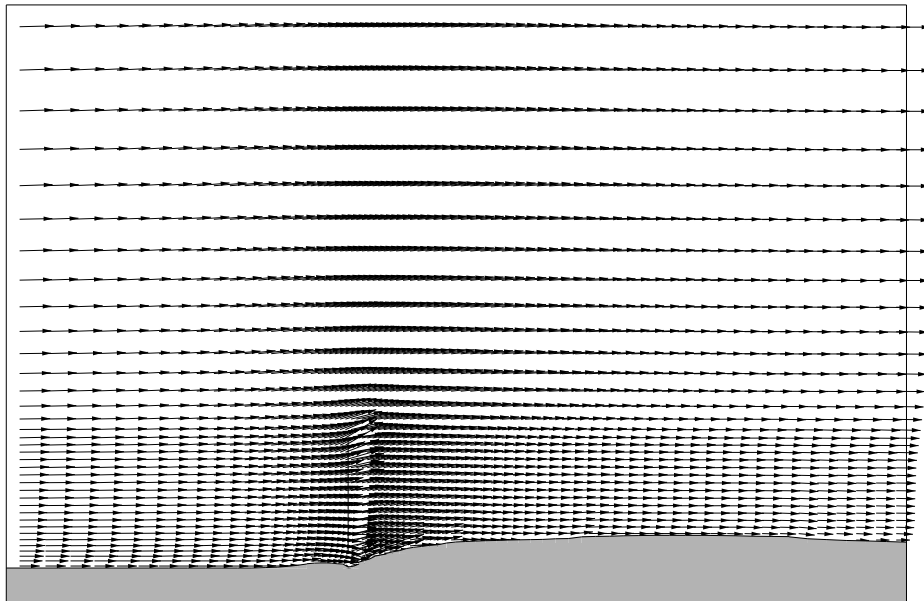


Figure 4.6. Snow drift development over time for $u_* = 0.50 \text{ m}\cdot\text{s}^{-1}$, (a) $t=40$ s, (b) $t=80$ s, (c) $t=120$ s, (d) $t=160$ s, (e) $t=200$ s

(a)



(b)

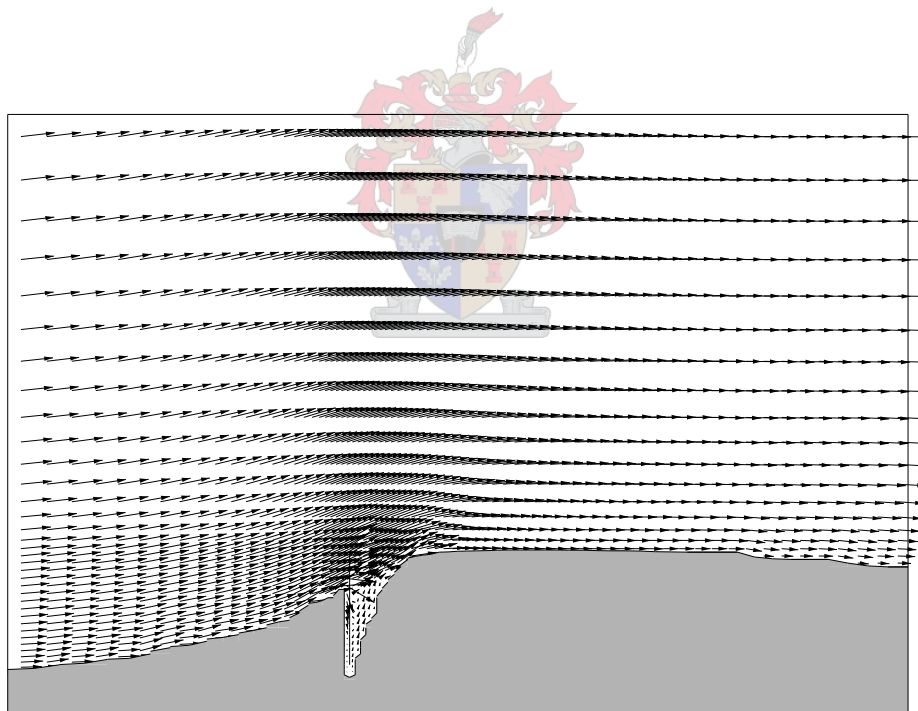


Figure 4.7. Velocity vectors in the vicinity of the two-dimensional snow fence before snow drifting starts (a) and at the end of the simulation (b) for an upstream shear velocity of $0.35 \text{ m}\cdot\text{s}^{-1}$

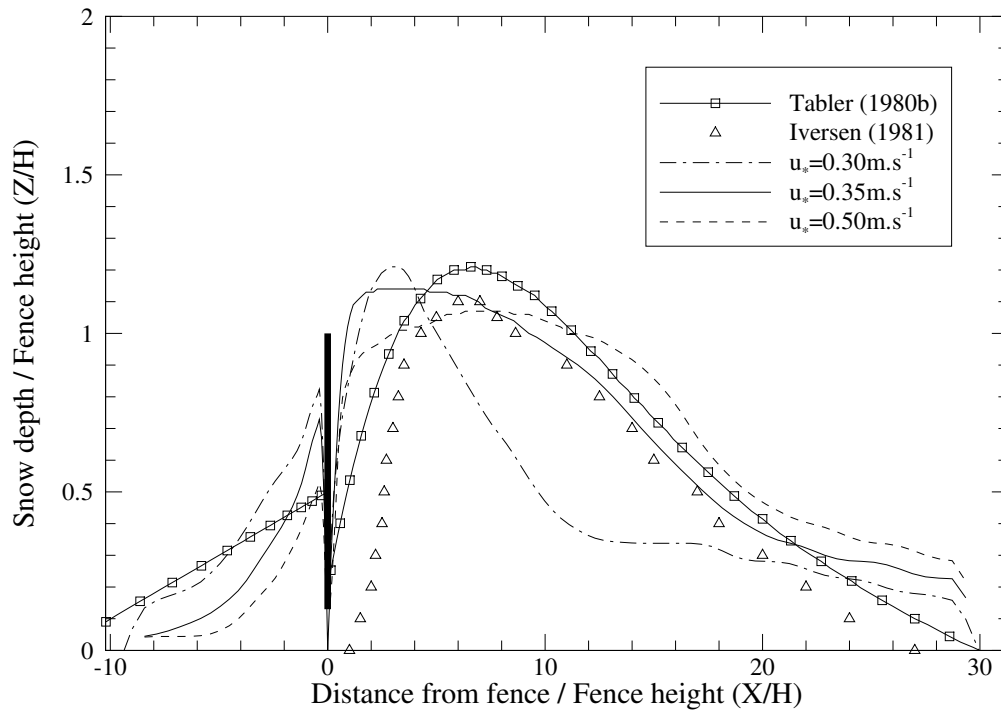


Figure 4.8. Snow drift profile development from simulated results for $u_* = 0.30 \text{ m}\cdot\text{s}^{-1}$, $u_* = 0.35 \text{ m}\cdot\text{s}^{-1}$ and $u_* = 0.50 \text{ m}\cdot\text{s}^{-1}$ compared to the empirical profile of Tabler (1980b) and Iversen (1981)

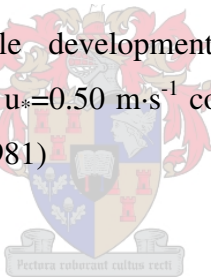


Table 4.2. Simulated snow drift around a 50% porous fence: characteristic dimensions

	Test 1	Test 2	Test 3	Tabler (1980a)
Approach shear velocity (u_*)	$0.30\text{m}\cdot\text{s}^{-1}$	$0.35\text{m}\cdot\text{s}^{-1}$	$0.50\text{m}\cdot\text{s}^{-1}$	
Leeward drift length L	30.0H	30.0H	32.0H	29.5H
Windward drift length l	12.0H	9.0H	6.0H	12.0H
Maximum leeward depth Y_{\max}	1.2H	1.15H	1.05H	1.2H
Location of Y_{\max}	2.5H	4.0H	8.0H	6.7H
Maximum windward depth y_{\max}	0.8H	0.7H	0.5H	0.47H
Location of y_{\max}	0.8H	0.8H	0.8H	0.4H
Average tail slope (12H-22H)	0.6°	3.1°	3.4°	3.6°

4.4. THREE-DIMENSIONAL NUMERICAL MODEL OF SNOW DRIFT AROUND A 50% POROUS FENCE

The same model parameters as employed in the two-dimensional simulations are used in the following simulation where the drift formation around a three dimensional snow fence is evaluated. A fence of the same dimensions used previously is employed but with a finite width of 10 m. The computational domain employed for this simulation is shown in figure 4.9.

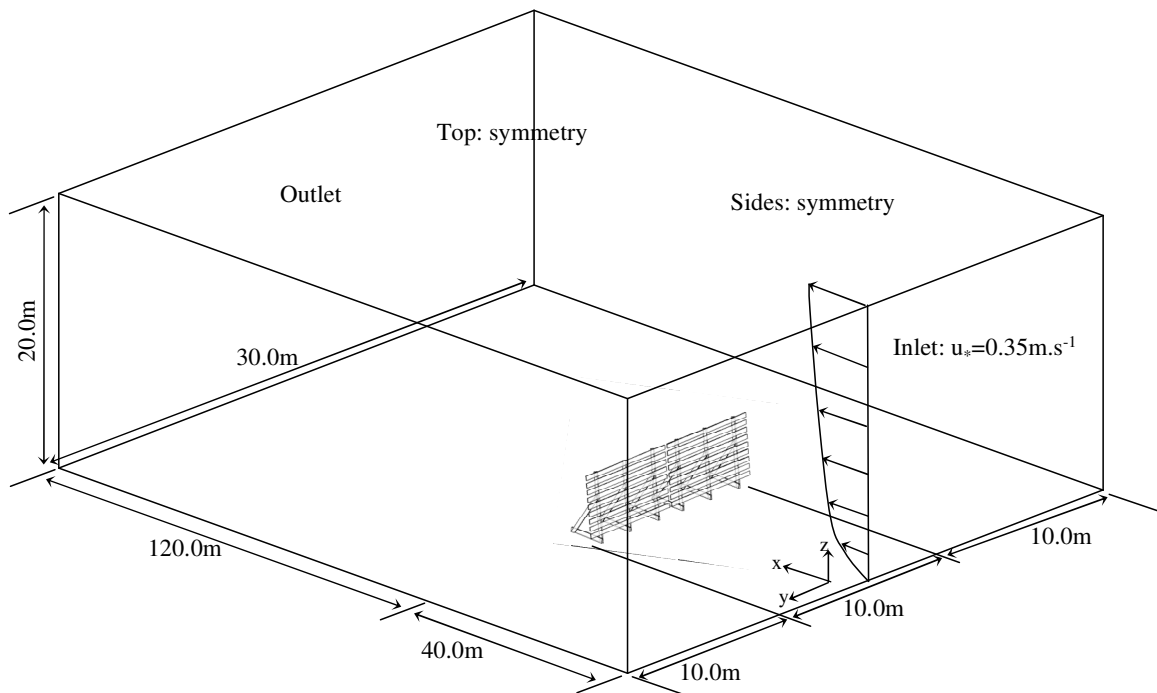
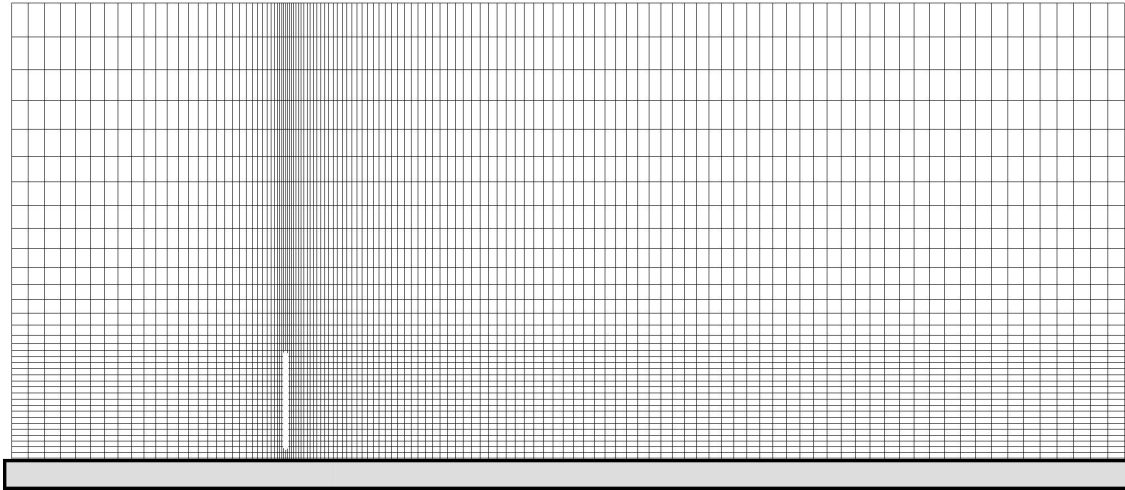


Figure 4.9. Computational domain for the three-dimensional simulation of snow drift around a 50% porous fence - fence details for illustrative purposes only

A three-dimensional mesh consisting of 121 x 51 x 41 cells was used with local refinement in the region of the 10 m porous fence as shown in figure 4.9 and 4.10.

The same solution parameters are employed as given in table 4.2 for the two-dimensional simulation. One inlet wind friction velocity of $u_* = 0.35 \text{ m}\cdot\text{s}^{-1}$, similar to the second test case given above, was simulated.

(a)



(b)

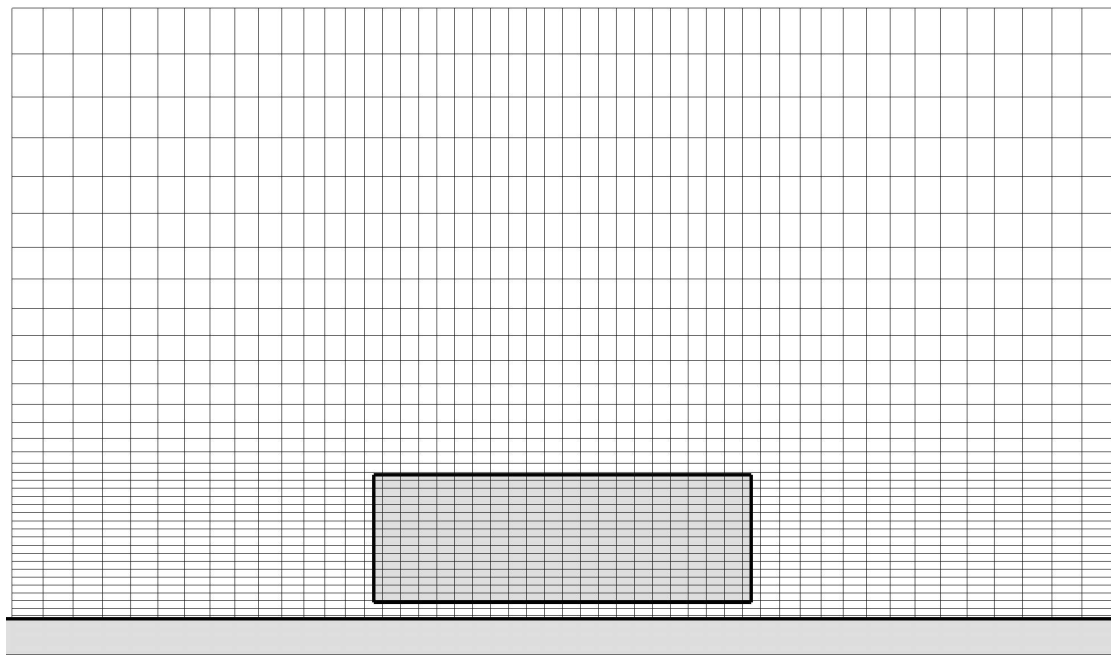
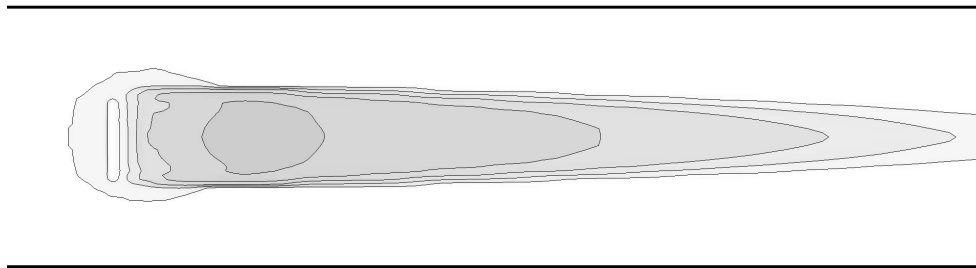


Figure 4.10. Computational mesh details in the xz -plane (a) and the yz -plane (b) for the three-dimensional simulation around a 50% porous fence - position of the porous baffle for illustration only

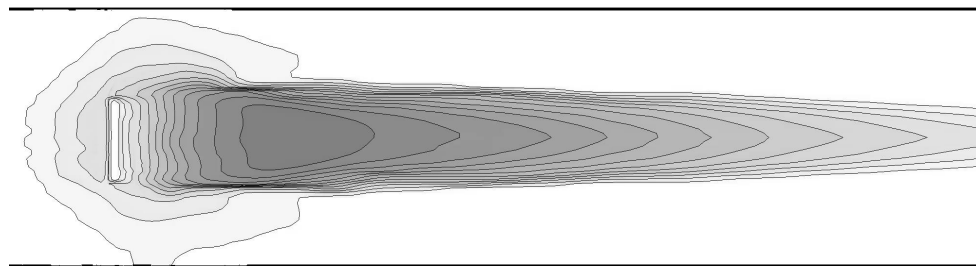
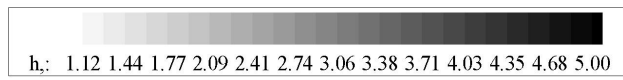
Figure 4.11 shows the height contours of the developing snow drift profile at three stages during the simulation namely, just after initiation of snow drift, during the simulation and at the end of the simulation. Figure 4.12 shows the three-dimensional profile of the snow drift at the end of the simulation.

The three dimensional prediction of the snow drift around the fence compares favourably with the two-dimensional results as well as the empirical results given by Tabler (1980b) and Iversen (1981), as shown in figure 4.13. The leeward drift profile is somewhat shorter and steeper than that predicted by the two-dimensional model. This is in better agreement with the measured profiles of Tabler (1980b). The windward drift is again small compared to the measured profile and may be influenced strongly by the upstream level of turbulence which affects the vertical turbulent diffusion i.e. more snow upstream of the fence is predicted to be entrained for the simulated scenario than was the case for the measured scenario. Wind tunnel snow fence models by Iversen (1981) however show a much less significant windward drift. The leeward drift shows a rather steep lateral edge to the drift near the fence where the high velocity wind sweep around the fence. It is believed that a smoother deposition pattern may have been predicted with additional mesh refinement at the vertical edges of the fence. The two-dimensional and the three-dimensional results indicate that the snow drift Model II predicts realistic drifts.

(a)



(b)



(c)

Pectora roborant cultus recti

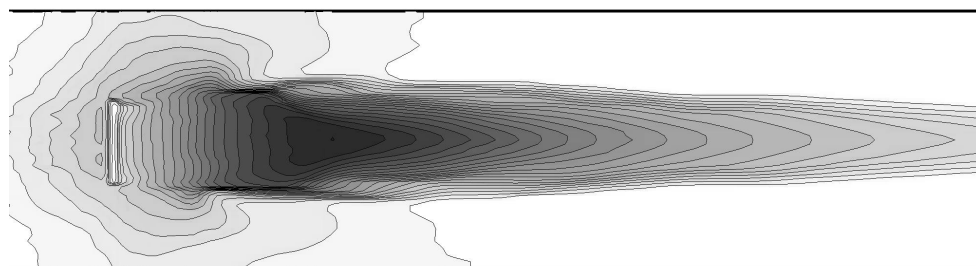
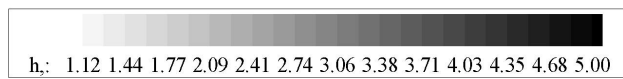
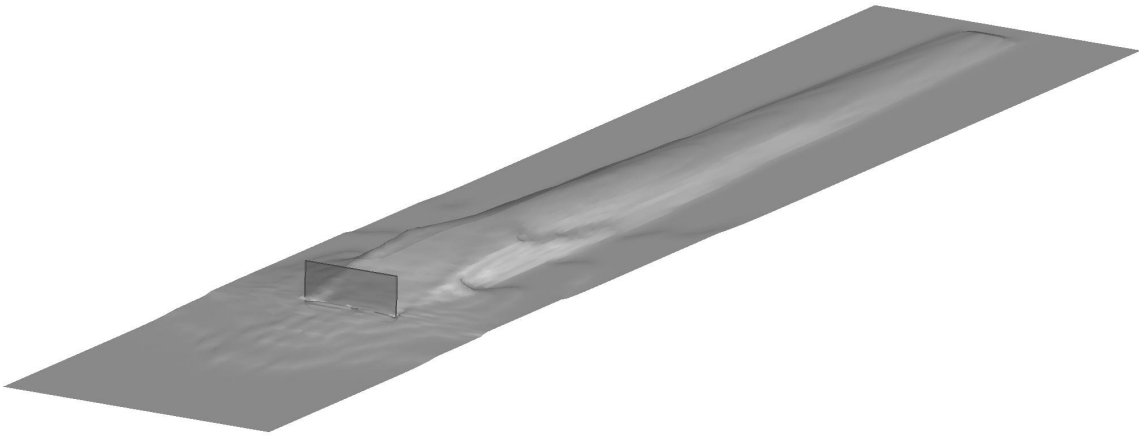


Figure 4.11. Height contours of the snow drift development at the (a) start of the drift, (b) at an intermediate stage during the simulation and (c) at the end of the simulation

(a)



(b)

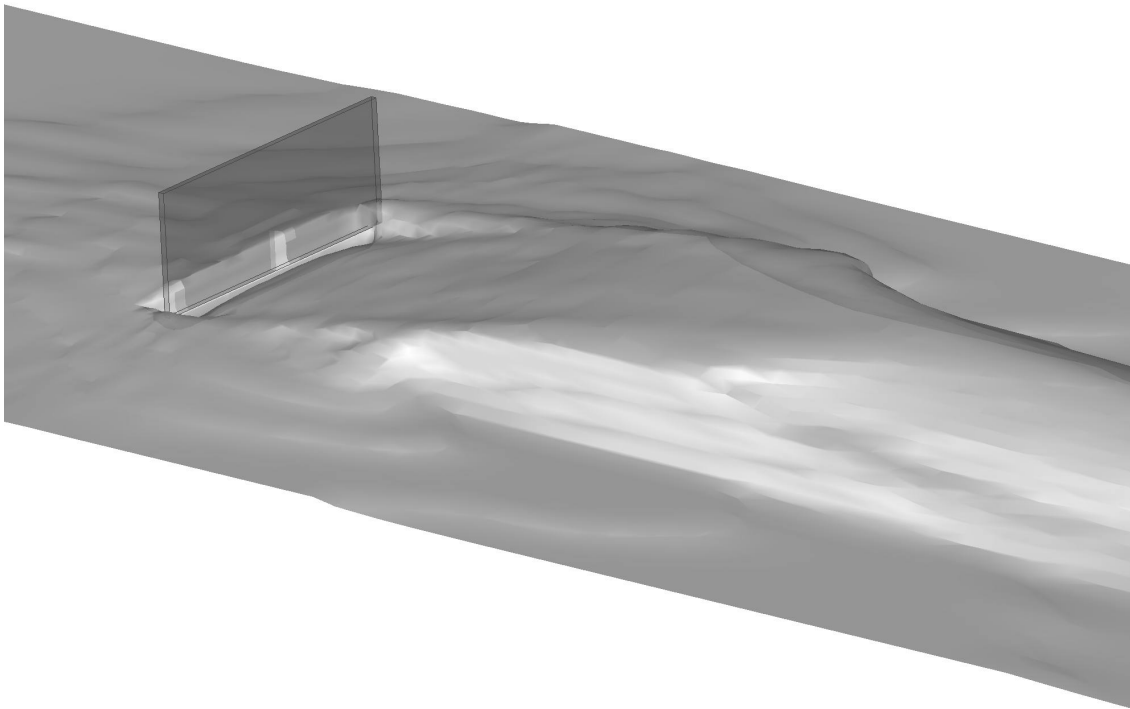


Figure 4.12. Two views of the three-dimensional profile of the snow drift surrounding a 50% porous fence with inlet wind friction velocity $u_* = 0.35 \text{ m} \cdot \text{s}^{-1}$

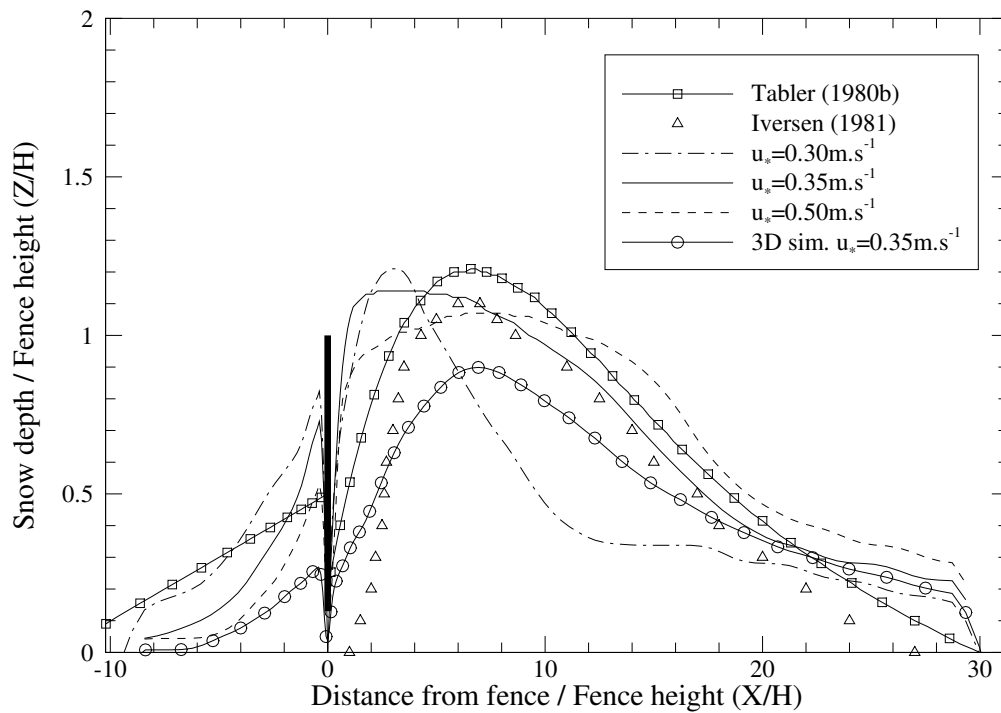
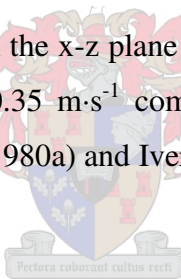
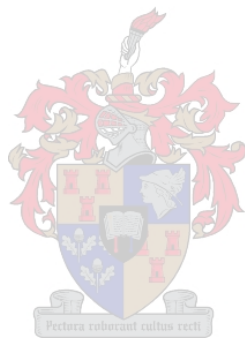
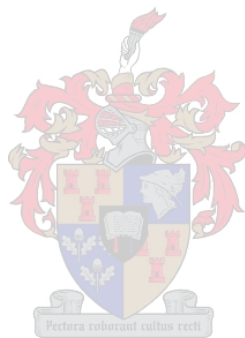


Figure 4.13. Snow drift profile in the x-z plane at $y=0.0$ m predicted by the three-dimensional simulation for $u_* = 0.35 \text{ m}\cdot\text{s}^{-1}$ compared to two-dimensional results and measurements from Tabler (1980a) and Iversen (1981)







5. FURTHER SNOW DRIFT VALIDATION

5.1. INTRODUCTION

An additional snow drift simulation is carried out for a slightly more complicated geometry for which large-scale experimental snow drift results are available. This test also allows the evaluation of the performance of the conservation based model to predict snow drifts under high flow conditions or in other words in regions dominated by high shear velocities.

5.2. SIMULATION OF SNOW DRIFT AROUND TWO ADJACENT CUBICAL BUILDINGS

5.2.1. Experimental results

A snow drift field experiment was carried out and reported by Thiis (2000), (2003) on the arctic island Spitzbergen of Norway. Two adjacent 2.5 m cubical buildings were evaluated, among other structures, for snow drifting during the winter of 1998-1999. The two cubical buildings were spaced 5.9 m apart. During the tests the approach wind angle varied between 10° and 15° off a direction normal to the front cube faces. Two wind events were recorded that resulted in snow drifting around the structures. The first was a moderate 10 m wind condition of approximately 10 m·s⁻¹ lasting for 3 days and the second a few days later, a stronger event of 15 m·s⁻¹ lasting for 2 days, Thiis (2003). The snow drift after both events were surveyed and the contour map of the snow drift development after the second event is shown in figure 5.1. It can be seen that two windward drifts are formed that meet in between the two cubes. The snow that passes between the cubes forms a large drift downwind between the cubes with its highest point approximately 2.5H downstream. The direction of the leeward tails of the drift is also slightly curved to follow the approaching wind direction. Two drifts are also formed at the outer leeward regions of both cubes. Very little deposition occurred in the near vicinity of the edges of the buildings.

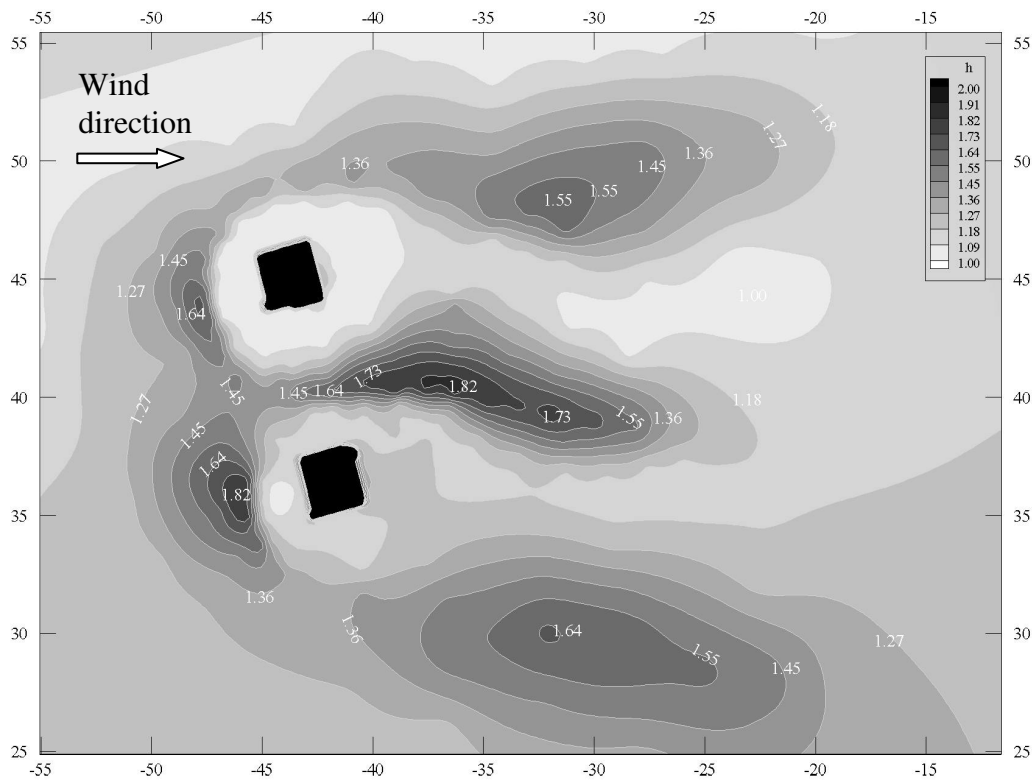


Figure 5.1. Contour map of snow drift development around two cubicle structures - contour data courtesy of Thiis (2003)

5.2.2. Simulation parameters

For this simulation a constant average wind condition corresponding to a shear velocity of $0.40 \text{ m}\cdot\text{s}^{-1}$ was selected with a saltation roughness parameter of 0.12. These values give approximately the same 10 meter wind speed as given in Thiis (2003) for the second wind condition of $15 \text{ m}\cdot\text{s}^{-1}$. The buildings simulated were orientated at an angle of 15° to the approaching wind direction similar to the measured wind condition. The computational domain is shown in figure 5.2. A computational mesh of $101 \times 91 \times 41$ cells was employed with local grid refinement in the vicinity of the buildings. This is shown in figure 5.3. Additional simulation parameters employed for this analysis are given in table 5.1.

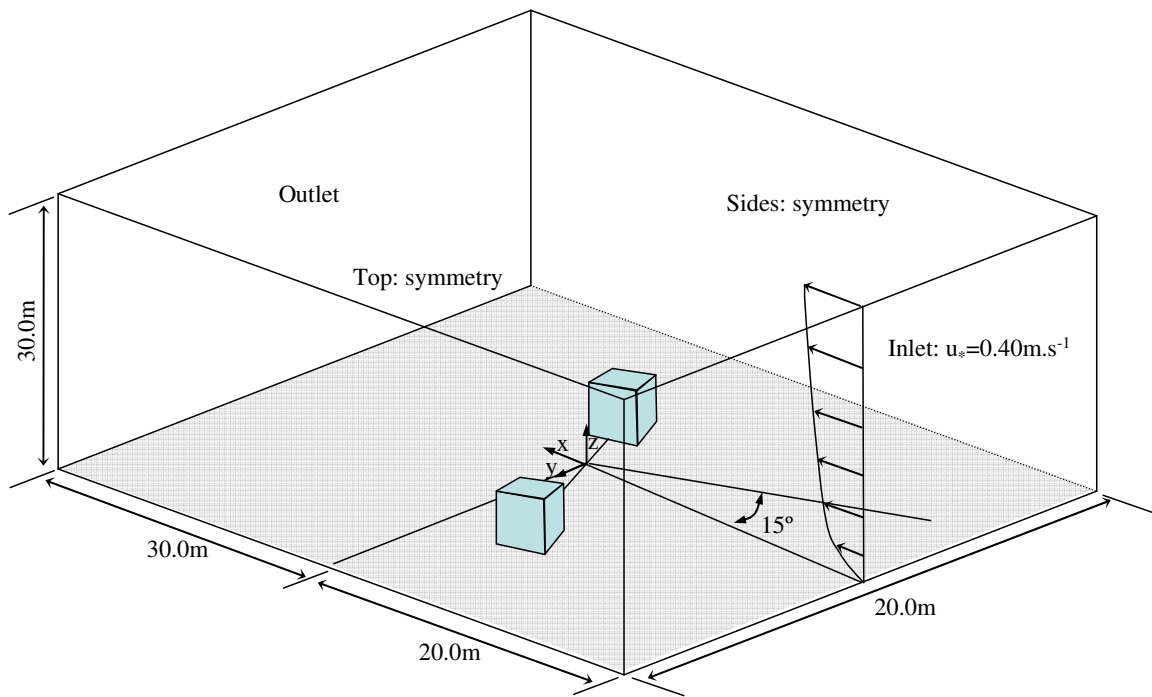


Figure 5.2. Computational domain for the three-dimensional simulation of the snow drift around two adjacent cubical buildings

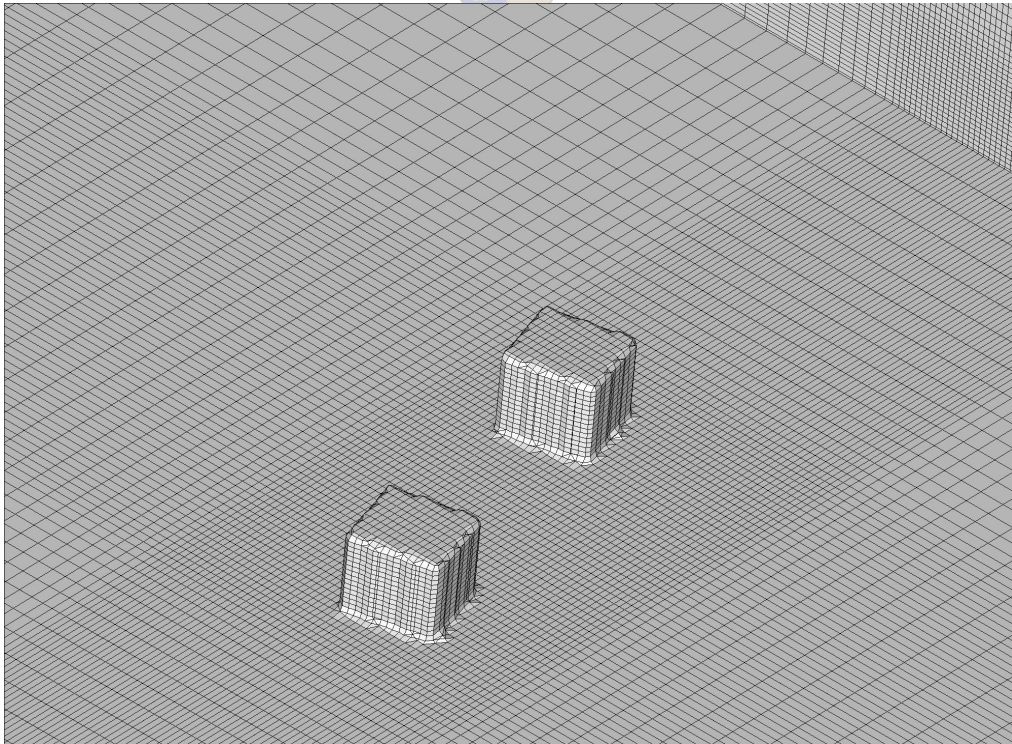
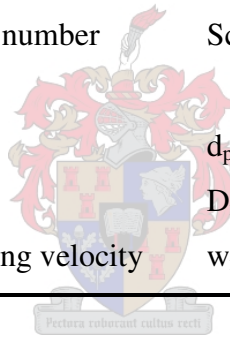


Figure 5.3. Computational mesh for simulation of the two adjacent cubes

Table 5.1. Parameters for the simulation around two adjacent cubes

		Test 1
Total simulation time	T	200 s
Drift initiation time	T_{acc}	20s
Inlet shear velocity	u^*	0.35
Flow approach angle		15°
Saltation roughness parameter	C_1	0.12
Surface roughness parameter	k	0.0001
Turbulent entrainment factor	α_1	0.7
Drift relaxation factor	α_{22}	0.5
Snow accumulation multiplier	α_{acc}	100.0
Interpolation scheme		2 nd order
Turbulent Schmidt number	Sc	1.0
Snow drift model		II
Mean particle size	d_p	110 μm
Drift coefficient	D_f	20.0
Snow particle settling velocity	w_f	0.45 $\text{m}\cdot\text{s}^{-1}$



5.2.3. Results and discussion

The near surface flow pathlines taken before the initiation of the drift routine are shown in figure 5.4. As shown in this figure, the flow approaching the cubes impinges on the windward cube faces and develops a recirculation horseshoe vortex system, point B, which travels around and accelerates between the two cubes, point A. Since the flow approached at an oblique angle to the cube windward face, the leeward arch vortex has shifted from behind the cube, as seen for the single cube results earlier, to the edge of the one outer windward corner of the cube and joined the lateral recirculation region of the other windward corner, position D. The leeward flow reattachment region is located at approximately 2H downstream, point E.

Figure 5.5 shows the near surface shear velocity contours before the initiation of any snow drift. High flow acceleration is present with high shear velocities predicted around the windward corners of both the cubes. A low shear velocity zone is simulated near the windward face of the cubes which corresponds to the recirculation region associated with the windward separation of the horseshoe vortex system. The flow is also accelerated as it passes between the cubes. The snow fraction ratio, the snow concentration divided by the upstream concentration at the same height, near the surface is given in figure 5.6 and indicates that the snow is concentrated in the channel between the cubes by the recirculation horseshoe vortex travelling around the cubes.

The erosion and deposition snow flux at the surface is shown in figure 5.7. This indicates that regions of possible snow deposition are windward of both cubes and leeward and between both cubes. Very little deposition will form leeward and against each cube wall. The resultant snow drift development during various stages of the simulation is shown in figure 5.8 and the three-dimensional drift prediction at the end of the simulation is shown in figure 5.9. This clearly shows the pronounced windward accumulation at both cubes similar to that predicted for a single cube. Between the two cubes another significant snow drift is formed while at the outer regions leeward of both cubes a very small drift is predicted. The drift predicted here is compared with the drifts observed by Thiis (2003), as shown in figure 5.1. The results of the comparison are summarised in table 5.2. The drift compares favourably with all the drift regions observed except for two discrepancies. Firstly, the observed windward drifts are slightly further upwind ($1.0H$ compared to $0.5H$) and the simulation did not predict significant drifts in the outer leeward regions as observed. It is believed that these discrepancies are caused by an inaccurate upwind boundary layer representation during the simulation and therefore a smaller horseshoe vortex system is being generated. Thus the windward drifts are formed much closer to the cube. In addition a less pronounced recirculation system travels around the cubes with smaller flow divergence leading to less deposition in the outer leeward regions. The predicted snow drift generally compares well with the observed drifts, both in location, magnitude and predominant direction. Both the observed and the simulated leeward drifts that formed between the cubes were deposited along the predominant wind direction with a slightly curved downwind tail. Thus the simulated drift also captured this observed phenomenon.

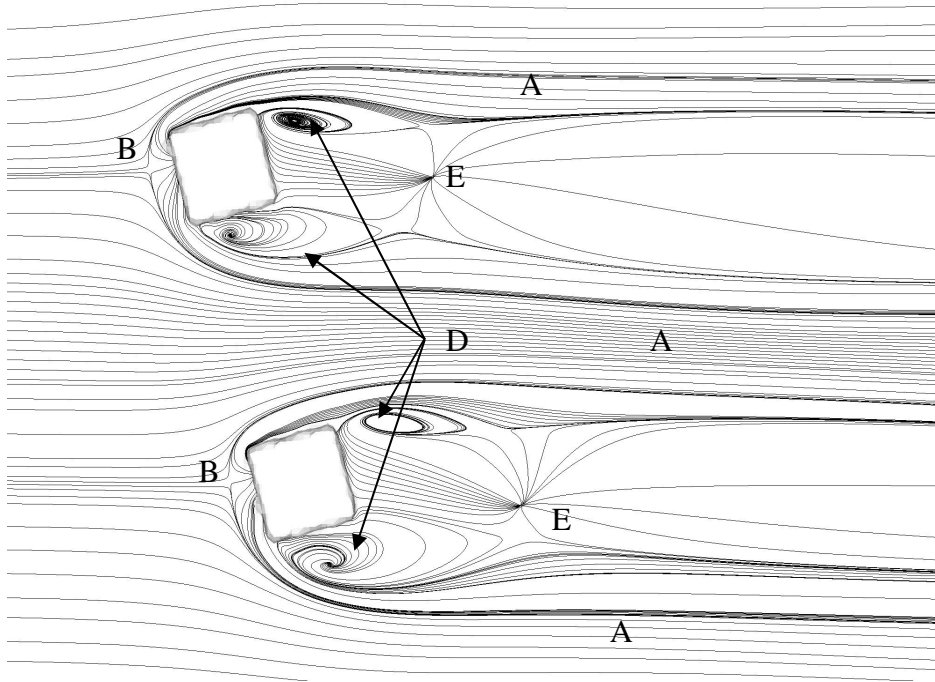


Figure 5.4. Streamline plot around the two adjacent cubes

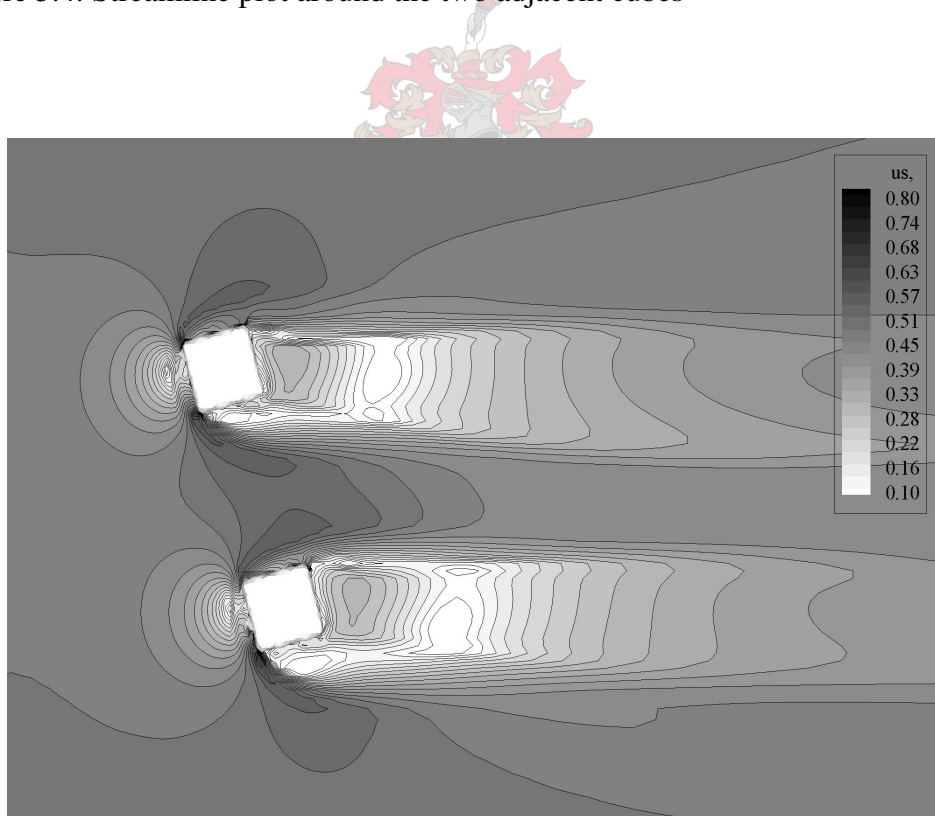


Figure 5.5. Shear velocity contour plot for two adjacent cubes after $T=20$ seconds

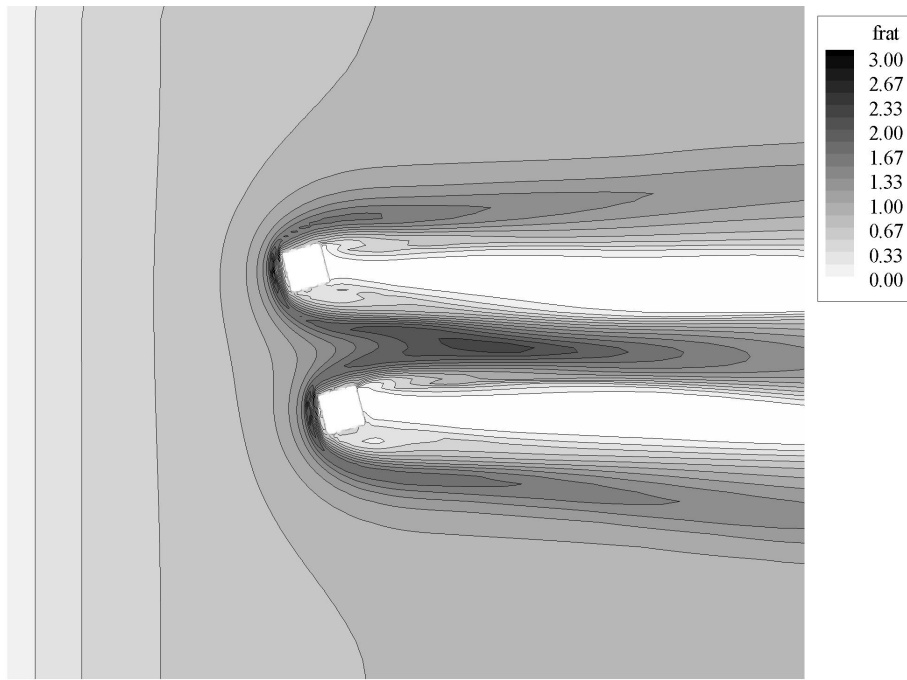


Figure 5.6. Near surface snow fraction contour plot around two adjacent cubes after T=20 s simulation

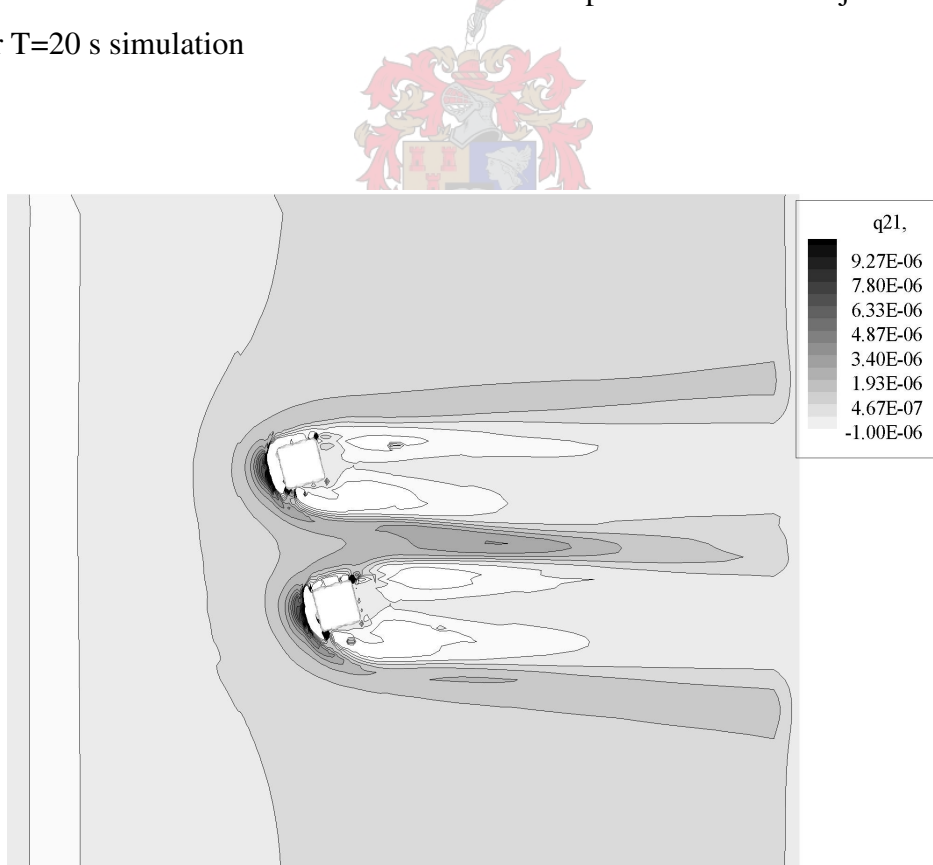


Figure 5.7. Snow deposition / erosion flux from surface for two adjacent cubes at T=20 s

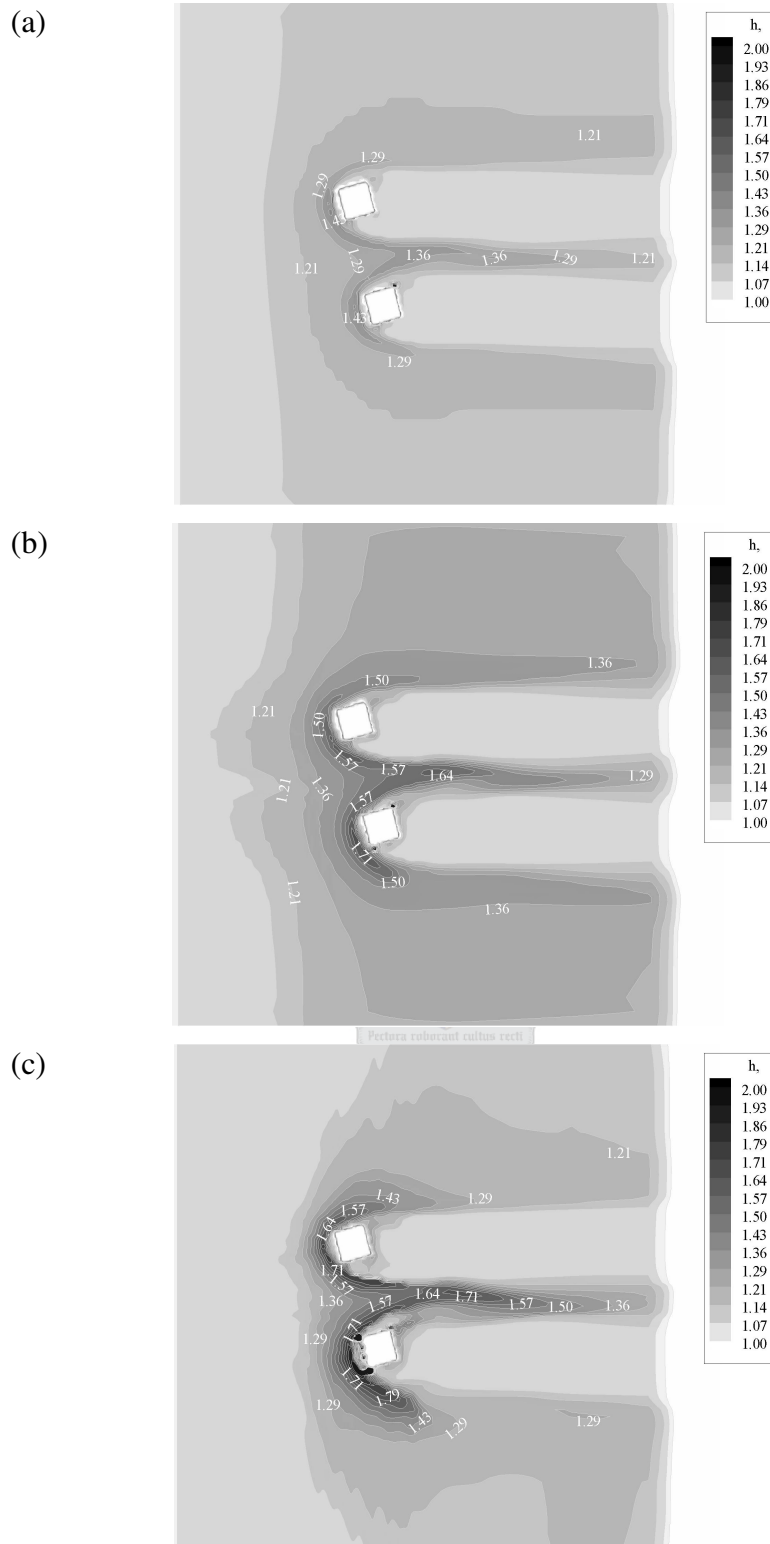


Figure 5.8(a)-(c). Snow drift height contour for two cubes at $t=30$ s, $t=45$ s and $t=60$ s

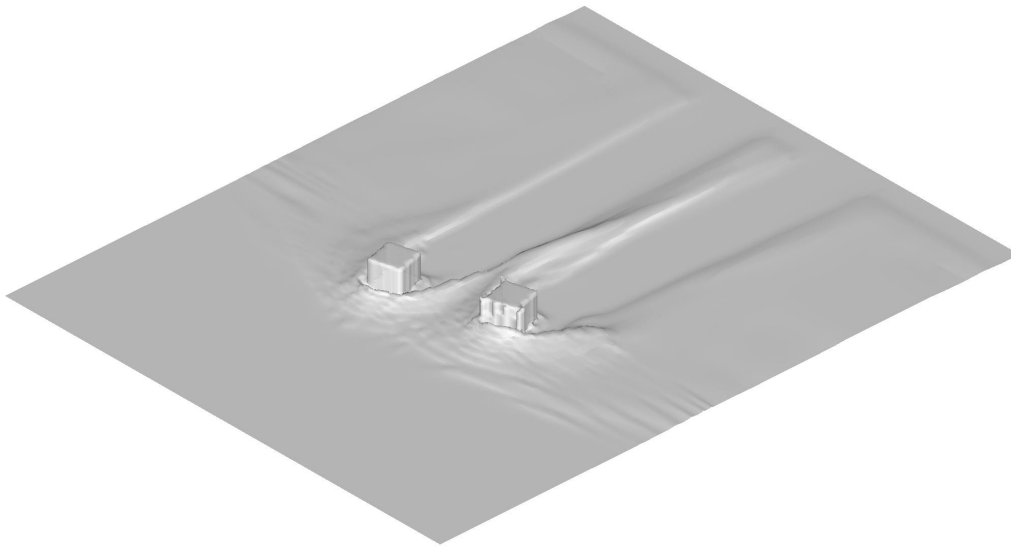
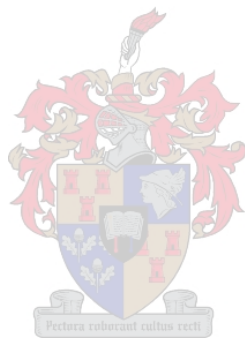


Figure 5.9. Three-dimensional snow drift development around two adjacent cubes at the end of the simulation

Table 5.2. Snow accumulation heights comparison between predicted and observed values for two adjacent cubes

	Model II	Observed
Snow accumulation maximum height:		
Windward accumulation, top cube	0.71	0.64
Windward accumulation, bottom cube	0.71	0.82
Leeward accumulation, both cubes	0.0	0.09
Leeward accumulation between cubes	0.71	0.82
Lateral accumulation, top cube	0.29-0.21	0.55-0.36
Lateral accumulation, bottom cube	0.29-0.43	0.64-0.36
Leeward location of maximum drift between cubes	3.0H	2.0H
Windward location of maximum windward drift	0.5H	1.0H



6. MODELLING SNOW DRIFT AROUND SANAE IV

6.1. INTRODUCTION TO THE PROBLEM

Some general aspects of the snow drifting phenomena surrounding SANAE IV were discussed in chapter 1. In this section a more detailed review of the problem at hand will be given with the results of the numerical simulation. As discussed in chapter 1 and shown in figure 1.3, SANAE IV is located in Dronning Maud Land in Antarctica just off the Fimbul ice-shelf on $71^{\circ}40'$ S, $2^{\circ}49'$ W. It is build on top of a rocky outcrop or nunatak called Vesleskarvet.

The station consists of three rectangular main buildings of similar shape joined by interconnecting links of smaller cross section. The profiles of the base and interconnecting links are rounded. The longitudinal axis of this streamlined station is aligned approximately 10° east of north and is supported on an array of steel columns approximately four meters above ground. The purpose of this aerodynamic shape and elevated design of the base is to decrease the form drag of the building during winds to lower the forces on the supporting columns, as well as to minimise the wind driven snow accumulation in the vicinity of the station and thereby reducing the snow removal maintenance and its environmental impact. Figure 6.1 shows a panoramic view of the SANAE IV station, including the main buildings and the interconnecting structure. Figure 6.2 shows the aerial view and general profile of the base and its position on the nunatak.

The station is exposed to severe meteorological conditions with gale force winds and accompanying blowing snow. Very specific and localised snow accumulation patterns are observed around the base after strong wind conditions. These winds approach the station from a predominantly north eastern to south eastern direction and causes snowdrifts leeward of the interconnecting links of approximately 60 m long, 3 m high and in a direction along the prevailing wind direction, as indicated in figure 6.2 and pictured in figure 6.1.



Figure 6.1. Panoramic view of SANAE IV viewed from the edge of the southern buttress of Vesleskarvet towards the north-east.

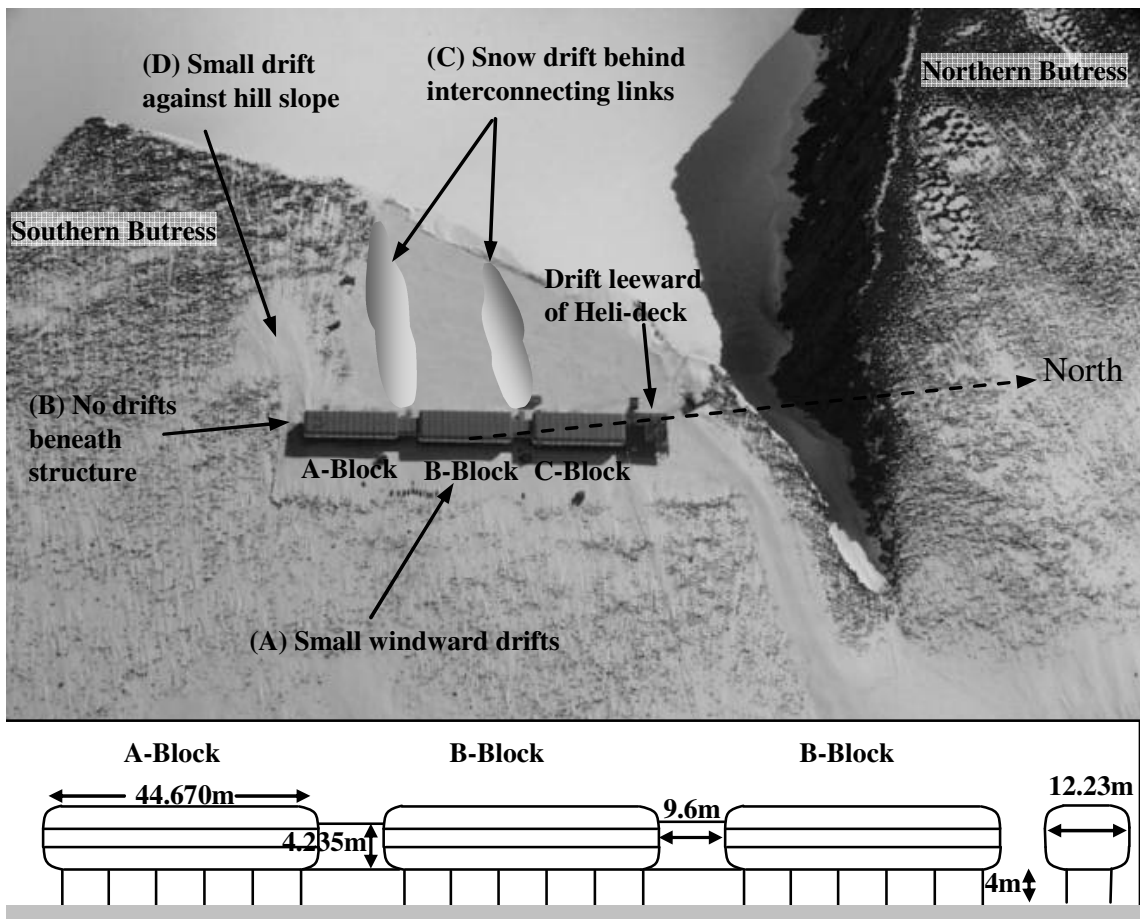


Figure 6.2. SANAE IV layout on Vesleskarvet, Antarctica showing regions of localised snow drift

6.2. OUTDOORS SNOW DRIFT EXPERIMENTAL MODEL

Some of the more recent investigations into snow drifts surrounding buildings as well as Antarctic research stations are mentioned below. Kim et al. (1991) and Kwok et al. (1992) carried out wind tunnel experiments to evaluate snow drifting around a model of Syowa station (Japan) as well as elevated single and grouped on-ground and above-ground facilities. Their results indicated that leeward snow accumulation mostly disappeared for a building height to height from ground ratio of larger than 0.5. Their work also presented some notable leeward riming formations. Smedley et al. (1993) investigated the effects of wind deflectors on the snow drift around a workshop at Davis station, Antarctica. Their work indicated that a rounded deflector increased the overall snow drift volume but effectively removed the drift away from the leeward wall. Angular deflectors proved ineffective. Delpech et al. (1998) carried out wind tunnel tests at the CSTB Jules Verne (France) snow wind tunnel to study the possible snow accumulation characteristics surrounding the new Concordia station in Antarctica. Their work proposed and tested the effects of wind deflection panels to channel the flow between and underneath the station main buildings. The snow drift tests indicate that the deflection panels may be a suitable mechanism to minimise the snow drifts. Sundsbø (1998) carried out numerical simulations to test the effect of wind deflection fins on the leeward side of a two-dimensional rectangular building. The numerical results indicated that the deflector placed at the top edge of the building could increase the velocity field near the leeward bottom corner of the building and subsequently reduce the snow drift at this location. The resultant snow drift was also moved further downstream from the building.

The main areas of snow deposition surrounding the SANAE IV station are highlighted in figure 6.2. In the context of the following discussion the windward side is considered east since the predominant winds, as well as winds that transport snow particles up towards the base, range from north-easterly to south-easterly. Firstly, small windward drifts form along the length of the base (A) and generally follow the outline of the building i.e. the drifts extended downwind in the link areas. These drifts are approximately less than one meter above ground and assumed stable since these have never been removed since the completion of the new station. No significant snow drifts form anywhere directly underneath the station structure (B) as snow is constantly eroded from the exposed sharp edged rocks by the accelerated wind stream. On the leeward side of the base different deposition areas are found.

The most important and also the drifts studied in this work are those formed directly behind each of the two interconnecting structures (C1 and C2). These are approximately 15 m wide, 4 m high and 60 m in length with its highest point 20 m leeward of the link and level with the underside of the main building. From observations during storms it was found that these longitudinal drifts are formed during short times (48 h) during heavy winds ($20 \text{ m}\cdot\text{s}^{-1}$) and that their longitudinal axis are aligned with the wind direction during formation, Beyers and Harms (2003a). These drifts are removed once a year during the austral summer. On the southern end of the base a smaller amount of snow drift is also found that seems stable and covers the leeward mountain slope (D). On the northern end of the station and leeward of the helicopter deck another area of uniform snow deposition, approximately 0.5 m thick, is formed during strong wind conditions.

The aim of this work and the numerical simulations are to understand the important flow mechanisms causing the localised snow drift behind the interconnecting links (area C in figure 6.2), to replicate this drift formation by means of three-dimensional numerical flow simulations and to propose some mechanisms which may minimise the deposition of snow in these areas. These are the main drift areas that require yearly snow removal due to the large volume of the drift and the concern of them limiting the access into the station. Two of the three entrances into the station are positioned on the western side of these interconnecting link structures and accessed via a staircase from the ground. The other entrance is via the helicopter deck. During the research periods in the austral summer of 2001 and 2002 the following hypothesis was formulated as to test the cause of this local snow drift phenomena, Beyers and Harms (2000). Firstly, the approaching snow flux seemed constant along the length of the base and that the localised deposition did not originate from a non-uniform upwind snow concentration. Secondly, the topographical contours are not constant leeward of the base but did not seem to greatly influence the snow deposition since no significant deposition occurred behind the main buildings even though the terrain profile differs between the three main buildings. From visual and electronic media observation made during two severe wind conditions at the time of this investigation it was observed that snow exiting from underneath the main buildings is channeled towards the interconnecting link leeward zone. This was described as a 'snow river' and is also predicted in the numerical analysis presented hereafter.

It was also observed that during moderate winds the snow passes relatively undisturbed underneath the structure with small longitudinal drifts forming behind the supporting columns along the length of the base. These finger-like drifts did not continue to grow but were eventually destroyed as wind conditions progressively increased and shear erosion increased. As the wind conditions became stronger a localised drift started to form in the area leeward of the staircase behind both the link structures. The snow transported leeward of the link was also observed to be swirling even far downstream of the link. The formation of the drift behind the link structures was believed to be influenced by the three-dimensional flow disturbance trailing off the edges of the base structure where the main building joins the link section of narrower width. Thus a trailing vortex type flow is expected to be generated from the two leeward edges of the main buildings in this section. This vortex structure could then also explain the snow being channeled underneath the main buildings towards the link section.

In order to evaluate some of the possible mechanisms that cause the snow drifts, a scale model of a section of the base was built to carry out outdoors experimental snow drift studies in an area near SANAE IV. A description of the tests and its results can be found in Appendix G. The experimental similarity tests, as described in Appendix G, shed some light into three areas of concern namely, the influence of the staircases on the drift development, the influence of the mountain slope leeward of the station and the influence of the support columns. Firstly, the scale model tests showed that the longitudinal drifts could be duplicated under light wind conditions and the similarity theory results of the deposition times agreed reasonably with the actual observed drift developments times. The scale model did not include any staircase or the extensive support column network but still reproduced the drifts. Thus it is believed that neither the staircase nor the support columns are the cause of the start of deposition but may influence the drift development. This was supported by accounts from the South African Public Works Department (PWD) personnel responsible for maintenance at the base during the summer months who mentioned that the drifts formed at SANAE IV even when the staircases were removed. The area around the scale model was flat and was not shaped to conform to the area around SANAE IV. Very similar drifts formed behind the scale model which suggests that the windward and leeward mountain topography have very little influence on the initiation of the leeward drifts. The scale model tests also showed that drifts formed on the northern and southern leeward edges which may explain the presence of snow

drifts around the northern end of SANAE IV. The southern end of SANAE IV is the only area where the mountain slope rises somewhat steeply behind the station, possibly leading to the flow accelerating (or rather an area of slower deceleration as the flow exits beneath the structure) with subsequently less snow deposition. During most of the outdoor tests the scale model remained clear of snow although the snowdrifts behind the outer edges and the link eventually merged to gradually become one large mass of snow behind the base. This suggests that the drifts at SANAE IV may after prolonged periods of no maintenance, fill the entire area behind SANAE IV. Wind directions may also change and start drift behind the longitudinal drifts filling the areas adjacent to the drifts.

6.3. THREE-DIMENSIONAL NUMERICAL SIMULATION

6.3.1. The numerical model

One of the biggest concerns regarding the simulation of the snow drift surrounding a large scale structure such as SANAE IV is the grid resolution. The earlier simulation attempts with the three-dimensional cube indicated that sufficient grid resolution is necessary in order to capture important primary and secondary flow effects such as the presence and position of arch and horseshoe vortex systems. However, a similar grid resolution applied to the SANAE IV station model would require approximately 3 million cells. This would result in inappropriate simulation times with the present CPU capacity. Extensive simulation tests showed that a grid of 81 x 91x 41 cells are suitably fine to achieve a fair degree of grid independent results and also resolves some secondary flow phenomena such as the secondary swirl flow around the leeward edges of the station, discussed later in the text. The computational domain used in the simulation is shown in figure 6.3 and the computational mesh in figure 6.4. Two simulations were carried out with two different inlet velocities. The inlet velocities selected were $u_{10}=10 \text{ m}\cdot\text{s}^{-1}$ and $u_{10}=15 \text{ m}\cdot\text{s}^{-1}$. Inlet turbulent velocity profile is given by equation (2.146) and the turbulent characteristics by equations (2.150) and (2.151). The additional numerical simulation parameters are summarised in table 6.1.

Table 6.1. Simulation parameters for the three-dimensional SANAE IV simulation using Model II

		Test 1	Test 2
Total simulation time	T	200 s	200 s
Drift initiation time	T_{acc}	20 s	20 s
Inlet shear velocity	u_*	$0.35 \text{ m}\cdot\text{s}^{-1}$	$0.50 \text{ m}\cdot\text{s}^{-1}$
Flow approach angle		0°	0°
Saltation roughness parameter	C_1	0.0035	0.0035
Surface roughness parameter	k	0.0001	0.0001
Turbulent entrainment factor	α_1	0.7	0.7
Drift relaxation factor	α_{22}	0.5	0.5
Snow accumulation multiplier	α_{acc}	100.0	100.0
Interpolation scheme		2 nd order	2 nd order
Turbulent Schmidt number	Sc	1.0	1.0
Snow drift model		II	II
Mean particle size	d_p	$110 \mu\text{m}$	$110 \mu\text{m}$
Drift coefficient	D_f	20.0	20.0
Snow particle settling velocity	w_f	$0.45 \text{ m}\cdot\text{s}^{-1}$	$0.45 \text{ m}\cdot\text{s}^{-1}$

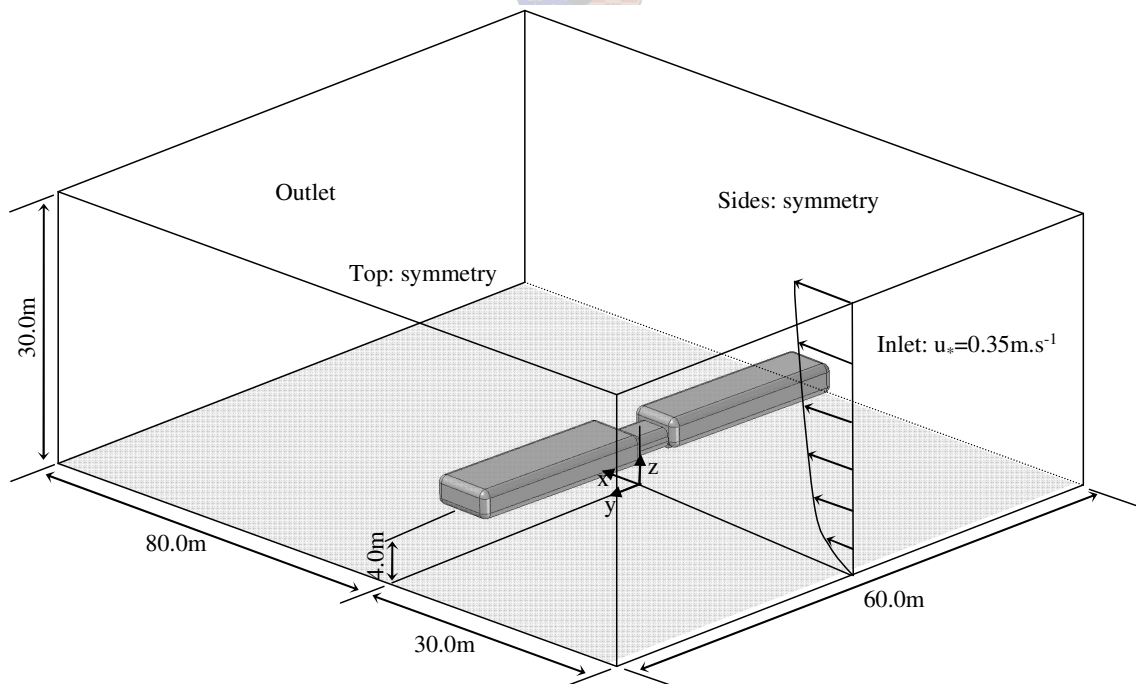


Figure 6.3. Computational domain for the three-dimensional flow simulation around SANAE IV.

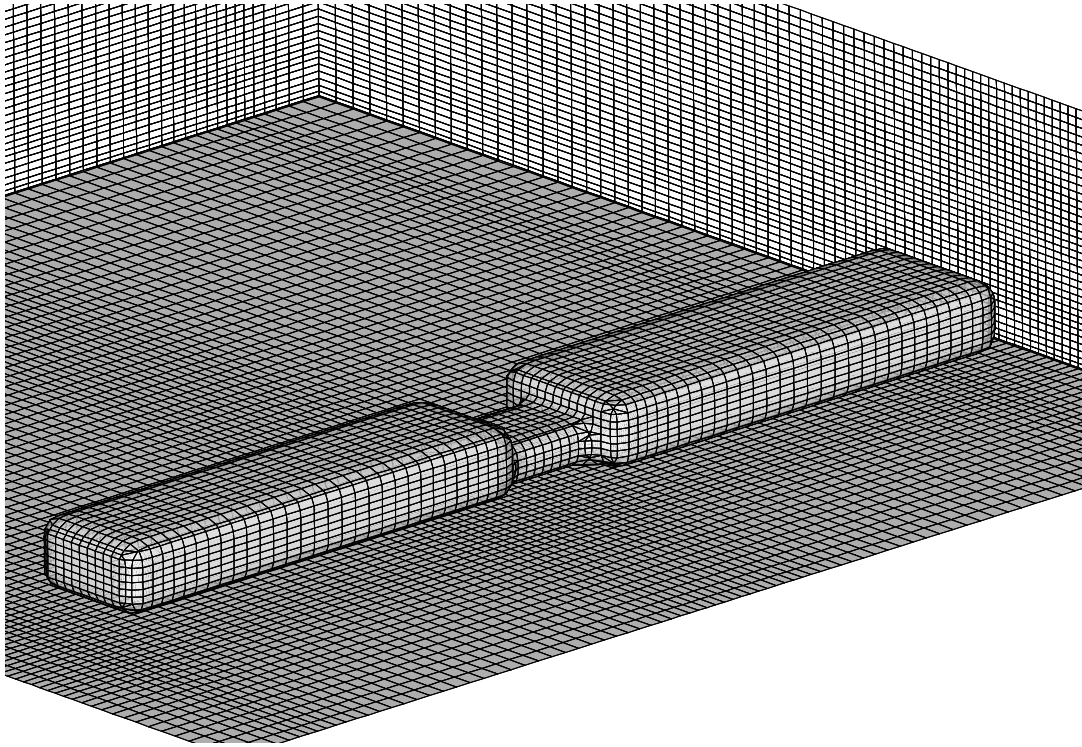


Figure 6.4. Mesh details for SANAE IV simulation

6.3.2. Simulation results and discussion

The simulation was run for 20.0 s simulation time to allow the upstream conditions to reach the outlet boundary condition before the drifts are allowed to develop. The u-velocity contour in the xz-plane at $y=0$ m and $y=20$ m and before the snow drift was initiated, are shown in figure 6.5 and 6.6 respectively. This shows the acceleration over and underneath the building structure. Figure 6.5 is taken in the plane through the middle of the main building and figure 6.6 through the plane in the middle of the link section. For both sections the flow decelerates relatively quickly as it exits underneath the structure. The flow that exits the main buildings shows a degree of vortex shedding which along with an increase in turbulence level leeward of the buildings will lead to better vertical mixing of the near surface snow. This study does not intend to investigate the details of the vortex shedding although its presence in the numerical results is not unexpected since vibrations were experienced during strong wind conditions at SANAE IV. The numerical prediction of the vortex shedding causes a fluctuation in the drift formation since the near surface velocity gradients are periodic. This is damped by the drift accumulation function which essentially balances the instantaneous drift flux to its mean drift flux. The results show interestingly that a different degree of vortex

shedding is present behind the main buildings but that it is not present leeward of the interconnecting link.

The surface friction velocity plots are shown in figure 6.7 and figure 6.8 for test 1 and test 2 respectively. This indicates that the flow leeward of the main buildings quickly returns to close to its upstream value while the flow leeward of the link building remains at a lower friction velocity than the upstream value. The reason for this could be attributed to a strong swirling flow caused by the transition in the base structure geometry at the connection between the link and the main section. Figure 6.9 and figure 6.10 indicate the near surface v -velocity plot for test 1 and test 2 respectively and indicates strong secondary flow influences near the surface and leeward of the edges of the main building. The location of this secondary flow structure is explained by means of figure 6.10. The higher approaching wind velocity for test 2 leads to higher acceleration beneath the structure as well as more enhanced secondary effects near the surface.

Figure 6.12 shows a streamline plot for test 1 around the region behind the leeward corner of the main building. The trailing vortices from both building edges are swirling in opposite direction as shown in the vector plot of figure 6.13(a)-(c). This swirling flow is present between the main buildings and also leeward of the outer edges of the main buildings. This is one of the reasons why the snow is transported towards the link from the main buildings as evident from the plot of the snow fraction.

The surface shear velocity, as per figures 6.7 and 6.8, shows that the flow accelerates as expected underneath the building with the highest shear velocity achieved beneath the interconnecting link. This may be due to the additional mass of air being channeled around the upstream edges of the main building into the narrower link section. Downstream along the length of the building the flow again decelerates but does not reach the upstream values within the downstream length. It is evident that no region exists where the flow decelerates significantly below the theoretical threshold condition for the cessation of saltation which means that the snow drift model based on threshold conditions, Model I, would not generate any substantial deposition pattern. However, since there is strong acceleration and deceleration upstream and downstream of the building one expects to find local regions of erosion and deposition.

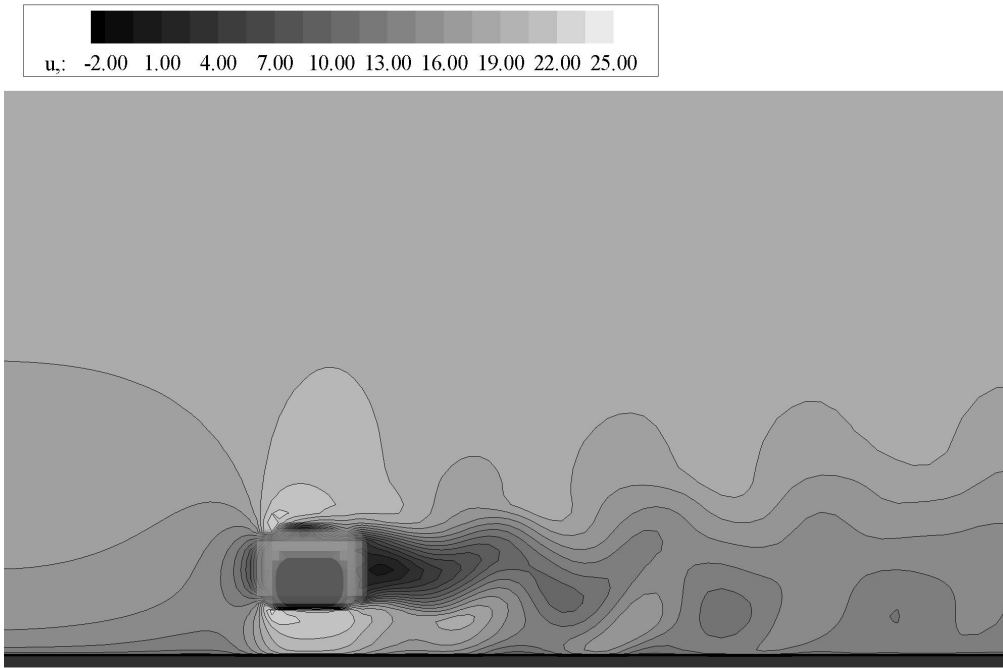


Figure 6.5. u-velocity contour plot, Test 1, at t=20 s at main building section

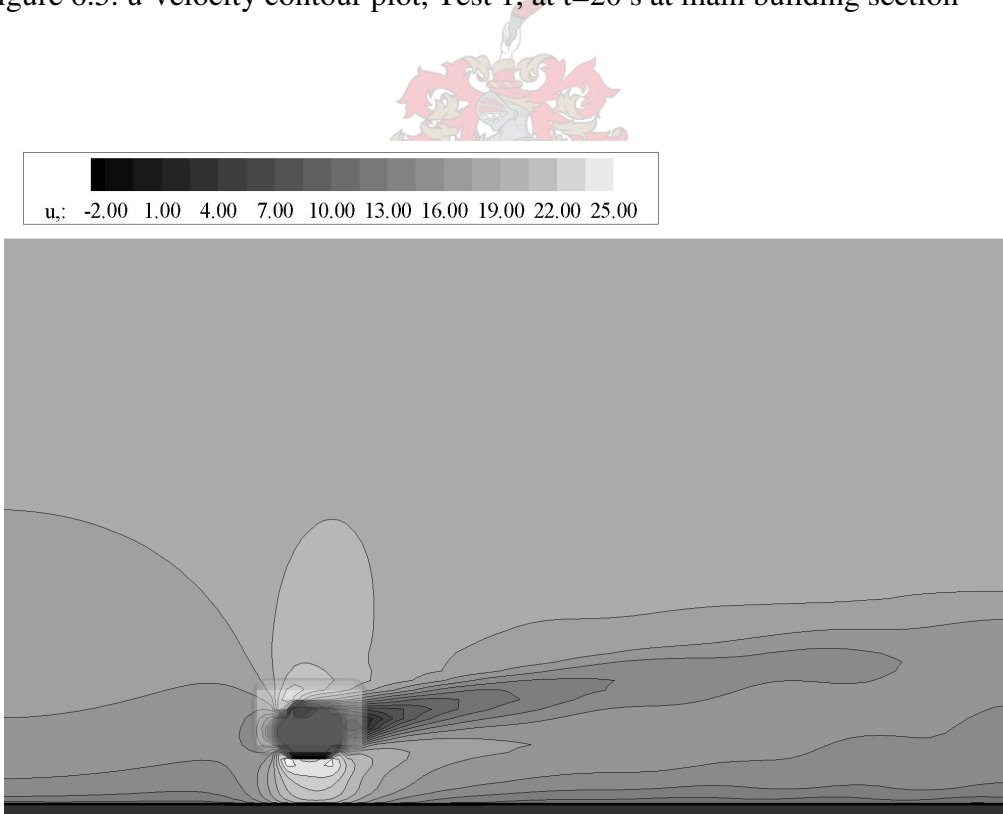


Figure 6.6. u-velocity contour plot, Test 1, at t=20 s at interconnecting link section

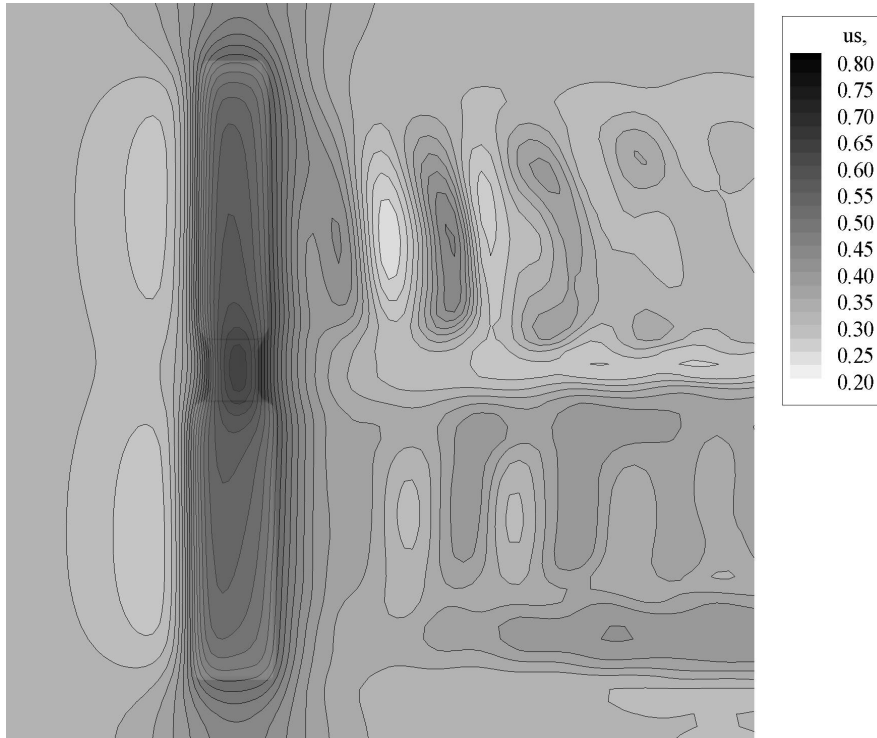


Figure 6.7. Shear velocity contour plot for test 1 after $t=20$ s

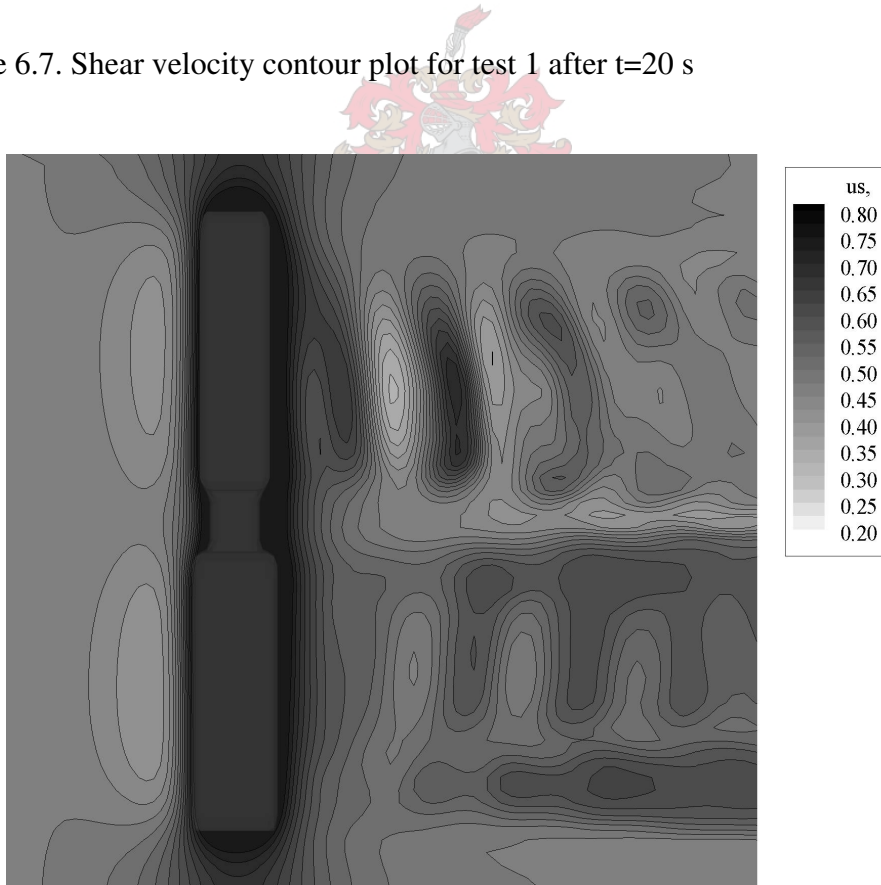


Figure 6.8. Shear velocity contour plot for test 2 after $t=20$ s

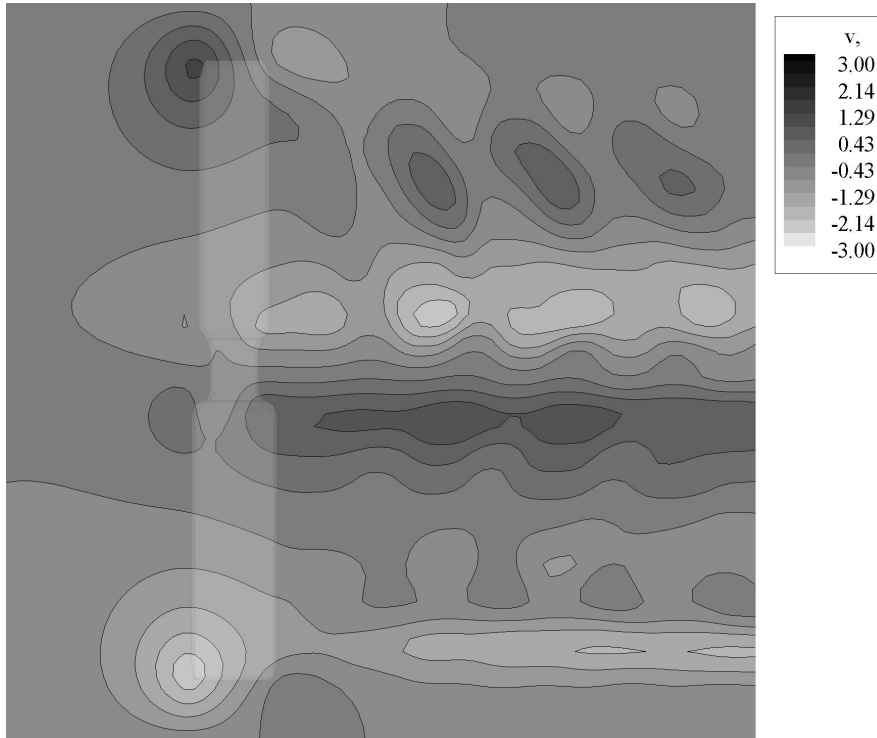


Figure 6.9. v-velocity contour at the first near surface control volume, test 1, $t=20$ s

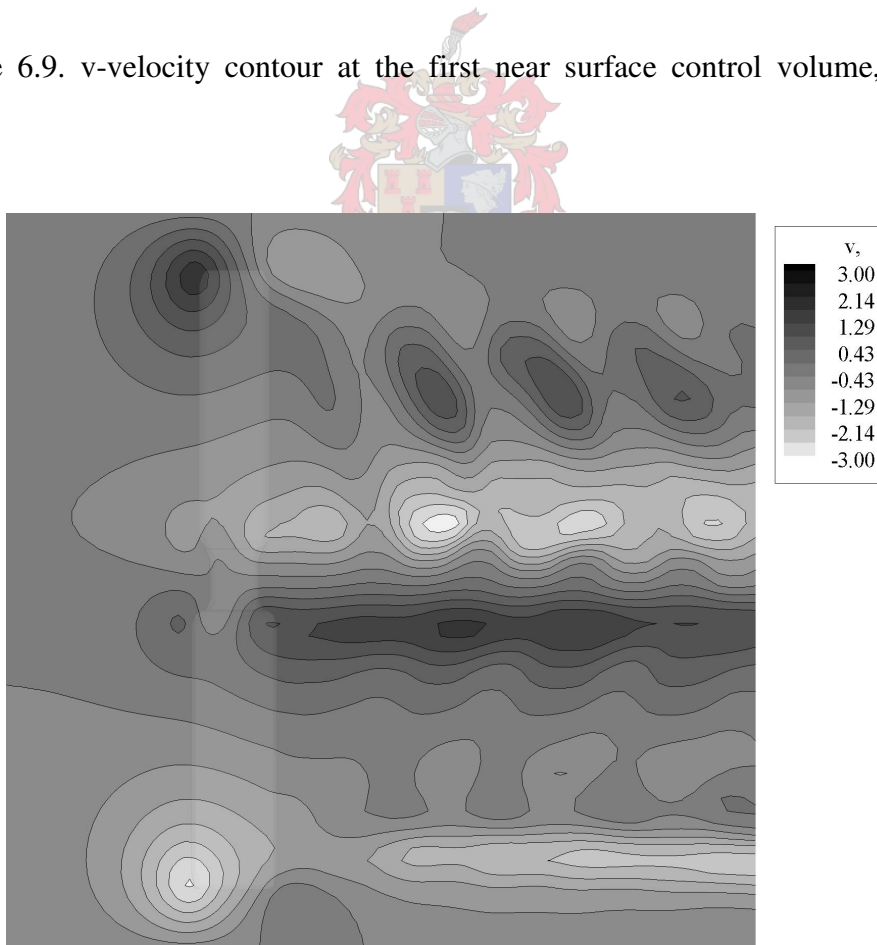


Figure 6.10. v-velocity contour at the first near surface control volume, test 2, $t=20$ s

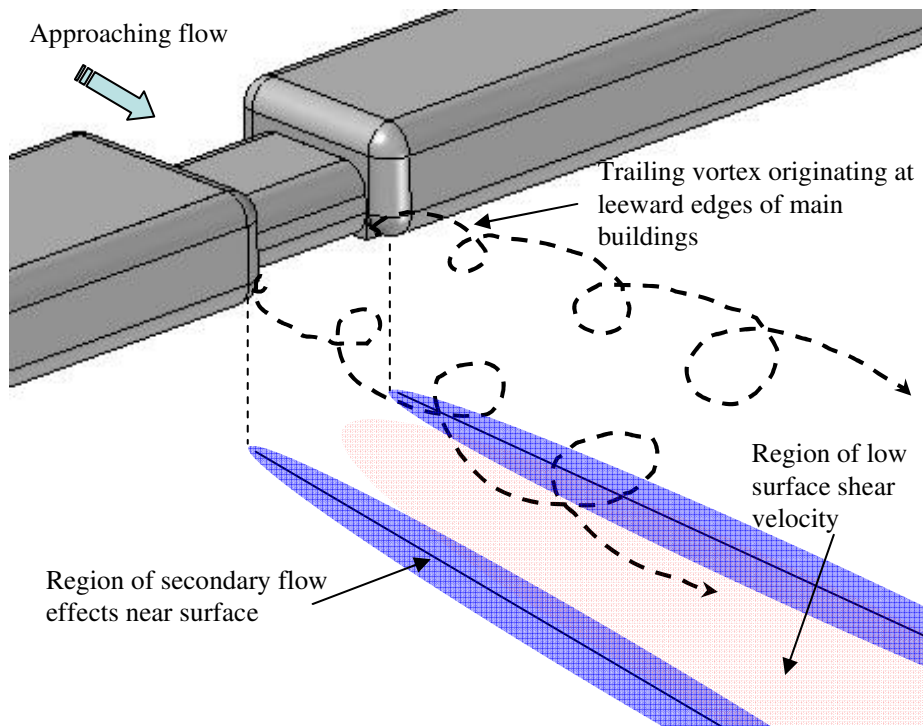


Figure 6.11. Schematic of the swirling flow leeward of the link section between the main buildings at SANAE IV

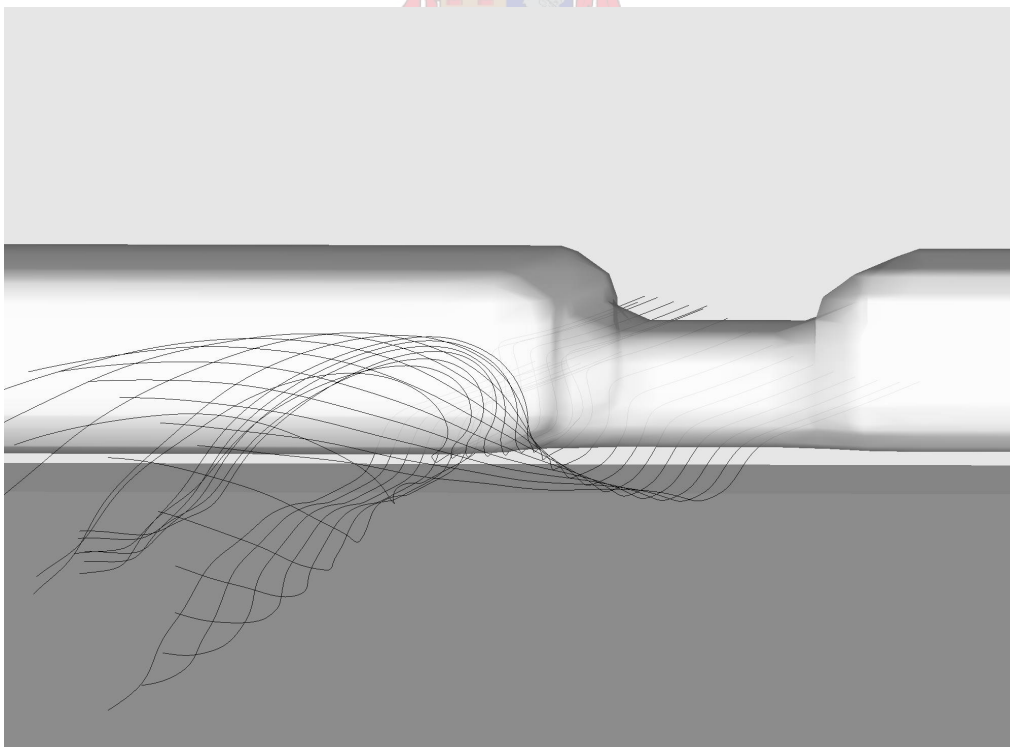
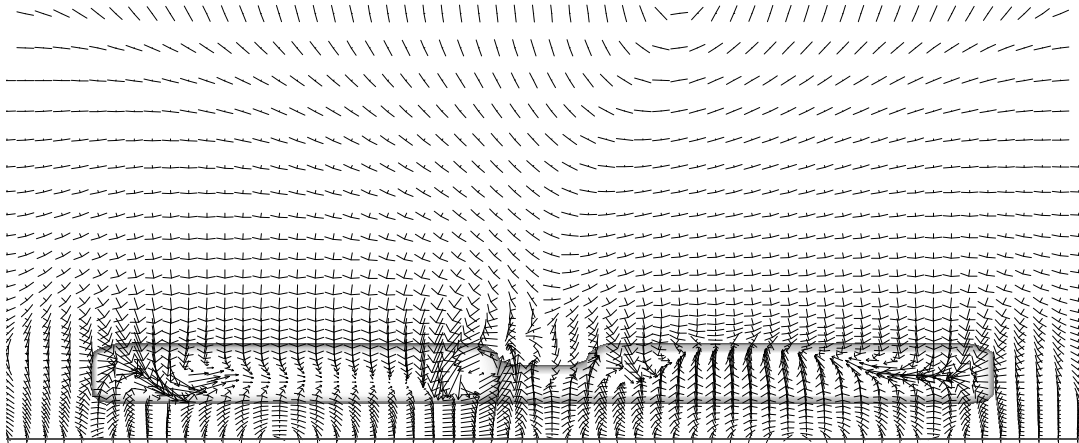
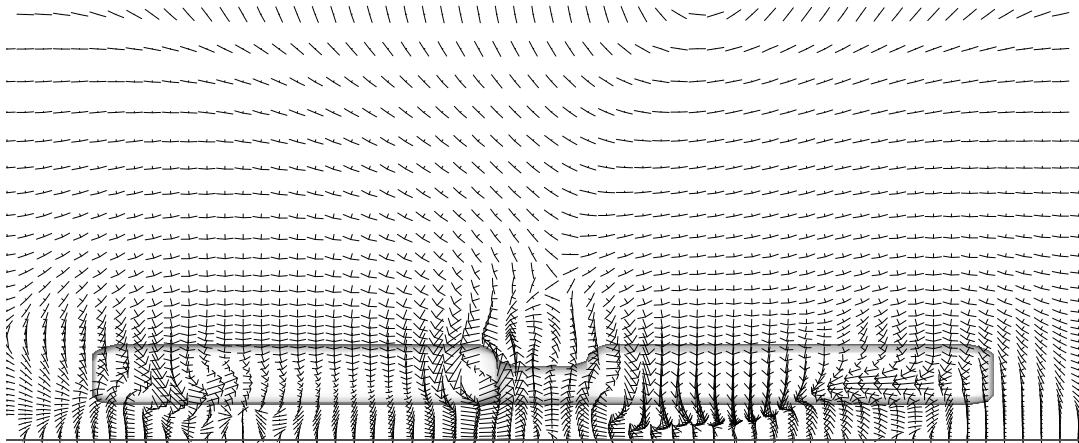


Figure 6.12. Streamline plot around the leeward corner of the main building B

(a)



(b)



(c)

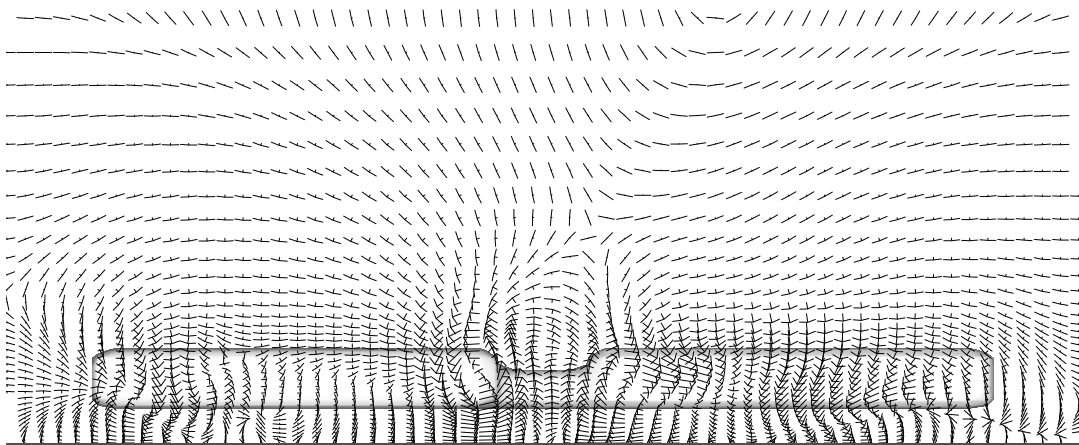


Figure 6.13. Vector plot (test 1) in the yz-plane at (a) $x=12$ m, (b) $x=17$ m and (c) $x=25$ m

The contour plot of the near surface snow fraction ratio, the local fraction of snow divided by the inlet snow fraction at the same height is given in figures 6.14 and 6.15. This indicates that most of the upstream snow is channeled around the outer edges of the building as well as underneath the building in the region of the interconnecting link. The strong acceleration below the building is also associated with an increase in the turbulent energy leading to enhanced suspension of snow through diffusion (simulated through the increased effective viscosity). This local concentrating effect of the building assists the downstream localised snow drift development since it provides increased snow for settling downwind of the link building and the outer edges. On the other hand, the enhanced mixing behind the main buildings diminishes the near surface snow concentration leeward of these structures. These results suggest that the upstream flow velocity does not have a significant influence on the secondary flow characteristics but may have increased snow deposition rates due to higher upstream available snow fractions. Figures 6.16 and 6.17 compare the local erosive and deposition snow flux for test 1 and test 2. From these plots it is evident that deposition (positive values) will occur along the windward edge of the SANAE IV structure as well as leeward of the building at the outer edges and behind the link buildings. Strong erosive fluxes (negative values) are predicted underneath the building in the region of strong flow acceleration and increased turbulence. The initial deposition fluxes for both test cases are similar even though the approaching snow concentration for test 2 is more. Thus the higher snow concentration contribution to the deposition may possibly be offset by the increased shear for test case 2. However, for test case 2 the average assumed particle diameter was the same as for test case 1. The settling velocity for both test cases is therefore the same. It could be argued that the higher approaching velocity would support a larger mean particle size within the wind and these particles may have slightly higher vertical settling velocities in which case the deposition flux for test case 2 would be higher than test case 1. This is not investigated in the present work but could be a significant factor in increasing the rate of deposition during higher wind velocities. The location and contour shape of the downstream positive value (deposition) are similar for tests 1 and 2 but the magnitude is different. Thus the same snow drift develops but at slightly different rate.

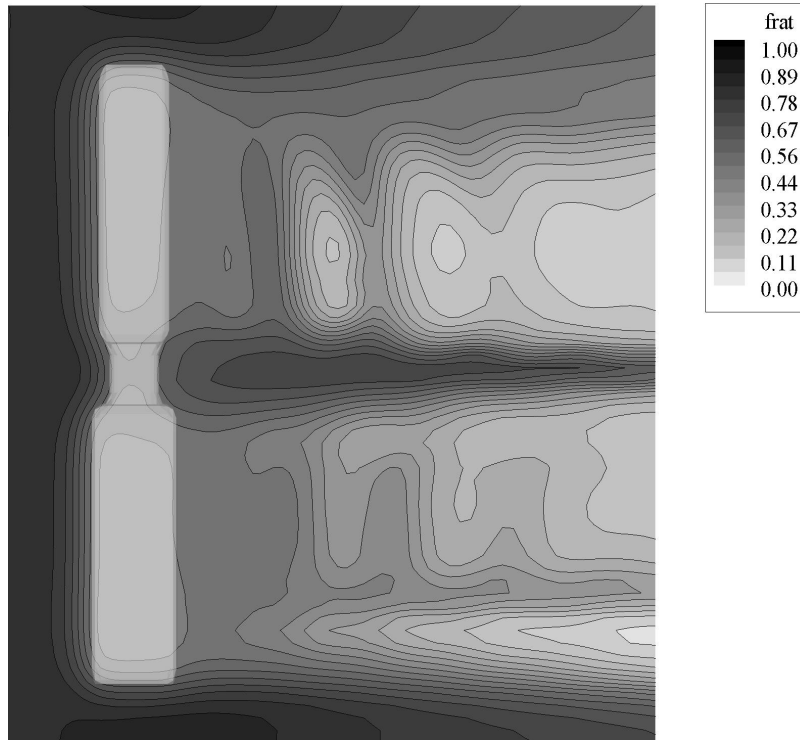


Figure 6.14. Near surface snow fraction contour plot, Test 1, after $t=20$ s simulation

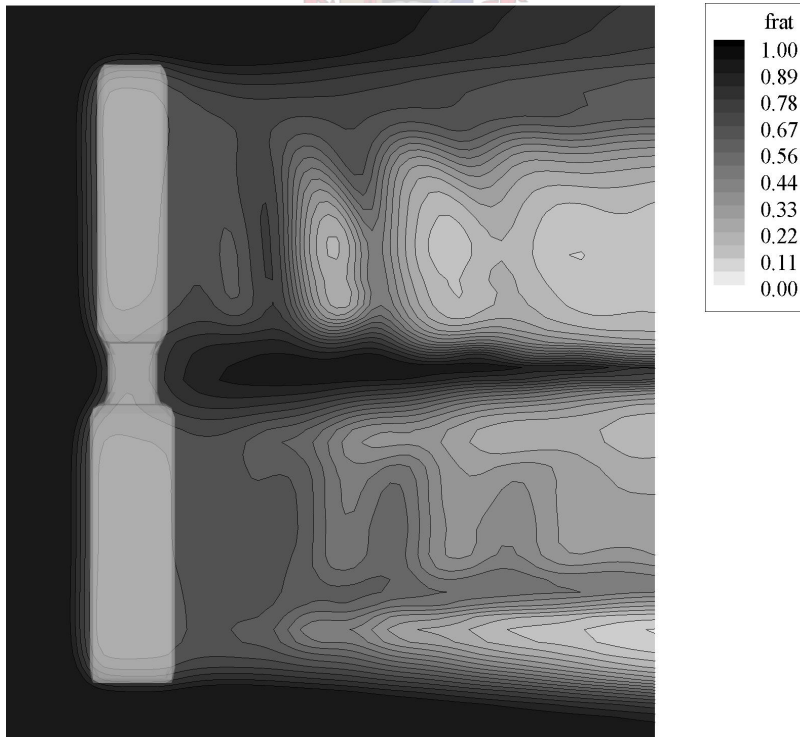


Figure 6.15. Near surface snow fraction contour plot, Test 2, after $T=20$ sec. simulation

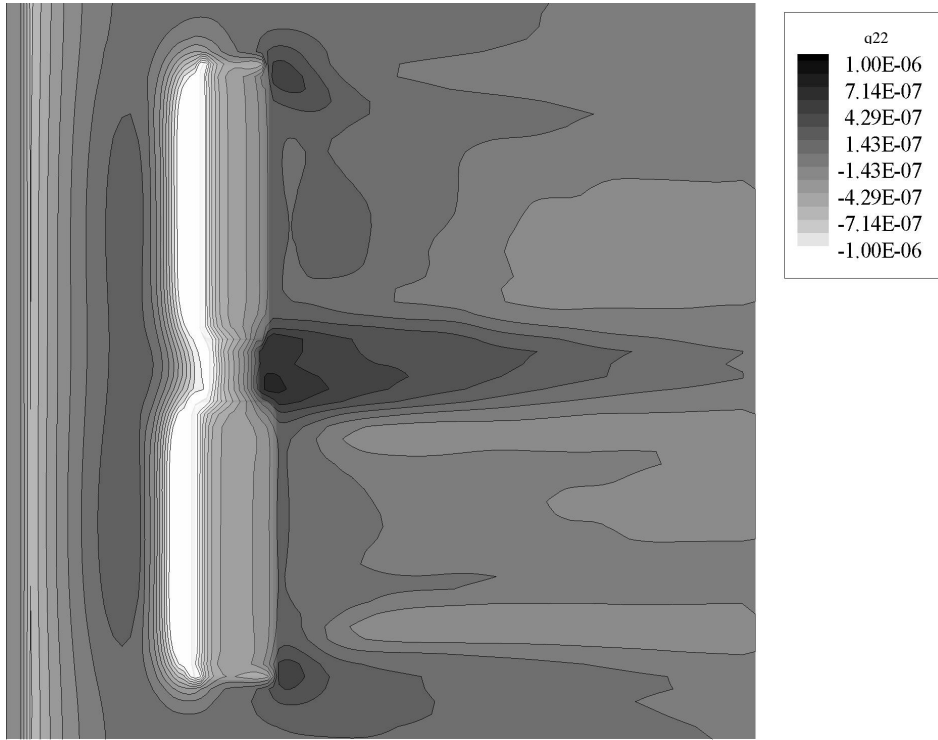


Figure 6. 16. Snow deposition / erosion flux from surface for test 1 at $t=20$ s

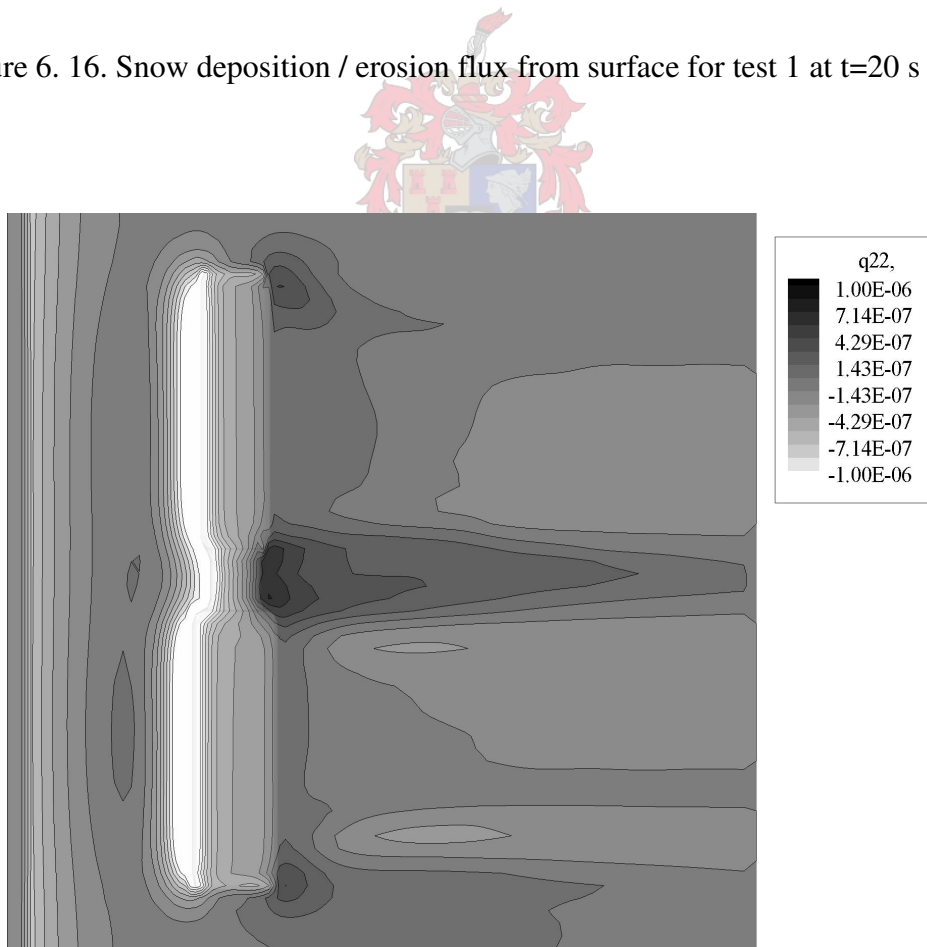
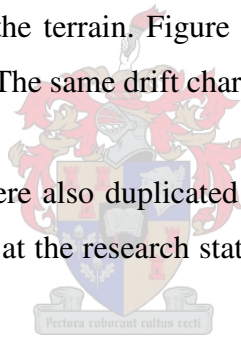


Figure 6.17. Snow deposition / erosion flux from surface for test 2 at $t=20$ s

Figures 6.18(a)-(c) and 6.19(a)-(c) show the snow drift development for test 1 and test 2 respectively. The drifts formed are similar in shape and location as mentioned above. The leeward drift behind the link is slightly more pronounced for test 2, probably due to the increased snow mass transport through the link. In both cases the leeward drifts behind the main buildings are similar and significantly less than the drifts at the link and leeward of the outer edges of the building. This suggests that the secondary flow present here strongly influences the increased snow drift formation.

Figure 6.20 and 6.21 show the resultant three-dimensional snow drift for test 1 and test 2. The characteristic snow drift behind the link is clearly visible for both test cases while the much less pronounced drift adjacent to the link build-up and behind the main building is also evident. These drift formations clearly correspond to the drifts observed at SANAE IV. Figure 6.22 shows the drifts that formed during a 3 day blizzard before 3 January 2004. This also shows the two drifts formed behind each link and the diminished drifts between them. These drifts were removed by bulldozing the terrain. Figure 6.23 shows the drift formation on 12 January 2004 after another blizzard. The same drift characteristics are shown.

These types of longitudinal drifts were also duplicated during a scale model test of SANAE IV undertaken during the field work at the research station. Details of these tests are given in Appendix G.



The following conclusions may be drawn from the results as described above. The main causes for the strong drift development behind the interconnecting link are:

- a) Channeling of snow upstream from the main building into and underneath the interconnecting link structure that leads to higher snow concentrations exiting the link area as compared to the main building. The same phenomena occur on the outer edges of the main buildings.
- b) Highest flow acceleration beneath the interconnecting link and subsequently the highest flow deceleration exiting the link areas. The deposition of snow is, amongst other things, proportional to the deceleration.
- c) Secondary flow phenomena assist the channeling of snow exiting underneath the main buildings towards the interconnecting link. The secondary flow also generates strong cross-streamwise flow and concentration gradients which assist the deposition of more snow.

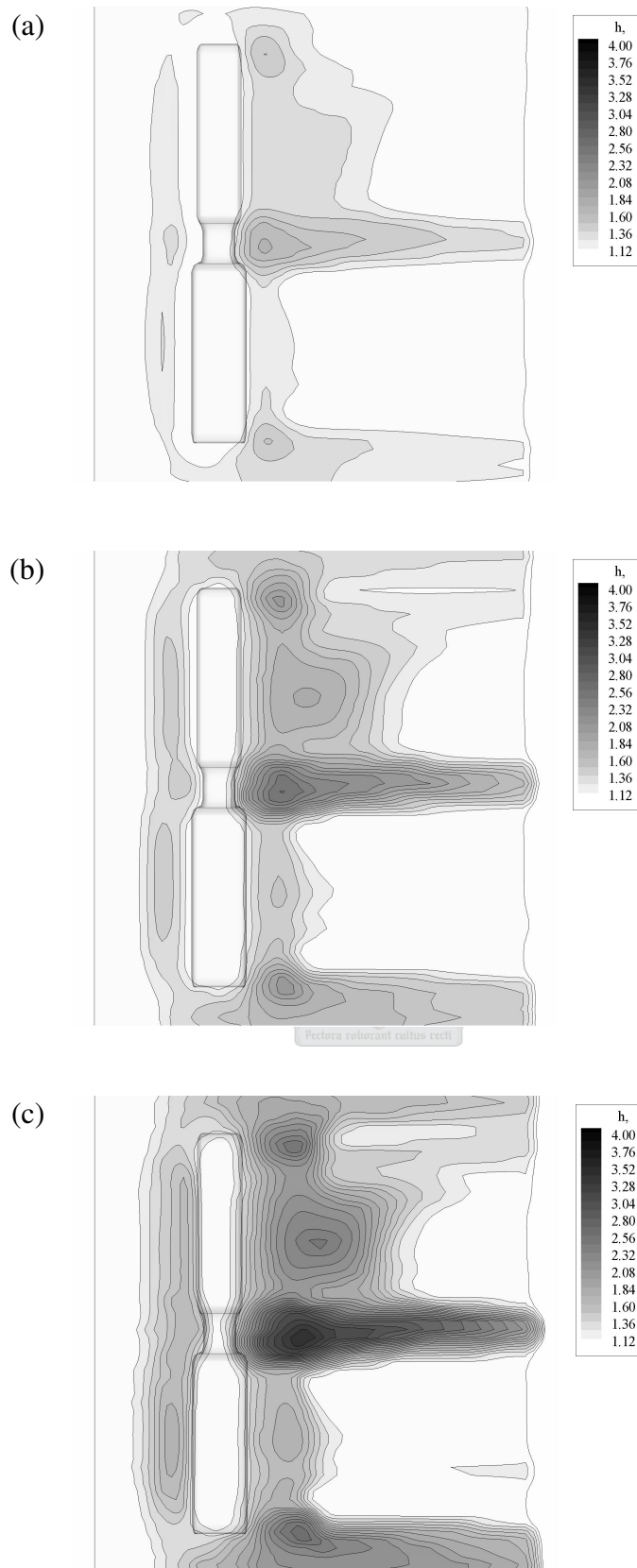


Figure 6.18(a)-(c). Snow drift height contour for SANA E IV drift simulation Test 1 at $t=60$ s, $t=120$ s and $t=200$ s

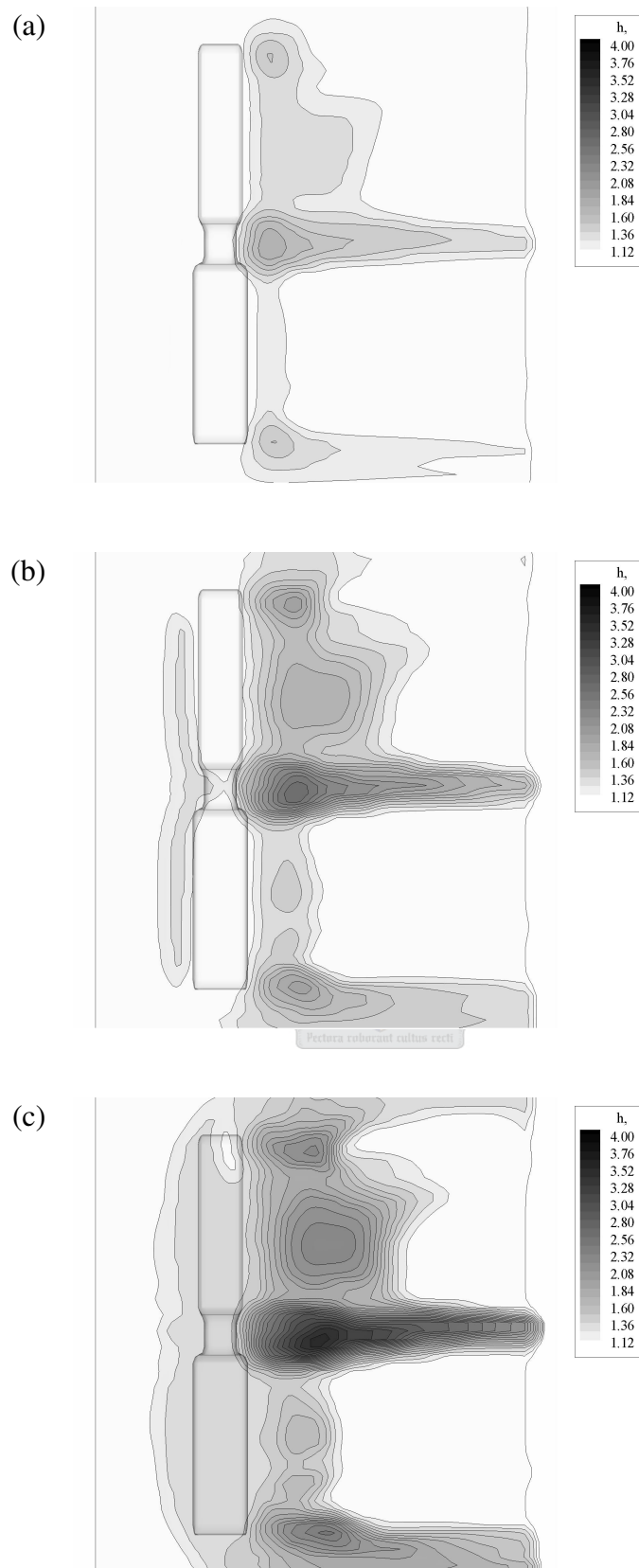


Figure 6.19(a)-(c). Snow drift height contour for SANA E IV drift simulation Test 2 at $t=60$ s, $t=120$ s and $t=200$ s

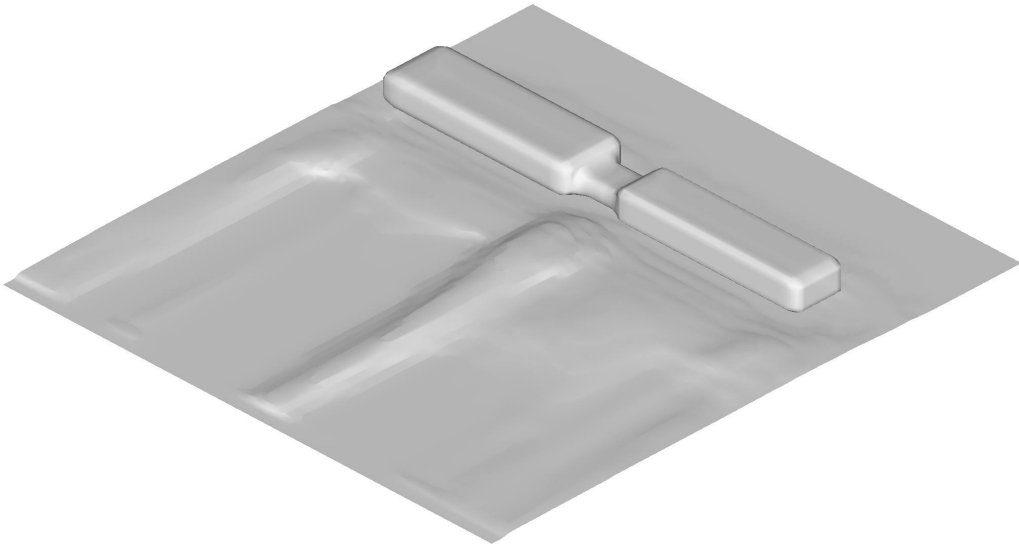


Figure 6.20. Three-dimensional snow drift development at the end of the simulation, Test 1

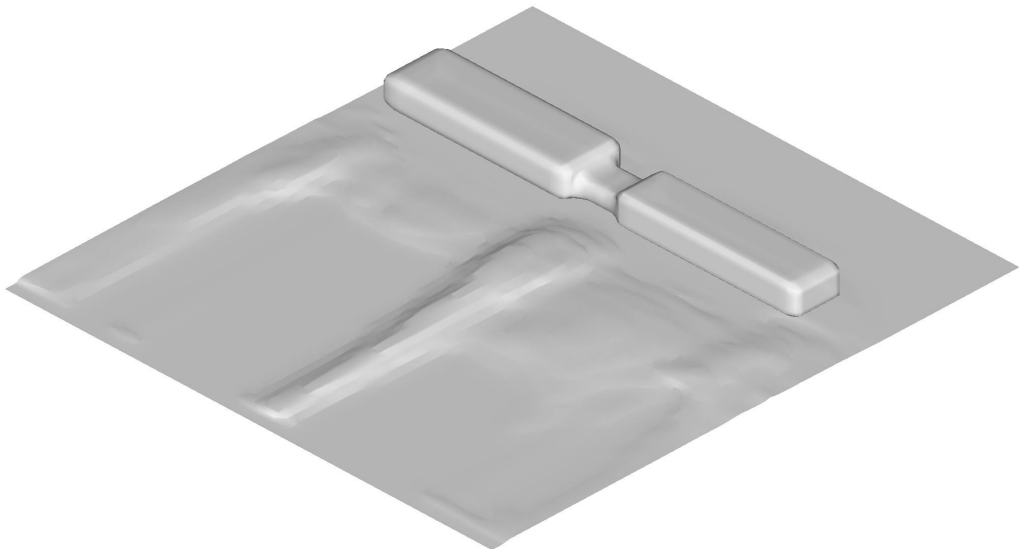


Figure 6.21. Three-dimensional snow drift development at the end of the simulation, Test 2

(a)



(b)



Figure 6.22. Snow drift behind the interconnecting links on 3 January 2004 after a blizzard

(a)

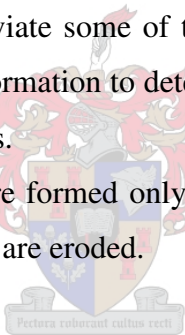


(b)



Figure 6.23. Snow drift behind the interconnecting links on 12 January 2004 after a second blizzard.

- d) The drift development initiation does not depend on the inlet or approach velocity profile since the results show that similar deposition / erosion regions are created. However, the mass flux of transported snow is proportional to the approach velocity to the power of more than 3 and therefore higher wind speeds will have an order of magnitude larger approaching snow flux. The present results indicate that the potential higher deposition rates due to larger snow concentrations for this situation may be offset by the increased shear and turbulent mixing caused by the higher wind velocities.
- e) The flow stream exiting the main buildings is highly turbulent and fluctuates which leads to an enhanced vertical suspension of snow. Thus the near surface snow concentration is effectively lowered due to this diffusion process and this has a strong influence on the availability of near surface snow for settling and deposition.
- f) The present snow drift model again provides good agreement with observed drifts. It is however difficult to maintain the accuracy of the present method in the fixed Cartesian frame and a boundary fitted grid would alleviate some of these inaccuracies. However, the model does provide us with the necessary information to determine the mechanisms for the initiation and developments of the localised drifts.
- g) It seems that the windward drifts are formed only during the lower wind velocities while during high wind velocities these drifts are eroded.



6.4. SANAE IV DESIGN MODIFICATIONS NUMERICAL SIMULATION

6.4.1. Proposed design modifications

In the following section two design modifications are evaluated to investigate their effect on the minimisation or elimination of the snow drift development leeward of the interconnecting structures. A similar computational domain and numerical simulation parameters are employed and one wind condition is evaluated, namely one corresponding to a shear velocity of $u_* = 0.35 \text{ m}\cdot\text{s}^{-1}$. The first conceptual design evaluated is Modification 1 and includes the addition of a solid baffle plate installed vertically and along the length of the leeward edge of the interconnecting link as shown in figure 6.24. This baffle plate should increase the flow velocity exiting the link building but should also enhance turbulent mixing to ensure a lower near ground snow concentration. It may furthermore modify the secondary flow structure

leeward of the edges of the main building to diminish the effects of the trailing vortex generated by the existing structure. The baffle may be installed onto the leeward supporting columns and just below the bottom panels of the interconnecting link, as indicated in figure 6.24. The gap between the link wall panels and the baffle should allow impinging flow to pass above and below the panel. Modification 2 evaluates the SANAE IV structure with the interconnecting link removed and replaced by a wider and continuous structure that joins the two main buildings flush with each other without the abrupt geometry change. The main buildings are not the same width and therefore a slight taper would be necessary. This modification is evaluated to see what the snow accumulation will be without the presence of the interconnecting links as they are.

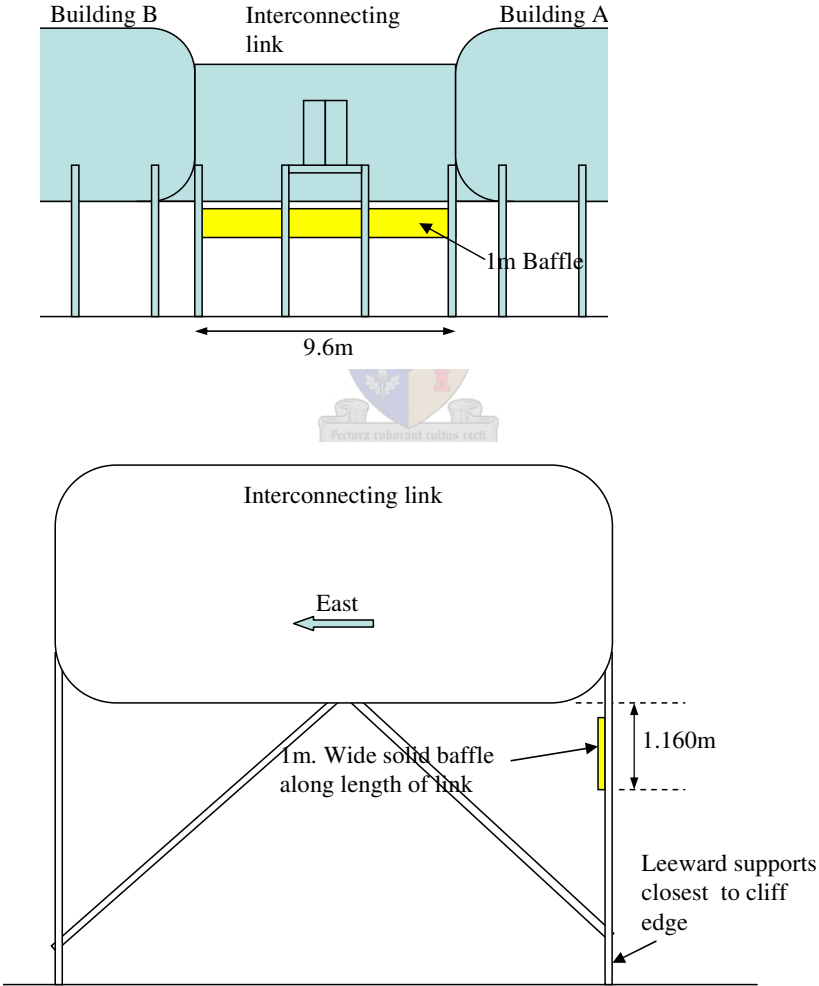


Figure 6.24. SANAE IV Modification 1 – 1 meter vertical baffle plate installation at the interconnecting link (top) front view, (bottom) side view

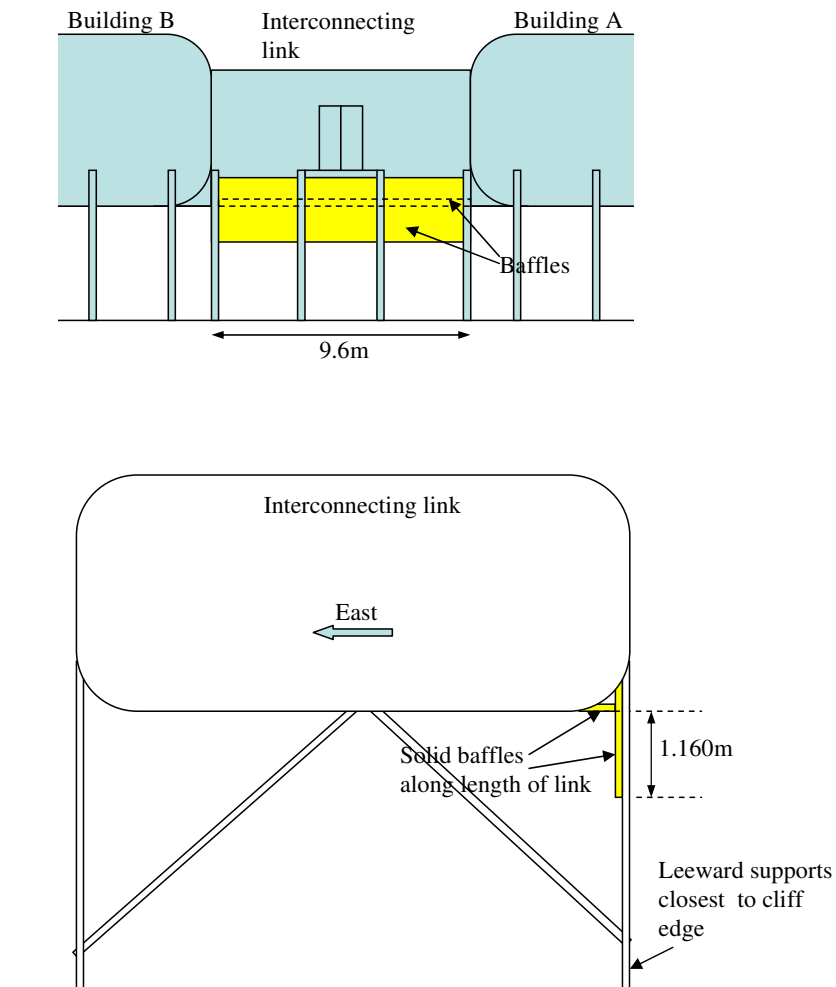


Figure 6.25. SANAE IV Modification 3 –Vertical and horizontal baffle plate installation at the interconnecting link (top) front view, (bottom) side view

Modification 3 is similar to modification 1 but the vertical baffle is extended upward along the leeward support pillar to join flush with the interconnecting leeward wall. An additional horizontal baffle is positioned below the link against the vertical baffle to effectively remove the leeward rounded edge of the structure as shown in figure 6.25.

All simulations are run for 200 s and the resulting snow drift development evaluated and compared.

6.4.2. Results, discussion and recommendation

The idea of installing baffle plates to remove or redirect snow around buildings or roads is not new. Sundsbø (1998) presented numerical results to evaluate the efficiency of wind deflection fins to remove snow drift adjacent to buildings by increasing wind scour. Lang and Blaisdell (1998) tested passive snow removal by means of a vortex blower. This triangular vortex blower showed good promise to remove snow from the Pegasus runway at McMurdo in Antarctica. The present numerical simulation intends to evaluate the effect of such a scour principle on the snow drift leeward of the link buildings at SANAE. These design proposals given here do not include any evaluation of the effects such modifications may have on the structural integrity of the SANAE IV construction.

The snow drift development for Modification 1 during the course of the simulation is shown in figure 6.26 and 6.29. This show that a reduction in the overall snow deposition is achieved when compared with the results of the earlier simulations as per figures 6.18 and 6.20. The snow drift leeward of the link has been scoured away and has been replaced by two new deposits of snow laterally away from the original location. Thus it seems that this design may be partly successful since it increases the velocity behind the link and modifies the swirling motion behind the link. This design is very promising mainly because of its simplicity and its potential ease of implementation. This also makes it ideal for experimental testing purposes.

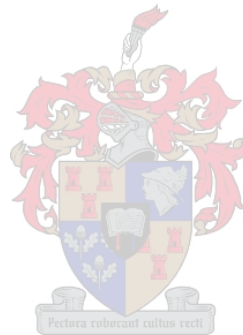
The snow drift development for Modification 2 during the course of the simulation is shown in figures 6.27 and 6.30. This indicates that the overall snow deposition in the link area is diminished although a slight downwind drift is still present leeward of the link area. This is significantly lower than for the same wind condition but with the original link structure in place as per figure 6.18 and 6.20. The disadvantage is that although this design may be successful it will also be expensive to design and fabricate and would require extensive logistical management to install. The difference in the widths of the main buildings would also complicate the design.

The snow drift development for Modification 3 is shown in figures 6.28 and 6.31. This shows that the drift leeward of the link is effectively removed but that two lesser drifts have formed laterally to the original drift position, similar to that predicted for modification 1. The

windward drifts have also become slightly more pronounced and moved downwind and underneath the structure. This suggests that this modification may be successful if the vertical baffle is made slightly shorter.

It is proposed that the solid baffle plates as per modification 3 are installed underneath and along the length of the interconnecting link to experimentally evaluate the numerical results given above. It is recommended that the vertical baffle be split into widths of approximately 500mm to test the effect of various baffle widths on the snow drift formation.

The results have shown that the present numerical model can predict realistic drifts around such elevated structures and that it can be used to evaluate various design concepts to minimise snow drifting. It has also simulated and highlighted one complexity of managing snow drifts around structures, that is, that any design change that removes drifts from one area almost always creates a new drift adjacent or near the original drift.



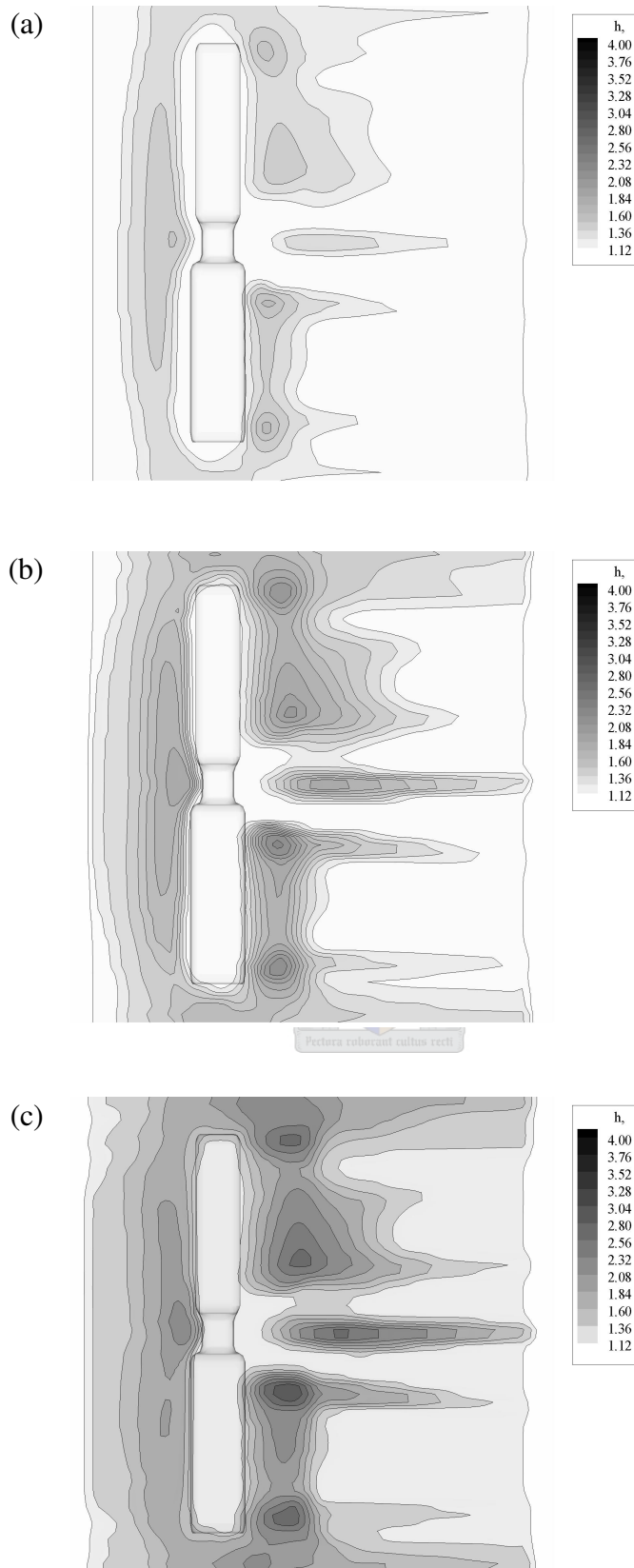


Figure 6.26(a)-(c). Snow drift height contour for SANAE IV drift simulation Modification 1 at $t=60$ s, $t=120$ s and $t=200$ s

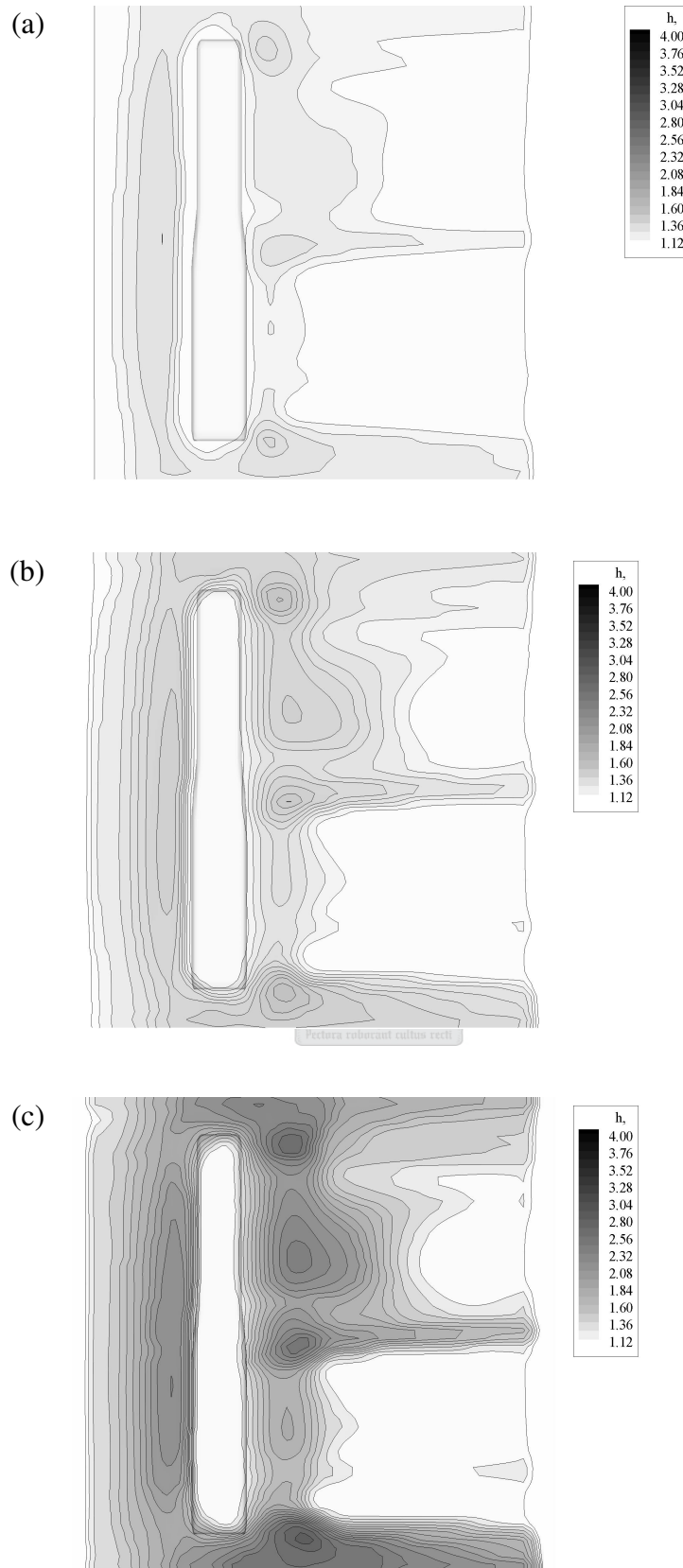


Figure 6.27(a)-(c). Snow drift height contour for SANA E IV drift simulation Modification 2 at $t=60$ s, $t=120$ s and $t=200$ s

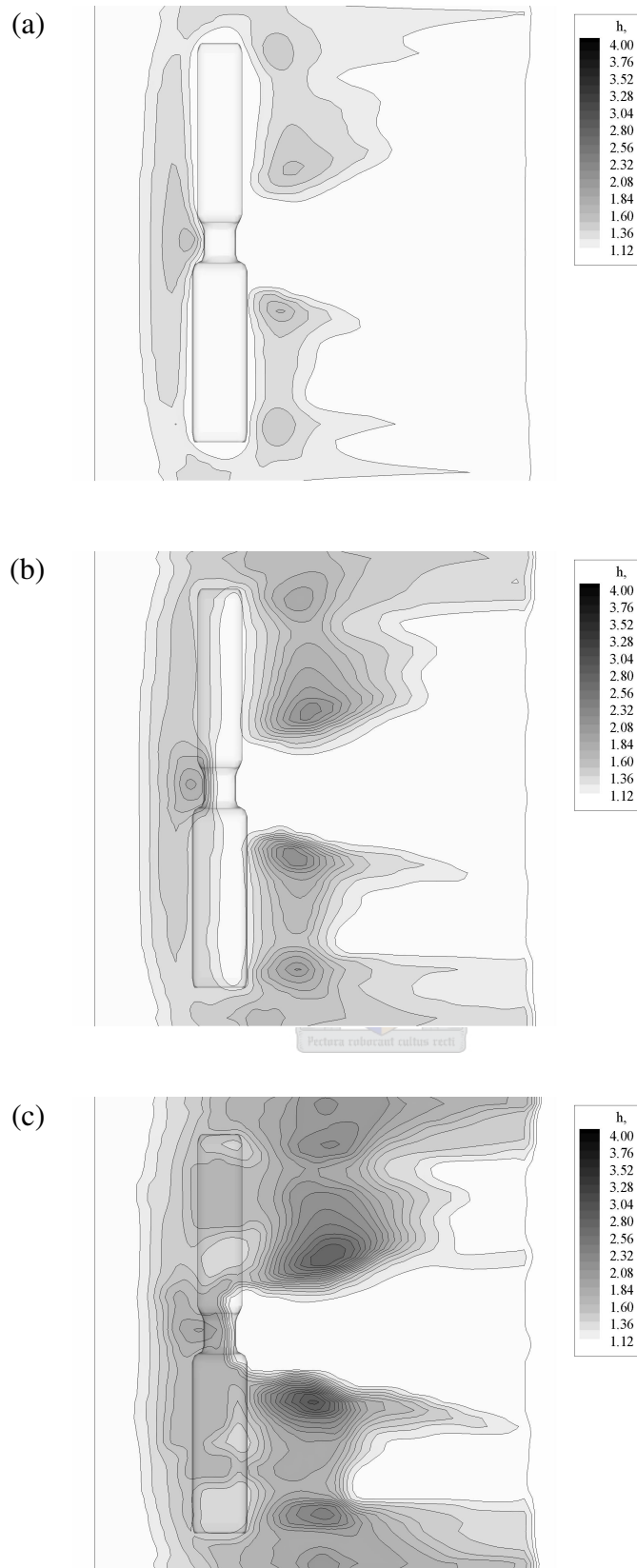


Figure 6.28(a)-(c). Snow drift height contour for SANAE IV drift simulation Modification 3 at $t=60$ s, $t=120$ s and $t=200$ s

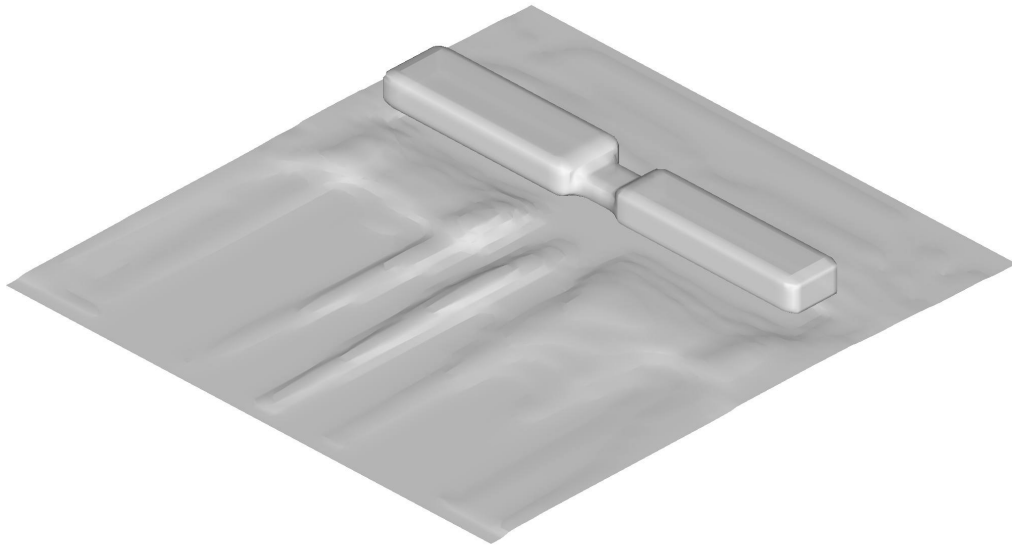


Figure 6.29. Three-dimensional snow drift development at the end of the simulation for Modification 1

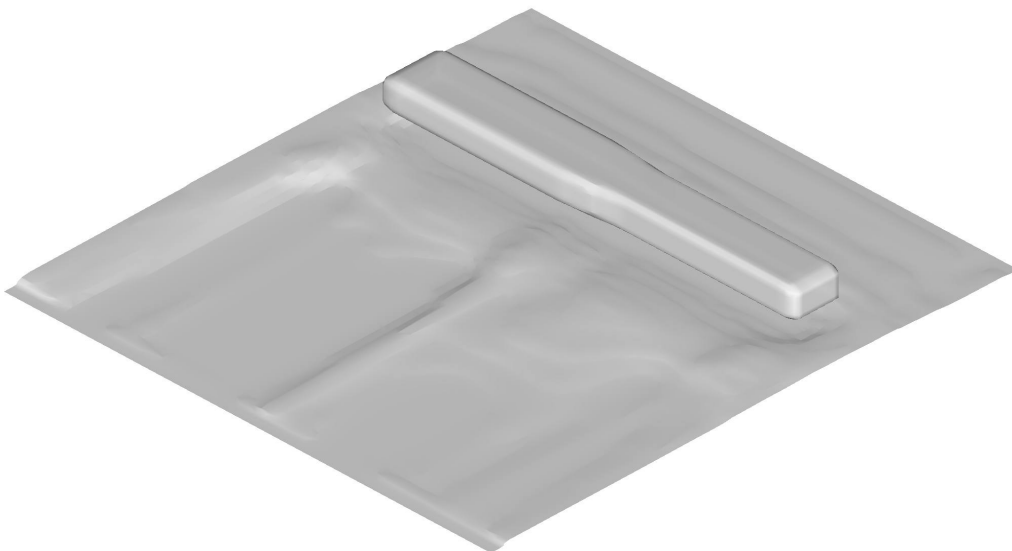


Figure 6.30. Three-dimensional snow drift development at the end of the simulation for Modification 2

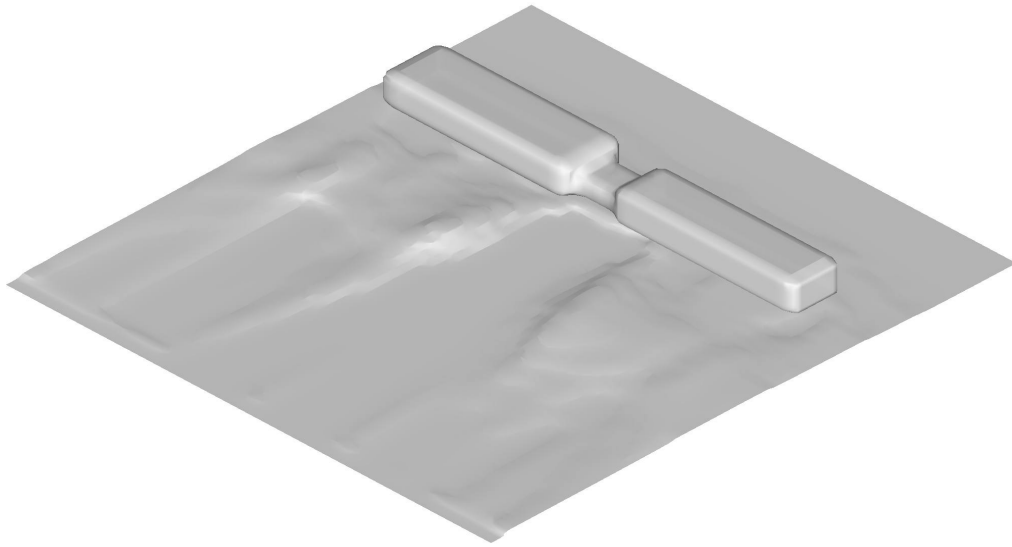


Figure 6.31. Three-dimensional snow drift development at the end of the simulation for Modification 3





7. CONCLUSION

7.1. NUMERICAL SNOW DRIFT MODELLING

The first objective of this work was to determine the snow deposition mechanisms responsible for the snow drift formation around structures and especially the elevated structure of the South African research station, SANAE IV, in Antarctica. To achieve this, a thorough theoretical understanding of the wind driven snow transport processes and its drift mechanisms were required. The wind driven snow and air mixture is considered to be highly dilute and governed by the appropriate mixture transport equations. Minimal momentum transfer between phases is assumed and only limited to the drag between the dispersed particles and the air flow resulting in a slip or drift velocity between phases. One of the key issues in the understanding of the deposition characteristics of saltating and suspended snow has always been the threshold shear velocity. Initially, a model that uses this threshold criterion to determine whether erosion or deposition takes place was used. For conditions below threshold shear velocity, the deposition flux is assumed to be proportional to the product of the vertical settling flux and a somewhat arbitrary dimensionless shear velocity function. This model does not take into account the effects of the vertical flux of snow due to turbulence and since its formulation relies mainly on shear velocity functions it ignores the effects of near surface flow divergence and snow concentration gradients. For above threshold conditions the erosive flux is found as a function of the excess shear stress at the surface i.e. the above threshold shear stress is proportional to the eroded snow flux.

It was found during the course of the work that the threshold based models give seemingly accurate results especially for snow drift simulations of surface mounted obstacles. The simulation results presented in this work show that the threshold based formulation and description remains questionable since being, at best, too simplistic or at worst fundamentally unphysical and could therefore not be considered generic or appropriate for all flow conditions. Their failing was evident when high shear deposition characteristics were to be simulated or where secondary flow effects were expected to influence deposition and erosion. For high velocity flow fields, such as typically found during strong and severe wind conditions as is common in Antarctica, the wind shear velocity at the snow surface does not necessarily drop below threshold conditions where winds approach obstacles. Such conditions

may exist for elevated obstacles where the flow passes and accelerates underneath the obstacle and is also present near surface mounted obstacles where the flow accelerates to high shear velocities around the windward corners of an object. The threshold based models could therefore not predict deposition in these areas since the onset of deposition is only dependent on a lower than threshold shear velocity region. Subsequently a conservation based model was developed and evaluated to overcome this deficiency. This model determines the deposition or erosion flux onto or from the surface from the snow mass conservation in the near surface flow domain. This method was found to be more successful and also considered more suitable and physically representative of the flow processes at hand. For such a model the deposition and erosion mechanisms are assumed to be governed by essentially the balance between vertical settling or suspension and the horizontal snow mass flux divergence. Then, for one, deposition may occur in regions of very high shear but where negative gradients of streamwise or cross-streamwise velocities or concentrations are present. Thus the effects of secondary flow structures on drift formation are accounted for in the model.

In order to validate the performance of the numerical models, a few simple simulation test cases were selected for which experimental results and observations of snow drift are available. Firstly both the drift predictions found by using the threshold based model and the conservation based model were evaluated and compared against the observed drift formation around a three-dimensional cube. The observations were made during field tests of drift patterns and wind conditions at SANAE IV in Antarctica. Both the models predicted snow drifts in good agreement with the observed patterns but the results from the conservation model were considered more appropriate and generally in better agreement. This is especially true for the deposition of snow around the outer edges of the windward corners of the cube, a region of high shear velocity. The threshold model also predicted drifts forming against the windward cube wall, contradictory to the observations which showed that the wall remained clear of snow throughout the duration of the tests. This erroneous windward drift prediction was successfully eliminated by employing the conservation based approach. This is attributed to the effects of the strong vertical mixing caused by turbulence near the surface at and around the windward face of the cube. This effectively enhances the vertical entrainment of snow, an effect not accounted for in the threshold based model.

The conservation based model was further validated against available snow drift results from other research work for a standard porous snow fence as well as for snow drift observations made around two adjacent cubical buildings. For the snow fence simulations a typical Wyoming type fence with 50% porosity and with a bottom gap was selected and simulations carried out for three different wind conditions that exceeded the threshold shear velocity in varying degrees. Only the conservation based snow drift scheme was employed and the predictions showed good agreement with the observed and measured snow drift shape and location around the fence. Both two- and three-dimensional simulations were performed. All results indicated that the windward drift formation was mainly caused by near surface flow deceleration upstream of the fence which gradually diminished as this drift increased in height and the deceleration was reduced. The results suggested that the upstream boundary layer thickness and turbulence characteristics will greatly influence the windward drift formation by modifying the vertical mixing effect modelled by means of the eddy viscosity. Leeward of the fence the deposition is initially governed by vertical settling and flow deceleration in the near surface layer. As the drifts develop they encounter the higher shear layers and turbulence levels of the flow passing through and over the top edge of the fence causing diminishing deposition and eventually the equilibrium drift profile.

The simulations performed for the two adjacent cubes tested the snow drift predictions where the flow approached the cubical buildings at an oblique angle to the windward normal face of the structure. The drift predictions again compared favourably with measured results. The predicted snow drifts followed the edge of the two horseshoe vortex systems generated around the cubes, similar to the results of the single cube simulations. This again highlighted the importance of the effects of strong near surface flow divergence and vertical turbulent mixing on the deposition of snow. Again the upstream boundary layer characteristics influence the development and size of the recirculation horseshoe vortex structure. A thinner boundary layer will cause a smaller windward recirculation region which places the horseshoe vortex system nearer to the cube structure and causing deposition to occur closer to the walls. Alternatively a thicker approaching boundary layer will cause a more pronounced and larger recirculation region with the deposition along the edge of the horseshoe vortex system being further away from the walls. More snow will then be entrainment by this vortex causing larger depositions lateral and downstream of the cube.

The validation simulations showed that the conservation based model predicted realistic drift formations for three different flow situations. Importantly, the same model was used with success for all test cases under consideration without the need for recalibration of simulation parameters to achieve agreeable results. Although the model includes and is influenced by the selection of the turbulent Schmidt number, here arguably kept constant at unity, it is also strongly dependent on the description of the upstream boundary layer characteristics.

7.2. SANAE IV SIMULATIONS AND RESULTS

The numerical validations were followed by simulations to predict the snow drift characteristics around the South African research station, SANAE IV, in Antarctica and especially to evaluate the drift formation leeward of the interconnecting link buildings. These longitudinal snow drifts behind the interconnecting link structures were the focus of field experiments during summer field excursions to Antarctica during which large scale observations and scale model experiments were carried out. Wind profile measurements were also made in the vicinity of SANAE IV to determine the boundary layer characteristics. The field tests primarily investigated causes for the drift formations behind the station. The experiments suggested that the supporting structures, the location of staircases and the terrain topography at and around SANAE IV have minimal influence on the initiation of the drifts leeward of the station while the presence of strong swirling flow and trailing edge vortex structures were considered to be important phenomena causing these drifts. The deposition mechanisms for SANAE IV were believed to be caused by three processes. Firstly by strong flow deceleration effects such as where the flow exits underneath the structure and especially leeward of the link areas. Secondly, higher snow concentrations are present leeward of the link area due to channeling of the snow towards the link area. Thirdly, significant secondary flow characteristics are present leeward of the outer edges of the main buildings leading to downstream swirl with associated near surface flow disturbances.

The subsequent numerical simulation of the snow flow surrounding the SANAE IV station was able to depict these flow phenomena and also predict the snow drift characteristics in very good agreement with observations made at the SANAE IV station. Firstly two simulations were carried out at two different approaching wind speeds to evaluate the effects

of an increasing wind velocity and its associated increase in the transported snow mass flux. It was found from these simulation results that the approaching wind velocity does not necessarily influence the initiation of the drifts and that it does not, somewhat unexpected, influence the rate of drift formation. This may primarily be due to the order of magnitude increase in snow flux being offset by an increase in the shear erosion and enhanced turbulent mixing. The predicted near surface shear velocity were also considerably higher than the threshold shear velocity without any flow separation suggesting that the deposition mechanisms were governed more by flow divergence and secondary flow effects than by vertical settling alone. A threshold based approach could therefore not predict any realistic snow drift formation behind the station especially under conditions of high approaching wind velocities. The causes for the snow drifts are mainly due to the presence of high snow concentrations being channeled around the main buildings and underneath the interconnecting links, due to the strong deceleration of the flow leeward of the link and importantly due to the secondary flow effects of a trailing vortex generated at the edge of the main buildings.

Further simulations were carried around the same SANAE IV station but with the addition of design modification proposals that may diminish the snow drift formation. When considering design changes to facilitate snow drift elimination from one area it is necessary to ensure that the drift is not just moved to a different area. It was intended to evaluate a design that does not necessarily move the drift to a wider area along the length of the base but rather move the drift further away from the base or to ensure strong suspension of snow so that deposition does not occur before the snow reaches the edge of the cliff.

A simulation was performed that tested a station design where the interconnecting link was removed and two main buildings joined by means of a continuous structure. This modification resulted in the elimination of the trailing vortex system and reduced the snow drift behind the original link structure. However, this modification is considered too expensive and difficult to install for practical application.

Further simulations tested the effects of simple baffle plate installations on the existing structure and the results suggest that a vertical and horizontal plate installed below and along the leeward length of the link building may cause a reduction in the snow drift leeward of the link building. The numerical work indicates that this may be due to somewhat higher flow

velocity and increased turbulence leeward of the link. This leads to enhanced turbulent mixing and more vertical entrainment of snow which diminishes the snow concentration behind the link. The secondary flow structure is also disturbed. This design proposal may be easy to evaluate experimentally since it is simple in design and simple to install. It is strongly suggested that further research is undertaken to evaluate these design changes with wind tunnel or additional outdoors on-site tests.

In summary, the general research objective of this work was to further develop the fundamental understanding of snow drifting in wind and to develop a method to facilitate the numerical simulation of snow drifts around general three-dimensional structures using computational fluid dynamics. As mentioned above, two methods were employed namely the threshold and conservation based methods. It is believed that the conservation based method is superior mainly because of its better representation of the flow phenomena. The research contribution is made in the validation of the threshold and conservation based models against real test results for a three-dimensional cube, a porous snow fence, a group of two adjacent cubical buildings and lastly against observed results of the elevated structure of SANAE IV. The conservation based model predictions of the snow drift was successful in achieving good agreement for all the test cases under consideration. This study shows that the conservation based models hold great promise, while threshold models are simple to implement but due to their somewhat artificial description of the physical processes can not predict snow drift under real and complicated wind conditions such as at high wind velocities. The work also highlighted the flexibility of the FAVOR method as implemented in the FLOW3D architecture to facilitate the temporal surface adaptation in a three-dimensional flow domain. This study has been successful in using the FAVOR principles of FLOW3D combined with a more physically representative conservation based deposition scheme to predict transient snow drift development in a three-dimensional computational domain.

7.3. RECOMMENDATIONS FOR FUTURE WORK

The development of a snow drift model based on the conservation based approach in general CFD codes using multigrid or unmatched control volume architecture does allow much greater flexibility in simulating flow around complex geometries and will result in more

efficient use of processing power. This will require extensive programming expertise and assistance from existing CFD code developers. Terrain adaptation in an unstructured approach would provide significant advancement for drift simulation in complex terrains and over large topographies. The implementation of a temporal terrain adaptation scheme may prove complicated for an unstructured boundary fitted domain representation as compared to the FAVOR description especially for three-dimensional domains.

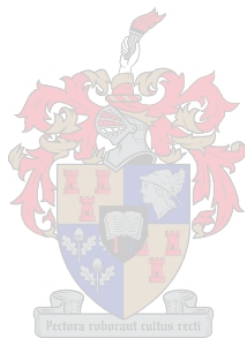
During the course of all simulations presented in this thesis an attempt has been made to carry out grid independence test as far as possible given the constraints of the presently available computing power. It is believed that a fair degree of grid independence was achieved and only the results of the final grid resolutions used are presented. The results of the numerous dependency tests are not included here for the sake of brevity. However, the snow drift models presented here should benefit from further extensive grid dependency tests to determine, for one, that the calculation of deposition fluxes is largely independent of the level of blocking of the near surface control volume.

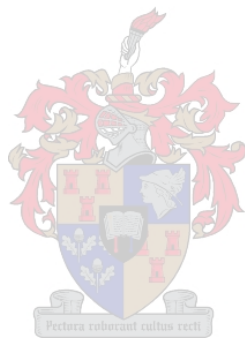
A better understanding and modelling of the saltation principles i.e. an introduction of non-equilibrium or non-steady saltation fluxes into the conservation based model remains crucial as well as the effect the condition of the snow pack has on an erosive or saltation snow flux. The metamorphosis of the snow pack may even be evaluated as a function of time during field tests of deposition events or by coupling Discreet Element Method (DEM) simulations with wind flow boundaries to determine the release flux of snow during saltation as a function of snow pack characteristics.

The particle deposition flux determined at present for the conservation based model (or threshold model for that matter) still assumes that the deposition flux deposits its particles instantaneously and within the same control volume at the end of each time step during the simulation. This is not physically correct since the particles that are determined to be settling will do so at a trajectory strongly influenced by their local velocity as well as the particle response to turbulence and / or convective and diffusive field conditions. Thus the theory and model needs to be investigated and developed that, for example, allows deposition to follow the settling trajectory and release the instantaneous deposition flux over the settling or saltating trajectory length.

This work showed that the use of a constant vertical fall velocity and a turbulent Schmidt number equal to unity provided realistic snow drift predictions. It is known that this approach also remains physically simplistic since the eddy diffusivity it is coupled to the particle size distribution which significantly influences the deposition flux under certain conditions. The work does seem to suggest that the flow divergence is also a strong contributor to deposition even though this may be modified dramatically by different turbulent Schmidt numbers and particle size effects. Furthermore, the present model uses the standard $k-\varepsilon$ turbulence model which is widely considered inappropriate for environmental wind flows and especially for such flows in regions of strong flow curvature, separation and impingement. It is proposed that future snow drift models evaluate the performance of the conservation based models but with the addition of modifications to the turbulence model such as the implementation of a non-linear $k-\varepsilon$ turbulence model.

More experimental and numerical tests should be carried out to evaluate the performance of the conservation based models under high and low shear flows but where secondary flows are predominant. The deposition and erosion flux will be strongly influenced by the presence of vortex shedding behind a bluff body due to the fluctuating velocity and therefore changing sign of the streamwise velocity gradient. Therefore the periodic drift formation should be evaluated along with the influence of the vortex shedding that may enhance vertical mixing and possibly reduce the near surface snow concentration leading to reduced drift formation. Since elevated obstacles almost always generate periodic vortex shedding under environmental flow conditions, it may be appropriate to carry out wind tunnel tests for such elevated obstacles to investigate snow deposition under fluctuating or non-equilibrium conditions.





APPENDIX A: VOLUME AVERAGE THEOREMS

The theorems and formulations given here generally follow those described by Ishii (1975), Abou-Arab (1986), Soo (1990) and Fan and Zhu (1998). These theorems are integral to the derivation of the volume-time averaged transport equations for a multiphase fluid in a continuum.

Volume averaging:

The volume average of any quantity or property φ_k of phase k is

$$\langle \varphi_k \rangle = \frac{1}{V} \int_{V_k} \varphi_k dV \quad (\text{A.1})$$

where V is the volume of the control volume and V_k is the volume of the quantity of φ_k in the control volume. The volume average is also called the phase average. The intrinsic average of quantity or property φ_k of phase k is

$${}^i \langle \varphi_k \rangle = \frac{1}{V_k} \int_{V_k} \varphi_k dV \quad (\text{A.2})$$

which reflects the real physical quantity or property. Thus from equations (A.1) and (A.2) one finds a relationship that defines the phase average in terms of the intrinsic average i.e.

$$\langle \varphi_k \rangle = \frac{V_k}{V} {}^i \langle \varphi_k \rangle = \alpha_k {}^i \langle \varphi_k \rangle \quad (\text{A.3})$$

where α_k is the volume fraction of property φ_k of phase k in the control volume. This allows one to define the governing transport equations of each separate phase in terms of its Eulerian continuum.

Furthermore, volume averaging can only be applied to quantities per unit volume and therefore the intrinsic volume average of velocity is found from the average of momentum per unit volume. By approximating the intrinsic average of a product by the product of intrinsic averages as

$${}^i\langle\varphi_k u_{ki}\rangle \approx {}^i\langle\varphi_k\rangle {}^i\langle u_{ki}\rangle \quad (\text{A.4})$$

and using equation (A.3) one can then show that the intrinsic average of velocity is determined from the momentum per unit mass and volume i.e

$${}^i\langle u_{ki}\rangle = \left[\frac{1}{V_k} \int_{V_k} \rho_k u_k dV \right] \frac{1}{{}^i\langle \rho_k \rangle} = \frac{\langle \rho_k u_k \rangle}{\langle \rho_k \rangle} \quad (\text{A.5})$$

Time averaging:

The time average of a volume averaged quantity reads

$$\overline{\langle \varphi_k \rangle} = \frac{1}{T} \int_0^T \langle \varphi_k \rangle dt \quad (\text{A.6})$$

The volume time averaged instantaneous quantity may be represented by a mean quantity with a fluctuating component

$$\langle \varphi_k \rangle = \overline{\langle \varphi_k \rangle} + \langle \varphi'_k \rangle \quad (\text{A.7})$$

Furthermore, it can be shown that the following identities are valid

$$\langle \varphi'_k \rangle = 0 \quad (\text{A.8})$$

$$\overline{\langle \varphi_k \psi_k \rangle} = \overline{(\varphi_k + \varphi'_k)(\psi_k + \psi'_k)} = \overline{\varphi_k \psi_k} + \overline{\varphi'_k \psi'_k} \quad (\text{A.9})$$

Additional rules:

It can also be shown that the following rules are valid:

The sum of averages is the average of the sum

$$\langle \varphi_k \rangle + \langle \psi_k \rangle = \langle \varphi_k + \psi_k \rangle \quad (\text{A.10})$$

Equation (A.4) also determines that the volume-average of a product can be expressed in terms of the product of the volume averages i.e.

$$\langle \varphi_k u_{ki} \rangle = \langle \varphi_k \rangle {}^i\langle u_{ki} \rangle = \alpha_k {}^i\langle \varphi_k \rangle {}^i\langle u_{ki} \rangle \quad (\text{A.11})$$

The time average of a volume average quantity is equal to the volume average of a time averaged quantity

$$\overline{\langle \varphi_k \rangle} = \langle \overline{\varphi_k} \rangle \quad (\text{A.12})$$

As per Fan and Chu (1998) the following characteristic volume averaging theorems of derivatives are given.

Averaging of the gradient function

$$\langle \nabla \phi \rangle = \nabla \langle \phi \rangle + \frac{1}{V} \int_{A_k} \phi \mathbf{n}_k dA \quad (\text{A.13})$$

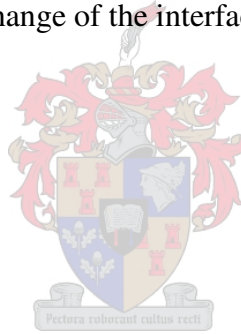
Averaging of the divergence function

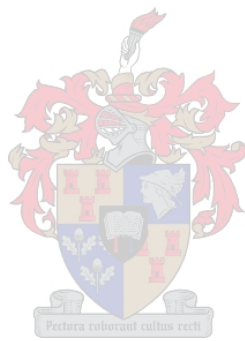
$$\langle \nabla \cdot \mathbf{u}_{ki} \rangle = \nabla \cdot \langle \mathbf{u}_{ki} \rangle + \frac{1}{V} \int_{A_k} \mathbf{u}_{ki} \cdot \mathbf{n}_k dA \quad (\text{A.14})$$

Averaging of the time derivative

$$\left\langle \frac{\partial}{\partial t} \phi \right\rangle = \frac{\partial}{\partial t} \langle \phi \rangle - \frac{1}{V} \int_{A_k} \phi_k \mathbf{u}_{s_i} \cdot \mathbf{n}_k dA \quad (\text{A.15})$$

where \mathbf{n}_k is the outwardly directed normal vector at the interface between phases, A_k is the interfacial area and \mathbf{u}_s is the rate of change of the interface position.





APPENDIX B: VOLUME-TIME AVERAGING OF THE CONTINUITY EQUATION

The instantaneous mass conservation equation for a single phase fluid without additional mass sources is given by

$$\frac{\partial \rho}{\partial t} + \frac{\partial}{\partial x_i} (\rho u_i) = 0 \quad (\text{B.1})$$

Applying volume averaging using equation (A.10) gives

$$\left\langle \frac{\partial \rho_k}{\partial t} \right\rangle + \left\langle \frac{\partial}{\partial x_i} \rho_k u_{ki} \right\rangle = 0 \quad (\text{B.2})$$

Using equations (A.14) and (A.15) one may rewrite equation (B.2) as

$$\frac{\partial}{\partial t} \langle \rho_k \rangle + \frac{\partial}{\partial x_i} \langle \rho_k u_{ki} \rangle = -\frac{1}{V_{A_k}} \int_{A_k} \rho_k (u_{ki} - u_{si}) \cdot n_{ki} dA \quad (\text{B.3})$$

In the absence of any phase changes this becomes

$$\frac{\partial}{\partial t} \langle \rho_k \rangle + \frac{\partial}{\partial x_i} \langle \rho_k u_{ki} \rangle = 0 \quad (\text{B.4})$$

Using equations (A.3) and (A.5) gives the instantaneous volume-averaged continuity equation

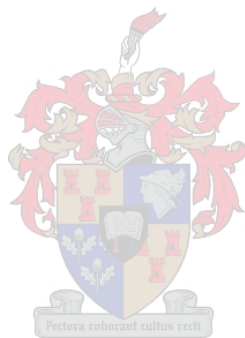
$$\frac{\partial}{\partial t} \alpha_k^i \langle \rho_k \rangle + \frac{\partial}{\partial x_i} \left(\alpha_k^i \langle \rho_k \rangle^i \langle u_{ki} \rangle \right) = 0 \quad (\text{B.5})$$

Assuming constant intrinsic density and applying time averaging to equation (B.5) one finds

$$\frac{\partial}{\partial t} \overline{\alpha_k} + \frac{\partial}{\partial x_i} \left(\overline{\alpha_k^i \langle u_{ki} \rangle} + \overline{\alpha_k' \langle u_{ki}' \rangle} \right) = 0 \quad (\text{B.6})$$

After dropping all brackets and overbars for simplicity, the volume time average continuity equation reads

$$\frac{\partial}{\partial t} (\alpha_k) + \frac{\partial}{\partial x_i} (\alpha_k \bar{u}_i) + \frac{\partial}{\partial x_i} (\alpha_k' u_i') = 0 \quad (\text{B.7})$$



APPENDIX C: VOLUME-TIME AVERAGING OF THE MOMENTUM EQUATION

The instantaneous momentum conservation equation for a single phase fluid is given by

$$\frac{\partial}{\partial t}(\rho_k u_{ki}) + \frac{\partial}{\partial x_j}(\rho_k u_{ki} u_{kj}) = -\frac{\partial p_k}{\partial x_i} + \frac{\partial}{\partial x_j}(\tau_{kij}) + \rho_k g_i \quad (C.1)$$

where the shear stress tensor is given for an incompressible fluid by

$$\tau_{kij} = \mu \left(\frac{\partial u_{ki}}{\partial x_j} + \frac{\partial u_{kj}}{\partial x_i} \right) \quad (C.2)$$

Applying volume averaging one finds using equation (A.10)

$$\left\langle \frac{\partial}{\partial t}(\rho_k u_{ki}) \right\rangle + \left\langle \frac{\partial}{\partial x_j}(\rho_k u_{ki} u_{kj}) \right\rangle = \left\langle -\frac{\partial p_k}{\partial x_i} \right\rangle + \left\langle \frac{\partial}{\partial x_j}(\tau_{kij}) \right\rangle + \langle \rho_k g_i \rangle \quad (C.3)$$

Employing equations (A.13), (A.14) and (A.15) to rewrite equation (C.3) yields

$$\begin{aligned} \frac{\partial}{\partial t} \langle \rho_k u_{ki} \rangle - \frac{1}{V} \int_{A_k} \rho_k u_{ki} u_{sj} \cdot n_{kj} dA + \frac{\partial}{\partial x_j} \langle \rho_k u_{ki} u_{kj} \rangle + \frac{1}{V} \int_{A_k} \rho_k u_{ki} u_{kj} \cdot n_{kj} dA = \\ - \frac{\partial}{\partial x_i} \langle p_k \rangle + \frac{1}{V} \int_{A_k} -p_k n_{ki} dA + \frac{\partial}{\partial x_j} \langle \tau_{kij} \rangle + \frac{1}{V} \int_{A_k} \tau_{kij} \cdot n_{kj} dA + \langle \rho_k \rangle g_i \end{aligned} \quad (C.4)$$

which is simplified to

$$\frac{\partial}{\partial t} \langle \rho_k u_{ki} \rangle + \frac{\partial}{\partial x_j} \langle \rho_k u_{ki} u_{kj} \rangle = -\frac{\partial}{\partial x_i} \langle p_k \rangle + \frac{\partial}{\partial x_j} \langle \tau_{kij} \rangle + \langle \rho_k \rangle g_i + \Gamma_{\tau_i} + \Gamma_{mi} \quad (C.5)$$

where the transfer of pressure and viscous stress across the phase interface is given by

$$\Gamma_{\tau_i} = \frac{1}{V} \int_{A_k} (-p_k n_{ki} + \tau_{kij} \cdot n_{kj}) dA \quad (C.6)$$

and the momentum transfer at the interface due to phase changes are given by

$$\Gamma_{mi} = -\frac{1}{V} \int_{A_k} \rho_k u_{ki} (u_{kj} - u_{sj}) \cdot n_{kj} dA \quad (C.7)$$

In the absence of phase changes equation (C.4) is simply given by

$$\frac{\partial}{\partial t} \langle \rho_k \mathbf{u}_{ki} \rangle + \frac{\partial}{\partial x_j} \langle \rho_k \mathbf{u}_{kj} \mathbf{u}_{ki} \rangle = - \frac{\partial}{\partial x_i} \langle p_k \rangle + \frac{\partial}{\partial x_j} \langle \tau_{kij} \rangle + \langle \rho_k \rangle g_i + \Gamma_{\tau_i} \quad (\text{C.8})$$

Using equation (A.5) and applying time averaging to equation (C.5) one finds for the first term on the left hand side

$$\frac{\partial}{\partial t} \overline{\langle \rho_k \mathbf{u}_{ki} \rangle} = \frac{\partial}{\partial t} \overline{\langle \rho_k \rangle^i \langle \mathbf{u}_{ki} \rangle} = \frac{\partial}{\partial t} \left(\overline{\langle \rho_k \rangle^i \langle \mathbf{u}_{ki} \rangle} + \overline{\langle \rho'_k \rangle^i \langle \mathbf{u}'_{ki} \rangle} \right) \quad (\text{C.9})$$

and for the second term on the left hand side of equation (C.8) one finds

$$\begin{aligned} \frac{\partial}{\partial x_j} \overline{\langle \rho_k \mathbf{u}_{kj} \mathbf{u}_{ki} \rangle} &= \frac{\partial}{\partial x_j} \overline{\langle \rho_k \rangle^i \langle \mathbf{u}_{kj} \mathbf{u}_{ki} \rangle} = \frac{\partial}{\partial x_j} \overline{\langle \rho_k + \rho'_k \rangle^i \langle (\mathbf{u}_{kj} + \mathbf{u}'_{kj})(\mathbf{u}_{ki} + \mathbf{u}'_{ki}) \rangle} = \\ &= \frac{\partial}{\partial x_j} \overline{\langle \rho_k \rangle^i \langle \mathbf{u}_{kj} \rangle^i \langle \mathbf{u}_{ki} \rangle} + \left(\overline{\langle \rho_k \rangle^i \langle \mathbf{u}'_{kj} \mathbf{u}'_{ki} \rangle} + \overline{\langle \rho'_k \rangle^i \langle \mathbf{u}'_{kj} \mathbf{u}'_{ki} \rangle} \right) + \\ &= \frac{\partial}{\partial x_j} \overline{\langle \mathbf{u}_{kj} \rangle^i \langle \mathbf{u}_{ki} \rangle} + \overline{\langle \rho'_k \rangle^i \langle \mathbf{u}'_{ki} \rangle} + \overline{\langle \rho'_k \rangle^i \langle \mathbf{u}'_{kj} \rangle^i \langle \mathbf{u}_{ki} \rangle} \end{aligned} \quad (\text{C.10})$$

The terms on the right hand side of equation (C.8) after time averaging is

$$- \frac{\partial}{\partial x_i} \overline{\langle p_k \rangle} = - \frac{\partial}{\partial x_i} \langle \overline{p_k} \rangle \quad (\text{C.11})$$

$$\frac{\partial}{\partial x_j} \overline{\langle \tau_{kij} \rangle} = - \frac{\partial}{\partial x_j} \langle \overline{\tau_{kij}} \rangle \quad (\text{C.12})$$

$$\overline{\langle \rho_k \rangle g_i} = \langle \overline{\rho_k} \rangle g_i \quad (\text{C.13})$$

Combining terms and applying equation (A.3) while assuming that the fluid density remains constant, gives the volume-time averaged momentum equation for phase k in the continuum.

Dropping overbars and brackets for simplicity gives

$$\begin{aligned} \frac{\partial}{\partial t} (\alpha_k \bar{u}_{ki} + \alpha'_k u'_{ki}) + \frac{\partial}{\partial x_j} (\alpha_k \bar{u}_{kj} \bar{u}_{ki}) &= - \frac{1}{\rho_k} \frac{\partial (\alpha_k p_k)}{\partial x_i} + \frac{1}{\rho_k} \frac{\partial}{\partial x_j} (\tau_{kij}) + \alpha_k g_i \\ + \frac{\Gamma_{ki}}{\rho_k} - \frac{\partial}{\partial x_j} (\bar{u}_{kj} (\rho_k \alpha'_k u'_{ki}) + \bar{u}_{ki} (\rho_k \alpha'_k u'_{kj})) \end{aligned} \quad (\text{C.14})$$

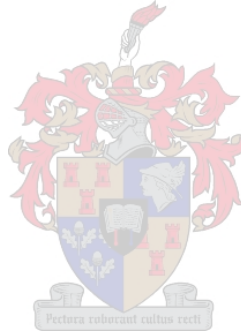
where the last term on the right hand side of equation (C.14) accounts for the momentum flux due to the eddy mass diffusion of phase k and the apparent stress tensor given by

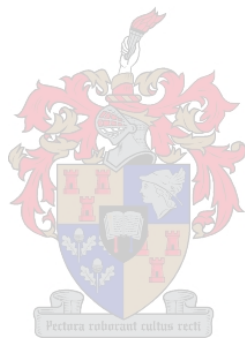
$$\tau_{kij} = \alpha_k \mu_k \left(\frac{\partial \bar{u}_{ki}}{\partial x_j} + \frac{\partial \bar{u}_{kj}}{\partial x_i} \right) - \alpha_k \rho_k \overline{u'_{ki} u'_{kj}} + \overline{\rho_k \alpha'_k u'_{ki} u'_{kj}} \quad (\text{C.15})$$

If the last term in equation (C.15) is negligible along with the momentum transfer due to the eddy mass diffusion terms in equation (C.14) then equation (C.14) is simplified to

$$\frac{\partial}{\partial t}(\alpha_k \bar{u}_{ki}) + \frac{\partial}{\partial x_j}(\alpha_k \bar{u}_{kj} \bar{u}_{ki}) = -\frac{1}{\rho_k} \frac{\partial(\alpha_k p_k)}{\partial x_i} + \frac{1}{\rho_k} \frac{\partial}{\partial x_j}(\tau_{kij}) + \alpha_k g_i + \frac{\Gamma_{\tau_i}}{\rho_k} \quad (\text{C.16})$$

$$\tau_{kij} = \alpha_k \mu_k \left(\frac{\partial \bar{u}_{ki}}{\partial x_j} + \frac{\partial \bar{u}_{kj}}{\partial x_i} \right) - \alpha_k \rho_k \overline{u'_{ki} u'_{kj}} \quad (\text{C.17})$$





APPENDIX D: THE DISPERSED PHASE MASS CONSERVATION EQUATION (DIFFUSION EQUATION)

The starting point for the dispersed phase diffusion equation is the volume-time averaged continuity equation of a general phase k, equation (B.7)

$$\frac{\partial}{\partial t}(\alpha_k) + \frac{\partial}{\partial x_i}(\alpha_k \bar{u}_{ki}) + \frac{\partial}{\partial x_i}(\alpha'_k u'_{ki}) = \phi_s \quad (D.1)$$

The term on the right hand side of equation (D.1) accounts for phase change of dispersed phase per unit volume or an additional mass source per unit volume. For no phase change or additional mass sources $\phi_s=0$.

Considering only a snow source contribution from precipitation gives

$$\phi_s = \frac{\partial}{\partial x_i}(\alpha_k w_i) \quad (D.2)$$

where the precipitation vector w_j equals the snow particle fall velocity

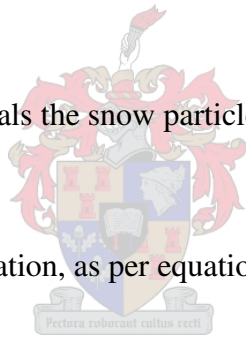
$$w_i = 0\bar{i} + 0\bar{j} - w_f \bar{k} \quad (D.3)$$

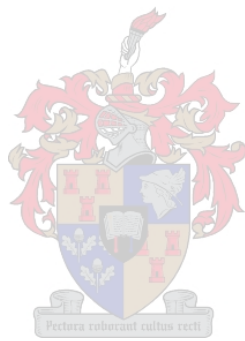
The volume averaged snow concentration, as per equation (A.3) is given by

$$\eta_k = \alpha_k \rho_k \quad (D.4)$$

Introducing equations (D.2) and (D.4) into (D.1) yields

$$\frac{\partial}{\partial t}(\eta_k) + \frac{\partial}{\partial x_i}(\eta_k \bar{u}_{ki}) = - \frac{\partial}{\partial x_i}(\eta'_k u'_{ki} + \eta_k w_i) \quad (D.5)$$





APPENDIX E: ANALYTICAL SOLUTION OF THE TURBULENT VELOCITY PROFILE

Neutral conditions

For steady two-dimensional horizontal flow in the surface layer we may assume that the flow characteristics vary only with height. The viscous and apparent stress terms in the Navier Stokes equation then reduce to

$$\tau_{xz} = \mu \frac{\partial u}{\partial z} - \overline{\rho u'w'} \quad (\text{E.1})$$

In order to approximate the turbulent flux term one may employ a first order closure scheme or K-theory, credited to Schmidt (1925) and Prandtl (1925), although Prandtl states that it originates from Boussinesq (1877). This theory is analogous to kinetic gas theory i.e. gas particles collide with each other and travel a discrete distance between collisions (the particle mean free path). First order closure only assumes that fluid parcels mix with each other from time to time and in between mixing events travel the so-called mixing length. This theory allows one to relate the turbulent fluxes to a gradient of mean quantities. One may then formulate a relationship for the vertical eddy flux of any conservative scalar property i.e.

$$-\overline{\rho u'_i \phi'} = \rho K_\phi \frac{\partial u_i}{\partial x_j} \quad (\text{E.2})$$

Employing equation (E.2) to re-write equation (E.1) as

$$\tau_{xz} = \rho(\nu + K) \frac{\partial u}{\partial z} \quad (\text{E.3})$$

For steady state conditions we see that the change in the stress vector in the Navier Stokes equations is negligible in the surface layer which implies that the stress is constant. This allows one to define a friction velocity

$$u_* = \sqrt{\frac{\tau}{\rho}} \quad (\text{E.4})$$

The shear stress is constant in the inner layer and decaying to zero in the outer layer to the edge of the boundary layer. In the inner layer (0.15δ) the shear stress consists of rapidly decaying viscous stress and rapidly increasing Reynolds stress. The outer layer consists only

of gradually vanishing Reynolds stress up to the edge of the boundary layer, Zippe and Graf (1983) among others.

The eddy exchange coefficient, K , in neutral atmospheres are normally written in terms of a length scale, κz , and a velocity scale, u_* , the friction velocity, Bintanja (2000a) so that

$$K_x = \kappa u_* z \quad (\text{E.5})$$

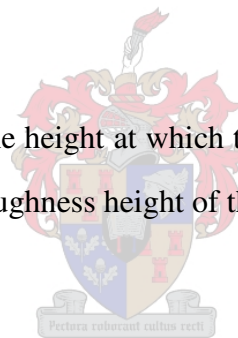
Near the surface, the molecular viscosity effects are usually insignificant compared to turbulent fluxes and the combination of equations (E.3), (E.4) and (E.5) gives

$$\frac{\kappa z}{u_*} \frac{\partial u}{\partial z} = 1 \quad (\text{E.6})$$

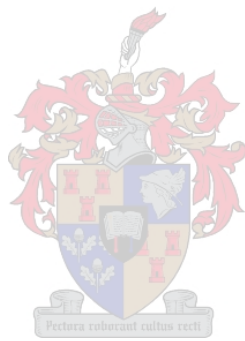
which upon integration in height gives the well-known logarithmic velocity profile used for neutrally stable atmospheric boundary layers i.e.

$$u = \frac{u_*}{\kappa} \ln \left(\frac{z}{z_0} \right) \quad (\text{E.7})$$

The constant of integration, z_0 , is the height at which the mean wind speed tends to zero and is to some extent indicative of the roughness height of the surface.







APPENDIX F: ANALYTICAL SOLUTION OF THE SNOW CONCENTRATION PROFILE

For horizontal homogeneous flow without sublimation the particle concentration equation for the air-snow mixture reads

$$\frac{\partial \eta}{\partial t} = \frac{\partial}{\partial z} \left(-\overline{\eta'w'} - w_f \eta \right) \quad (\text{F.1})$$

This is simplified by first-order closure i.e. K-theory to yield

$$\frac{\partial \eta}{\partial t} = \frac{\partial}{\partial z} \left(\kappa u_* z \frac{\partial \eta}{\partial z} - w_f \eta \right) \quad (\text{F.2})$$

resulting in the steady state vertical particle distribution equation given by

$$\frac{\partial}{\partial z} \left(\kappa u_* z \frac{\partial \eta}{\partial z} - w_f \eta \right) = 0 \quad (\text{F.3})$$

Vertical integration of equation (F.3) gives

$$\kappa u_* z \frac{\partial \eta}{\partial z} - w_f \eta = P \quad (\text{F.4})$$

where the vertical flux of snow particles at the surface is given by P, namely

$$P = \left(\kappa u_* z \frac{\partial \eta}{\partial z} - w_f \eta \right)_{z=0} \quad (\text{F.5})$$

When snow fall is ignored the vertical transport of snow is only a balance of the downward gravitational settling and the upward turbulent diffusivity as per the left hand side of equation (F.4) resulting in (for P=0) in

$$\frac{\partial \eta}{\partial z} = \frac{w_f \eta}{\kappa u_* z} \quad (\text{F.6})$$

which upon height integration gives

$$\ln(\eta) = \beta \ln(z) + C \quad (\text{F.7})$$

To find the integration constant we assume a known reference density, η_r , at a reference height, z_r , which gives

$$C = \ln(\eta_r) - \beta \ln(z_r) \quad (\text{F.8})$$

Inserting equation (F.4) into (F.3) yields the well known suspension concentration equation of Shiotani and Arai (1953)

$$\frac{\eta}{\eta_r} = \left(\frac{z}{z_r} \right)^\beta \quad (\text{F.9})$$

where

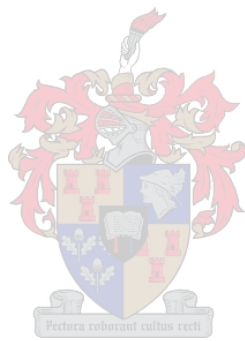
$$\beta = - \frac{w_f}{\kappa u_*}$$

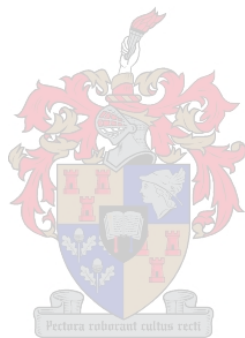
Budd et al. (1966) used this equation to determine the suspended snow concentration profile. Experiments have shown that the best fit for the snow concentration profile is a function of height to the power of -1 while the theory suggest a power of $-w_f / \kappa u_*$, Mellor and Fellers (1986).

Kobayashi et al. (1985) derive the same equation but include the mass source term due to falling snow ($P \neq 0$). The resulting equation is

$$\eta = \frac{P}{w_f} + \left(\eta_r - \frac{P}{w_f} \right) \exp\left(\frac{-w_f}{K} z \right) \quad (\text{F.10})$$

where K is the eddy diffusivity. The asymptote of equation (F.10) for $z \rightarrow \infty$ gives the falling snow fall density during drifting snow conditions. Thus when snow flux is measured during blowing snow conditions this asymptote may give the falling snow mass flux which may otherwise be extremely difficult to determine.





APPENDIX G: EXPERIMENTAL MODELLING

G.1. INTRODUCTION

The new SANAE IV research station was completed in 1996 and operation commenced in 1997. The station is situated on top and on the edge of a nunatak, a rocky outcrop, named Vesleskarvet, 71° 40' S 2° 49' W, in Dronning Maud Land, Antarctica. The base structure consists of three main sections raised on support columns 4 m above the ground surface. The main sections are joined via interconnecting passages. Figures 6.1 and 6.2 show the layout and plan of the SANAE IV base as well as its position on the nunatak.

One aim of the aerodynamic design of the base is to minimize the accumulation of wind driven snow in the vicinity of the base and thereby reducing the impact of the base on the environment as well as reducing snow removal maintenance. Leeward of the interconnecting passages, localised snowdrift formations are formed during high intensity winds with accompanying blown snow. These snowdrifts are approximately 60 m long, 3 m high and run from the leeward side of the base along the predominant wind direction. The approaching winds with accompanying blowing snow approach the base predominantly from the northeast, east or the southeast. Figure 6.2 illustrates the location of the snowdrifts behind the SANAE IV station. The aim of the present research is to evaluate and model this snow flow and local snow buildup phenomena and snowdrift formation in order to understand their governing parameters. Once the modelling procedure is found to be accurate it could assist the critical evaluation of possible remedial design proposals. In order to perform the necessary snow buildup modelling, the relevant similitude requirements need to be met and the approaching wind velocity profiles need to be determined in order to evaluate the surface roughness and shear velocity parameters for the problem at hand. This is described below. In the text below the 1:25 base model is referred to as the model and the as-built SANAE IV station is referred to as the prototype.

G.2. FIELD EXPERIMENTS

The field testing consisted of two periods where observations and measurements were carried out at two different locations. The first set of wind measurements was carried out on a large

snow covered area in the vicinity of the SANAE IV station (71°39'S 2°48'W). This is also the area where the experimental modelling was carried out with the 1:25 scale model of the base. The model scale factor was selected primarily to ensure that possible snow drifting conditions would not necessarily bury the model during higher wind conditions, as would be the scenario for a smaller scale model. However, an even larger scale model would have been preferred but proved impractical due to present logistical constraints for transport and field erection. Future research could employ larger scale models that would probably prove more effective over a wider range of snow drifting conditions. The measurements were taken from 1 January 2002 to 28 January 2002 during the Antarctic summer research season.

The scale model study area was selected since no obstructions are nearby and it is situated 2 km upwind of the nunatak on which SANAE IV is built. The prevailing winds experienced in this area are northeastern, eastern or southeastern winds with rare katabatic winds approaching from the south. The winds measured during the test period are considered not to be katabatic. The Geophysics Division from Helsinki University, Finland, measured the snow properties in the testing area during their FINNARP-2000 expedition. The measured bulk snow density of the surface layers ranged between $450 \text{ kg}\cdot\text{m}^{-3}$ and $550 \text{ kg}\cdot\text{m}^{-3}$. The precipitating snow particle as well as older surface snow particles taken from the Aboa research station, 72°S, 10°W, are shown in figure G.1. The snow properties at the SANAE IV location are assumed to be similar to those shown here. The snow surface in this test area consisted mainly of old compacted snow covered with small sastrugi present at the start of the test period.

The wind profiles were measured with four MCS 7 aluminium cup type anemometers, mounted on a 6m mast and positioned 0.5 m, 1.4 m, 2.7 m and 5.5 m above the snow surface. The sensors were mounted on horizontal arms 0.5 m in length and orientated in a north-south direction to minimise interference from the weather mast. The mast was initially placed 200 m east of the 1:25 scale model. The scale model was orientated similarly to the existing station orientation, shown in figure 6.2. The wind velocities were logged at 15-minute intervals on a MCS 120 RS232 digital logger. The time of initiation of blowing snow was also logged through visual observation to determine the threshold wind speed for snow saltation. The extrapolated 10 m wind speeds for the duration of the test period are shown in figure G.2. The threshold 10 m wind speed was found to be $8\text{m}\cdot\text{s}^{-1}$. This is in general agreement with

observations by Li and Pomeroy (1997). Since very little snow precipitation occurs in the area it is assumed that the snow is old and wind hardened with high threshold velocity characteristics.

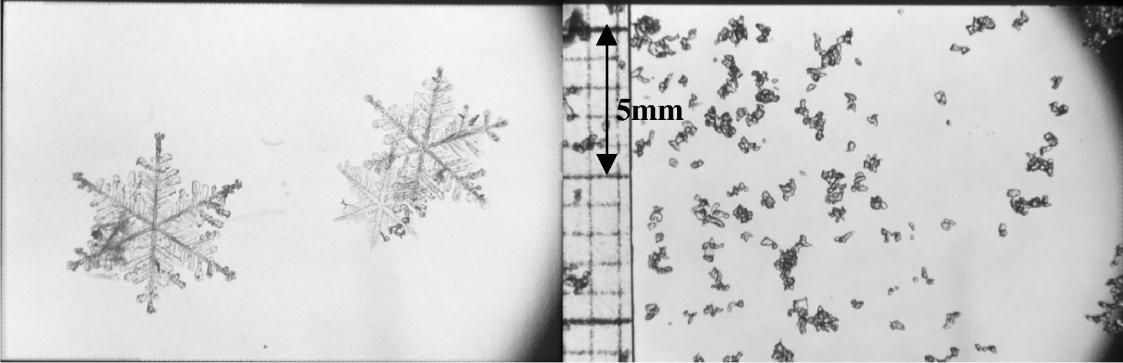


Figure G.1. Snow particles evaluated near Aboa during FINNARP-2000. Courtesy of Eija Karkas, Division of Geophysics, University of Helsinki, Finland. (left) Precipitating snow flakes, and (right) top surface layer

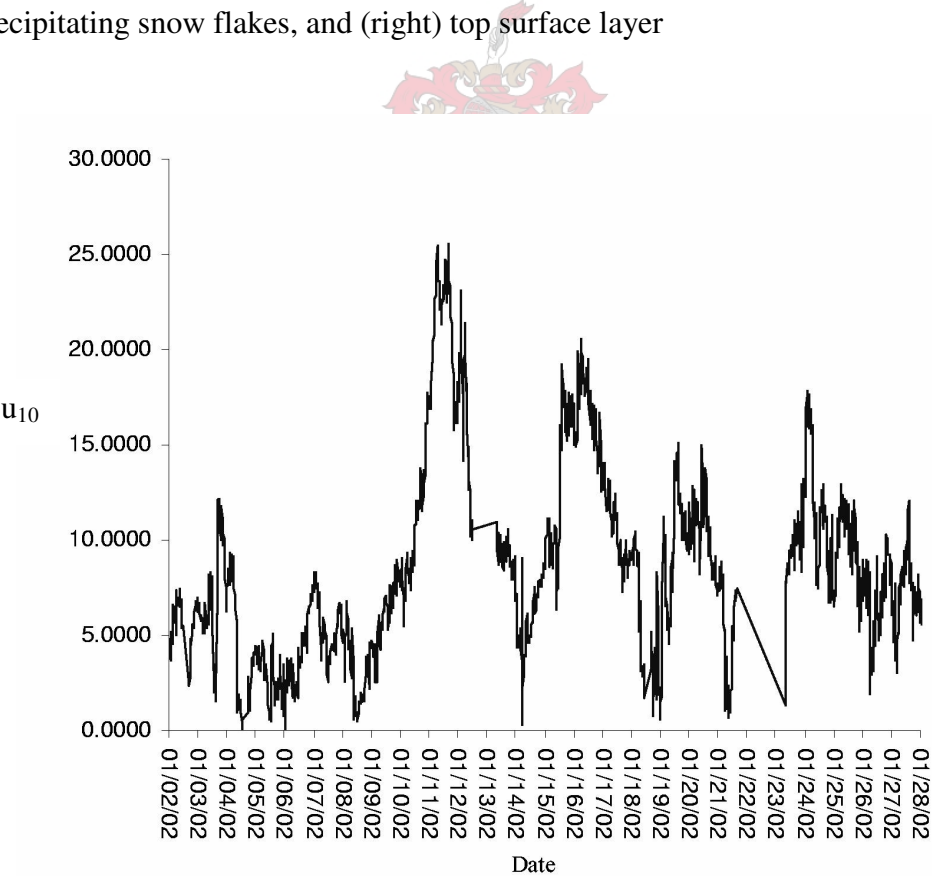


Figure G.2. Extrapolated 10 m wind speeds measured at SANAE IV during January 2002.

During this observation period two major storms occurred with wind speeds in excess of the threshold wind speed. The first and heaviest of the two storms lasted from approximately 10 January to 12 January 2002 and corresponded to snow accumulation of approximately 0.5m in the test area. Figure G.3 shows the weather mast with wind sensors and the 1:25 scale model of the SANAE IV research station A and B sections with interconnecting link.

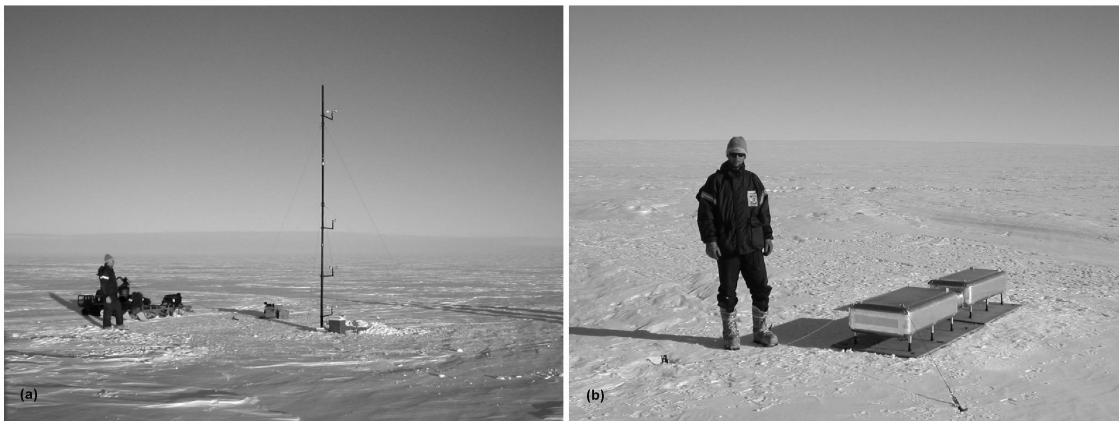


Figure G.3. Weather mast for wind velocity profiles at first measurement site (a) and the author next to the SANAE IV 1:25 scale model (b)

The second set of measurements was carried out near the SANAE IV base, on top of the nunatak, from 18 January 2002 onwards, to establish wind profile information near the location of the research station. The surface of the hill here is covered in snow with scattered rocks protruding approximately 0.3m above surface. The measurement site was located west of the first site. It was assumed that the change in wind direction between the two sites is negligible due to the gradual slope of the hill towards the second site. The data gathered during the two measurement periods provides the necessary wind velocity profiles for both the model area (snow covered area) and prototype area (rocky hill near SANAE IV), which are subsequently used in the similarity analysis discussed below. Wind direction data was obtained from the automatic weather station located at the research station. No other wind velocity measurements were taken near the model or the prototype.

G.3. THEORETICAL APPROACH

The near ground turbulent wind velocity profile for stable atmospheric conditions may be developed from the logarithmic near wall velocity profile, White (1991) and is commonly presented in the form

$$\frac{u}{u_*} = \frac{1}{\kappa} \ln\left(\frac{z}{z_0}\right) \quad (\text{G.1})$$

for situations where the surface roughness is small in comparison to the height scale. Measurements by Budd (1966) and Liljequist (1957) demonstrated that this equation is also valid for blowing snow conditions although Kind and Murray (1982) and Janin and Cermak (1988) have pointed out that sediment laden velocity profiles are better described by Coles law of the wake, White (1991), for the upper 90% of the boundary layer. A regression analysis was performed to fit an exponential curve of the form, $z = bm^u$, through the wind velocity data obtained from the wind sensors. From this regression analysis and equation (G.1) we find the surface roughness and shear velocity functions from

$$z_0 = b \quad (\text{G.2})$$

$$u_* = \frac{\kappa}{\ln(m)} \quad (\text{G.3})$$

With these values the 10m wind speed may be extrapolated from equation (G.1) and is presented in figure (G.2). The average regression coefficient for the fit of the measured data to equation (G.1) is $R^2=0.958$ for $u_{10}>3.0 \text{ m}\cdot\text{s}^{-1}$. Bagnold (1941) showed that the effective surface roughness for sand laden flows may be described as a function of the square of the shear velocity i.e.

$$z_0 = \frac{c_1 u_*^2}{2g} \quad (\text{G.4})$$

Blowing snow may be regarded as a similar process, Budd (1966), Liljequist (1957), Sundsbø (1997), and numerous researchers have presented their results to suit equation (G.4), with the constant c_1 depending on the quality of the snow and the snow surface. Bagnold (1941) also proposed a correlation in a different form namely

$$z_0 = c_1 \exp\left(\frac{-0.4 \cdot c_2}{u_*}\right) \quad (\text{G.5})$$

with $c_1=0.003$ and $c_2=2.5$. Tabler (1980a) suggests equation (G.5) with $c_1=0.0019$ and $c_2=2.15$. Table G.1 summarises earlier results as well as results from the present work.

Table G.1. Proportionality constant c_1 for use in equation (G.19)

		c_1
Tabler (1980a) 75% snow covered lake		0.02648
Tabler (1980a) 20%-60% snow covered lake		0.00710
Pomeroy (1988)		0.12
Owen (1980)		0.0207
Budd (1966)		0.0122
Liljequist (1957)		0.0305
SANAE IV: Snow covered area with small sastrugi	$k \approx 0.0$	0.0035
SANAE IV: Snow covered nunatak with rocks	$k \approx 0.3$	0.094

For flow over a smooth plate one may find from equation (G.1)

$$z_0 = \frac{v}{9.53u_*} \quad (G.6)$$

The surface roughness parameters calculated from the wind profile data gathered in the present study are compared to the values calculated from the above correlations and the results, as shown in figure (G.4), are discussed below.

The present data can be grouped into two categories, the data gathered in the snow-covered area before 18 January 2002 and the data gathered on top of Vesleskarvet thereafter. In the period before 18 January 2002, the first storm occurred after three days of exceptionally warm weather, day temperatures of approximately +4 °C. This essentially meant that the old snow in the test area ‘thawed’. This should result in higher required threshold wind speeds and smaller effective surface roughness due to less snow saltating at lower wind speeds, Tabler (1980a). The data obtained shows large scattering for $0.2 \leq u_* \leq 0.4$. This seems to follow the trend of the data of Liljequist (1957) as given by Tabler (1980a). The data measured at SANAE IV for the snow-covered area and $u_* \geq 0.4 \text{ m}\cdot\text{s}^{-1}$ best fits the curve

$$z_0 = \frac{0.0027u_*^2}{2g}, R^2 = 0.33 \quad (G.7)$$

with 95 % confidence interval for coefficient c_1 ranging between 0.0025 and 0.0029. The scattered data are mostly higher values than those predicted by equation (G.7) and originate from data measured during the early stages of the experiment. This may suggest that the strong wind conditions progressively smoothed and wind hardened the snow surface in the vicinity of the wind mast. Equation (G.7) gives roughness values marginally smaller than those found from equation (G.4) for up to 60 % snow cover, Tabler (1980a).

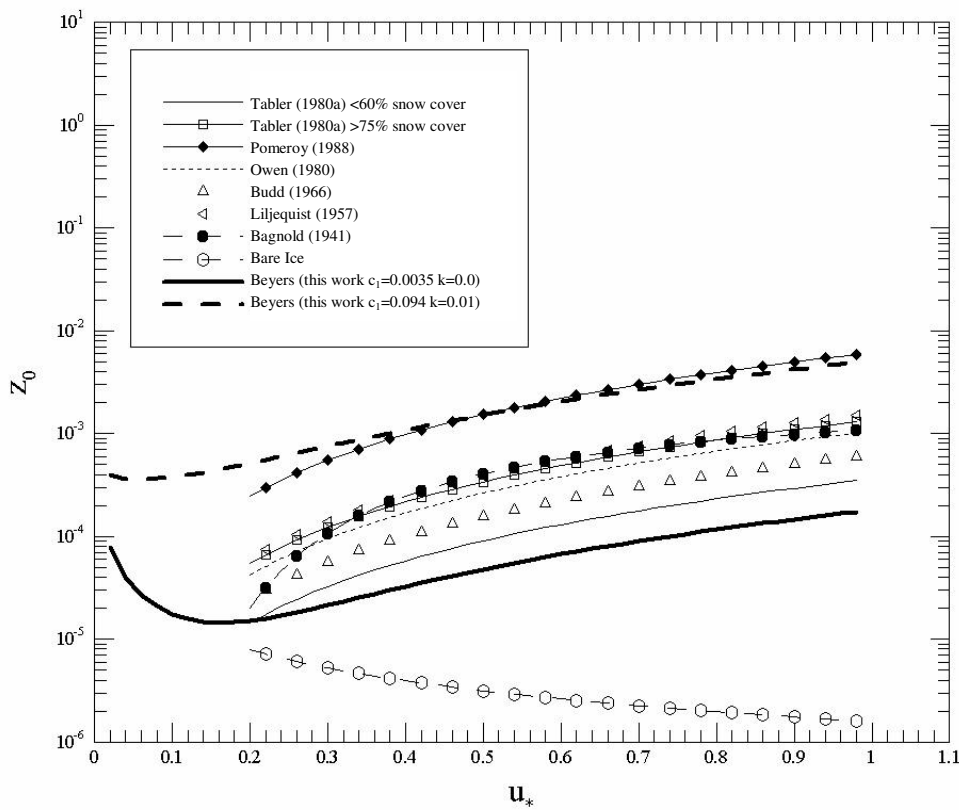


Figure G.4. Roughness height as a function of shear velocity at SANAE IV for the snow covered area and on top of Vesleskarvet (rock cover)

During the later stages of the wind measurements carried out from 10-12 January 2002, a heavy deposition of blown snow, approximately 0.5 m deep, occurred throughout the test area as well as on the rock covered hill at SANAE IV. Therefore the subsequent wind conditions may have corresponded to slightly lower threshold wind speeds to entrain snow particles from the surface. As mentioned earlier, the wind mast was moved to the top of Vesleskarvet and

located in the vicinity of SANAE IV. The surface roughness parameters calculated from the data that was gathered here after 18 January 2002, best fits the curve

$$z_0 = \frac{0.0845u_*^2}{2g} \quad (G.8)$$

for $u_* \geq 0.4 \text{ m}\cdot\text{s}^{-1}$ although poor regression coefficients are found when fitting equation (G.4). However, the 95% confidence interval for coefficient c_1 ranges between 0.07551 and 0.0935. Equation (G.8) is applicable to the snow covered area with protruding rocks ($k = 0.3 \text{ m}$). Equations (G.7) and (G.8) are applicable for $u_* > u_{*t}$ and describe the effective surface roughness and include the combined effects of the natural surface quality as well as the additional roughness due to the presence of creeping and saltating snow particles, Tabler (1980a). Performing the above regression analysis simply by employing equation (G.1) does not include the stability effects of the suspended snow particles on the resulting velocity profile, Bintanja (1998), (2000a), (2001a). Bintanja (1998), (2000a) present a modified logarithmic velocity profile, which includes these particle buoyancy effects, based on an Obukhov length for particle stratification. This velocity profile equation reads

$$u(z) = \frac{u_*}{\kappa} \left[(1 + A\alpha) \ln\left(\frac{z}{z_0}\right) + \frac{A(z - z_0)}{L_\eta} \right] \quad (G.9)$$

where for the simplicity in the present analysis $A=5.5$ and

$$\alpha = -0.06295 + 0.4369u_* - 0.8334u_*^2 + 0.6792u_*^3 - 0.2046u_*^4$$

as per Bintanja (1998). The Obukhov length for particle stratification, Bintanja (2000a), may be given by

$$L_\eta = u_*^2 \rho_a / \left(\xi g \kappa^2 \frac{\partial \eta}{\partial z} \right) \quad (G.10)$$

Although debatable, the ratio of the eddy exchange coefficients for momentum and for particle suspension, ξ , is assumed to equal 1 for the present analysis. In the absence of snow flux measurements, the suspended snow mass concentration gradient in equation (G.10) is presently found from an equation derived by Pomeroy and Male (1992) i.e.

$$\eta(z) = 0.8 \exp\left[-1.55\left(4.784u_*^{-0.544} - z^{-0.544}\right)\right] \quad (G.11)$$

By employing equation (G.9) to (G.11) in the regression analysis, slightly different coefficients are found for equation (G.4). The resultant modified equation (G.7) for the first set of data now reads

$$z_0 = \frac{0.0035u_*^2}{2g}, R^2 = 0.71 \quad (G.12)$$

with 95% confidence interval for coefficient c_1 ranging between 0.0033 and 0.0037. The resultant modified equation (G.8) for the second set of data now reads

$$z_0 = \frac{0.0940u_*^2}{2g} \quad (G.13)$$

with 95% confidence interval for coefficient c_1 ranging between 0.0881 and 0.0998.

These new equations are considered to better describe the surface roughness in the presence of suspended snow since it is found from a velocity profile which includes the potential stability effects of suspended snow. Equations (G.12) and (G.13) are subsequently used in the similarity analysis discussed below.

For single-phase flows over rough surfaces we may deduce

$$z_0 = \frac{v}{9.53u_*} + 0.0315k \quad (G.14)$$

where k is the effective height of a surface roughness, Nikuradse (1933). Equations (G.14) with (G.12) or (G.13) may be represented by a single function to describe a velocity profile including drifting snow over surfaces of varying roughness namely

$$\frac{u}{u_*} = \frac{1}{\kappa} \ln\left(\frac{zu_*}{v}\right) + B - \Delta B(k^+, s^+) \quad (G.15)$$

where $B=5.5$ and in similar manner to White (1991) for rough flow in pipes

$$\Delta B(k^+, s^+) = \frac{1}{\kappa} \ln(1 + 0.3k^+ + s^+) \quad (G.16)$$

$$k^+ = \frac{ku_*}{v} \quad (G.17)$$

and additionally introducing the parameter

$$s^+ = 9.53 \frac{c_1 u_*^3}{2gv} \quad (G.18)$$

where c_1 is the constant given in Table G.1. The applicability of the Nikuradse (1933) sand grain roughness parameter does remain questionable for the present work, White (1991) and needs further verification. The effective surface roughness function calculated from equation (G.15) is then given for completeness as

$$z_0 = \frac{v}{9.53u_*} + 0.0315k + \frac{c_1 u_*^2}{2g} \quad k \leq 0.01 \quad (G.19)$$

and is shown in figure G.5 for both the snow covered area as well as the rocky hill measured near the SANAE IV base. Note that the curve for the rocky area was found with an effective roughness height of $k=0.01$ instead of the earlier mentioned $k=0.3$.

Another important correlation is found from the evaluation of the shear velocity as a function of the 10 m wind speed. Here Tabler (1980a) suggests

$$u_* = 0.024u_{10}^{1.18} \quad (G.20)$$

for a 75% snow covered lake and

$$u_* = 0.0241u_{10}^{1.12} \quad (G.21)$$

for 20%-60% snow cover. For bare ice he suggests

$$u_* = 0.0347u_{10}^{0.92} \quad (G.22)$$

Pomeroy (1988) gives

$$u_* = 0.02264u_{10}^{1.295} \quad (G.23)$$

The data gathered before 18 January 2002 in the snow covered area follows the curve

$$u_* = 0.024u_{10}^{1.16}, R^2 = 0.65 \quad (G.24)$$

when employing equation (G.1) to find the corresponding 10m velocities. When equation (G.9) is used in the analysis to include particle buoyancy stability effects, the results change slightly to

$$u_* = 0.024u_{10}^{1.19}, R^2 = 0.69 \quad (G.25)$$

The data gathered after 18 January 2002 on top of the rocky hill fits the curve

$$u_* = 0.023u_{10}^{1.23}, R^2 = 0.79 \quad (G.26)$$

when employing equation (G.1) to find the corresponding 10 m velocities. Again by employing equation (G.9) instead, this data set fits the curve

$$u_* = 0.022u_{10}^{1.23}, R^2 = 0.78 \tag{G.27}$$

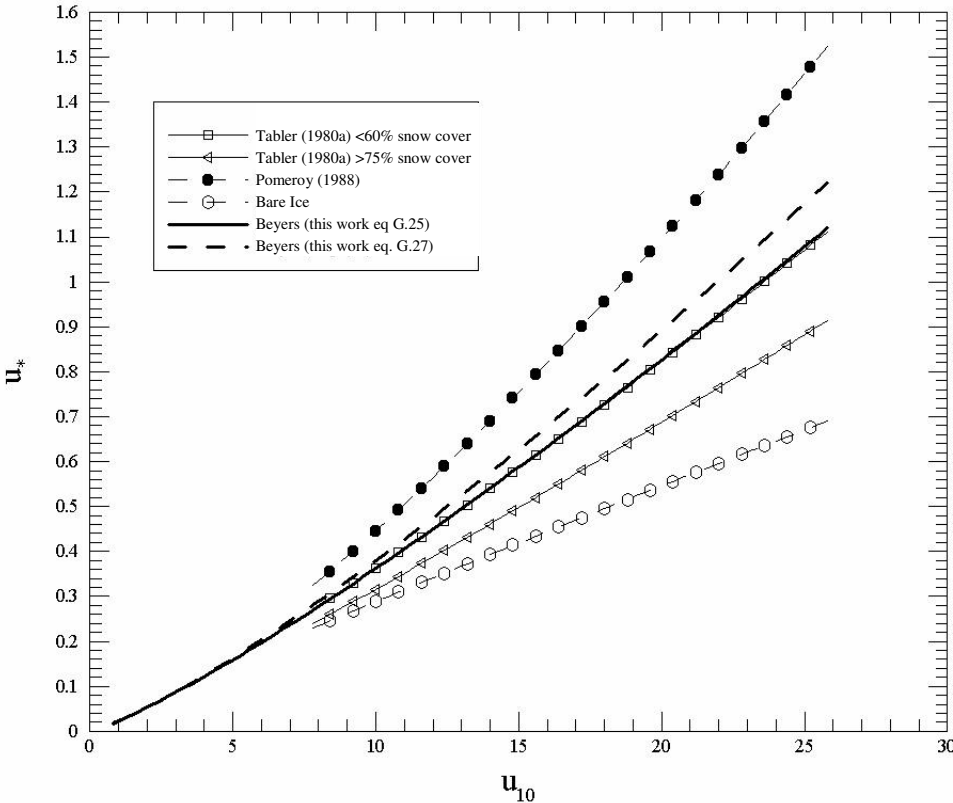


Figure G.5. Shear velocity as a function of 10m wind speed for SANAE IV at the snow covered area and on top of Vesleskarvet (rock cover)

Equations (G.25) and (G.27) are subsequently used in the similarity analysis discussed below. Figure G.5 shows the comparison between the shear velocity function results derived from the data gathered at SANAE IV and those obtained from the correlations described above. As intended, equation (G.27) follows the larger u_* values due to the presence of the rocky protrusions in addition to the saltating snow.

G.4. SNOW MODELLING THEORY

In order to model the large-scale snow buildup phenomena behind structures it is necessary to meet geometric, kinematic (scaling of velocities and accelerations) and dynamic (scaling of forces) similitude requirements. Of these, only the more important similarity parameters are discussed below. Firstly geometric similarity should be enforced through the relationship

$$\frac{D_p}{L} \quad (G.28)$$

Since our length scales change between model and prototype even though the snow particle diameter remains the same, we cannot meet this requirement exactly. The basic requirement of dynamic similarity may be measured with the Froude number (ratio between inertial and gravitational forces). Taking into account possible density differences, the densimetrical Froude number is presented by Weubben (1978) or Tabler (1980a) i.e

$$\frac{u_{*t}^2}{D_p g} \frac{\rho_a}{\rho_p - \rho_a} \quad (G.29)$$

and the threshold densimetrical geometrical Froude number

$$\frac{u_{*t}^2}{L g} \frac{\rho_a}{\rho_p - \rho_a} \quad (G.30)$$

The Froude number forces a relationship between the length and the velocity of the model but implies that one cannot scale Froude numbers and Reynolds numbers simultaneously, White (1991). For outdoors modelling such as the present work, the densimetric Froude number reduces to the conventional threshold Froude numbers since density differences are ignored. The effective roughness height parameter is

$$\frac{\rho_a u_*^2}{\rho_p g L} \quad (G.31)$$

and is the same as the geometrical Froude number discussed above for the present work.

The deposition or erosion mechanisms may be modelled through the similarity of the particle ejection process namely

$$\frac{u_*}{u_{*t}} \quad (G.32)$$

Kind's (1982) roughness height Reynolds number is given as

$$\frac{u_{*t}^3}{2gv} \quad (G.33)$$

Similarity of gravity and fluid forces are maintained through

$$\frac{u_f}{u} \quad (G.34)$$

where the snow particle fall velocity is given for simplicity by $u_f = 2.6u_{*t}$, Kwok et al. (1992). Peterka and Petersen (1990) present the saltation length and height from Owen (1980) i.e.

$$l_s = \frac{10.3u_*^2}{g} \quad (G.35)$$

$$h_s = \frac{0.81u_*^2}{g} \quad (G.36)$$

which is again similar to Froude number scaling for outdoors snow modelling. It often becomes impossible to meet all of the requirements mentioned above simultaneously, especially with outdoors modelling situations and therefore some of the similitude requirements need relaxation. For one, kinematic and dynamic similarity cannot be met simultaneously but could only be scaled effectively for a period of time, Tabler (1980a). Anno (1984), (1990) furthermore suggests that Froude number scaling is not as important as the scaling of threshold friction velocity ratios to the actual friction velocity ratios. He proposes that the effective roughness height does not have a strong effect on the shape of the snowdrift. Peterka and Petersen (1990) however suggests that the scaling u/u_t may be relaxed as long as $u/u_t > 1.4$. They also argue that saltation length and therefore the Froude number may be relaxed if the saltation length is small in comparison to the horizontal length of deposition. In order to address the above problem one may employ time scaling. Anno (1990) suggest the following time scaling parameter

$$\frac{TQ\eta}{\rho_p F^2} \quad (G.37)$$

and Iversen (1980) proposed time scaling according to

$$\frac{1}{2} \frac{\rho_a}{\rho_p} \frac{u^2}{gL} \left[1 - \frac{u_t}{u} \right] \frac{uT}{L} \quad (\text{G.38})$$

In order to employ the time scaling as proposed by Anno (1990), equation (G.37), one requires knowledge of the snow mass flux. This quantity was not measured for the present work. Many authors, Budd (1966), Pomeroy and Gray (1990), Pomeroy and Male (1992), Takeuchi (1980) and Mellor and Fellers (1986) provide relationships to calculate this quantity with a diverse range of results. For the present work the total mass flux relationship is calculated from

$$Q = \int_0^{\infty} q dz \quad (\text{G.39})$$

where the mass flux, q , is given by Mellor and Fellers (1986) as

$$\begin{aligned} q = & \exp(10.089 - 0.41049 \ln(z) - 122.03(1/u_{10}) - 0.13256(\ln(z))^2 \\ & - 14.446 \ln(z)(1/u_{10}) - 0.0059773(\ln(z))^3 + 3.2682(\ln(z))^2(1/u_{10}) \\ & + 114.13 \ln(z)(1/u_{10})^2 + 2290.0(1/u_{10})^3 \end{aligned} \quad (\text{G.40})$$

The suspension mass flux is found by integrating equation (G.40) for $H_s < z < 20$ m and is added to the total saltation mass flux calculated for $z < H_s$ from the relationship from Pomeroy and Gray (1990) i.e.

$$Q_{\text{salt}} = \frac{0.68\rho}{u_* g} u_{*t} (u_*^2 - u_{*t}^2) \quad (\text{G.41})$$

The resultant sum of the suspension and saltation total mass flux fits the curve

$$Q = 0.8065u_*^{3.118}, \quad R^2 = 0.98 \quad (\text{G.42})$$

when u_* is given by equation (G.25). Sugiura et al. (1998) and Nishimura et al. (1998) measured saltation snow flux in a wind tunnel and derived an empirical formula for total saltating snow flux given by

$$Q_{\text{salt}} = 1.42u_*^{3.96} \quad (\text{G.43})$$

Ignoring density effects and with the present 1:25 scale model, equations (G.42) and (G.37) give the prototype/model time ratio as

$$\frac{T_p}{T_m} = \frac{Q_m}{Q_p} \left(\frac{L_p}{L_m} \right)^2 = 625 \left(\frac{u_{*m}}{u_{*p}} \right)^{3.118} = 819 \left(\frac{u_m^{1.19}}{u_p^{1.23}} \right)^{3.118} \quad (\text{G.44})$$

In comparison, equation (G.38) reduces to

$$\frac{T_p}{T_m} = 625 \left(\frac{u_m}{u_p} \right)^2 \left(\frac{u_m - 8}{u_p - 8} \right) \quad (\text{G.45})$$





Figure G.6. (a) Snow buildup behind 1:25 scale model on 13 January 2002 at 10:45, $L=1.2$ m, $H=0.15$ m, $W=0.3$ m, $T=1$ h, $u=10$ m·s⁻¹. (b) Actual snow buildup behind SANA E IV interconnecting links.

G.5. MODELLING RESULTS

During the course of the tests, a period of milder wind conditions existed that resulted in suitable snow buildup behind the scale model of the base. This occurred on 13 January 2002 from 9:00 AM – 2:00 PM and corresponded to an average wind velocity of $9.13 \text{ m}\cdot\text{s}^{-1}$ for the duration of the test. The characteristic snow buildup behind the model and the end of this period is shown in figure G.6(a) along with the characteristic dimensions of this snowdrift. The snow buildup was defined well and similar in shape to that typically found behind the SANA E IV station, as shown in figure G.6(b). The buildup behind the scale model was located, in the same position as found at SANA E IV, directly behind the interconnecting link and it followed the southeastern wind direction. Two smaller snowdrifts also formed on the leeward side behind the two outermost corners of the model.

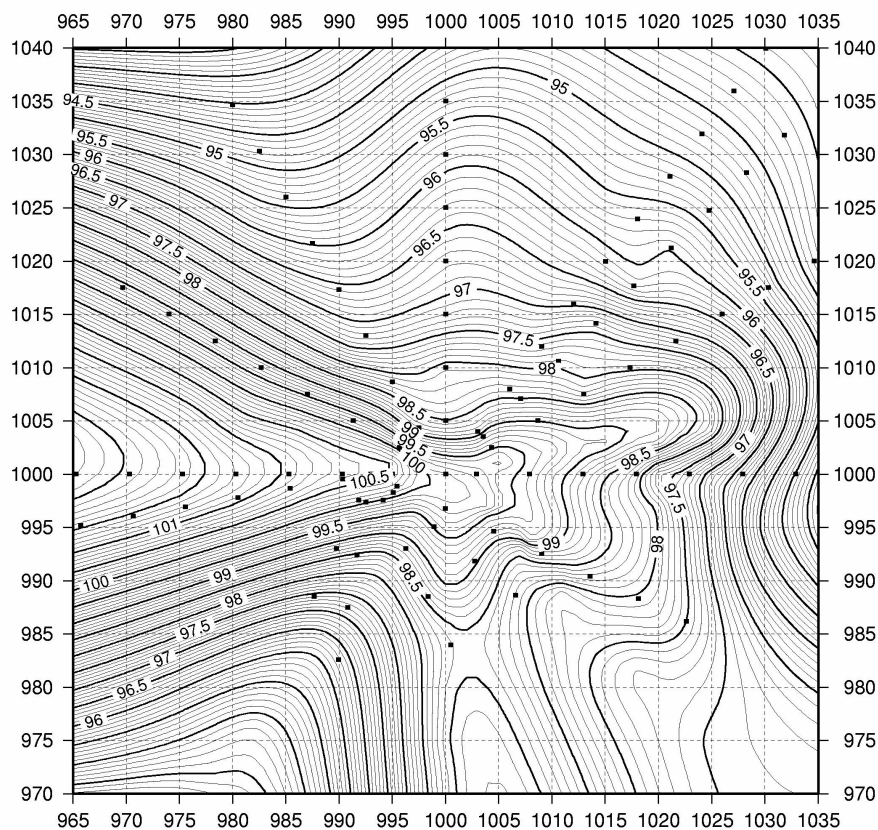


Figure G.7. Snow buildup behind SANA E IV during 15-17 January 2002, $L=40 \text{ m}$, $H=3.0 \text{ m}$, $W=15.0 \text{ m}$, $T=66 \text{ h}$, $u=15 \text{ m}\cdot\text{s}^{-1}$. Contour map from GMT Version 3.4 done by Mr. Axel Ruelke, Institut fuer Planetare Geodaesie, TU Dresden, Germany.

Strong wind conditions were measured from 15 January 2002 12:00 AM to 17 January 2002 6:00 AM with average wind speeds of $13.71 \text{ m}\cdot\text{s}^{-1}$. The resulting snow deposition behind the SANAE IV research station was measured after this 66 hour period and the measured buildup is shown in figure G.7 along with its characteristic dimensions. The geometry of the snow buildup was measured at various positions and the contour map shown in figure G.7 was made with GMT V3.4 software.

The actual snow buildup characteristics are compared to the scaled snow buildup times in accordance with the theory presented and shown in table G.2. It is clear that there exists good similarity between the time to form the characteristic buildup behind the scale model and the time to form a larger buildup behind the real base when using Iversen time scaling, equation (G.38). Equation (G.37) overestimates the time required to reach similar snowdrifts behind the research station. As shown in Table G.2, the biggest mismatches are found in the geometrical Froude number scaling and the particle ejection process scaling. Kwok et al. (1992) and Smedley et al. (1993) have made similar observations. The particle scaling and particle densimetrical Froude number show good similarity. The particle ejection scaling for the model is somewhat lower than 1.4 as required by Peterka and Petersen (1990). However, the saltation length and height for both the scale model and the prototype are small in comparison to the actual snow buildup observed.

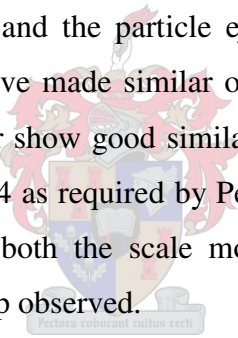
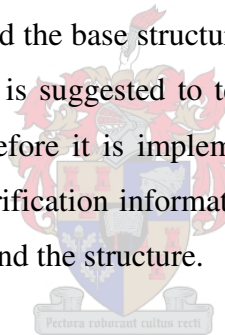


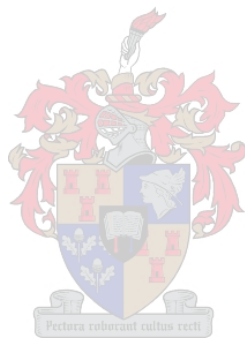
Table G.2. Modelling parameter values

Modelling parameter	Eq. no.	Model value	Prototype value
Observed properties:		L=0.16 m, D _p =0.5 mm ρ _a =1.1 kg·m ⁻³ , ρ _p =900 kg·m ⁻³ u _{*t} =0.23m·s ⁻¹ , T=1.0 h	L=4.0 m, D _p =0.5 mm ρ _a =1.1 kg·m ⁻³ , ρ _p =900 kg·m ⁻³ u _{*t} =0.32m·s ⁻¹ , T=66 h
$\frac{D_p}{L}$	G.28	0.003	0.000125
$\frac{u_{*t}^2}{D_p g} \frac{\rho_a}{\rho_p - \rho_a}$	G.29	0.0203	0.0201
$\frac{u_{*t}^2}{L g} \frac{\rho_a}{\rho_p - \rho_a}$	G.30	6.334E-5	2.514E-6
$\frac{\rho_a u_*^2}{\rho_p g L}$	G.31	8.664E-5	9.448E-6
$\frac{u_*}{u_{*t}}$	G.32	1.170	1.940
$\frac{u_{*t}^3}{2g\nu}$	G.33	70.942	70.131
$\frac{u_f}{u}$	G.34	8.112E-2	5.385E-2
l_s / L	G.35	0.730	0.079
h_s / L	G.36	0.057	0.006
$\frac{TQ\eta}{\rho_p F^2}$	G.37	4.108	2.072
$\frac{1}{2} \frac{\rho_a}{\rho_p} \frac{u^2}{gL} \left[1 - \frac{u_t}{u} \right] \frac{uT}{L}$	G.38	825.151	992.861
$\frac{T_p}{T_m}$	G.43		130.71
$\frac{T_p}{T_m}$	G.44		54.85
$\frac{T_p}{T_m}$	Observed		66.1

G.6. CONCLUSION

The present work provides functions for the effective surface roughness and the friction velocity for two locations in the vicinity of the SANAE IV research station in Antarctica. These functions are incorporated into a new function describing the velocity profile for the conditions present, as a function of surface roughness and snow surface characteristics. The measured wind velocity data was fitted to a modified logarithmic velocity profile of Bintanja (1998), to account for the potential stability effects of suspended snow particles on the resultant surface roughness and shear velocities. The snow buildup behind a 1:25 scale model of a section of the actual research station is compared to buildup found behind the base. The effectiveness of scaling the snow buildup behind the model to a larger prototype scale could therefore be evaluated. The results presented here support the theory that the Froude number or saltation length scaling may be relaxed and that time scaling in accordance with Anno or Iversen parameters should provide good similarity. Iversen's time scaling parameter was found to be more accurate for the present work. The present results suggest that the outdoors modelling of the snow buildup behind the base structure is a valuable measure of real buildup behind the actual base. Therefore it is suggested to test proposed modifications to the base structure first on the scale model before it is implemented at the large station. The results found here also provide valuable verification information for use in the numerical modelling of the snow buildup phenomena behind the structure.







APPENDIX H: VISIBILITY IN BLOWING SNOW

The effect of wind velocity on visibility is evident from the fact that falling snow may correspond to visibility in excess of 1000 m while the same snow concentration during a blizzard reduces visibility to 60 m. Takeuchi and Fukuzawa (1985) measured visibility in blowing snow conditions and provided a relationship for visibility (in metres) as a function of blowing snow flux

$$V_{iz} = \frac{683.0}{q + 0.125} + 2.6 \quad (H.1)$$

where q is the horizontal snow flux ($\text{g}\cdot\text{m}^{-2}\cdot\text{s}^{-1}$) at a specified height which may given by

$$q = \eta(z)u(z) \quad (H.2)$$

The suspended snow concentration in equation (H.2) may be found from the relationship of Pomeroy and Male (1992) i.e.

$$\eta(z) = 0.8 \exp\left(-1.55\left(4.78u_*^{-0.544} - z^{-0.544}\right)\right) \quad (H.3)$$

and by employing the logarithmic velocity profile for the horizontal wind speed one finds

$$q = 800 \exp\left(-1.55\left(4.78u_*^{-0.544} - z^{-0.544}\right)\right) \frac{u_*}{\kappa} \ln\left(\frac{z}{z_0}\right) \quad (H.4)$$

From our relationship for aerodynamic surface roughness measured at SANAE IV i.e.

$$z_0 = \frac{C_1 u_*^2}{2g} \quad (H.5)$$

where $C_1=0.0035$, Beyers and Harms (2003a) for wind hardened snow surface conditions near SANAE IV. The friction velocity as a function of 10 m wind speed was also derived for SANAE IV and given by

$$u_* = 0.024u_{10}^{1.19} \quad (H.6)$$

Combining equations (H.1), (H.4), (H.5) and (H.6) gives

$$V_{iz} = \frac{683.0}{19.2e^{\left(-1.55\left(37.041u_{10}^{-0.647} - z^{-0.544}\right)\right)} \frac{u_{10}^{1.19}}{\kappa} \ln\left(\frac{2gz}{C_1 0.000576u_{10}^{2.38}}\right) + 0.125} + 2.6 \quad (H.7)$$

Figure H.1 illustrates equation (H.7) as a function of 10 m wind velocity as measured at SANAE IV and for an eye level height of 1.8 m above ground.

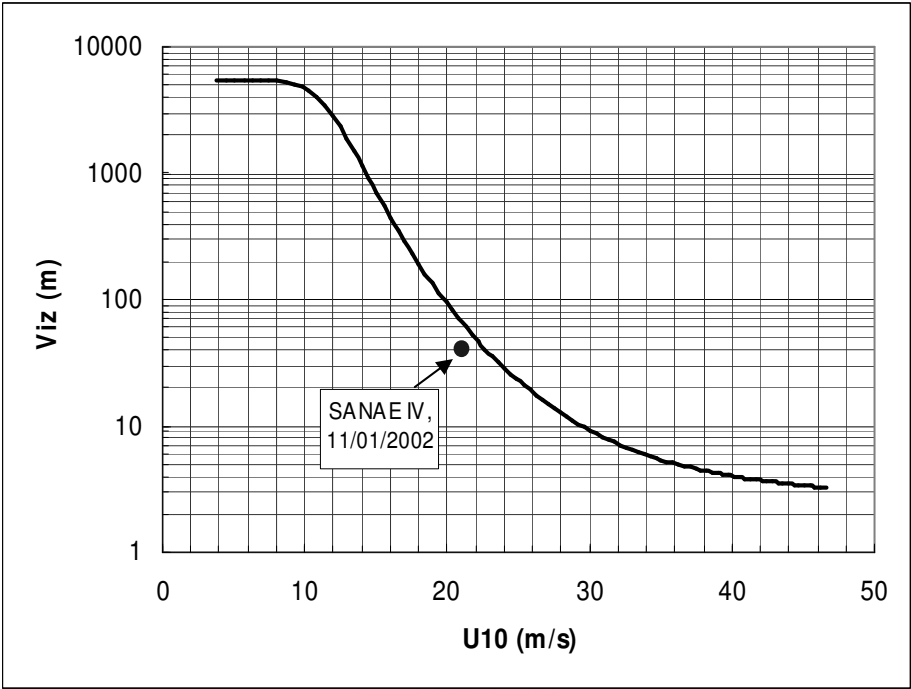
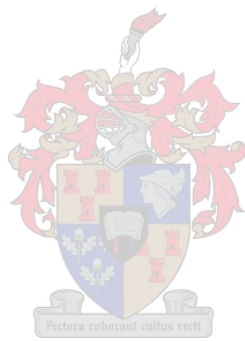


Figure H.1: Visibility during blowing snow conditions at $z=1.8$ m above snow surface as a function of 10 m wind speed

On 11 January 2002 severe winds in excess of $20 \text{ m}\cdot\text{s}^{-1}$ were measured at SANAE IV. From photographic records taken during this blizzard a visibility of approximately 40 m at eye level was determined. This is marked on figure H.1 which gives at least some crude proof that the snow flux profiles experiences at SANAE may follow the general theory and empirical relationships described in the thesis.





APPENDIX I: MODIFIED k- ϵ TURBULENCE MODELS

It is believed that great improvement may be made to the snow accumulation topography by employing a different, more advanced turbulence model that could reproduce the anisotropic nature of the real flow to some degree. Boundary layer turbulence is strongly affected by streamline curvature, high normal strains and separation regions, Castro (2003) and various two-equation eddy viscosity models exist that are modifications of the standard k- ϵ turbulence model to account for such streamline curvature, swirling flows or low Reynolds number effects. Importantly, even if the standard k- ϵ turbulence model resolves some of the secondary swirling flow patterns expected around a bluff body, i.e. the horseshoe vortex system, it does not mean that the shear or normal strain within this system is accurately reproduced. Thus, capturing the recirculation regions is not enough; capturing them accurately is of primary importance in establishing the correct near surface shear stress. This in turn could greatly influence deposition or erosion characteristics at the snow surface. To this end the present research evaluated some modifications to the practical and standard k- ϵ turbulence model for future reference to improve the accuracy of the simulated flow field and its associated snow drift.

Abe et al. (1993) investigate a new low-Reynolds number k- ϵ turbulence model applied to a backward facing step. Kobayashi et al. (1993) provide details of an anisotropic k- ϵ turbulence model applied to a backward facing step. Zhang et al. (1992) give a good description of the algebraic stress model (ASM) applied to strongly swirling flows. Ehrhard and Moussiopoulos (2000) provide details of a non-linear k- ϵ turbulence model for atmospheric boundary layer around obstacles. Lakehal and Rodi (1997) provide details of a low Reynolds number wall function for the k- ϵ turbulence model. Durbin (1993), (1995) (1996) and Iaccarino and Durbin (2003) provide details of the promising k- ϵ - v^2 - f method which solves an additional two equations for the vertical velocity fluctuation and a damping function in order to provide some degree of anisotropy to the isotropic eddy viscosity assumption. The method also modifies the production of dissipation proportional to the strain rate by means of a function $C_{\epsilon l}(P_k)$.

Many k-ε turbulence model modifications include so called ad hoc modifications to the C_μ term to account for reduced turbulence levels in swirling flows. The Kato-Launder modification, Kato and Launder (1993), to the k-ε turbulence model removes the excessive production of turbulent kinetic energy in impingement regions. This overproduction is due to the non-zero normal stresses in such regions. The model replaces the original turbulent kinetic energy production term with

$$P_k = \nu_t \Omega S \quad (I.1)$$

where the vorticity scale is defined by

$$\Omega = \sqrt{\frac{1}{2} \left(\frac{\partial u_i}{\partial x_j} - \frac{\partial u_j}{\partial x_i} \right)^2} \quad (I.2)$$

and the eddy viscosity given by equation (2.59).

For simple shear flows $S = \Omega$ while in stagnation regions $\Omega = 0.0$. This model was used with success by Murakami and Mochida (1995) to model the flow around a two- and three-dimensional cube and give significantly more accurate results compared to the original k-ε model. The disadvantage of the Kato-Launder model is that while it will decrease the production of turbulent kinetic energy correctly where the vorticity scale is smaller than the strain rate scale, it will also overestimate this where the vorticity scale exceeds the strain rate. Some mathematical inconsistencies are also due to the modification of only the production term in the turbulent kinetic energy equation and a subsequent inconsistency in modeling the Reynolds stress terms, Tsuchiya et al. (1997), Murakami (1998).

Tsuchiya et al. (1997), Murakami (1998) proposed a modification that seems to overcome this issue. Instead of modifying the turbulent production term, their model only modifies the expression for the eddy viscosity to reflect the effects of the normal strains in regions of strong streamline curvature

$$\nu_t = C_\mu^* \frac{k^2}{\varepsilon} \quad C_\mu^* = C_\mu \frac{\Omega}{S} \quad \left(\frac{\Omega}{S} < 1 \right) \quad (I.3)$$

$$\nu_t = C_\mu^* \frac{k^2}{\varepsilon} \quad C_\mu^* = C_\mu \quad \left(\frac{\Omega}{S} \geq 1 \right) \quad (I.4)$$

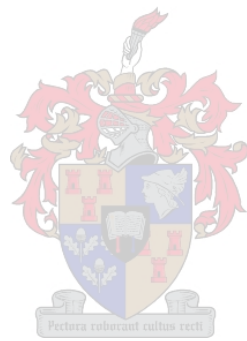
This model was extensively validated against the standard k-ε model, Kato-Launder model and wind tunnel tests for two- and three-dimensional flows around bluff bodies with favourable results, Tsuchiya et al. (1997).

Castro (2003) and Castro and Apsley (1997) state that the turbulence models need to account for the fact that the turbulence structure will respond to mean flow curvature and longitudinal strains. The standard k-ε model can not do this. To overcome this deficiency, Leschziner and Rodi, in Apsley (1995), first modified the eddy viscosity concept by dividing C_μ by a factor dependent on the local streamline curvature. Apsley (1995) adapted their function to suit a three-dimensional approach i.e.

$$C_\mu^* = \frac{C_\mu}{1 + 4\phi^2 \left(\frac{k}{\varepsilon}\right)^2 \frac{\partial U_s}{\partial n} \frac{U_s}{R_c}} \quad (I.5)$$

Hanjalic and Launder (1980) also noted that the turbulent dissipation is enhanced by streamwise strains. The model by Apsley (1995) accounts for this by changing the production terms in the dissipation rate equation to

$$\frac{\varepsilon}{k} \left(C'_{\varepsilon 1} \mu_t \left(\frac{\partial \bar{u}_i}{\partial x_j} + \frac{\partial \bar{u}_j}{\partial x_i} \right) \frac{\partial \bar{u}_i}{\partial x_j} - C''_{\varepsilon 1} \nu_t (2S_{ns})^2 \right) \quad (I.6)$$



REFERENCES

Abe, K., Nagano, Y. and Kondoh, T., Numerical prediction of separating and reattaching flows with modified low-Reynolds-number $k-\varepsilon$ model, *Journal of Wind Engineering and Industrial Aerodynamics*, vol. 46 & 47, pp. 85-94, 1993.

Abou-Arab, T.W., Turbulence models for two-phase flows, in Cheremisinoff (ed.), *Encyclopedia of Fluid Mechanics 3, Gas-Liquid Flows*, Gulf Public., Houston, 863-907, 1986.

AbuOmar, M.M. and Martinuzzi, R.J., An experimental investigation of the flow around a surface mounted pyramid, 14th Annual ASCE Engineering Mechanics Division Conference, Washington D.C., June, 2000.

Alhajraf, S., Numerical simulation of drifting sand, PhD Thesis, School of Mechanical Engineering, Cranfield University, Cranfield, United Kingdom, 2001.

Alhajraf, S., Numerical simulation of sand and snow drift at porous fences, *Proceedings of ICAR5/GCTE-SEN Joint Conference*, Texas Technical University, Lubbock, Texas, U.S.A, p. 208, 2002.

Alhajraf, S., Computational fluid dynamic modeling of drifting particles at porous fences, *Environmental Modelling and Software*, vol. 19, issue 2, pp. 163-170, 2004.

Anderson, R.S. and Haff, P.K., Wind modification and bed response during saltation of sand in air, *Acta Mechanica*, Supplementum 1, Aeolian grain transport 1: Mechanics, pp. 21-52, 1991.

Anno, Y., Requirements for modelling a snowdrift, *Cold Regions Science and Technology*, vol. 8, pp. 241-252, 1984.

Anno, Y., Modelling a snowdrift by means of activated clay particles, *Annals of Glaciology*, vol. 6, pp. 48-58, 1985.

Anno, Y., Snow deflector built at the edge of a road cut, *Cold Regions Science and Technology*, vol. 12, pp. 121-129, 1986.

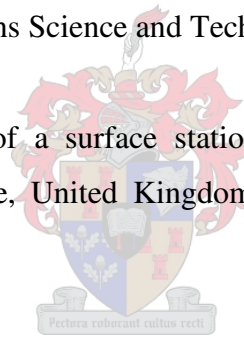
Anno, Y., Froude number paradoxes in modeling of snowdrift, *Journal of Wind Engineering and Industrial Aerodynamics*, vol. 36, pp. 889-891, 1990.

Apsley, D.D., Numerical modelling of neutral and stably stratified flow and dispersion in complex terrain, PhD Thesis, University of Surrey, United Kingdom, 1995

Bagnold, R.A., *The physics of blown sand and desert dunes*, Methuen and Co. Ltd., London, United Kingdom, 1941.

Bartelt, P. and Lehning, M., A physical SNOWPACK model for the Swiss avalanche warning Part I: numerical model, *Cold Regions Science and Technology*, vol. 35, pp. 123-145, 2002.

Bateman, A.P., The performance of a surface station on an Antarctic ice shelf, British Antarctic Survey report, Cambridge, United Kingdom, received from d.blake@bas.ac.uk., 2003.



Baumeister, T. and Marks, L.S., Gas cleaning, dusts, clouds, smokes, in *Mechanical Engineers Handbook*, McGraw Hill Book Co., New York, 1958.

Becker, S., Lienhart, H. and Durst, F., Flow around three-dimensional obstacles in boundary layers, *Journal of Wind Engineering and Industrial Aerodynamics*, vol. 90, pp. 265-279, 2002.

Bekker, M.D., Snow studies in Germany, National research council of Canada, Commission on Soil and Snow Mechanics, technical memo no. 20, p. 83, 1951.

Berry, D.L., Forrest, P.E. and Braun, P.E., Foundation design for the elevated station, *Civil Engineering Magazine*, December 2000.

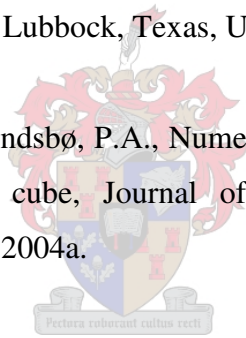
Beyers, J.H.M. A finite volume method for the analysis of the thermo-flow field of a solar chimney collector, MSc Thesis, Mechanical engineering department, Stellenbosch University, Stellenbosch, South Africa, 2000.

Beyers, J.H.M. and Harms, T.M., Research project proposal, numerical modeling of the snow flow characteristics surrounding the SANAE IV base, Vesleskarvet, Antarctica, Mechanical engineering department, Stellenbosch University, Stellenbosch, South Africa, May 2000.

Beyers, J.H.M. and Harms, T.M., Outdoors modelling of snowdrift at SANAE IV research station, Antarctica, Journal of Wind Engineering and Industrial Aerodynamics, vol. 91, pp. 551-569, 2003a.

Beyers, J.H.M., Sundsbø, P.A. and Harms, T.M., Numerical simulation and verification of drifting snow around a cube, Proceedings of the 11th International Conference on Wind Engineering, Texas Tech University, Lubbock, Texas, USA, June, pp. 1886-1893, 2003b.

Beyers, J.H.M., Harms, T.M. and Sundsbø, P.A., Numerical simulation of three-dimensional, transient snow drifting around a cube, Journal of Wind Engineering and Industrial Aerodynamics, vol. 92, pp. 725-747, 2004a.



Beyers, J.H.M, Harms, T.M. and Sundsbø, P.A., Numerical simulation of snow drifting around an elevated obstacle, Proceedings of the 5th Conference on Snow Engineering, Davos, Switzerland, pp.185-191, July, 2004b.

Binder, J.L. and Hanratty, T.J., Use of Lagrangian methods to describe drop deposition and distribution in horizontal gas-liquid annular flows, Int. Journal of Multiphase Flow, vol. 18, no. 6, pp. 803-820, 1992.

Bintanja, R., The interaction between drifting snow and atmospheric turbulence, Annals of Glaciology, vol. 26, pp. 167-173, 1998.

Bintanja, R., Snowdrift suspension and atmospheric turbulence, Part I: Theoretical background and model description, Boundary-layer Meteorology, 95, pp. 343-368, 2000a.

Bintanja, R., Snowdrift suspension and atmospheric turbulence, Part II: Results of model simulations, *Boundary-layer Meteorology*, 95, pp. 369-395, 2000b.

Bintanja, R., Buoyancy effects induced by drifting snow particles, *Annals of Glaciology*, vol. 32, pp. 147-152, 2001a.

Bintanja, R., Snowdrift sublimation in a katabatic wind region of the Antarctic Ice sheet, *Journal of Applied Meteorology*, vol. 40, pp. 1952-1966, 2001b.

Blake, D., The development of structures for Halley station in Antarctica, British Antarctic Survey report, d.blake@bas.ac.uk, 2003.

Boussinesq, T. V., *Mem. Pre. Acad. Sci.*, 3rd Edition, Paris XXIII, p. 46, 1877.

Bradley, E.F. and Mulhearn, P.J., Development of velocity and shear stress distributions in the wake of a porous shelter fence, *Journal of Wind Engineering and Industrial Aerodynamics*, vol. 15, pp. 145-156, 1983.

Britter, R.E., Hanna, S.R., Briggs, G.A. and Robins, A., Short-range vertical dispersion from a ground level source in a turbulent boundary layer, *Atmospheric Environment*, vol. 37, pp. 3885-3894, 2003.

Brooks, W.D., The rationale for above-surface facilities, *Civil Engineering Magazine*, December, 2000.

Budd, W.F., The drifting of non-uniform snow particles, *Antarctic Research Series*, vol. 9, pp. 59-69, 1966.

Budd, W.F., Dingle, W.R. and Radok, U., The Byrd snow drift project: outline and basic results, *Studies in Antarctic Meteorology*, vol. 9, pp. 71-134, 1966.

Businger, J.A, Eddy diffusion and settling speed in blown snow, *Journal of Geophysical research*, vol. 70, no. 14, pp. 3307-3313, 1965.

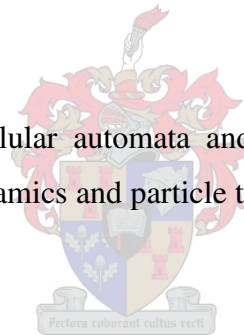
Carrier, G.F., On slow, viscous flow, Final report, Office of Naval Research, Brown University, Providence, U.S.A., Contract no. NR-653(00), 1953.

Castro, I.P. and Robins, A.G., The flow around a surface-mounted cube in uniform and turbulent streams, *Journal of Fluid mechanics*, vol. 79, part 2, pp. 307-335, 1977.

Castro, I.P. and Apsley, D.D., Flow and dispersion over topography: a comparison between numerical and laboratory data for two-dimensional flows, *Atmospheric Environment*, vol. 31, no. 6, pp. 839-850, 1997.

Castro, I.P., Flow and dispersion over hills, *QNET-CFD Network Newsletter*, vol. 2, no. 1, pp. 14-17, 2003.

Chopard, B. and Masselot, A, Cellular automata and lattice Boltzmann methods: a new approach to computational fluid dynamics and particle transport, *Future Generation Computer Systems*, vol. 16, pp. 249-257, 1999.



Decker, R., A continuum mixture theory with an application to turbulent snow, air flows and sedimentation, *Journal of Wind Engineering and Industrial Aerodynamics*, vol. 36, pp. 877-887, 1990.

Delaunay, D., Lakehal, D. and Pierrat, D., Numerical approach for wind loads prediction on buildings and structures, *Journal of Wind Engineering and Industrial Aerodynamics*, vol. 57, pp. 307-321, 1995.

Delpech, P., Palier, P. and Gandemer, J., Snowdrifting simulation around Antarctic buildings, *Journal of Wind Engineering and Industrial Aerodynamics*, vol. 74-76, pp. 567-576, 1998.

Déry, S.J. and Taylor, P.A., Some aspects of the interaction of blowing snow with the atmospheric boundary layer, *Hydrological Processes*, 10, pp. 1345-1358, 1996.

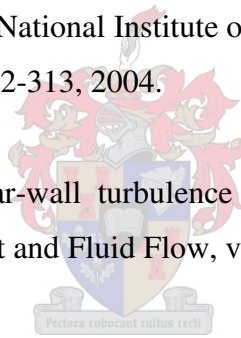
Déry, S.J., Taylor, P.A. and Xiao, J., The thermodynamic effects of sublimating, blowing snow in the atmospheric boundary layer, *Boundary layer Meteorology*, vol. 89, pp. 251-283, 1998.

Doorschot, J.J.J., and Lehning, M., Equilibrium saltation: mass fluxes, aerodynamic entrainment, and dependences on grain properties, *Boundary-layer Meteorology*, vol. 104, pp. 111-130, 2002.

Dover, S.E., Numerical modelling of blowing snow, PhD Thesis, Department of Applied Mathematics, University of Leeds, United Kingdom, 1993.

Drücker, C., Wilhelms, F., Oerter, H., Frnezele, A., Gernandt, H. and Miller, H., Design, transport, construction and operation of the summer base Kohnen for ice-drilling in Dronning Maud Land, Antarctica, *Memoirs of National Institute of Polar Research*, Special issue no. 56, *Ice Drilling Technology 2000*, pp. 302-313, 2004.

Durbin, P.A., Application of a near-wall turbulence model to boundary layers and heat transfer, *International Journal of Heat and Fluid Flow*, vol. 14, no. 4, pp. 316-323, 1993.



Durbin, P.A., Separated flow computations with the $k-\epsilon-v^2$ model, *American Institute of Aeronautics and Astronautics*, vol. 33 (4), pp. 659-664, 1995.

Durbin, P.A., On the $k-3$ stagnation point anomaly, *International Journal of Heat and Fluid flow*, vol. 17, pp. 89-90, 1996.

Durst, F., Milojevic, D. and Schöning, B., Eulerian and Lagrangian predictions of particulate two-phase flows: a numerical study, *Applied Mathematical Modeling*, vol. 8, pp. 101-115, 1984.

Dyunin, A.K., Solid flux of snow-bearing air flow, Report NRC TT-1102, National Research Council of Canada, Ottawa, 1963.

Eaton, J.K. and Fessler, J.R., Preferential concentration of particles by turbulence, *Int. Journal for Multiphase Flows*, vol. 20 Suppl, pp. 169-209, 1994.

Ehrhard, J.E., and Moussiopoulos, N., A new non-linear turbulence model for similarity flows around building shaped structures, *Journal of Wind Engineering and Industrial aerodynamics*, vol. 88, pp. 91-97, 2000.

Fan, L. and Zhu, C., *Principles of gas-solid flows*, Cambridge University Press, Cambridge, 1998.

Ferziger, J.H. and Perić, M., *Computational methods for fluid dynamics*, 3rd Edition, Springer, Berlin, Germany, 2002.

Finney, E.A., Snow drift control by highway design, East Lansing, Michigan, Michigan Engineering Experimental Station, vol. 15, no. 2, bull. 86, 56 pages, 1939.

Gauer, P., Blowing and drifting snow in Alpine terrain: numerical simulation and related field measurements, *Annals of Glaciology*, vol. 26, pp. 174-178, 1998.

Gerdel, R.W., Snow drifting and engineering design, *Meteorological Monographs*, vol. 4, no. 22, pp. 57-64, 1960.

Gilbert, G.K., Transportation of debris by running water, Department of the Interior, United States Geological Survey, Professional paper no. 86, Washington D.C., U.S.A. Government printing office, 1941.

Goliger, A., Wind tunnel tests on the new SANAE base, Council for Scientific and Industrial Research South Africa, Building Technology Division, report contract no. 550 22933, pp. 1-14, August, 1991.

Greeley, R. and Iversen, J.D., *Wind as a geological process on Earth, Mars, Venus and Titan*, Cambridge University Press, Cambridge, United Kingdom, 1985.

Greene, E.M., Liston, G.E. and Pielke Sr., R.A., Simulation of above treeline snowdrift formation using a numerical snow-transport model, *Cold Regions Science and Technology*, vol. 30, pp. 135-144, 1999.

Gurer, I., Sato, T., Kosugi, K., Kamata, Y. and Sato, A., Comparison of the models of different types of snow fences in cold wind tunnel, *Proc. XIth International Winter Road Congress*, Sapporo, Japan, June, 2002.

Haehnel, R.B. and Lever, J.H., Field measurements of snowdrifts, *Proceedings of the ASCE Workshop on the Modelling of Windblown Snow and Sand*, Snowbird, Utah, 1994, p 1-14.

Hanjalic, K. and Launder, B., Sensitizing the dissipation equation to irrotational strains, *ASME Journal of Fluids Engineering*, vol 102, p.32, 1980.

Harris, J.M., An introduction to the geology, biology and conservation of nunataks in Dronning Maud Land, Antarctica, 1st edition, Department of Environmental Affairs and Tourism, June, 1996.

Heacox, K., Antarctica, the last continent, *National Geographic Destinations: Antarctica*, National Geographic Society, Washington D.C., United States, pp. 1-199, 1998.

Hirt, C.W., Volume-fraction techniques: powerful tools for wind engineering, *Journal of Wind Engineering and Industrial Aerodynamics*, vol. 46 & 47, pp. 327-338, 1993.

Hoxey, R.P. and Richards, P.J., Flow patterns and pressure field around a full scale building, *Journal of Wind Engineering and Industrial Aerodynamics*, vol. 50, pp. 203-212, 1993.

Humphrey, J.A.C., Fundamentals of fluid motion in erosion by solid particle impact, *International Journal of Heat and Fluid Flow*, vol. 11, no. 3, pp. 170-195, 1990.

Huser, A., Pål Jahre Nilsen and Skåtun, H., Application of k-ε model to the stable ABL: Pollution in complex terrain, *Journal of Wind Engineering and Industrial Aerodynamics*, vol. 67-68, pp. 425-436, 1997.

Iaccarino, G. and Durbin, P., Unsteady RANS simulations using the v^2 -f model, Center for turbulent research, Annual Research Briefs, pp. 203-269, 2003.

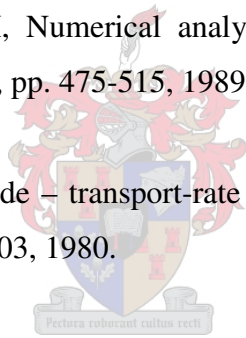
Ishii, M., Thermo-fluid dynamic theory of two-phase flow, Collection de la Direction des Études et Recherches D'électricité de France, Eyrolles, France, 1975.

Ishii, M. and Zuber, N., Drag coefficient and relative velocity in bubble, droplet and particulate flows, American Institute of Chemical Engineers Journal, vol. 52, no. 5, pp. 843-855, 1979.

Ishii, M. and Mishima, K., Two-fluid model and hydrodynamic relations, Nuclear Engineering Design, vol. 82, pp. 107-126, 1984.

Ishii, R., Umeda, Y. and Yuhi, M, Numerical analysis of gas-particle two-phase flows, Journal of Fluid Mechanics, vol. 203, pp. 475-515, 1989.

Iversen, J.D., Drifting snow similitude – transport-rate and roughness modelling, Journal of Glaciology, vol. 26 no. 94, pp. 393-403, 1980.



Iversen, J.D., Comparison of wind tunnel model and full scale snow fence drifts, Journal of Wind Engineering and Industrial Aerodynamics, vol. 8, 231-249, 1981.

Janin, L.F and Cermak, C.E., Sediment laden velocity profiles developed in a long boundary-layer wind tunnel, Journal of Wind Engineering and Industrial Aerodynamics, vol. 28, pp. 159-168, 1988.

Johansen, S.T., The deposition of particles on vertical walls, Int. Journal for Multiphase Flow, vol. 17, no. 3, pp. 355-376, 1991.

Johnson, G.D.B. (1852), Nogle ord om snedreev, snefog og snefonner, (in Norwegian), P.T. Mallings Forlags-Boghandel, Christiania, reprinted in faximilia scinetie et technical Norwica, vol. 31, NTH, Trondheim, Norway, 1969.

Jones, W.P. and Launder, B.E., The prediction of laminarization with a two-equation model of turbulence, *Int. Journal of Heat and Mass Transfer*, vol. 15, pp. 301-314, 1972

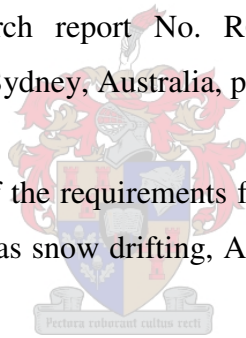
Kallio, G.A. and Reeks, M.W., A numerical simulation of particle deposition in turbulent boundary layers, *Int. Journal for Multiphase Flow*, vol. 15, no. 3, pp. 433-466, 1989.

Karkas, E., personal communication, FINNARP 2000, Division of Geophysics, Department of Physical Sciences, University of Helsinki, Finland, eija.karkas@helsinki.fi, 2001.

Kato, M. and Launder, B.E., The modelling of turbulent flow around stationary and vibrating square cylinders, *Proceedures of the 9th Symposium on Turbulent Shear Flow*, Kyoto, Japan, 1993.

Kim, D.H., Kwok, K.C.S. and Rohde, H.F., Similitude requirements of snowdrift modelling for Antarctic environment, Research report No. R634, School of Civil and Mining Engineering, University of Sydney, Sydney, Australia, pp. 1-32, 1991.

Kind, R.J., A critical examination of the requirements for model simulation of wind induced erosion/deposition phenomena such as snow drifting, *Atmospheric Environment*, vol. 10, pp. 219-227, 1976.



Kind, R.J. and Murray, S.B., Saltation flow measurements relating to modeling of snowdrifting, *Journal of Wind Engineering and Industrial Aerodynamics*, vol. 10, pp. 89-102, 1982.

Kind, R.J., Snowdrifting: a review of modelling methods, *Cold Regions Science and Technology*, vol. 12, pp. 217-228, 1986.

Kind, R.J., Concentration and mass flux of particles in aeolian suspension near tailings disposal sites or similar sources, *Journal of Wind Engineering and Industrial Aerodynamics*, vol. 41-44, pp. 217-225, 1992.

Kobayashi, D., Studies of snow transport in low level drifting snow, Institute of Low Temperature Science, Report no A34, Sapporo, Japan, 1973.

Kobayashi, S., Ishikawa, N. and Ohata, T., Katabatic snow storms in stable atmospheric conditions at Mizuho station, Antarctica, *Annals of Glaciology*, vol. 6, pp. 229-231, 1985.

Kobayashi, T., Morinihi, Y. and Togashi, S., Estimation of anisotropic k- ϵ model on the backward-facing step flow by LES data base, *Journal of Wind Engineering and Industrial Aerodynamics*, vol. 46 & 47, pp. 77-84, 1993.

Kwok, K.C.S., Kim, D.H., Smedley D.J. and Rhode, H.F, Snowdrift around buildings for Antarctic environment, *Journal of Wind Engineering and Industrial Aerodynamics*, vol. 41-44, pp. 2797-2808, 1992.

Lakehal, D. and Rodi, W., Calculation of the flow past a surface-mounted cube with two-layer turbulence models, *Journal of Wind Engineering and Industrial aerodynamics*, vol. 67&68, pp. 65-78, 1997.

Lang, R.M. and Blaisdell, G.L., Passive snow removal with a vortex generator at the Pegasus runway, Antarctica, *Annals of glaciology*, vol. 26, pp. 213-236, 1998.

Launder, B.E. and Spalding, D.B., The numerical computation of turbulent flows, *Computational Methods in Applied Mechanics and Engineering*, vol. 3, pp. 269-289, 1974.

Lee, B.E., Tu, J.Y. and Fletcher, C.A.J., On numerical modelling of particle-wall impaction in relation to erosion prediction: Eulerian versus Lagrangian method, *Wear*, pp. 179-188, 2002a.

Lee, S.J. and Kim, H.B., Laboratory measurement of velocity and turbulence field behind porous fences, *Journal of Wind Engineering and Industrial Aerodynamics*, vol. 80, pp. 311-326, 1999.

Lee, S.J. and Lim, H.C., A numerical study on flow around a triangular prism located behind a porous fence, *Fluid Dynamic Research*, vol. 28, pp. 209-221, 2001.

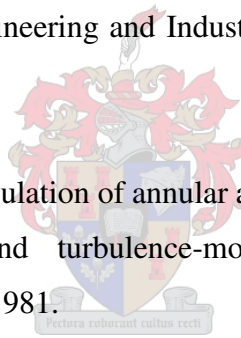
Lehning, M., Doorschot, J., Radeschall, N. and Bartelt, P., Combining snow drift and SNOWPACK model to estimate snow loading in avalanche slopes, in Snow Engineering, Hjort-Hansen, Holand, Loset and Norem (eds), Balkema, pp. 113-122, 2000.

Lehning, M., Bartelt, P., Brown, B., Fierz, C. and Satyawali, P., A physical SNOWPACK model for the Swiss avalanche warning Part II: snow microstructure, Cold Regions Science and Technology, vol. 35, pp. 147-167, 2002a.

Lehning, M., Bartelt, P., Brown, B. and Fierz, C, A physical SNOWPACK model for the Swiss avalanche warning Part III: meteorological forcing, thin layer formation and evaluation, Cold Regions Science and Technology, vol. 35, pp. 170-184, 2002b.

Leschziner, M.A., Computational modelling of complex turbulent flow – expectations, reality and prospects, Journal of Wind Engineering and Industrial Aerodynamics, vol. 46 & 47, pp. 37-51, 1993.

Leschziner, M.A. and Rodi, W., Calculation of annular and twin parallel jets using various discretisation schemes and turbulence-model variations, Journal of Fluids Engineering, vol. 103, pp. 352-360, 1981.



Li, L. and Pomeroy, J.W., Estimates of threshold wind speeds for snow transport using meteorological data, Journal of Applied Meteorology, vol. 36, pp. 205-213, 1997.

Liljequist, G., Energy exchange of an Antarctic snow field, Norwegian-British-Swedish Antarctic expeditions 1949-1952, Scientific. Research., vol. 2 part 1c, 1957.

Liston, B.L., Brown, R.L. and Dent, J.D., A two dimensional computational model of turbulent atmospheric surface flows with drifting snow, Annals of Glaciology, vol. 18, pp. 281-286, 1993.

Liston, G.E. and Sturm, M., A snow-transport model for complex terrain, Journal of Glaciology, vol. 44, no. 148, pp. 498-515, 1998.

Lun, Y.U., Mochida, A., Murakami, S., Yoshino, H. and Shirasawa, T., Numerical simulation of flow over topographic features by revised k- ϵ models, *Journal of Wind Engineering and Industrial Aerodynamics*, vol. 91, pp. 231-245, 2003.

Maeno, N., Naruse, R., Nishimura, K., Takei, I., Ebinuma, T., Kobayashi, S., Nishimura, H., Kaneda, Y. and Ishida, T., Wind tunnel experiments on blowing snow, *Annals of Glaciology*, vol. 6, pp. 63-67, 1985.

Mann, G.W., Surface heat and vapour budgets over Antarctica, PhD Thesis, The Environment Centre, University of Leeds, Leeds, United Kingdom, 1998.

Martinuzzi, R. and Tropea, C. The flow around surface-mounted, prismatic obstacles placed in a fully developed channel flow, *Journal of Fluids Engineering*, vol. 115, pp. 85-92, 1996.

Masselot, A., A new numerical approach to snow transport and deposition in wind: a parallel lattice gas model, PhD Thesis, Department of Information Technology, University of Genève, Genève, Switzerland, 2000.

Mavroidis I., Griffiths, R.F. and Hall, D.J., Field and wind tunnel investigations of plume dispersion around single surface obstacles, *Atmospheric Environment*, vol. 37, pp. 2903-2918, 2003.

McLaughlin, J.B., Numerical computation of particle-turbulence interaction, *Int. Journal for Multiphase Flows*, vol. 20 supplement, pp. 211-232, 1994.

Melbourne, W.H, and Styles, D.F., Wind tunnel tests on a theory to control Antarctic drift accumulation around buildings. Proceedings, International Research Seminar, Wind Effects on Buildings and Structures, Ottawa, Canada, pp. 135-173, 1967.

Mellor, M. and Fellers, F., Concentration and flux of wind-blown snow, Special report (U.S. Army Cold Regions Research and Engineering Laboratory), pp. 86-11, 1986.

Michaux, J.L., Naai-Bouvet, F., Naaim, M., Lehning, M. and Guyomarc'h, G., Effect of unsteady wind on drifting snow: first investigations, *Natural Hazards and Earth System Sciences*, vol. 2, pp. 129-136, 2002.

Miles, S. and Westbury, P., Practical tools for wind engineering in the built environment, *QNET-CFD Network Newsletter*, vol. 2, no. 2, pp. 11-14, 2003.

Mols, B. and Oliemans, R.V.A., A turbulent diffusion model for particle dispersion and deposition in horizontal tube flow, *International Journal for Multiphase Flow*, vol. 24, no. 1, pp. 55-75, 1998.

Mols, B., Mittendorf, I. and Oliemans, R.V.A., Results from a two-dimensional turbulent diffusion-model for dispersion and deposition of droplets in horizontal annular dispersed gas/liquid flow, *International Journal of Multiphase Flow*, vol. 26, pp. 949-975, 2000.

Moore, I., Mobbs, S.D., Ingham, D.B. and King, J.C., Numerical modelling of blowing snow around buildings, *International Glaciology Society*, vol. 20, pp. 341-346, 1994.

Moore, I., Numerical modeling of blowing snow around buildings, PhD Thesis, Department of Applied Mathematical Studies, University of Leeds, Leeds, United Kingdom, 1995.

Murakami, S., Mochida, A., Hayashi, A. and Sakamoto, S., Numerical study on velocity-pressure field and wind forces for bluff bodies by k- ϵ , ASM and LES, *Journal of Wind Engineering and Industrial Aerodynamics*, vol. 41-44, pp. 2841-2852, 1992.

Murakami, S., Mochide, A. and Hibi, K., Three-dimensional numerical simulation of air flow around a cubic model by means of large eddy simulation, *Journal of Wind Engineering and Industrial Aerodynamics*, vol. 25, pp. 291-305, 1987.

Murakami, S., Comparison of various turbulence models applied to a bluff body, *Journal of Wind Engineering and Industrial Aerodynamics*, vol. 46 & 47, pp. 21-36, 1993.

Murakami, S. and Mochida, A., On turbulent vortex shedding flow past 2D square cylinder predicted by CFD, *Journal of Wind Engineering and Industrial Aerodynamics*, vol. 54-55, pp. 191-211, 1995.

Murakami, S., Overview of turbulence models applied in CWE-1997, *Journal of Wind Engineering and Industrial Aerodynamics*, vol. 74-76, pp. 1-24, 1998.

Naaïm, M., Naaïm-Bouvet, F., and Martinez, H., Numerical simulation of drifting snow: erosion and deposition models, *Annals of Glaciology*, vol. 26, pp. 191-196, 1998.

Naaïm-Bouvet, F., Naaïm, M. and Michaux, J.L., Snow fences on slopes at high wind speed: physical modelling in the CSTB cold wind tunnel, *Natural Hazards and Earth System Sciences*, vol. 3/4, pp. 137-145, 2002.

Nikuradse, J., Strömungsgesetze in rauhen Rohre, *Forsch. Arb. Ing. –Wes*, no. 361, 1933.

Nishimura, K., Sugiura, K., Nemoto, M. and Maeno, N., Measurements and numerical simulations of snow-particle saltation, *Annals of Glaciology*, vol. 26, pp. 183-190, 1998.

Nøkleberg, L. and Sørentvedt, T., Erosion of oil and gas industry choke valves using computational fluid dynamics and experiment, *International Journal of Heat and Fluid Flow*, vol. 19, pp. 636-643, 1998.

Norem, H., Design criteria and location of snow fences, *Annals of Glaciology*, vol. 6, pp. 68-70, 1985.

Olowsen P, Snow drift modelling reaches new heights, *FLUENT Spring newsletter*, pp. 14-15, 2004.

Owen, P.R., Saltation of uniform grains in air, *Journal of Fluid Mechanics*, vol. 20, pp.225-242, 1964.

Owen, P.R., Sand movement mechanism, Workshop on Physics of Desertification, International Centre for Theoretical Physics, Trieste, Italy, 1980.

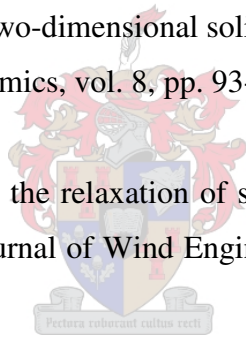
Packwood, A.R., Flow through porous fences in thick boundary layers: comparisons between laboratory and numerical experiments, *Journal Wind engineering and Industrial Aerodynamics*, vol. 88, pp. 75-90, 2000.

Paterson, D.A and Apelt, C.J., Computation of wind flows around three dimensional buildings, *Journal of Wind Engineering and Industrial Aerodynamics*, vol. 24, pp. 193-213, 1986.

Paterson, D.A and Apelt, C.J., Simulation of flow past a cube in a turbulent boundary layer, *Journal of Wind Engineering and Industrial Aerodynamics*, vol. 35, pp. 149-176, 1990.

Perera, M.D.A.E.S., Shelter behind two-dimensional solid and porous fences, *Journal of Wind Engineering and Industrial Aerodynamics*, vol. 8, pp. 93-104, 1981.

Peterka, J.A. and Petersen, R.L., On the relaxation of saltation length as a modeling criteria for particulate transport by wind, *Journal of Wind Engineering and Industrial Aerodynamics*, vol. 36, pp. 867-876, 1990.



Pomeroy, J.W., Wind transport of snow, PhD Thesis, Division of Hydrology, University of Saskatchewan, Saskatoon, Saskatchewan, 1988.

Pomeroy, J.W., A process-based model of snow drifting, *Annals of Glaciology*, vol.13, pp. 237-240, 1989.

Pomeroy, J.W. and Gray, D.M., Saltation of snow, *Water Resources Research*, vol. 26, no. 7, pp. 1583-1594, 1990.

Pomeroy, J.W. and Male, D.H., Steady-state suspension of snow, *Journal of Hydrology*, vol. 136, pp. 275-301, 1992.

Radok, U., Snow drift, *Journal of Glaciology*, vol. 19, no. 81, pp. 123-139, 1977.

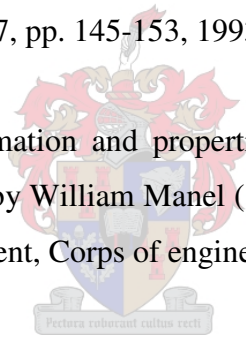
Ranga Raju, K.G., Garde, R.J., Singh, S.K. and Singh, N., Experimental study on characteristics of flow past porous fences, *Journal of Wind Engineering and Industrial aerodynamics*, vol. 29, pp. 155-163, 1988.

Rasmus, K., personal communication, FINNARP 2000, Division of Geophysics, Department of Physical Sciences, University of Helsinki, Finland, kai.easmus@helsinki.fi.2000.

Raupach, M.R. and Lu, H., Representation of land-surface processes in aeolian transport models, *Environmental Modelling and Software*, vol. 19, pp. 93-112, 2004.

Richards, P.J. and Hoxey, R.P., Appropriate boundary conditions for computational wind engineering models using the k- ϵ turbulence model, *Journal of Wind Engineering and Industrial aerodynamics*, vol. 46 & 47, pp. 145-153, 1993.

Rikhter, R.D., Snow cover, its formation and properties, Moscow-Leningrad, Izdatel stvo Akademia NAUK SSSR, translated by William Manel (150) rev. ed., Translation 6, Snow Ice and Permafrost Research Establishment, Corps of engineers, US Army, pp. 66 , 1945.



Roots, E.F. and Swithinbank, C.W.M., Snow drifts around buildings and stores, *Polar Record*, vol. 7, pp. 380-387, 1955.

Saffman, P.G., The lift on a small sphere in a slow shear flow, *Journal of Fluid Mechanics*, vol. 22, pp.385, 1965.

Sakamoto H. and Arie, M., Flow around a cubic body immersed in a turbulent boundary layer, *Journal of Wind Engineering and Industrial Aerodynamics*, vol. 9, pp 275-293, 1982.

Sato, T., Uematsu, T., Nakata, T. and Kaneda, Y., Three dimensional numerical simulation of snowdrift, *Journal of Wind Engineering and Industrial Aerodynamics*, vol. 46-47, pp. 741-746, 1993.

Schmidt, R.A., Threshold wind-speeds and elastic impact in snow transport, *Journal of Glaciology*, vol. 26, no. 94, pp. 453-467, 1980.

Schmidt, R.A., Estimates of threshold windspeed from particle sizes in blowing snow, *Cold Regions Science and Technology*, vol. 4, pp. 187-193, 1981.

Schmidt, R.A., Vertical profiles of wind speed, snow concentration, and humidity in blowing snow, *Boundary-layer Meteorology*, vol. 23, pp. 223-246, 1982.

Schmidt, R.A., Snow surface strength and the efficiency of relocation by wind, *Cold regions hydrology symposium*, American Water Resources Association, pp. 355-358, 1986a.

Schmidt, R.A., Transport rate of drifting snow and the mean wind speed profile, *Boundary-layer Meteorology*, vol. 34, pp. 213-241, 1986b.

Shah, K.B. and Ferziger, J.H., A fluid mechanics view of wind engineering: Large eddy simulation of flow past a cubic obstacle, *Journal of Wind Engineering and Industrial Aerodynamics*, vol. 67&68, pp. 211-224, 1997.

Shiotani, M and Arai, H., A short note on the snow storm, *Congress of Applied Mechanics*, Science council of Japan, 1953.

Smedley, D.J., Kwok, K.C.S. and Kim, D.H., Snowdrifting simulation around Davis Station workshop, *Antarctica, Journal of Wind Engineering and Industrial Aerodynamics*, vol. 50, pp. 153-162, 1993.

Sommerfield, R. and Businger, J.A, The density profile of blown snow, *Journal of Geophysical Research*, vol. 70, no. 14, pp. 3303-3306, 1965.

Soo, S.L., *Multiphase fluid dynamics*, Sciences Press, Beijing, China, 1990.

Sugiura, K., Nishimura, K., Maeno, N. and Kimura, T., Measurements of snow mass flux and transport rate at different particle diameters in drifting snow, *Cold Regions Science and Technology*, vol. 27, pp. 83-89, 1998.

Sun, X., Ishii, M., Kelly, J.M., Modified two-fluid model for the two-group interfacial area transport equation, *Annals of Nuclear Energy*, vol. 30, pp. 1601-1622, 2003.

Sundsbo, P.A., Numerical modelling and simulation of snow drift, PhD Thesis, The Norwegian University Science and Technology, Trondheim, Norway. Narvik Institute of Technology, Department of Building Science, Narvik, Norway, 1997.

Sundsbo, P.A., Numerical simulation of wind deflection fins to control snow accumulation in building steps, *Journal of Wind Engineering and Industrial Aerodynamics*, vol. 74-76, pp. 543-552, 1998.

Sundsbo, P.A. and Bang, B., Snow drift control in residential areas – field measurements and numerical simulations, *Proceedures of the 4th International Conference on Snow Engineering*, pp. 377-382, Trondheim, Norway, 2000.

Sundsbo, P.A., Blower snow fence application in North Norway, personal communication, pas@hin.no, 2003.

Tabler, R.D., Self-similarity of wind profiles in blowing snow allows outdoor modelling, *Journal of Glaciology*, vol. 26, no. 94, pp. 421-434, 1980a.

Tabler, R.D., Geometry and density of drift formed by snow fences, *Journal of Glaciology*, vol. 26, no. 94, pp. 405-419, 1980b.

Tabler, R.D., Snow transport as a function of wind speed and height, *Cold Regions Engineering: Proceedings of the 6th International Specialty Conference*, pp. 729-738, 1991a.

Tabler, R.D., Snow fence guide, Strategic Highway Research Program, National Research Council, Washington DC, report number, SHRP-W/FR-91-106, pp. 1-61, 1991b.

Takahashi, S., Characteristics of drifting snow at Mizuho station, Antarctica, *Annals of Glaciology*, vol. 6, pp. 71-75, 1985.

Takeuchi, M. and Fukuzawa, Y., Light attenuation and visibility in blowing snow, *Annals of Glaciology*, vol. 6, pp. 311-313, 1985.

Takeuchi, M., Vertical profile and horizontal increase of snow-drift, *Journal of Glaciology*, vol. 29, pp. 481-492, 1980.

Thiis, T.K., Large-scale measurements of snowdrifts around flat-roofed and single-pitch-roofed buildings, *Cold Regions Science and Technology*, vol. 30, pp. 175-181, 1999.

Thiis, T.K., Experimental validations of numerical simulations of snowdrifts around buildings and in terrain, PhD Thesis, The Norwegian University Science and Technology, Trondheim, Norway, Narvik Institute of Technology, Department of Building Science, Narvik, Norway, 2000.

Thiis, T.K., Large scale studies of development of snowdrifts around buildings, *Journal of Wind Engineering and Industrial Aerodynamics*, vol. 91, pp. 829-839, 2003.

Tominaga, Y. and Mochida, A., CFD prediction of flowfield and snowdrift around a building complex in a snowy region, *Journal of Wind Engineering and Industrial Aerodynamics*, vol. 81, pp. 273-282, 1999.

Tsuchiya, M., Murakami, S., Mochida, A., Kondo, K. and Ishida, Y., Development of a new k- ϵ model for flow and pressure fields around a bluff body, *Journal of Wind Engineering and Industrial Aerodynamics*, vol. 67 and 68, pp. 169-182, 1997.

Tsuchiya, M., Tomabechei, T. and Ueda, H., Wind effects on snowdrift on stepped flat roofs, *Journal of Wind Engineering and Industrial Aerodynamics*, vol. 90, pp. 1881-1892, 2002.

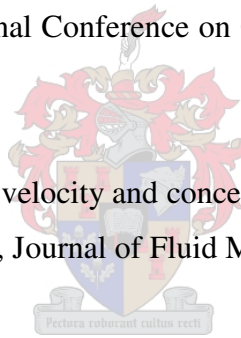
Tsukiyama, H., Tajima, Y., Yao, M. and Arai, H., Solution method of the time transient moving boundary problems using generalized porous media technique, *Journal of Wind Engineering and Industrial Aerodynamics*, vol. 46 & 47, pp. 381-391, 1993.

Tu, J.Y., Fletcher, A.J. and Behnia, M., Numerical modelling of three-dimensional fly-ash flow in power utility boilers, *International Journal of Numerical Methods in Fluids*, vol. 24, pp. 787-807, 1997.

Van den Broeke, M., Van As, D., Boot, W. and Snellen, H., EPICA-Netherlands Atmospheric boundary layer experiment (ENABLE), Kohnen and Neumayer station, December 2001-March 2002, Institute for Marine and Atmospheric Research, Utrecht University, The Netherlands, 2002.

Waechter, B.F. and Williams, C.J., Snowdrift design guidance for the New South Pole Station, *Procedures of the International Conference on Cold Regions Engineering ASCE*, pp. 57-68, 1999.

Wang, L. and Maxey, M.R., Settling velocity and concentration distribution of heavy particles in homogeneous isotropic turbulence, *Journal of Fluid Mechanics*, vol. 256, pp. 27-68, 1993.



Wang, Q. and Squires, K.D., Large eddy simulation of particle deposition in a vertical turbulent channel flow, *International Journal for Multiphase Flow*, 22 no. 4 pp. 667-683, 1996.

Wang, Q., Squires, K.D., Chen, M. and McLaughlin, J.B., On the role of the lift force in turbulence simulations of particle deposition, *International Journal of Multiphase Flow*, vol. 23 no. 4, pp. 749-763, 1997.

Weubben, J.L., A hydraulic model investigation of drifting snow, US Cold Regions Research and Engineering Laboratory, report 79-16, 1978.

White, F.M., *Viscous fluid flow*, 2nd edition, MCraw-Hill, New York, USA, 1991.

Wilcox, D.C., Turbulence modelling for CFD, DWC Industries, La Canada, USA, 1993.

Wilson, J.D., Numerical studies of flow through a windbreak, *Journal of Wind engineering and Industrial Aerodynamics*, vol. 21, pp. 119-154, 1985.

Xiao, J., Bintanja, R., Déry, S.J., Mann, G.W. and Taylor, P.A., An intercomparison among four models of blowing snow, *Boundary-layer Meteorology*, 97, pp. 109-135, 2000.

Zhang, J., Nieh, S. and Zhou, L., A new version of algebraic stress model for simulating strongly swirling turbulent flows, *Numerical Heat Transfer, Part B*, vol. 22, pp. 49-62, 1992.

Zhonglong, W. and Yuan, C., Research and prevention of snow-drifts by blower fences, *Journal of Glaciology*, vol. 26, no. 94, pp. 435-445, 1980.

